Effects of disorder in iron-based superconductors

Sultan Demirdis

Effects of Disorder in Iron-Based Superconductors

Sultan Demirdiş
Laboratoire des Solides Irradiés
Ecole Polytechnique

Thése pour l'obtention du grade de

Docteur de l'Ecole Polytechnique

Soutenue publiquement le 18 décembre 2012 devant le jury composé de:

Thierry Klein	Président
Cyril Proust	Raporteur
Christoph Meingast	Raporteur
Véronique Brouet	Examinateur
Dimitri Roditchev	Examinateur
Luca Perfetti	Examinateur
Cornelis Jacominus van der Beek	Directeur

Décembre, 2012

Acknowledgements

La préparation de cette thèse réalisée au sein du Laboratoire des Solides Irradiés m'a permis de collaborer avec plusieurs personnes qui m'ont beaucoup appris et ont contribué de façons diverses à mon travail. Je voudrais tout d'abord remercier mon directeur de thèse, Kees van der Beek, avec qui j'ai parcouru un long chemin depuis notre connaissance en 2007 alors que j'étais une étudiante qui commencait son Master en Turquie. Dès notre premier contact il m'a fait confiance et a soutenu ma volonté et mon enthousiasme pour venir faire ma thése en France, à l'école Polytechnique. Merci Kees, pour ta patience, ta disponibilité et pour toutes les connaissances que tu m'as transmises. Je remercie Martine Soyer, notre directrice du laboratoire, pour sa disponibilité et son écoute en cas de problème divers qu'une étudiante étrangère comme moi peut rencontrer au cours de ces trois années. Je remercie Marcin Konczykowski pour son accueil au sein de l'équipe Supra. Je remercie les membres de jury d'avoir accepté d'évaluer mon travail et en particulier mes deux rapporteurs qui ont lu mon manuscrit en détail et m'ont aidé á l'améliorer.

Une thèse expérimentale ne peut pas être réalisée sans échantillons, pour cela je voudrais remercier nos collaboratrices, Florence Rullier-Albenque, Dorothée Colson et Anne Forget pour nous avoir fourni les cristaux supraconducteurs à base de fer de la famille "122" dopès au Co et au Ni. Je remercie aussi nos collaborateurs japonais, Takasada Shibauchi et plus particulièrement Shigeru Kasahara qui a synthétisé les cristaux de $BaFe_2As_2$ dopé au P.

J'ai eu aussi l'occasion de voyager au cours de cette thèse; en Pologne, en France, en Écosse et deux fois en Argentine pour la réalisation des expériences de décoration de Bitter. À ce propos, je voudrais remercier à Hernan Pastoriza pour son accueil dans son laboratoire (Laboratorio de Bajas Temperaturas) à Bariloche et pour le diner très convivial chez lui où nous (Kees, Yanina, Moira et Moi) avons eu le plaisir de gouter à ses délicieuses pizzas. Yanina Fasano a été une collègue puis une amie, merci de m'avoir hébergé chez toi une semaine quand la maison d'hôte du centre était en rénovation. Yanina m'a

initié à la technique de décoration de Bitter et m'a permis de me sentir comme chez moi par rapport à l'utilisation et manipulation de tous ses équipements. Je n'oublie pas bien sure mes amis argentins sans lesquels ces deux moi en Argentine n'auraient pas été pareils. René merci pour ta disponibilité et tes coups de main quand j'en avais besoin, je te souhaite une bonne continuation dans la science, bon courage pour la fin de thèse et une vie heureuse avec ta jolie Valeria. Je remercie Juan pour les mesures de profilomètre à Bariloche. Moira, merci pour ta bonne humeur, tes conseils encourageants, ton amitié et pour la belle soirée que nous avons passée (Kees,Fede, Moira,Matilde,Tatiana et Moi) dans ton appartement lors de ton séjour à l'école Polytechnique. Je te souhaite une vie heureuse avec Fede et ta petite Matilde. Revenons au LSI, comment ne pas remercier Jérôme, notre ingénieure crygéniste avec qui j'ai commencé vraiment du niveau de "cryogenics for dummies" et nous sommes arrivés à mettre en place une nouvelle technique expérimentale, un nouveau cryostat pour la mesure de résistance de surface. Je te souhaite, une bonne continuation dans ta vie professionnelle et une vie heureuse avec Émilie et tes deux petites filles Jeanne et Manon. Je voudrais ici remercier aussi Piotr Gierlowski qui est un spécialiste dans le domaine des hyperfréquences et qui nous a fourni la cavité résonante en Nb. Je remercie Julien qui de nombreuses fois m'a donné un coup de main avec l'analyseur de réseau. Je remercie Isabelle Maurin du PMC pour m'avoir donné libre accès pour l'utilisation du SQUID. Merci à Pierre Eugène pour le coup de main avec le MET pour mes échantillons irradiés , même si ce travail laborieux n'a pas abouti au succès. Je voudrais aussi citer l'équipe Sirius; Vincent, Bruno, Thierry. Je remercie aussi le personnel administratif du laboratoire, Christine, Isabelle, Sylvie et Sabrina.

Je rétrécis mon cercle et voudrais faire un clin d'oeil à tous mes amis qui m'ont accompagné au quotidien. Tatiana, une amie toujours de bon conseil, une collègue prête à vous aider et dépanner quand vous en avez besoin, notre organisatrice de sortie et notre pâtissière préférée, tes gâteaux vont nous manquer. Mi, très heurese de t'avoir connue et encore merci pour toutes les petites attentions que tu as eues pour nous. Je vous souhaite à toutes les deux le meilleur pour votre vie professionnelle et personnelle. Haad, merci pour ta compagnie sur ce campus désert de l'X, pour nos sorties shopping et nos longues discussions autour d'une tasse de thé. Je souhaite la réalisation de tous tes projets futurs. Ikbal merci de m'avoir tenue compagnie durant ton bref passage au LSI, je te souhaite la réussite dans ta thèse. Ngoc , je te félicite pour ton courage et

te souhaite une bonne continuation et une longue vie heureuse avec ta petite famille. Willem bon courage pour la suite, je te promets de te rappeler pour l'Oktoberfest.

Je conclus avec une pensée à ma famille, je remercie ma mère et mon père qui sont en Turquie, pour leur soutien. Je remercie mon frère pour son accueil dès mon arrivée en France et pour nos voyages de découverte en France et en Europe. J'espère t'accueillir bientôt au nouveau chez moi et nous allons bien sures continuer nos voyages de découvertes en Europe. Merci aussi pour le coup de main pour l'organisation du pot et pour sa logistique, évidemment tu es l'homme de la situation.

Sultan Demirdiş

Abstract

The pinning of vortices is used as a probe for the identification of disorder and its effect on superconductivity in 122-type iron-based superconductors. Using a new analysis method taking into account the interaction of individual vortices with their neighbors, pinning energies and pinning forces in $Ba(Fe_{1-x}Co_x)_2As_2$ are extracted from the vortex distributions in the regime of small fields. The correlation of measurements of the critical current density j_c with the spatial distribution of vortices shows that pinning in this particular regime is due to the heterogeneity of superconducting properties, on the scale of 20-100 nm. Application of the same analysis procedure on the vortex structure in $BaFe_2(As_{1-x}P_x)_2$ with less density fluctuations, shows that the pinning forces and energies depend on the doping level x. Both j_c measurements and pinning force distributions independently yield a mean distance between pinning centers of about 90 nm, increasing with increasing P-content x. Combination of the above results and critical current density measurements lead to the conclusion that the low field plateau observed in j_c curves, followed by a power-law decrease, emerges from strong pinning due to nm scale heterogeneity of superconducting properties. Attention is also paid to the weak collective pinning contribution that manifests itself at higher fields > 1 T. Notably, this contribution is consistently analyzed in terms of quasiparticle scattering and mean free path fluctuations. In order to test this premise irradiation of Co, Ni and P-doped 122-type iron-based compounds with high-energy 2.5 MeV electrons is performed for several doping levels of the materials and to different doses. Such irradiation introduces atomic sized point-like defects. Following irradiation it appears that the critical temperature T_c shows a similar depression for all studied materials. The weak collective contribution to j_c in Co-doped is found to clearly increase. Moreover this contribution appears after irradiation of the P-doped compound in which it was previously absent. This allows one to confirm the role of atomic point-like pins as scatterers in Ni and Co-doped compounds, as well as the hypothesis that these defects are at the origin of the weak collective pinning contribution to j_c at larger fields.

L'ancrage des vortex est utilisé comme une sonde pour l'identification du type de désordre et son effet sur la supraconductivité dans la famille 122 des supraconducteurs à base de fer. Une nouvelle technique d'analyse obtenue d'images de décoration de Bitter prenant en compte l'interaction de chaque vortex avec ses voisins, a permis d'obtenir l'énergie et la force de piégeage dans $Ba(Fe_{1-x}Co_x)_2As_2$, dans le régime de bas champ magnétique. La corrélation avec des mesures de courant critique j_c a montré que le piégeage des vortex dans ce composé est due à l'hétérogénéité des propriétés supraconductrices sur une échelle de 20-100 nm. Application de la même méthode d'analyse pour les vortex dans le $BaFe_2(As_{1-x}P_x)_2$ a montré que l'énergie et la force d'ancrage dépendent du dopage x. Les mesures de j_c et de la distribution des forces de piégeage ont montré que la distance moyenne entre différents centres de piégeage est de l'ordre de 90 nm et que cette distance augmente quand on augmente le conteneur en P. La combinaison de ces résultats avec les mesures de j_c mène à la conclusion que l'ancrage fort des lignes de flux due à l'hétérogénéité des propriétés supraconductrice à l'échelle de nm est à l'origine de la constante observé à des champ faibles dans les courbes de j_c ainsi que la diminution en loi de puissance qui suit. On traite également la contribution d'ancrage faible collectif à j_c, qui se manifeste à des champs magnétiques plus importants, de l'ordre de 1 T. Cette contribution a été analysée en terme de la diffusion des quasiparticules et de la fluctuation spatiale du libre parcours moyen. Afin de tester l'hypothèse avancé ci-dessus, l'irradiation aux électrons d'énergie 2.5 MeV, sur les composés dopé au Co, Ni et P de la famille 122 a été réalisé à des différentes doses pour plusieurs dopage de ces matériaux. Ce type d'irradiation introduit des défauts ponctuels de taille atomique dans le matériau. La température critique T_c de tous les matériaux étudiés diminue après irradiation de façon similaire. Une claire augmentation de la contribution d'ancrage faible collectif à j_c dans le composé dopé au Co a été observée. De plus, cette contribution qui, avant irradiation, était absente dans tous les dopages du composé au P, apparait après irradiation. Les défauts ponctuels de taille atomique, diffuseur des quasiparticules, dans les supraconducteurs à base de fer sont donc à l'origine de la contribution d'ancrage faible collectif à j_c.

Contents

List of Figures

LIST OF FIGURES

Chapter 1

Motivations

A new type of $s_{\pm}$ superconductivity involving strong coupling between electron and hole bands and a sign change of the superconducting order parameter has been proposed for iron-based superconductors (a new family discovered in 2008) as one goes from one band to another. Several experimental studies have been performed on different compounds of this new family of materials in order to probe the existence or the absence of sign-changing in the order parameter. On the other hand, it is predicted that in the case of a sign-changing s-wave symmetry, superconductivity is very sensitive to the crystalline disorder, and, more particularly, to interband quasiparticle scattering.

The goal of the thesis is the identification of crystalline disorder in iron-based superconductors, and its effect on their electronic properties and superconductivity. For this, different experimental approaches are used. The first, well recognized for applied aspects of superconductivity, but less so for accessing more fundamental studies, is the characterization of crystalline disorder by the measurement of the vortex pinning properties and the critical current density. The second is the measurement of the surface resistance, which, in the superconducting state, is representative of the quasiparticle density of states and scattering.

It was proposed that in iron based superconductors [44], for magnetic fields above 1 T the critical current density is determined by the scattering of quasiparticles in the vortex cores, a mechanism effective due to the small-scale (< 3 nm) fluctuations of the dopant atom positions. In addition to this, the remarkable absence of this mechanism in the isovalently substituted $BaFe_2(As_{1-x}P_x)_2$ material, in contrast to other compounds of the same family, suggested that the charged carried by the dopant atoms might are responsible for flux pinning mediated by quasiparticle scattering [44].

In addition to this, vortex imaging studies performed using different techniques and

by several groups in a large range of magnetic field from 0.1 T up to 9 T have revealed highly disordered vortex structure in all studied compounds. In our Bitter decoration study performed on different compounds of the 122 family, we have pointed out by correlating different experimental techniques (DMO, j_c measurements, Bitter decoration) that spatial heterogeneity of superconducting properties on nm scale is at the origin of flux pinning mechanism and the critical current density for this particular regime of low magnetic fields. These nm scale heterogeneity also reported on the STS/STM studies of the same compound by different groups [75; 277] supported the existence of important spatial variations of superfluid density, and, becomes a possible candidate as being at the origin of the so called phase coexistence in the underdoped regime of 122 type compounds.

In order to test these ideas, high energy electron irradiation of the different materials under study is performed using the Pelletron accelerator Sirius of the Laboratoire des Solides Irradiés. This kind of irradiation introduces microscopic point defects (Frenkel pairs), with a density proportional to the electron dose. The effect of these irradiations on different physical properties of the iron-based superconductors, such as the critical temperature T_c, the critical current density j_c and surface resistance R_s were studied in order to better understand the quasiparticle scattering mechanism and the effects of atomic sized point-like disorder.

In the introduction 2 are discussed the basic phenomena of superconductivity, the characteristic lengths such as the penetration depth λ_L and the coherence length ξ as well as the superconducting gap. After the description the mixed state in Type II superconductors and vortices, the vortex dynamics and vortex pinning theories are discussed in details. Chapter 3 is an introductory chapter for iron-based superconductors that presents the generic phase diagrams and band structures for different type of compounds, the antiferromagnetic order of parent compounds and the superconducting gap structure are also discussed. A summary of recent experimental results revealed by different techniques is also presented in this chapter that ends with a state of art of the vortex pinning studies performed on iron-based superconductors.

Chapter 4 is one of the experimental chapters where the magneto-optical imaging (MOI) technique is described in details with the working principle of the setup and its physical basis. Faraday effect which is at the origin of this technique is also described. MOI technique allows one to discard samples with macroscopic defects as well as those with important chemical heterogeneities before further experimental studies. The temperature dependence of the critical current density and the with of the superconducting transition can be measured with this technique. Few examples of these measurements were presented in this chapter that ends by the description of an other complementary experimental technique,

Hall probe magnetometry, that allowed us to perform local magnetic measurements at larger fields up to 2 T.

In Chapter 5 one can find an historical overview of the Bitter decoration technique used in this thesis. The physical basis of this technique and the experimental working principle of the setup used in this work are also discussed.

In Chapter 6, a study of the vortex pinning in the Co-doped $BaFe_2As_2$ is presented. Amorphous vortex configurations observed in this compound using Bitter decoration technique were studied using a new analysis technique, that takes into account the interaction of individual vortices with their neighbors. Then the correlation of the Bitter decoration datas and the critical current densities were presented. The latter revealed that the heterogeneity of the superconducting properties such as the spatial heterogeneity of T_c on the nm scale is the origin of the observed highly disordered vortex ensembles as well as the strong pinning mechanism at the origin of the low-field critical current density.

In Chapter 7 presents the study of vortex pinning , using the same data analysis procedure, in the isovalently substituted $BaFe_2(As_{1-x}P_x)_2$. The study revealed vortex ensembles with less density fluctuations in this compound. Analysis of the Bitter decoration images allowed us to extract the pinning forces and pinning energies of this compound. It is found that the mean distance between effective pins is about 90 nm and that increases when one increases the P content x. This result is found in agreement with the evolution of the mean free path of the β orbits with P content x reported in the literature by Shishido *et. al.* The weak collective pinning contribution to the critical current density is also considered for this compound and is found absent in all doping levels. This pinning mechanism was proposed to be due to the quasiparticles in the vortex cores; it manifest itself as a second plateau, at magnetic fields above a few tenths of a T to 1 T.

In order to link the flux pinning properties in the regime of quasi-particle scattering rate, a new experimental setup based on the cavity perturbation method that is described in Chapter 8. This chapter presents in details the cavity perturbation experiment established for the measurements of the surface resistance R_s. In addition to this atomic-sized point like disorder is introduced using high-energy 2.5 MeV electron irradiation with the Pelletron accelerator SIRIUS of the Labpratoire des Solides Irradiés. In Chapter 9, a systematic study of the evolution of different superconducting properties under the effect of electron irradiation for $Ba(Fe_{1-x}Co_x)_2As_2$ $BaFe_2(As_{1-x}P_x)_2$ and $Ba(Fe_{1-x}Ni_x)_2As_2$ single crystals is presented. An important annealing effect (70 %) for the Co-doped samples is revealed when the crystals are heated to room temperature after low temperature irradiation. The magnitude of the contribution to the critical current density at larger fields above 1 T is found clearly to increase in the Co-doped compound, while this contribution absent in all

doping levels previously in the P-doped compounds appears clearly after the introduction of point-like defects by electron irradiation. From the increase of the weak collective pinning contribution to j_c, the number of defects (Fe vacancies) created by irradiation is estimated. The measured surface impedance for Ni and Co-doped samples before and after electron after irradiation increases. These results allowed us to confirm the role of the atomic-sized defects as scatterers in iron-based superconductors, as well as the hypothesis that these defects are at the origin of the weak collective pinning contribution to j_c.

Chapter 2

Introduction

Superconductivity was discovered in 1911 by the physicist Heike Kamerlingh Onnes in Leiden university in the Netherlands [105]. This remarkable phenomenon is a combination of electric and magnetic properties that appear in certain metals when they are cooled down to low temperature. Such low temperatures first became available in 1908 when Heike Kamerlingh Onnes liquified helium and reached 4.2K. He then decided to study the resistivity of metals at low temperatures and proposed to study Hg, the purest available metal of that time. The repeated experiments confirmed that the resistance of mercury goes sharply to zero at the critical temperature T_c=4.15 K (see Figure 2.1). Later on Kamerlingh Onnes discovered that lead and tin (rather bad conductors at room temperature) also present zero resistance below T_c=6 K and 3.7 K respectively. Kamerlingh Onnes recognized that this was a new state of the material with electrical properties quite unlike those previously known. This was "the superconducting state".

2.1 Basic phenomena

In 1933 W. Meissner and R. Ochsenfeld [245], discovered that a superconductor, cooled down below T_c, excludes the magnetic field and behaves like a "perfect diamagnet". They found that not only a magnetic field is excluded from entering a superconductor as might be explained by the sole property of perfect conductivity, but also that a field in a sample originally in the normal state is expelled as it is cooled through T_c. This could not be explained by perfect diamagnetism which would trap the flux. From this it was understood that it has to be an intrinsic property of the superconducting state. The existence of a reversible Meissner effect implies that superconductivity will be suppressed by a critical magnetic field H_c determined by equating the energy $\frac{1}{2}\mu_0 H^2$ per unit volume to the

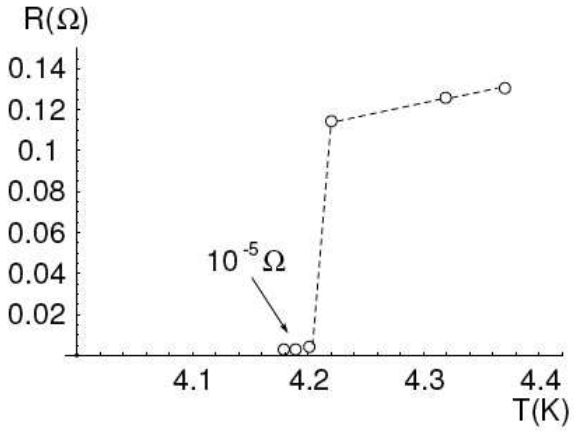

Figure 2.1 Data from Onnes pioneering works. The plot shows the electric resistance of the mercury vs. temperature.

superconducting condensation energy, i.e.

$$\frac{1}{2}\mu_0 H^2 = F_n(T) - F_s(T) \tag{2.1}$$

where, $F_n(T)$ and $F_n(T)$ are the Helmholtz energies per unit volume in zero field for the normal and superconducting states respectively. The behavior of the critical magnetic field with temperature was found empirically to be parabolic,

$$H_c(T) \approx H_c(0)\left[1 - \left(\frac{T}{T_c}\right)^2\right]. \tag{2.2}$$

In the absence of magnetic field at T=T_c the transition is of second order while in the presence of an applied field the superconducting-normal transition is of first order with associated an discontinuity in the specific heat.

An interesting observation leading to appreciate the role of phonons in superconductivity was the "isotope effect" [180; 184; 243]. It is found that the critical field in the limit of low temperature and the transition temperature T_c vary as

$$T_c \approx H_c(0) \approx \frac{1}{M^\alpha}, \tag{2.3}$$

where M is the isotopic mass of the material. Inspired by this result Daunt and Mendelssohn suggested, in 1946, the existence of an energy gap Δ of order of $k_B T_c$, between the ground state and the quasiparticle excitations [116]. It was also predicted theoretically in 1953 by

Ginzburg and in 1956 by Bardeen. Quantitative experimental evidence was reported by Corak *et. al.* from precise measurements of the specific heat where the authors showed that the electronic specific heat below T_c has an exponential dependence as following [246; 247],

$$C_{es} \approx \gamma T_c a e^{-bT_c/T} \tag{2.4}$$

here, the normal state electronic specific heat is given by $C_{en}=\gamma T$, a and b are numerical constants. This implies a minimum excitation energy per particle of about 1.5 T_c. The presence of the energy gap in the spectrum of the elementary excitations has been observed in many ways. The existence of the gap was confirmed experimentally by electromagnetic absorption measurements performed by Glover and Tinkham in 1956 [187] . Figure 2.2 shows the threshold for the absorption of electromagnetic radiation, or the threshold voltage for electron tunneling between two films of superconducting material separated by a thin oxide layer, in this case Al.

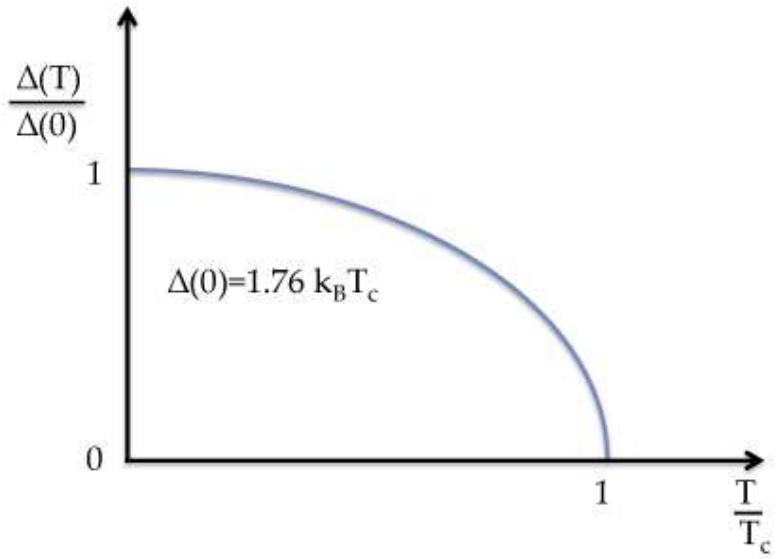

Figure 2.2 The superconducting gap versus temperature in Al determined by electron tunneling.

2.2 London penetration depth λ_L

The London brothers H. and F. London [73] have proposed a phenomenological description of the basic facts of superconductors with a theory based on a two-fluid type concept with superfluid and normal fluid densities n_s and n_n associated with velocities v_s and v_n. The

densities satisfy n_s+n_n=n, where n is the average electron number per unit volume. When a time-varying magnetic field is applied on a superconductor, this produces an electric field obeying the Maxwell's equation $\nabla \times \vec{E} = -\partial B/\partial t$. In a normal metal the presence of this electric field is responsible for the generation of eddy currents, while in superconductors it leads to the acceleration of the superfluid current. The resulting super-current give rise to a magnetic field of direction opposite to that of the external field. If the external applied field is weak enough, the magnetic field lines are totally excluded from the superconducting volume screened by the super-current. This 'perfect diamagnetism' can be described by the theory of the London brothers [73].

The force exerted on the super-electrons (Cooper pairs)of mass m and charge -2e under an electric field is given by

$$\vec{F} = m^* \frac{\mathbf{d}\vec{v_s}}{dt} = -2e\vec{E} \tag{2.5}$$

where $\vec{v_s}$ represents the velocity of superfluid carriers. The super-current density is

$$\mathbf{J} = -2en_s\vec{v}_s, \tag{2.6}$$

where n_s is the local density of the superconducting carrier. By combining Equation (2.5) and (2.6) one obtains the first London equation ("so called acceleration equation")

$$\frac{\mathbf{d}\vec{J}_s}{dt} = \frac{n_s e^2}{m}\vec{E}. \tag{2.7}$$

We are only interested in the stationary state i.e., we assume n_n and n_s to be uniform in space, this is the restriction of the London theory, which will overcome Ginzburg-Landau theory. The curl of the first London equation is,

$$\frac{\partial}{\partial t}\nabla \times \vec{J}_s = \frac{n_s e^2}{m}\nabla\vec{E} = -\frac{n_s e^2}{m}\frac{\partial \mathbf{B}}{\partial t}. \tag{2.8}$$

This can be integrated in time to give,

$$\nabla \times \vec{J}_s = -\frac{n_s e^2}{m}\mathbf{B} + \mathbf{C}(\mathbf{r}) \tag{2.9}$$

where the last term is the integration constant at each point inside the superconductor. $\mathbf{C}(\mathbf{r})$ should be determined from the initial conditions. If we start from a superconducting material in zero applied magnetic field , one has $\vec{J}_s \equiv 0$ and $\mathbf{B} \equiv 0$ initially so that $\mathbf{C}(\mathbf{r}) = 0$. To describe the Meissner-Ochsenfeld effect, one has to consider the case of a material becoming superconducting (by cooling) in a non-zero applied field. To account for the flux expulsion, the Londons postulated that $\mathbf{C} \equiv 0$ regardless of the history of the

system. this leads to

$$\nabla \times \vec{J_s} = -\frac{n_s e^2}{m}\mathbf{B}, \tag{2.10}$$

the second London equation. Together with Ampére's law,

$$\nabla \times \mathbf{B} = \mu_0 \vec{J_s} + \mu_0 \vec{J_n} \tag{2.11}$$

there is no displacement current in the stationary state, one has,

$$\nabla \times \nabla \times \mathbf{B} = -\frac{4\mu_0 n_s e^2}{m^*}\mathbf{B} + \mu_0 \sigma_n \nabla \times \mathbf{E} = -\frac{4\mu_0 n_s e^2}{m^*}\mathbf{B} - \mu_0 \sigma_n \frac{\partial \mathbf{B}}{\partial t}. \tag{2.12}$$

One drops the last term since we are interested in the stationary state using an identity of vector calculus,

$$-\nabla(\nabla.\mathbf{B}) + \nabla^2 \mathbf{B} = \frac{4\mu_0 n_s e^2}{m^*}\mathbf{B}, \tag{2.13}$$

or

$$\nabla^2 \mathbf{B} = \frac{1}{\lambda^2}\mathbf{B} \tag{2.14}$$

where λ is the London penetration depth of the superconductor (see Figure 2.3),

$$\lambda = \sqrt{\frac{m^*}{4\mu_0 n_s e^2}}. \tag{2.15}$$

In order to take into account the temperature dependence Gorter and Casimir [39] considered n to be the total density of carriers and separated it into n_n , the density carriers in normal state and n_s, the density carriers in the superconducting state. At low temperature ($T < T_c$) $n = n_s$ and $n_n = 0$, while above T_c, n=n_n and n_s=0. They derived the relative on $n_s(T) = n[1-(T/T_c)^4]$, correct especially for temperatures close to T_c. The temperature dependence of the London penetration depth λ_L is given by

$$\lambda(T) = \frac{\lambda(0)}{\left[1 - \left(\frac{T}{T_c}\right)^4\right]^{1/2}}. \tag{2.16}$$

2.3 Coherence length ξ

The coherence length is the measure of the distance within which the density of superconducting electron pairs way change in a spatially varying magnetic field. Pippard has proposed in 1953 a modification of the London equation in which the current density at a

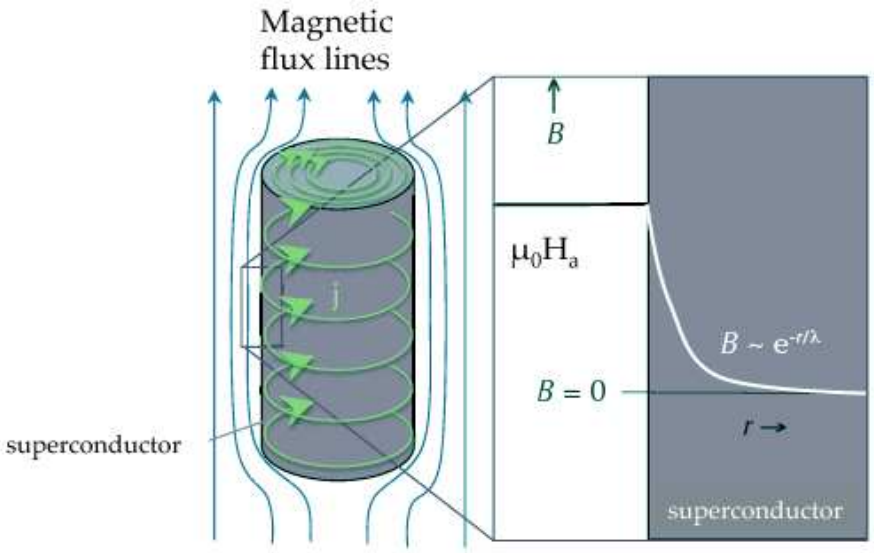

Figure 2.3 Penetration of magnetic flux into a superconductor, London penetration depth λ_L.

point is given by an integral of the vector potential over a region surrounding the point [4]

$$\mathbf{j}(\mathbf{r}) = -\frac{3}{4\pi c\Lambda\xi_0}\int \frac{\mathbf{R}[\mathbf{R}.\mathbf{A}(\mathbf{r}')]}{R^4} e^{-R/\xi} dr', \tag{2.17}$$

where $\Lambda = m/ne^2$, n is the number of superconducting electrons, $\mathbf{R} = \mathbf{r} - \mathbf{r}'$ and the effective coherence length $\frac{1}{\xi} = \frac{1}{\xi_0} + \frac{1}{l}$, where ξ_0 is the coherence length and l is the mean free path. The BCS theory evaluates the spatial distribution of the current density and exhibit it in a form similar to that proposed by Pippard. They wrote the coherence length as

$$\xi_0 \approx \frac{\hbar v_0}{kT_c}, \tag{2.18}$$

where v_0 is average velocity of electrons at Fermi surface and 0.18 is the theoretical value.

2.4 Energy gap and BCS theory

Conventional superconductivity was well described in the microscopic scale by the Bardeen, Cooper and Schrieffer (BCS theory) [111]. They have proposed that even a weak attractive interaction between electrons caused by the electron-phonon interaction leads to an instability in the Fermi sea ground state. This gives raise to the formation of bound pairs of electrons that occupy states with equal and opposite momentum and spin (see Figure 2.4).

These bounded electrons are called *Cooper pairs* .

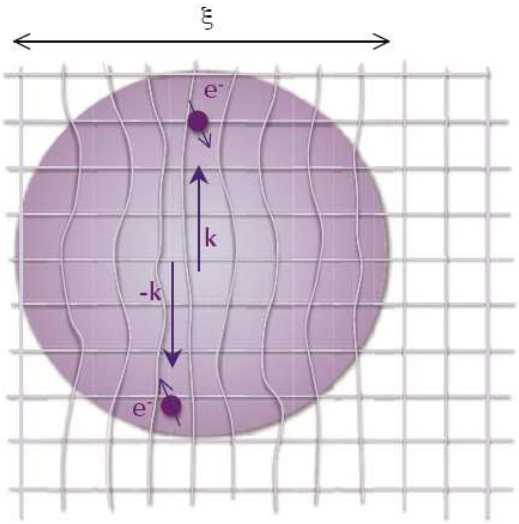

Figure 2.4 Cartoon of the formation of a Cooper pair mediated by phonon vibrations. Electrons of the Cooper pair have momentum k and -$k$and are coherent within the length ξ.

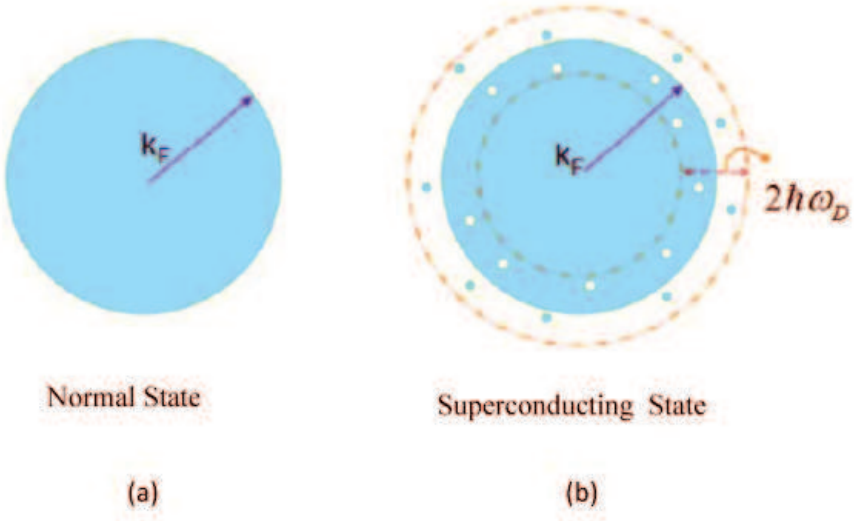

Figure 2.5 Schematic diagram of Fermi surface at (a) Normal ground state (b) Superconducting state

The bound pair is formed through the lattice polarization by the electrons. If the

electron-phonon interaction V is sufficiently important to overcome the repulsive Coulomb interaction, one will have an effective attractive interaction between the two electrons, whence they will form a Cooper pair thus we will have $e^* = 2e$ (Figure 2.4). By this interaction electrons within a thin shell of $\hbar\omega_D$ in the vicinity of the Fermi surface are attracted to each other (Figure 2.5). In the superconducting state the electrons are described by a macroscopic wave function,

$$\Psi = \sqrt{n_s}e^{i\phi} \tag{2.19}$$

The transition from the superconducting state to the normal state can be caused by the Cooper pair breaking or by the presence of the heterogeneity's which lead to the loose of the phase coherence of the Cooper pairs (the superfluid density goes to zero). The firs is classic scenario described as follows. The formation of Cooper pairs leads to an energy gap in the vicinity of the Fermi level at $T < T_{c.}$. In BCS theory, the critical temperature T_c and the superconducting energy gap Δ depends as the density state in the vicinity at the Fermi level and on the attractive potential V. This leads to a constant ratio between Δ and T_c for onventional superconductors. This result was in agreement with experimentally measured gap values [116; 164; 187]

$$\frac{2\Delta(0)}{k_B T_c} \simeq 3.53. \tag{2.20}$$

For weak-coupling superconductors, in which $\hbar\omega_D/\mathrm{k_B T_c} \gg 1$, $\Delta(\mathrm{T})/\Delta(0)$ is a universal function of $\mathrm{T/T_c}$ that decreases monotonically from 1 at T=0 to 0 at $\mathrm{T_c}$ as depicted in Figure 2.2. Close to T=0, the temperature variation is exponentially slow since $\mathrm{e}^{-\Delta/kT} \approx 0$. In this case the gap function Δ is nearly constant until an important number of quasiparticles are thermally excited. Close to the critical temperature $\mathrm{T_c}$ $\Delta(\mathrm{T})$ drops to 0 approximately as,

$$\frac{\Delta(T)}{\Delta(0)} \approx 1.74\left(1 - \frac{T}{T_c}\right)^{1/2}, T \approx T_c. \tag{2.21}$$

The elementary excitation energy can be expressed as

$$E_k = \sqrt{\varepsilon_k^2 + \Delta^2}. \tag{2.22}$$

To break a Cooper pair, an energy of at least 2Δ energy is needed (see Figure 2.6).The excitation energy is not constant as in a normal metal, but has the smallest value Δ at ε_F and larger for energies away from ε_F (see Figure 2.6). As temperature increases, more and more pairs break and the gap becomes smaller. T_c is the temperature at which the gap

decreases to 0 as shown in Figure 2.2.

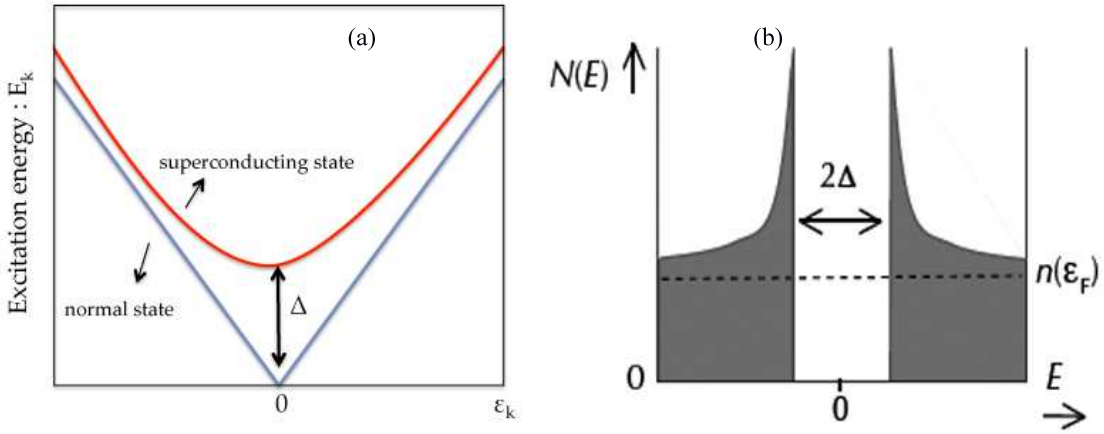

Figure 2.6 (a) Excitation energy spectrum for both superconducting and normal states. (b) Density of states for a superconductor and quasiparticle excitations.

The superconducting gap is a very important quantity in superconductors, not only because it determines their thermodynamic properties, but also it is closely related to the Cooper pairing state. By measuring the gap, information about the pairing symmetry which is determined by the pairing mechanism can be obtained. Figure 2.7 presents a schematic representation of the superconducting gap Δ in k space. Electron-phonon coupling usually leads to the isotropic s-wave symmetry with L=0 and S=0; the superconductor is called "fully gapped". For the multiband iron-based superconductors (Chapter 3) an antiferromagnetic spin fluctuation mechanism was proposed that leads to the so called $s_{\pm}$ pairing symmetry. The superconductor is fully gapped on both the electron and the hole sheets of the Fermi surface but with opposite signs between them. The anisotropic p-wave gap symmetry ($^3He, Sr_2RuO_4$) and d-wave gap symmetry characterizing the highT_c cuprates are also represented.

The magnitude of Δ a function of polar angle in k-space for different gap symmetries is clearly not the same. For different gap symmetries the angular dependence of the gap can be written as

$$g(x) = \begin{cases} 1 & \text{isotropic s-wave} \\ cos(2\varphi) & d_{x^2-y^2} - wave \\ sin(2\varphi) & d_{xy} - wave \end{cases}, \tag{2.23}$$

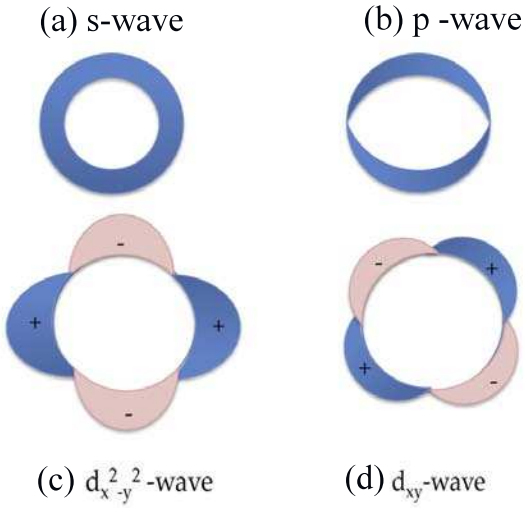

Figure 2.7 Different superconducting gap symmetry in k space.

thus the gap anisotropy is defined as

$$\Omega \equiv A - \frac{\langle \Delta(k) \rangle^2}{\langle \Delta(k)^2 \rangle} \tag{2.24}$$

which is zero for isotropic s-wave and 1 for d-wave symmetry.

2.5 Ginzburg-Landau Theory: Type I and Type II Superconductors

The Ginzburg-Landau (GL) theory derived from the Landau theory for second order thermodynamic phase transitions, postulates the existence of a superconducting order parameter represented by a complex wave function $\psi(\vec{r})$ which depends on the spatial variable (V.L. Ginzburg and L.D. Landau, 1950) [232; 237]. Its modulus is interpreted as being directly related to the superfluid density, $|\psi|^2 = n_s^*$. This theory is a generalization of the London theory in the case where the carrier density n_s^* can vary in space. In the superconducting state the GL free energy F_s is given by,

$$\mathrm{F}_s = F_n + \int_{\mathbf{v}} \left[a(T)\,|\psi(\vec{r})|^2 + \tfrac{b(T)}{2}\,|\psi(\vec{r})|^4 + \tfrac{1}{2m^*}\left|\left(\tfrac{\hbar}{i}\nabla - e^*A\right)\psi(\vec{r})\right|^2 + \tfrac{B^2}{2\mu_0} \right] \mathbf{d}^3r \quad (2.25)$$

where F_n is the free energy of the material in the normal state, V is the volume, m^* and e^* are the effective mass and the charge of the elementary carriers (Cooper pairs, the charge e^*=2e). **A** is the vector potential, **B** is the local magnetic induction in the material and a(T) and b(T) are two phenomenological constants. Sufficiently close to T_c, one can write, $a(T) = a'(T - T_c)$ where $a' > 0$ and $b(T) = b > 0$. If one minimizes the free energy F_s with respect to the order parameter ψ and the vector potential **A** one obtains two differential equations (Ginzburg-Landau equations), which describe the order parameter and the supercurrent density $\mathbf{j_s}$. From these equations, one deduces two characteristic lengths for superconductivity. The Ginzburg-Landau (GL) coherence length $\xi_{GL}(T)$ is the length scale that determines the extent of the spatial variations of the order parameter, the minimum distance on which the order parameter ψ vanishes. The coherence length can be written as:

$$\xi_{GL} = \left(\frac{\hbar^2}{2m^*|a'(T - T_c|} \right)^{1/2}. \quad (2.26)$$

The second characteristic length scale is the Ginzburg-Landau penetration depth $\lambda_{GL}(T)$, the length scale of the spatial variations of the vector potential **A** the magnetic induction **B**, and the current density **j**(**r**)

$$\lambda_{GL}(T) = \left(\frac{m^*}{(e^*)^2\mu_0 n_s^*} \right)^{1/2} = \left(\frac{m^*\beta}{(e^*)^2\mu_0|a'(T - T_c)|} \right)^{1/2}. \quad (2.27)$$

Thus we obtain the relation between the London penetration length and the Ginzburg-Landau penetration length is given as following [232; 237]

$$\lambda_L = 1.35\lambda_{GL} \quad (2.28)$$

Flux quantization in a type-II superconductor can be explained as doing analogy to the quantization of angular momentum in an atomic system. F. London introduce the concept of fluxoid $\Phi = \int \mathbf{B}.\mathbf{dS}$ associated to each normal region in the mixed state passing through

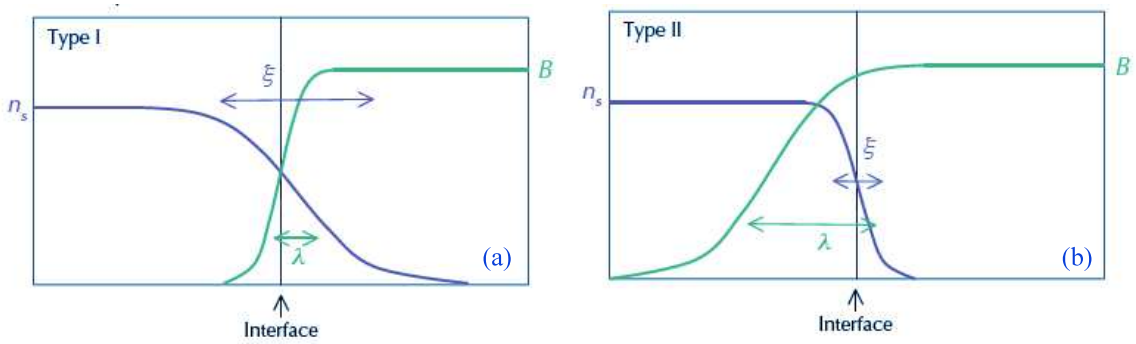

Figure 2.8 Length scales density the spatial variation of the magnetic induction B(x) and the order parameter $\psi(x)$ in type I and type II superconductors.(a)In type I superconductors $\kappa < 1/\sqrt{2}$, the system will be minimum if there is only one superconductor-normal interface at the surface of the sample the energy . (b) In a type II superconductor, $\kappa > 1/\sqrt{2}$, it will be energetically favorable to create as many as possible superconductor-normal interfaces by the penetration of the vortices (flux line) inside the sample.

the superconductor. His definition is the ordinary magnetic flux through an integration circuit. It follows that the fluxoid has the same value for any path around a given hole. Close to the critical temperature T_c , $\lambda_{GL}(T)$ and $\xi_{GL}(T)$ diverge as $(T-T_c)^{-1/2}$. Although the GL theory is valid at temperatures close to T_c, it gives consistent results over a large part of temperature range on which superconductivity exists. The GL ratio κ is given by

$$\kappa = \frac{\lambda_{GL}(T)}{\xi_{GL}(T)}. \tag{2.29}$$

This ratio allows one to classify superconductors in two types (type I and type II) such as depicted in Figure 2.8. For $\kappa < 1/\sqrt{2}$ ($\xi_{GL} > \sqrt{2}\lambda_{GL}$) , the free energy increases due to the penetration of the magnetic flux at a superconductor-normal (S-N) interface is not compensated by the condensation energy loss of the superconducting state. Thus this is energetically more favorable to limit the formation of these S-N interfaces (positive energy). The material will exclude the magnetic flux (Meissner state) until the thermodynamic critical field H_c where the condensation energy is totally compensated by the work done for diamagnetic energy. At H_a=H_c the material will transit to the normal state; this is the characteristic behavior of a type I superconductor. The thermodynamic critical field is given by

$$H_c = \frac{\phi_0}{\sqrt{8}\pi\mu_0\xi_{GL}\lambda_{GL}} \tag{2.30}$$

For $\kappa > 1/\sqrt{2}$ ($\xi_{GL}<\sqrt{2}\lambda_{GL}$), the superconducting state is stable against the formation of superconductor-normal interfaces. In 1957 Abrikosov [3] showed that an unlimited of subdivision into normal and superconducting domains until the limit ξ below which the gradient energy term would be excessive. The material is in the Meissner state until flux penetration which starts at a lower critical field called H_{c1}

$$H_{c1} \simeq \frac{\Phi_0}{4\pi\mu_0\lambda_{GL}^2}\ln(\kappa) \tag{2.31}$$

and reaching $B = H$ at the upper critical field H_{c2}

$$H_{c2} = \frac{\Phi_0}{2\pi\mu_0\xi_{GL}^2}. \tag{2.32}$$

For applied fields in the range $H_{c1} < H < H_{c2}$ the magnetic field penetrates inside the superconductor as quantized flux lines called vortices each vortex carries a flux quantum of $\Phi_0 = h/2e$ (see Figure 2.9) first predicted theoretically by Abrikosov [3]. The phase diagram of a type II superconductor is represented in Figure 2.9. Between H_{c1} and H_{c2} the superconductor is said to be in the mixed state or "Shubnikov phase", since there is a mixture of normal (vortices) and superconducting regions. The superconductivity persists until a certain upper limit of the applied magnetic field H_{c2}, above which the superconductivity is suppressed.

2.5.1 Abrikosov vortex

Because of flux quantization, the phase of the wave function of the is then 2π after a complete contour around the vortex. Thus each vortex can carry a quantum flux of Φ_0=h/2e=2.07×10^{-15} Wb. If one increases the average induction $\langle B\rangle$ in the superconductor this will only has an effect on the density of vortex inside the material which will increase $n_v=\langle B\rangle/\Phi_0$.

Abrikosov predicted theoretically, that the most energetically favorable configuration for a vortex lattice in the absence of any impurity in the superconducting material is the square array. His prediction was the square lattice with a small numerical error which was later rectified by Kleiner *et. al.* and showed that this is the hexagonal configuration which is the most favorable situation for all possible periodic [248] (see Figure 2.10). In the Meissner state $H_a<H_{c1}$ a superconducting surface current screens off the external magnetic field so that the magnetic induction B in the bulk superconductor vanishes. In the mixed state $H_{c1}<H_a<H_{c2}$ magnetic flux penetrates the superconductor in the form of vortices. As the external field increases toward H_{c2} the size of superconducting region between normal

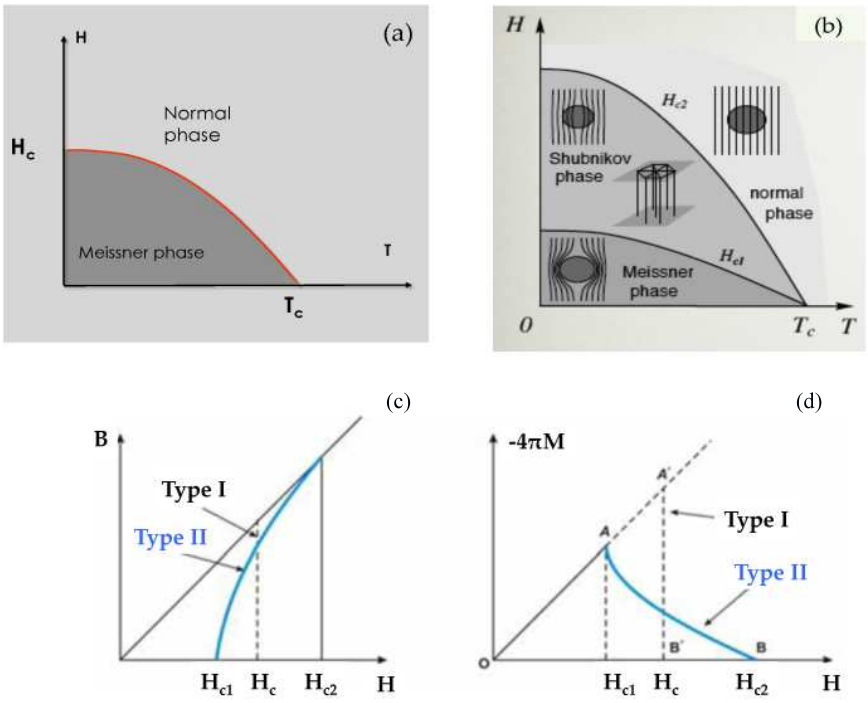

Figure 2.9 (a) Schematic (H-T) phase diagram for type I superconductors. For $H < H_c$ the superconductor is in the Meissner state and has a perfect diamagnetic behavior. For $H > H_c$ the magnetic field enter inside the totality of the superconductor and superconductivity vanishes. (b) Simplified phase digram for type II superconductors. For $H < H_{c1}$ the superconductor is in the Meissner state. The magnetic flux penetrates the superconductor at $H > H_{c1}$. For applied magnetic fields above H_{c2} the material returns to the normal state. (c) The induction in long cylinder as a function of the applied field for Type I and Type II superconductors; (d) The reversible magnetization curve of a long cylinder of Type I and Type II superconductor.

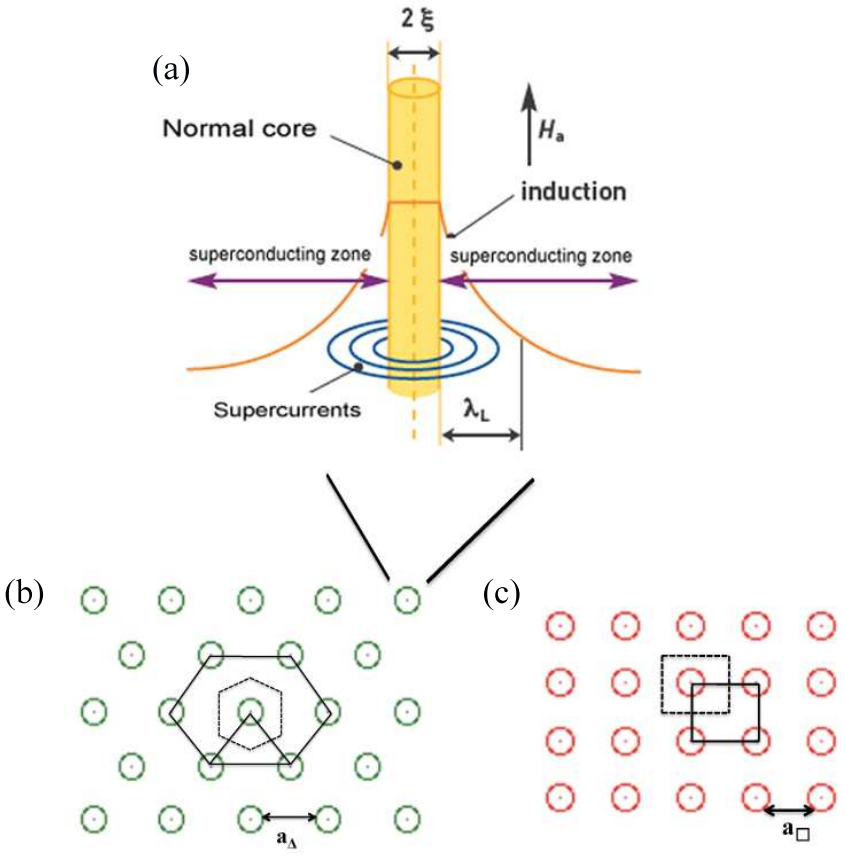

Figure 2.10 (a) Schematic representation of a vortex. The superconducting order parameter vanishes in the core of the vortex which is in the normal state, through where the magnetic field penetrate the superconductor and decreases exponentially over a distance of λ_L. (b) The hexagonal perfect lattice configuration of vortices with lattice parameter a_Δ=1.075 $(\Phi_0/B)^{1/2}$, (c) square lattice configuration of vortices with lattice parameter $a_\square$=$(\Phi_0/B)^{1/2}$

vortex cores shrinks to zero and the sample makes a continuous transition to normal state. The magnetization of a superconductor is defined as the magnetic moment per unit volume, $M=\frac{\mathcal{M}}{V}=\frac{1}{V}\oint_V \vec{r}\times j(\vec{r})d\vec{r}$. The M(H) dependence of a defect free type-II superconductor is reversible and after switching off the external field no magnetic flux is trapped inside.

2.6 Vortex dynamics

When a current density j is flowing inside a type-II superconductor in the mixed state, the Lorentz force acts on the vortex ensemble such that ,

$$\mathbf{F} = \mathbf{j} \times \mathbf{n_v \Phi_0} = \mathbf{j} \times \mathbf{B}. \tag{2.33}$$

This force tends to move the vortices perpendicular to **j** and **B** as shown in Figure 2.11. Due to the motion of vortices (flux quanta) with velocity v ,an electric field

$$\mathbf{E} = \mathbf{v} \times \mathbf{B} \tag{2.34}$$

is generated in the superconductor. In the absence of pinning the velocity is limited by the friction γ_c undergone by the vortex cores, $v=F_L/\gamma_c$. Hence the motion of an unpinned vortex lattice gives rise to a non-zero resistivity called the flux flow resistivity $\rho_f \equiv B^2/\gamma_c \approx \rho_n B/B^2$; here ρ_n is the normal state resistivity [112].

To achieve a loss-free current flow, the flux lines have to be pinned in order to prevent their motion. This role is fulfilled by crystalline inhomogeneities such as twin boundaries, dislocations, disorder emerging from crystal growth or artificially induced pinning sites (columnar or point defects). These defects will pin the vortex lines and prevent their motion until a threshold Lorentz force $F_p = j_c \times B$ is attained. Here j_c is the critical current density. At j_c the pinning force F_p will balance the Lorentz force

$$j_c = F_p/B. \tag{2.35}$$

Pinning has several consequences: the first one is that the current-voltage curve of a superconductor in a magnetic field is nonlinear (see Figure 2.11). The second one is the irreversibility of the magnetization curves. As an example the magnetization curve as a function of applied field for a bulk $YBa_2Cu_3O_7$ is shown in Figure 2.15.

The electrodynamics in the presence of pinning is usually described by the Bean critical state model. In this model, one assumes that j_c is independent of the magnetic field and of time. The flux lines can not penetrate freely at $H_a=H_{c1}$; their density is large at

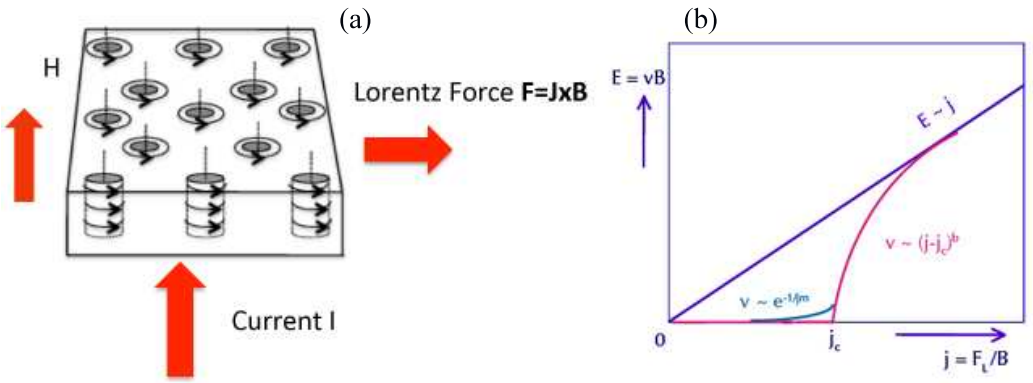

Figure 2.11 (a) Schematic representation of the Lorentz force on vortices in a type-II superconductor in mixed the state. (b)The E-j characteristic curve for a type-II superconductor in the absence (purple) and in the presence (pink) of vortex pinning. The green curve shows smoothing of the jump at j_c due to thermally activated vortex creep.

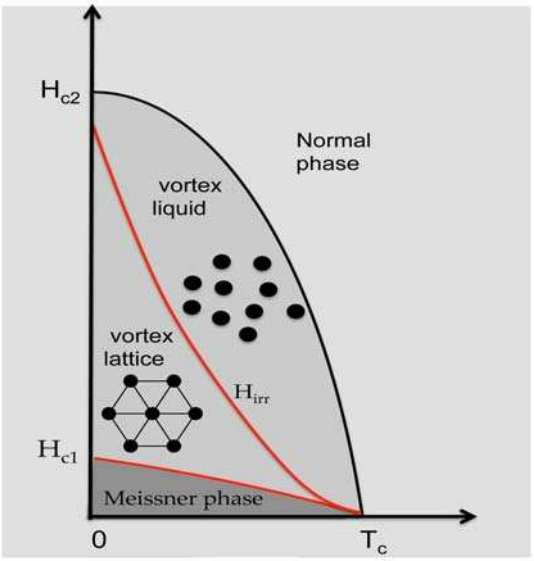

Figure 2.12 Schematic illustration of the phase diagram of type-II superconductors taking into account the vortex lattice transition due to thermal fluctuations. Vortices form the Abrikosov vortex lattice between the critical fields H_{c1} and H_{irr}. Due to thermal fluctuations the vortex lattice is solid only between H_{c1} and H_{irr} which is the irreversibility field along which the vortex solid transits to a liquid phase.

the surface and decreases with increasing distance from the surface because their entry is impaired by pinning. The pinning force exerted on the vortices by the defects in the material exactly balances the driving force Eq. 2.33 acting on each flux line due to the non-zero vortex density gradient and curvature. Therefore in the flux (vortex) penetrated regions, the current density can only be equal to the critical current density. The critical state equation $\vec{\nabla} \times \vec{B} = \mu_0 \vec{J_c}$ implies that the curl of the magnetic flux density in the regions is given by the critical current density.

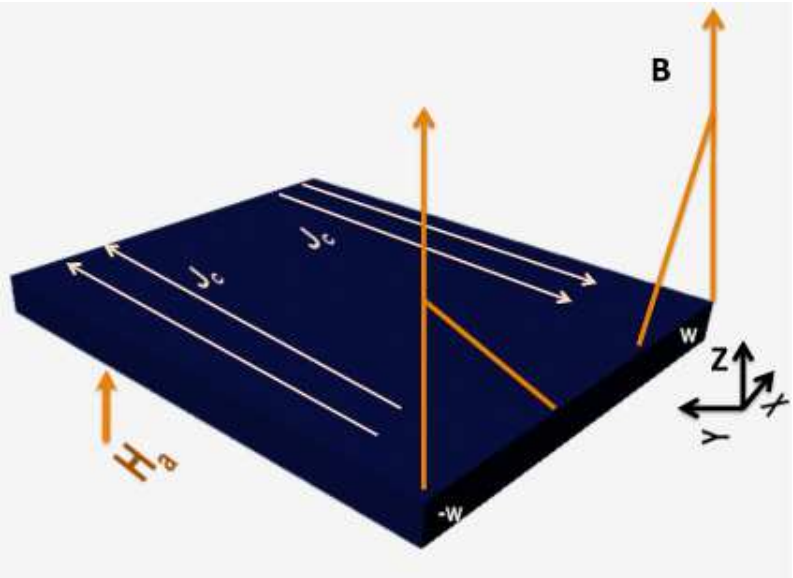

Figure 2.13 Example of the flux distribution in a type-II superconductor obeying Bean's critical state model. The Figure shows a type II superconducting infinite slab with the magnetic field H_a applied along the z-axis. In Bean's model, the slope of $B(x)$ is proportional to the critical current density such that $\nabla \times \mathbf{B} = \mu_0 j_c \mathbf{j}/|\mathbf{j}|$

Consider the case of a superconducting slab with thickness $2w$ along the x-axis and infinite in the other two directions, presented in Figure 2.13. The magnetic field is applied along the z-axis. In Bean's model, the screening current density may adopt only three different values, : 0 and $\pm J_c$. In the central zone, in which the magnetic induction is zero (i.e. where there are no vortices), the current density vanishes. As the applied field H_a is increased, for a sample initially in the Meissner state, the current density distribution in

the Bean critical state is given by equation (2.36),

$$J_y(x) = \begin{cases} j_c & -w < x \leqslant -a \\ 0 & |x| < a \\ -j_c & a \leqslant x < w \end{cases}, \tag{2.36}$$

while the flux density distribution is given by [65; 66]

$$B_z(x) = \begin{cases} 0 & 0 \leqslant |x| < a \\ \mu_0(|x| - a)j_c & a \leqslant |x| < w \\ H_a, & |x| \geqslant w \end{cases}, \tag{2.37}$$

with the position of the flux front a determined by $a = w - H_a/j_c$.

The situation is more complicated for other geometries. For the case of a thin film of a thickness of d, occupying the region $|x| < w$, $|z| < d/2$, and exposed to a perpendicular magnetic field, shown in Figure 2.13, the distribution of the current density and magnetic induction is given by [66]

$$j_y(x) = \begin{cases} j_c & {}_w < x \leqslant -a \\ -\frac{2j_c}{\pi} \arctan\left(\frac{x}{W}\sqrt{\frac{W^2-a^2}{a^2-x^2}}\right) & -a < x < a \\ -j_c & a \leqslant x < W \end{cases}, \tag{2.38}$$

$$B_z(x) = \begin{cases} 0 & |x| \leqslant a \\ B_f \ln\left(\frac{|x|\sqrt{W^2-a^2}+W\sqrt{x^2-a^2}}{a\sqrt{|x^2-W^2|}}\right) & |x| > a \end{cases}. \tag{2.39}$$

Here $B_f = \frac{1}{\pi}\mu_0 d j_c$ and $a = W/\cosh(\mu_0 H_a/B_f)$. These relations are illustrated in Figure 2.14.

Figure 2.15 relates the hysteretic magnetic moment to the field distribution in the superconductor for several values of applied magnetic field. Where the applied field exceeds H_{c1}, the magnetic field starts to penetrate the superconductor. At the field of full penetration H_p, the internal magnetic flux front reaches the center of the superconductor. At this field, the magnetization has its maximum diamagnetic value. For $H_{c1}<H_a<H_p$, the irreversible magnetization curve deviates only gradually from the straight line of perfect diamagnetism, demonstrating the strong shielding effect due to pinning. For applied fields $H_a>H_p$ Bean's model predicts $M=(H-\langle B\rangle)=-\frac{1}{2}\mu_0 H_p$, whereas in Figure 2.15 the magnetization $|M|$ starts to decrease. This is because of the reduction of the critical current

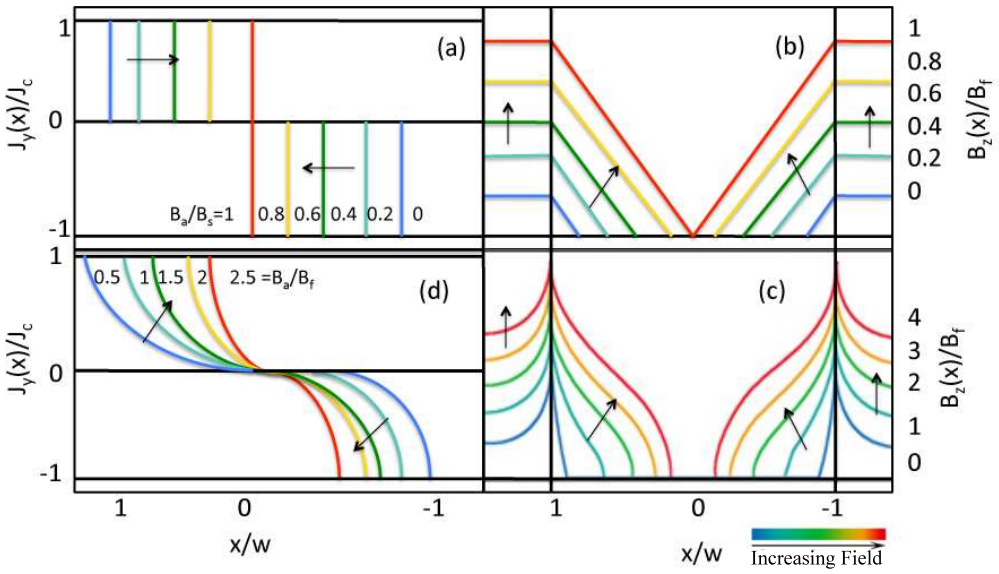

Figure 2.14 Profiles of the reduced screening current density $j_y(x)/j_c$ in (a) an infinite superconducting slab occupying the region $|x| < w$, and subjected to a parallel magnetic field, and (d) a thin film of thickness d, occupying the region $|x| < w$, $|z| < d/2$, and subjected to a perpendicularly oriented magnetic field. Profiles of the distribution of the reduced magnetic induction $B_z(x)/B_f$ for (a) the infinite superconducting slab (c) the thin film with a thickness d. The arrows indicate the progression of the profiles as H_a increases.

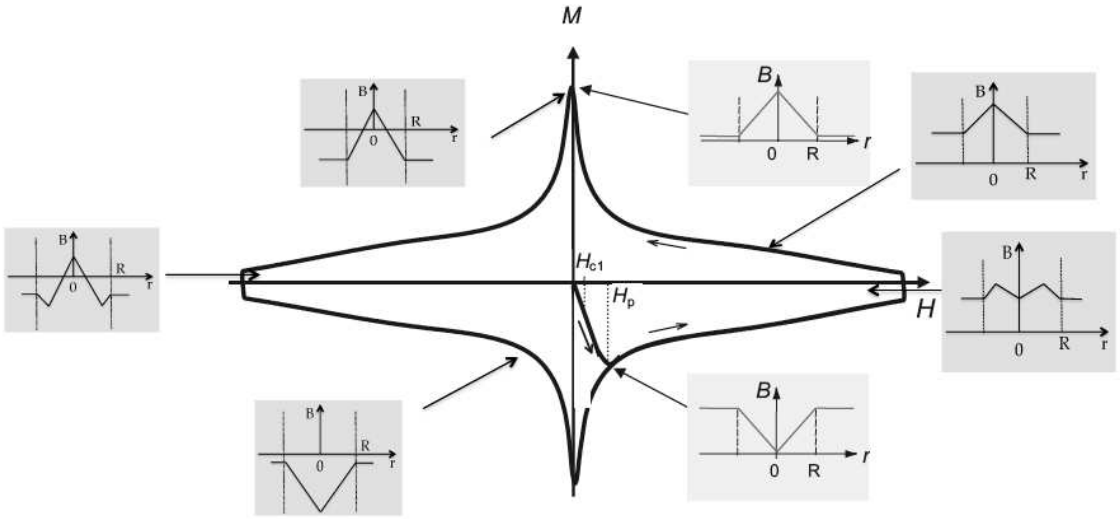

Figure 2.15 Field dependence of the magnetization in type-II superconductor. The small figures show the flux density profile across the superconductor width at various points on the magnetic hysteresis loop.

density with increasing magnetic field. As the external field is reduced the gradient of the local field near the sample edge changes its sign, but has the same absolute value, this corresponds to the sign reversal of the screening current. The magnetization now becomes positive because vortices are trapped in the superconductor by the pinning. The field profile obtained after switching off the external field is shown in the upper inset to Figure 2.15. The consequence of this field distribution is that the maximum trapped field; and therefore its magnetization, of a superconductor with pinning depends on its size. The irreversible magnetization vanishes at the irreversibility field H_{irr} above which vortex pinning is overcome by the thermal fluctuations acting on the vortex ensemble. In contrast to the reversible magnetization, which only vanishes at $H=H_{c2}$.

2.6.1 Flux creep

The Bean critical state corresponds to the non-equilibrium vortex (flux density) distribution caused by the presence of pinning. However, at non-zero temperature vortex lines can be unpinned by thermal fluctuations. Vortices then slowly progress along the flux density gradient. Thus the non-equilibrium magnetization decays with time, a process called *flux creep*. At current densities j close to the critical value, the free energy barrier for the activation of vortex motion is small and may be linearly expanded in $j_c - j$,

$U(j) = U_c(j_c - j)/j_c$. U_c is the pinning energy or energy gained by the vortices occupying the pins. j may be interpreted as being the energy gain due to the Lorentz force. This approximation is known as the Anderson-Kim model [179] and results in a logarithmic time dependence of the non-equilibrium part of the magnetic moment. In conventional low temperature type-II superconductors flux creep is a slow process: the ratio U_c/k_BT which can be extracted from the creep rate $S \equiv M^{-1}dM/dlnt$ is typically order of the of 10^3-10^4. The vortex velocity will be determined by the nucleation rate of a vortex-bundle that gives rise to a thermally activated jump [166] and has the form

$$v \propto v_0 e^{(-U(j)/k_BT)}. \tag{2.40}$$

The above expression can be combined with the Maxwell equations in order to get the equation of motion for the induction and the current density,

$$-\frac{\partial \mathbf{B}}{\partial t} = -\nabla \times \left[B \times \vec{v_o} e^{-U(j)/k_BT}\right] \tag{2.41}$$

or

$$-\frac{\partial \mathbf{j}}{\partial t} = \nabla \times \nabla \times \left[\vec{E_0} e^{-U(j)/k_BT}\right], \tag{2.42}$$

where $\vec{E_0} = \vec{v_0} \times B$.

It is possible to derive the time dependence of the average screening current density from the above equations. An approximate solution for j_s can be found as [42; 104; 159],

$$U(j_s(t)) = k_BT \ln\left(\frac{t_0 + t}{\tau}\right), \tag{2.43}$$

where the normalization time

$$\tau \equiv \tilde{\tau}\left[\frac{1}{T}\int_0^t \frac{j_s}{U_c}\left(-\frac{\partial U(j_s)}{\partial j_s}\right) dt'\right]^{-1} \tag{2.44}$$

describes the time scale of the relaxation [8] and

$$t_0 \equiv \tau \exp\left(\frac{U(j_0)}{k_BT}\right) \tag{2.45}$$

is the measure of the time regime in which transient contributions to $j_s(t)$ are important. j_0 is the current density at the onset of relaxation, $\tilde{\tau} = \frac{\Lambda}{\rho_f}\frac{k_BT}{U_c}$ and the self inductance of the sample $\Lambda \equiv \frac{1}{2}\mu_0 d\partial M/\partial j_s$. The temporal evolution for different flux creep models can be found by applying Equation 2.43.

In the Kim-Anderson model [188] the solution is

$$M \propto \left(1 - \frac{k_B T}{U_c} \ln\left(\frac{t+t_0}{\tau}\right)\right). \tag{2.46}$$

in the limit $U_c \gg k_B T$, $j \lesssim j_c$. In the limit $j \ll j_c$ or $U_c \leqslant k_B T$, known as thermally assisted flux flow [176] $U \approx U_c$ and Eq. 2.42 can be solved directly [52; 233]. The sustainable current density j_s decays as $j_s(T) = \sum_{i=1}^{\infty} \frac{e^{-t/t_i}}{\beta_n^2}$ with $t_i = (\Lambda/\rho_f)\exp(U_c/k_B T)$.

For the case of $U(j) = U_c \ln \frac{j_c}{j}$: the solution proposed for Eq. 2.43 is exact [176]. j_s decays according to a power law

$$j_s(t) = j_c \left(\frac{t+t_i}{\tau}\right)^{-k_B T/U_c}, \tag{2.47}$$

and the normalization time is given by $\tau = \tilde{\tau}$.

In the collective creep model, $U(j) = U_c(\frac{j_c}{j})^{\mu}$there is no exact solution known [227]. With logarithmic accuracy the current decays as

$$j_s(T) = j_c \left(\frac{k_B T}{U_c} \ln\left(\frac{t+t_i}{\tau}\right)\right)^{-1/\mu} \tag{2.48}$$

where $\tau \simeq \tilde{\tau}/\mu$.

2.6.2 Theories of pinning

The problem of calculating the critical current density, that is, the maximum pinning force exerted by the material disorder on the vortex ensemble, can be separated in two parts. The first concerns the interaction of individual pins with an individual vortex, while the second concerns the summation of the pinning forces acting on the vortex ensemble as a whole.

2.6.3 Vortex-pin interaction

In the following, the attractive interaction between a vortex and a single pin is considered. The attractive interaction at the origin of pinning arises from two different mechanisms. The first one is the pinning of the vortex core, "core pinning", while the second one is pinning due to the modification of the supercurrent distribution field circulating around the vortex core; this is dubbed "electromagnetic pinning". For the case of core pinning there are again two different mechanisms at play: pinning due to the spatial variation of the critical temperature or the condensation energy "δT_c-pinning" and pinning due to the scattering of the quasiparticles in the vortex cores the so-called "$\delta\kappa$-mechanism".

In the case of a defect of dimension $D_V \ll \xi$ smaller than the vortex core, only core pinning will be effective. Depending on the nature of the defect and the type of the material, either the "δT_c-mechanism" or the "$\delta\kappa$-mechanism" will be at the origin of pinning. On the other hand, the presence of a defect larger than the vortex core $D_V \gg \xi$ will render the core pinning unimportant compared to the "electromagnetic pinning".

The δT_c-mechanism arises because the vortex core which, is in the normal state, will be attracted by any defect that confers a lower T_c or a lower condensation energy to its immediate surroundings. The elementary pinning energy, *i.e.* or the maximum energy gained by having the vortex core coincide with such a single small pin, can be estimated by taking the product of the condensation energy $\frac{1}{2}\mu_0 B_c^2$ and the volume of the defect $\frac{4\pi}{3} D_V^3$,

$$U_p = \frac{B_c^2}{2\mu_0}\frac{4\pi}{3}D_v^3 = \frac{\Phi_0^2}{16\pi^2\mu_0\lambda^2\xi^2}\frac{4\pi}{3}D_v^3 = \frac{\pi}{3}\varepsilon_0\frac{D_V^3}{\xi^2}. \tag{2.49}$$

If one considers the pinning potential $U_p(r)$, that is the energy gained by placing the center of the vortex core a distance r from the defect, the elementary pinning force is given by $f_p = \frac{\partial U_p(r)}{\partial r}$. The maximum pinning force f_p is usually obtained for a displacement of $r = \xi$ so that

$$f_p \approx \frac{U_p}{\xi} \approx \varepsilon_0 \left(\frac{D_V}{\xi}\right)^3 = \varepsilon_0 \left(\frac{D_V^z}{\xi}\right)\left(\frac{D_V^{xy}}{\xi}\right)^2, \tag{2.50}$$

where D_V^z and D_V^{xy} are the dimensions of the defect along and perpendicular to the field direction. Thus the maximum force of a pin (vacancy, dopant atom) extent of $D_i \ll \xi$ can be estimated as the product of the fraction of the vortex core volume occupied by the defect and the vortex line energy ε_0 [41; 68].

For the case of the $\delta\kappa$-mechanism, it is energetically advantageous for the vortex core to coincide with regions of stronger quasiparticle scattering [68] . The pinning force is estimated as,

$$f_p = 0.3 g(\rho_D)\varepsilon_0 \left(\frac{\sigma_{tr}}{\pi\xi_{ab}^2}\right)\left(\frac{\xi_0}{\xi_{ab}}\right), \tag{2.51}$$

where $\sigma_{tr}{=}\pi \mathrm{D}_v^2$ is the transport scattering cross section, D_v is the effective range of the pin and $\mathrm{g}(\rho_D)$ is the Gor'kov function. The disorder parameter is $\rho_D{=}\hbar \mathrm{v}_F/2\pi \mathrm{T}_c l{\sim}\xi_0/l$, with v_F the Fermi velocity, l the mean free path and $\xi_0{\approx}1.35\xi(0)$ the BCS coherence length.

In the limit of an extended defect, $\mathrm{D}_i \gg \xi$ the "electromagnetic pinning" will be dominant. The defect will not occupy only the cortex core cross section, but also affect the screening supercurrent. The pinning energy U_p can be estimated by taking into account the energy gain due to the decrease of line energy due to the coincidence of vortex core and the

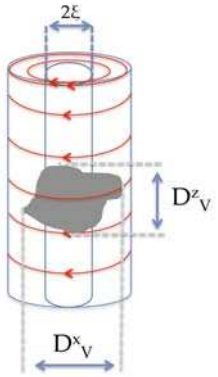

Figure 2.16 A cartoon of vortex pinning by an extended defect.

defect, to which one adds the kinetic energy gain outside the core. For an extension of the defect perpendicular to the field direction D^{xy}, the pinning energy can be approximated as $U_p \sim \varepsilon_0 D_V^z \ln\left(\frac{D_V^{xy}}{\xi}\right)$. The elementary pinning force can be thus estimated as

$$f_p = \varepsilon_0 \left(\frac{D_V^z}{\xi}\right) \ln\left(\frac{D_V^{xy}}{\xi}\right). \tag{2.52}$$

An interpolation between the limits of small and large defects in suggested in Ref. [82],

$$f_{p,max}^i \approx \mathcal{F}(T)\varepsilon_0 \left(\frac{D_i^z}{4\xi}\right) \ln\left(1 + \frac{D_i^2}{2\xi^2}\right) \equiv \varepsilon_0 \left(\frac{D_i^z}{4\xi}\right) \mathcal{F}(T). \tag{2.53}$$

Here $\mathcal{F}(T)$ is a function that takes into account smearing of the pinning potential by thermal fluctuations [166]. The maximum value of the elementary pinning force in either limit is given by the above expression by taking into account the different limits $D_V \gg \xi$ and $D_V \ll \xi$ in the logarithmic term of Eq 2.53.

2.7 Statistical summation

The critical current density in type-II superconductors is determined by the pinning force which holds the lattice when an applied current pushes the vortex lattice into motion. This pinning force arises from a large number of contributions from individual pins. In the presence of pinning sites, the vortex lattice deforms elastically to accommodate itself taking on an energetically most favorable configuration. The pinning contribution to the free energy of such a metastable vortex configuration, for a random distribution of pinning centers, must be found from a statistical summation. Since vortices will try to accommodate to the pinning landscape by shearing and bending in order to profit from the most favorable areas

, the total free energy will depend on the exact balance between the elementary pinning potential and the elastic energy loss from of the vortices' elastic deformations.

The summation of the elementary pinning forces acting on a vortex can be considered in two different limits, determined by the product of defect density n_d and the extent of the vortex core. In the limit $n_d \gg \xi^{-3}$, a large number of small defects contributes to the pinning of a given vortex: this is called "weak collective pinning". In this case the direct summation of the elementary pinning forces of each pin yields a very small number or zero: $\langle f_p \rangle$=0. Now if one considers that some of the regions in the random pinning potential array have a total pinning force that is slightly larger than the average value, these regions will act as trapping areas for the vortices. In other words, the pinning force will not be zero only because $\langle f_p^2 \rangle_{a_0^2} \neq 0$. An important question for this summation problem is over what length scale this averaging should be performed. Larkin and Ovchinnikov have attacked the situation as follows. For vortex lattice pinning in the presence of weak dense pins, averaging of the elementary pinning forces is performed over a unit cell (of sixfold coordinated vortices) to yield $\langle f_p^2 \rangle_{a_0^2}$, while for a single vortex it should be done over the vortex core $\langle f_p^2 \rangle_{\xi^2}$.

The limit between the two situations is again a question of length scales. If the pinning is weak, the disorder-induced displacements of the vortices are correlated and one is in the vortex lattice pinning regime. One may then define a correlation volume $V_c = L_c R_c^2$. The deformation of the vortex line will give rise to displacements of vortices from their lattice positions which are described in the Larkin-Ovchinnikov theory using the displacement correlators [82; 279]

$$B(r) = \langle |\mathbf{u}(r,z) - \mathbf{u}(0,z)|^2 \rangle^{1/2} \tag{2.54}$$

$$B(z) = \langle |\mathbf{u}(\mathbf{r},z) - \mathbf{u}(\mathbf{r},0)|^2 \rangle^{1/2}. \tag{2.55}$$

Here L_c and R_c are the longitudinal and transverse correlation lengths respectively, which define the correlation volume V_c. The correlation lengths are calculated from

$$B(R_c) = \langle |\mathbf{u}(R_c,z) - \mathbf{u}(0,z)|^2 \rangle^{1/2} = \xi \tag{2.56}$$

$$B(L_c) = \langle |\mathbf{u}(\mathbf{r},L_c) - \mathbf{u}(\mathbf{r},0)|^2 \rangle^{1/2} = \xi. \tag{2.57}$$

If the pinning is sufficiently strong, vortices will be sufficiently displaced by the disorder for the transverse correlation length R_c to drop below the vortex spacing a_0. The volume

pinning force F_p will ben determined by averaging over a single vortex. The limit between the two regimes is determined by the condition $R_c = a_0$. The average pinning force action the vortex lattice (bundle) pinning regime can be described using the correlation volume such that

$$F_p = \left(\frac{n_d \langle f_p^2 \rangle}{V_c} \right)^{1/2} \tag{2.58}$$

(units [N/m^3]) where the pinning energy is defined as $U_p = F_p V_c r_f$, and r_f is the range of the pinning potential. In the limit of single vortex pinning the pinning energy is defined as $U_p = F_p^{sv} L_c \xi$. The expression for the average pinning force is given by,

$$F_p^{sv} = \left(\frac{n_d \langle f_p^2 \rangle_{a_0^2}}{L_c} \right)^{1/2} \xi, \tag{2.59}$$

(units [N/m]). In the vortex lattice collective pinning regime the critical current density is determined by $j_c = \frac{F_p}{B}$, while in the limit of single vortex pinning it can be expressed as

$$j_c = \frac{F_p^{sv}}{\Phi_0} = \frac{(n_d \langle f_p^2 \rangle)^{1/2}}{\Phi_0 L_c^{1/2}} = \frac{\langle f_p^2 \rangle^{1/2} \xi}{\Phi_0 (n_d^{-1} L_c)^{1/2}}. \tag{2.60}$$

When the defect density decreases and the pins become more extended a crossover from weak collective pinning to so-called strong pinning occurs. In the appropriate limit $n_d \ll \xi^{-3}$ the average pinning force $\langle f_p \rangle$ acting on the vortex line is no longer zero. Namely, when the individual pins are sparse the elementary forces of the individual pinning centers no longer cancel. In this regime each pin will try to trap the vortex line, which will again seek out a most favorable configuration. However, in exploring the pinning potential, the vortex is limited by its own line tension (this will be dominant in the single vortex limit of strong pinning), and by the repulsive interaction with other vortices (this dominates in the vortex lattice limit of strong pinning). In order to perform the summation, one must now know the number of pins per vortex, length scale $\mathcal{L}$, the mean distance between effective pins. For the vortex lattice, the volume pinning force $F_p = \frac{f_p}{a_0^2 \mathcal{L}}$ (units [N/m^3]) , while in the single vortex limit it is given by $F_p = \frac{f_p}{\mathcal{L}}$ (units [N/m]).

In the vortex lattice limit of strong pinning, $\mathcal{L}$ is determined by the maximum allowable transverse displacement of a vortex, u_0, which can be estimated by by minimizing the energy of elastic deformation given by

$$U_{el} = c_{66} u^2 L + c_{44} \frac{u^2}{L} a_0^2. \tag{2.61}$$

Minimization of Eq. 2.61 with respect to L yields the optimum length $L_0 = a_0(c_{44}/c_{66})^{1/2} \approx 2\varepsilon a_0$, that is, the longitudinal scale of optimum vortex deformations. The distance u_0, to which a vortex may wander, is then obtained by equating the pinning energy gain U_p to $U_{el}(u_0, L_0)$. This gives,

$$u_0^2 = \frac{U_p}{(c_{44}c_{66})^{1/2}a_0} \approx \frac{U_p}{\varepsilon\varepsilon_0}a_0. \tag{2.62}$$

In the single vortex limit of the strong pinning, one calculates the energy of the elastic deformation as a function of displacement. Balancing the energy of the elastic deformation of a single line with the pinning energy $U_p = \varepsilon_1\left(\frac{u}{\mathcal{L}}\right)$, where $\varepsilon_1 \approx \varepsilon^2\varepsilon_0$ the line tension of a single vortex and ε is the anisotropy parameter of the superconductor, thus one has $u^2 = (U_p/\varepsilon_1)\mathcal{L}$. For a given U_p, the average $\overline{\mathcal{L}}$ is obtained in Ref [43] as

$$\overline{\mathcal{L}} = (\frac{1}{\sqrt{\pi}})\left(\frac{\varepsilon_1}{n_d U_p}\right)^{1/2}. \tag{2.63}$$

By inserting Eq. 2.63 one has $u^2 = (U_p/\pi n_d\varepsilon_1)^{1/2}$. The critical current density $j_c = f_p/\Phi_0\mathcal{L}$ is given by

$$j_c = n_d^{1/2}\frac{f_p}{\Phi_0}\left(\frac{\pi U_P}{\varepsilon^2\varepsilon_0}\right)^{1/2}. \tag{2.64}$$

Chapter 3

Iron-based superconductors

3.1 Introduction

Until 2008, researchers interested in unconventional superconductivity focused their work mostly on the so called high-T_c (high temperature superconductor) cuprates. The crystal structure of these compounds is composed of alternating conducting CuO_2 layers and layers that act as charge reservoirs. 20 years after the discovery of the high-T_c superconductors in 2006 the first superconducting iron pnictide compound was discovered by the team of professor Hosono in Japan [264]. This compound has some important characteristics. Its composition is that of successive layers of ($La^{3+}O^{2-}$) and iron pnictides ($Fe^{2+}P^{3-}$). Its T_c=3.2 K could reach temperatures above 5 K when the oxygen was partially substituted by fluorine. Two years later the same group of researchers realized the synthesis of $La(O_{1-x}F_x)FeAs$ with T_c=26 K [265].

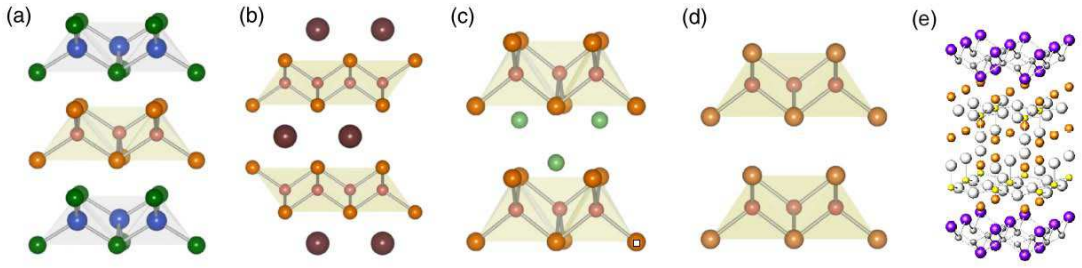

Figure 3.1 Crystal structures of (a) LaFeAsO (1111-family), (b) $BaFe_2As_2$ (122-family), (c) LiFeAs (111-family), (d) FeSe (11-family) and (e) $(Fe_2P_2)(Sr_4Sc_2O_6)$ (22426-family). Taken from Ref.[136] and Ref.[96].

Rapidly after their discovery , iron-based superconductors (IBS) have attracted the

interest of the condensed matter physics community who considered IBS as competitors for cuprates and even as potential candidates for future technological applications. Until now, several families of iron-based superconductor have been discovered. They are all characterized by a quasi- two dimensional crystallographic structure formed by successive layers of iron pnictide ($Fe^{2+}Pn^{3-}$) (here Pn represent the pnictogen atom, an element situated in column V of the periodic table) and by the presence of a magnetic order in their phase diagram. At high temperature, the crystallographic structure of all iron-based superconductors (IBS) is tetragonal at high temperature; Moreover, all superconducting compositions have a tetragonal structure. For underdoped IBS a structural transition to orthorhombic phase occurs at a temperature close to the transition to the antiferromagnetic phase.

Up to now, at least five families of superconducting pnictides have been found (see Figure 3.1). Disregarding the "111" LiFeAs type family and the end compounds LaFePO and KFe_2As_2, the undoped parent compounds show antiferromagnetic spin density wave (SDW) order. The metallic SDW phase present in the underdoped regime of iron based superconductors is one of the important differences with cuprates, that feature an antiferromagnetic Mott insulator phase in the underdoped region of their phase diagram. Upon doping or the application of pressure, the antiferromagnetic phase of the iron-based parent compound is progressively suppressed, by the decrease of T_{SDW}, until, at a critical doping, superconductivity appears. The Fermi surface of the iron based-superconductors generally consists of five different sheets: three hole pockets centered around the Γ point and two electron pockets around the M point of the Brillouin zone [97; 136] (see Figure 3.5 (a)). An exception is KFe_2Se_2, that has no hole-like sheets and KFe_2As_2 that has four distinct petal-like electron pockets away from the M point.

The first discovered family of "1111" compounds are the $RE(O_{1-x}F_x)FePn$ type materials. Here RE represents a rare earth element from lanthanide series [265], Their crystal structure is given in Figure 3.2. Crystal growth is very difficult for the "1111" family of compounds. The dimensions of the single crystals are quite small, of the order of one hundred micron on the side. This limits experimental studies on them. Figure 3.1, shows the phase diagram of the 1111-type IBS. No coexistence of the superconducting and magnetic phase is observed in the underdoped regime of the "1111" family.

The second family of IBS is designated "11" and was discovered in 2008 [81]. This family has the simplest chemical composition $FeSe_{1-x}$. It has T_c=8 K, a value that can go under pressure up to 27 K for some of the different compositions such as $FeSe_{1-x}$ Te_x [143] or $FeT_{1-x}S_x$ [267].

The third family of iron pnictides, also discovered in 2008, is the so called "122" family.

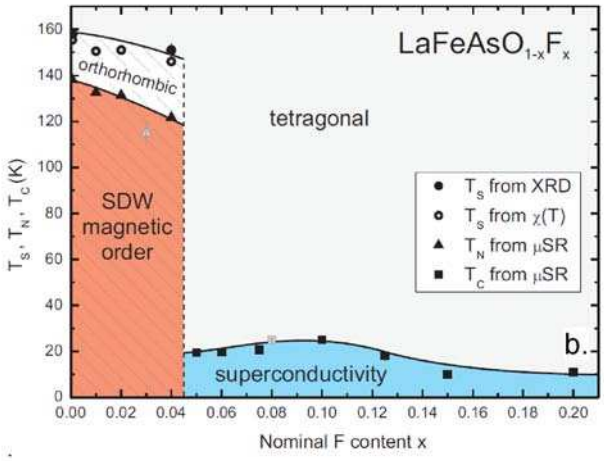

Figure 3.2 Phase diagram of $LaFeAsO_{1-x}F_x$ from Ref. [95].

This describes the compounds of $ATFe_2As_2$ type where AT is an alkaline earth element. The superconductivity can be induced into these systems by hole doping, that is by substitution of Ba with K or Sr [162] or by electron doping: that is by substitution of Fe with Co or Ni [17; 147]. Superconductivity can also be observed by isovalent substitution of Ru for Fe or P for As [207; 214]. All these dopant elements are different, so that one could expect diverse physical behavior upon doping with charge carrier into the superconducting layers, into the reservoir layers, or by isovalent substitution into the system. Nevertheless , the phase diagram of all these differently doped systems is very similar, and all doped compound have the same order of T_c (see Figure 3.3). The highest T_c in the "122" family is 38 K for $Ba_{1-x}K_xFe_2As_2$,($x = 0.4$) [162]. The high temperature crystal structure of $BaFe_2As_2$ is tetragonal. In the non-magnetic state, it is in the space group $I4/mmm$. At a temperature just above the antiferromagnetic transition, there is a structural transition to an orthorhombic phase of the space group $Fmmm$. The body-centered tetragonal unit cell and the orthorhombic unit cell are represented in Figure 3.6.

Finally, in december 2008, the "111" family is discovered. This has the typical composition AFeAs, where A is an alkali metal (Li, Na) [256]. These compositions are superconducting without any substitution or doping. Notably, LiFeAs becomes superconducting beneath $T_c = 18$ K and for the NaFeAs compounds T_c can reach to 25 K [48].

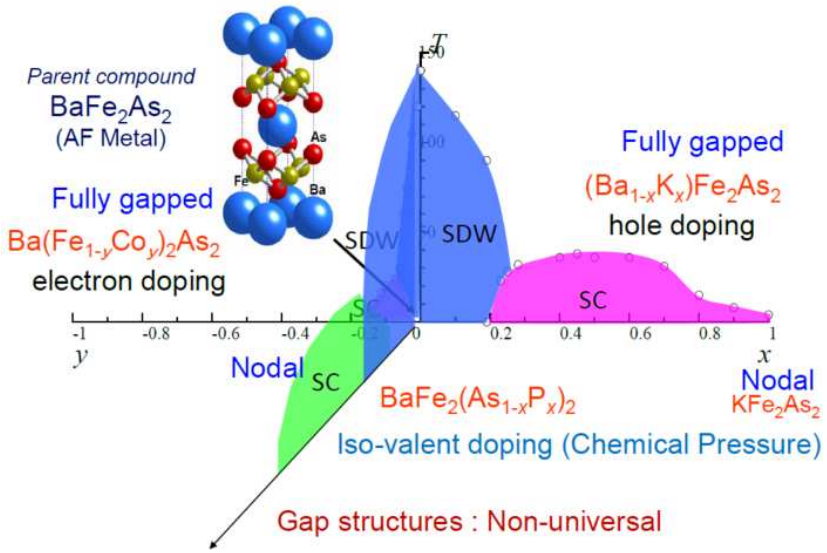

Figure 3.3 Generic phase diagram of the "122" compounds for different substitution.

3.1.1 Structure and phase diagram

The typical phase diagram of IBS features an orthorhombic low-temperature phase for the undoped parent compound (on the left-hand side of Fig. 3.2 and at the center of Fig. 3.3). This orthorhombic phase persists, for limited doping and / or applied pressure. The orthorhombic phase is associated with itinerant antiferromagnetism of spin-density wave (SDW) type. Whereas the structural and antiferromagnetic Néel transition temperature lie very close to each other in the 122-type compounds, they are quite clearly separated in the "1111" family of materials. The antiferromagnetism opens a gap on part of the Fermi surface, inducing the presence of petal-like reconstructed Fermi surface pockets. Generally, when these petal-like pockets are present, there is no superconductivity. Chemical substitution and/or the application of pressure induces (as one goes to the right in the phase diagram of Fig. 3.2, or, away from the origin in Fig. 3.3), a gradual structural change, reflected by the increase of the As-Fe-As bond angle to the value for a perfect tetrahedron, and an accompanying change of the As height with respect to the Fe plane. Upon this structural change, the Néel temperature of the SDW transition is gradually suppressed. It is widely thought that, at least, the initial suppression is due to the demise of the Fermi surface nesting between the hole-like cylinders in the center of the first Brillouin zone, and the electron pockets at the M point on zone boundary (see Fig. 3.5). Thus, upon substitution, the Fermi surface reconstruction disappears, and the full electron pockets

appear.

Further substitution (or application of pressure) leads to the full demise of antiferromagnetism, and the appearance of superconductivity, around the point in the phase diagram where T_{SDW} tends to zero. The critical temperature T_c rises, goes through a maximum, and tends back to zero in the overdoped region of the phase diagram. In some materials, such as (Ba,K)Fe_2As_2, it is possible to go to the extreme overdoped side of the phase diagram, *in casu*, KFe_2As_2, all the while retaining superconductivity.

The As-Fe-As bonding angles have a particular importance in iron-based superconductors. Figure 3.4 (b) shows that there are two non-equivalent angles denoted as α and β. Their difference with respect to the bond angle of a regular tetrahedron (α=109.47°) is clearly related to the decrease of the critical temperature T_c. The structural change incurred by chemical substitution may be an indication as to why superconductivity is induced by isovalently substitution, as well as by hydrostatic pressure, which both modify of the As-Fe-As bonding angle. Indeed, T_c is strongly influenced by the structural properties such as the tetrahedron angle and pnictogen height with respect to the Fe-plane. Notably P doping causes a reorganization of the crystal structure that influences T_c via its effect on the bandwidth [161]. It is thought that this particular type of chemical substitution causes many changes in band structure. For example Shishido *et. al.* reported that the volumes of the electron and hole-like Fermi surface pockets shrink linearly with decreasing x in isovalently substituted $BaFe_2(As_{1-x}P_x)_2$. This shrinkage is accompanied by a strong increase in the quasiparticle effective mass as x is tuned toward the maximum T_c [97]. Liu *et. al.* argued from ARPES measurements that marked changes in the Fermi surface accompany the onset of superconductivity in charged-doped $Ba(Fe_{1-x}Co_x)_2As_2$.

In the region of the phase diagram where T_{SDW} tends to zero, superconductivity and magnetism are thought by some to be competing states. On the other hand, the very antiferromagnetic fluctuations near a possible quantum critical point in this region of the phase diagram may well provide the bosonic interaction responsible for the formation of Cooper pairs. The question of microscopic coexistence (or, on the other hand, phase separation) of superconductivity and magnetism has therefore attracted much interest. For the case of the K-doped "122" compound Nuclear Magnetic Resonance (NMR) [89], Muon Spin Rotation (μSR) [173] and Magnetic Force Microscopy (MFM) measurements [173] have shown the separation into non-magnetic regions, and regions with magnetic order. This might be an indication for microscopic scale phase separation. Inosov *et. al.* have also supported the argument of the possible phase separation. Their microstrain measurements on the K-doped "122" compound using X-ray and neutron diffraction, were interpreted as being consistent with electronic phase separation. For different doping levels of $NdFeAsO_{1-x}F_x$,

both van der Beek *et. al.* [41] and Qiu *et. al.* reported the absence of coexistence evidence for the superconducting and antiferromagnetic states for the studied compositions [272]. Shen *et.al.* argued, that there is phase separation (with superconducting islands) in their single crystals of $K_{0.8}Fe_{1.6}Se_2$ [20]. The latter authors, and as well as Lu *et. al.*, from their work on the K and Co-doped "122" compounds, raised the idea whether these phase separation originates from crystalline heterogeneity [254]. It seems that coexistence of superconductivity and magnetism is a property that depends on the type of material under study.

For the Co-doped "122" material, both NMR [266] and μSR measurements [25] indicate that all Fe sites participate in magnetic order as expected for the coexistence of SDW magnetism and superconductivity. Last but not least, neutron diffraction measurements on the underdoped Co-compound showed that the magnetic Bragg peak intensity decreases when entering the superconducting region [6; 58]. These results were interpreted as being an indication for a strong interaction between the superconducting and the SDW states, and that the same electrons contribute both to the SDW and superconducting states. Therefore, it is not easy to draw any clear conclusion from these observations.

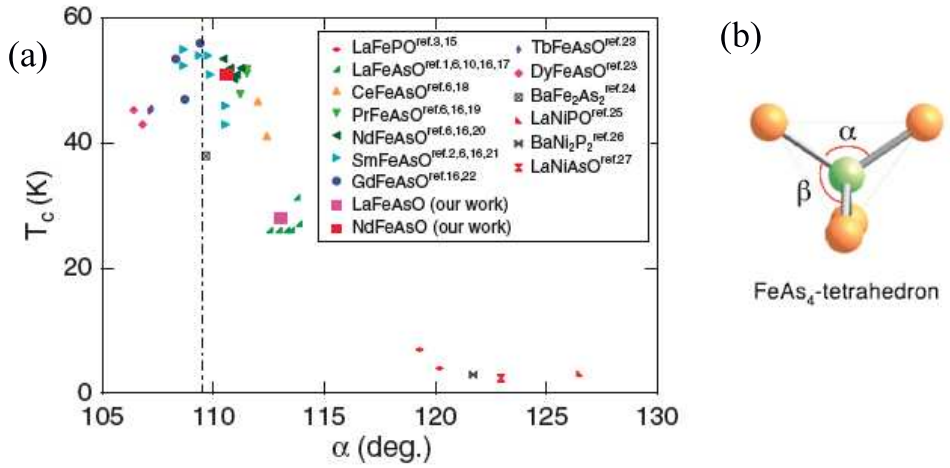

Figure 3.4 (a) T_c vs As-Fe-As bond angle for various pnictide superconductors. Formulas of parent compositions of superconductors are depicted in the inset. Crystal structure parameters of samples showing almost maximum T_c in each system are selected. The vertical dashed line indicates the bond angle of a regular tetrahedron (α=109.47°). (b) As-Fe-As bond angles and are illustrated with an FeAs4-tetrahedron. From Ref.[27].

3.1.2 Fermiology

Early ARPES work of Ding *et. al.* performed on the K-doped "122" system revealed the general topology of the Fermi surface, the nature of pockets and the shape of cylinders in the 122 compounds [88]. More recent work performed on both $BaFe_2As_2$ and $Ba(Fe_{1-x}Co_x)_2As_2$ showed significant variation of the size of the Fermi surface cylinders in the k_z-k_y plane along the z-axis, particularly around the Γ point, yielding clear evidence for the 3D character [244]. This 3D character is seen both in the undoped compound, but was more pronounced around both the Brillouin zone hole Γ center and electron M corner pockets in the Co-doped compound. This 3D character was also reported for other substitutions of the "122"-type compound [22; 192; 220]. The fermiology of the parent compounds exhibits a temperature dependence due to the strong influence of the magnetic moment on the band structure below T_{SDW}. Yi *et. al.* reported on detailed measurements of the Fermi surface reconstruction in $BaFe_2As_2$, with multiple new bands appearing [168]. Their ARPES data show, in addition to two hole pockets centered at the Γ point, the appearance of four small surrounding "petal shaped" electron pockets at the M point. Liu *et. al.* followed the evolution of the magnetic-ordering induced additional hole-like pockets revealed by Yi *et. al.* at the M point in $Ba(Fe_{1-x}Co_x)_2As_2$ as a function of Co doping, and found that they disappear at the point in the phase diagram where superconductivity appears. Liu *et. al.* argued that the pairing interaction due to spin fluctuations is suppressed by long range magnetic order, which is indicated by the additional Fermi surface features [32]. Fuglsang Jensen *et. al.* performed an ARPES study on the undoped parent compound $BaFe_2As_2$ they reported that the imperfect nesting between and electron pockets can explain the formation of gaps and residual residual metallic pockets. Beyond this nesting picture, they have observed shifts and splittings of numerous bands at the transition [155; 230]. Brouet *et. al.* have reported on the Ru substituted "122" compound. They showed, by resolving the different Fermi surface pockets and deducing the number of hole and electron carriers from their volumes that Ru induces neither hole nor electron doping. However, the Fermi surface pockets are about twice larger than in $BaFe_2As_2$ [229].

3.1.3 Band structures in "122" and "1111" type compounds

The key for the understanding of the superconductivity mechanism in the IBS are their normal-state properties. The microscopic interaction determining the anti-ferromagnetism in the orthorhombic phase, and the corresponding antiferromagnetic fluctuations around a putative quantum critical point, is a very serious candidate for the pairing mechanism and superconductivity. In order to elucidate the possible nesting origin of antiferromagnetism,

many band structure calculations have been carried out for these systems. In IBS all five Fe 3*d*-orbitals contribute to the density of states near the Fermi energy level. This is an indication that the mechanism for the metallic conduction is due to charge carriers in the FeAs layers. Results on band calculations using the density functional theory in the local density approximation (LDA) for LaFeAsO primitive tetragonal structure are shown in Figure 3.5 [50]. Figure 3.5 (a) shows the presence of hole-like Fermi surface sheets surrounding the Γ point of the Brillouin zone, and electron bands at the M points. Calculations show that the energy bands are very sensitive to the distance of the As planes from the Fe planes [138; 139; 140]. The density of states versus energy is given in Figure 3.5 (b). The sates at E_F are primarily of Fe , character indicating the predominant electronic conduction. LDA band calculation for the 122-type parent compound $BaFe_2As_2$ [150] is shown in Figure 3.5. Again, the hole-like bands cross the Fermi surface around the Γ-point, as in LaFeAsO, but due to the doubling of the unit cell the electron bands are at the X point instead of the M point. The electron pockets in both compounds are at the same positions in the reciprocal space with respect to the respective direct lattices. This means that the nesting wave vector between the electron and hole pockets for all of the IBS and parent compounds is the same $\mathbf{Q}_{nesting}$=(1/2,1/2) in tetragonal notation.

3.1.4 Origin of the antiferromagnetic ordering

The parent compounds of both the "1111" and "122"-type materials are metals and exhibit antiferromagnetic spin density wave (SDW) order. The high temperature $T > T_{SDW}$ paramagnetic state is characterized by a magnetic susceptibility with an unusual linear temperature dependence ($\chi \propto T$) [141; 191]. The magnetic structure in LaFeAsO is characterized by the ordering wave vector $(\frac{1}{2}\ \frac{1}{2}\ \frac{1}{2})_T$=$(1\ 0\ \frac{1}{2})_O$ (where T and O correspond to the tetragonal and orthorhombic structures respectively). The low temperature ordered magnetic moment is 0.36 μB. The SDW magnetic order on Fe atoms is depicted in Figure 3.6. Neutron diffraction experiments on the "122"-type compounds show a larger ordered magnetic moment than in the "1111" materials (apart from NdFeAsO, in which the moment in borne by the Nd atoms). The size of the ordered moment is fairly similar for different members of the AFe_2As_2 family. One observes 0.99 μB [273] in single crystal $BaFe_2As_2$ (grown with Sn flux), $\mu = 0.87\mu_B$ [185] in powder $BaFe_2As_2$, $\mu = 0.94\mu_B$ in single crystals of $SrFe_2As_2$, $\mu = 1.01\mu_B$ [137] in $SrFe_2As_2$ powder and 0.8 μB in $CaFe_2As_2$ single crystals.

While the nature of the ordered state in these materials has been discussed widely, there is growing consensus that it originates from the itinerant electrons; Namely, part of the electron– and hole–like Fermi surface sheets map onto each other by a two-dimensional commensurate nesting vector $\mathbf{Q}(\pi,\pi)$ (see Figure 3.5 (a)). With the exception for the "11"-

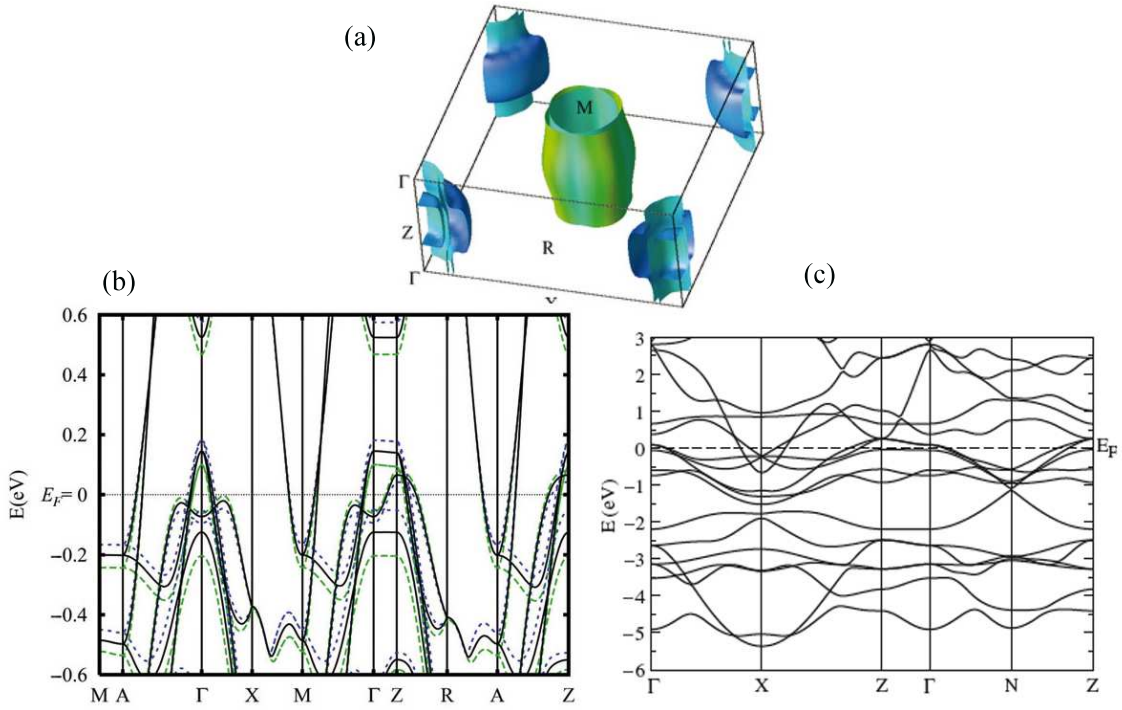

Figure 3.5 (a) Fermi surfaces of LaFeAsO, shaded by the value of the Fermi velocity v_F. The centre of the Brillouin zone is shifted to the corners of the figure. The hole Fermi surfaces sheets are at the corners of the figure, the Γ point, while the electron pockets are in the center, surrounding the M point. (b) LDA band structure of LaFeAsO. The solid black curves give the band structure for the observed crystal structure. Taken from Ref. [50]. (c) LDA band structure for body-centered-tetragonal (bct) $BaFe_2As_2$. One can clearly the hole-like Fermi surface crossings around the Γ–point, and the electron-like crossings around the X-point. Taken from Ref. [150].

type IBS, this nesting vector is the same as the commensurate antiferromagnetic ordering wave vector [74; 210]. Itinerant magnetism is also supported by the reduced magnetic moments and the decrease of the density of states near the Fermi energy level in the magnetic phase of IBS. In addition, it has been proposed that the nearest neighbour and next-nearest neighbour interactions between Fe moments are both antiferromagnetic and of comparable strength, leading to magnetic frustration [225]. The latter scenario is one of the suggestions to provide an explanation for the structural phase transition, as the lattice distortion relieves the magnetic frustration [225; 278]. It was suggested that the structural transition from a "nematic" ordered phase at a temperature above the SDW transition.

In Ref. [154] it was expressed that one is dealing with local moment antiferromagnetism

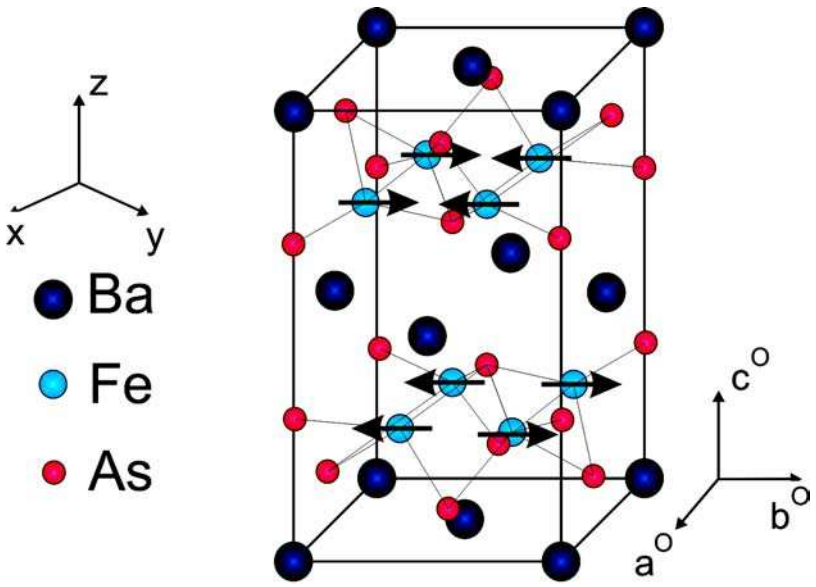

Figure 3.6 SDW order configuration in the parent compound $BaFe_2As_2$: the spin of Fe atoms are represented by arrows.

with itinerant (RKKY-type) exchange. It was claimed that both the low temperature magnetic order and structural distortions can be explained in this manner. Finally, it was proposed in Ref. [27] that both the magnetic and structural transitions are driven by orbital physics and that the structural transition is, in fact, a ferro-orbital ordering transition. This proposal explains the coupling between the structural and magnetic transitions and is consistent with the rather large ordering temperature .

3.2 Theoretical Approaches

The first theoretical proposal for the superconducting pairing mechanism IBS, immediately after their discovery was that by Mazin *et. al.* [109]. The authors argued against conventional superconductivity in these systems. They pointed out the very high value of the magnetic susceptibility and LaFeAsO, higher than any that in known conventional superconductor in which superconductivity is ought to be suppressed by spin fluctuations. The susceptibility in the pure compound is large; upon doping with F, it becomes even larger. Very strong electron-phonon interactions would be required to overcome the destructive effects of such spin fluctuations. The ab *initio* calculations performed by the same authors on the electron-phonon spectral weight function and coupling revealed results which can in no way explain the relatively high transition temperature in these compounds, *i.e.*

$T_c \geq 26$ K. The DFT Fermi surface calculations performed for the LaFeAsO as a function of doping (with x in the region of $0.04 - 0.05$) shows that the 3D pocket fills with electron doping, leaving a highly 2D electronic structure with two heavy cylinders and two lighter (and larger) electron cylinders.

Upon doping, the broad antiferromagnetic spin fluctuations near the M point in the Brillouin zone remain present; however the tendency to magnetism existing at zero doping is suppressed. The fluctuations, too broad to induce stable magnetism, create a circularly symmetric superconducting state with order parameter of opposite signs on the electron and hole pockets. This state was dubbed $s_{\pm}$ superconductivity. One of the interesting features of the proposed $s_{\pm}$ is that the coherence factor for exciting quasiparticles on the Fermi surface sheets with opposite signs of the order parameter were reversed compared to conventional coherence factors. Only slightly later, Kuroki *et. al.* proposed a model including all five Fe d bands by applying the random phase approximation (RDA) [139]. The argued that, indeed, extended s-wave pairing arises from the nesting of the disconnected Fermi surfaces, but pointed out that d-wave pairing is also a candidate for these systems, notably when the pairing interaction between different electron sheets, or different parts of the same electron sheet, is important (RHS of Fig. 3.8). The premise of a pairing interaction between electron-like Fermi surface sheets (β sheets), as well as the specific inclusion of the different orbital character in the derivation of the pairing interaction, naturally lead Kuroki *et al.* to propose the possibility of gap nodes intersecting the β Fermi surface. This is due to the spin fluctuations arising from the β_1-β_2 nesting, which gives rise to a sign change in the gap on that β_1 and β_2 Fermi surfaces. They have found that this nodal line moves out of the β Fermi surface for parameter values for which spin fluctuations due to a β_1-β_2 nesting become less effective. They conclude that spin fluctuation modes realize unconventional, extended s-wave pairing where the gap changes sign when one crosses a nesting vector [140]. The same authors also reported on the effect of the lattice structure on spin fluctuations mediated superconductivity by adapting the five band model to the lattice of LaFeAsO, NdFeAsO, as well as LaFePO [138]. Applying RDA calculations, they revealed that the gap function and the strength of the superconducting instability were determined by the cooperation or competition of spin fluctuation modes arising from different types of nesting of the Fermi surfaces, which are, of course, sensitively affected by the lattice structure. For example, Kuroki *et al.* have reported a competition between β_1-β_2 and α-β nestings. This yields different superconducting gap structures such as low-T_c nodal and high-T_c nodeless pairings. In a more recent study Kontani *et. al.* proposed that moderate electron-phonon interaction due to the Fe ion oscillation can induce d-orbital fluctuations. The latter give rise to strong pairing interaction yielding an s-wave state without sign

change (s_{++}-state) [92]. They argued that, as impurity concentration is increased, there should be crossover from $s_{\pm}$ to s_{++}-state.

3.3 Gap structure of iron-based superconductors

Approximately eight years after their discovery, the superconducting gap symmetry of the cuprates has been established by Tsuei *et. al.* as being d-wave [26]. In less than half that time, a significant number of experimental studies have reported evidence, of some kind or another, for the $s_{\pm}$-state predicted by Mazin *et. al.* [14; 92; 109; 228]. Most prominent is the spin resonance by inelastic neutron scattering (INS), which is thought to demonstrate the sign-change of the superconducting gap function [167; 269]. It was also proposed that the possible coexistence of the superconducting order and SDW in the underdoped regime of the phase diagrams is an indication for the $s_{\pm}$ symmetry [14].

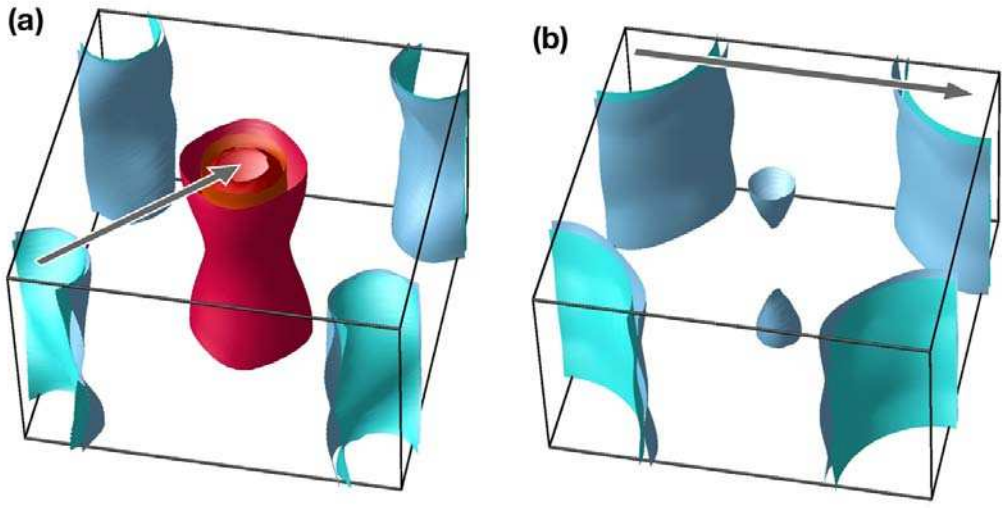

Figure 3.7 (a) Calculated Fermi surfaces for $Ba(Fe_{1.94}Co_{0.06})_2As_2$ and (b) $K_{0.8}Fe_2Se_2$. Different shades of red denote hole Fermi surfaces, and different shades of blue the electron ones. The arrows show quasinesting vectors. Taken from Ref.[108].

On the other hand, multiple studies performed on iron-based superconductors have shown that the multi-band nature of low-energy electronic excitations is expressly involved in the physics of the pairing mechanism [14]. The experimental data show a very different behavior of the superconducting gap structure from one family to another, and, even in the same family as chemical doping or pressure is increased [177]. Various experimental studies

reported the evidence of presence of gap nodes. ARPES measurements revealed that there is a strong electron-phonon coupling in LiFeAs [2], and that the measured gap anisotropy in that material cannot be explained with $s_{\pm}$ symmetry , but can be accounted for by orbital fluctuations assisted by phonons [93; 211]. The recent discovery of "122*-type" ($A_xFe_{2-y}Se_2$, A = K, Rb, Cs, and Tl) materials [118] , with their large local moment $3.3\mu_B$/Fe [238] and different Fermi surfaces (no hole pockets) argues against the $s_{\pm}$-state, at least in some of the iron-based superconducting compounds.

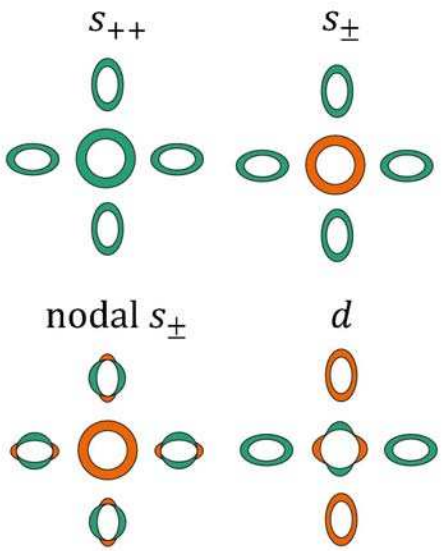

Figure 3.8 Cartoon of order parameters under discussion in the Fe-pnictide superconductors represented in the 2-dimensional, 1-Fe Brillouin zone. Different colors stands for different signs of the gap. Taken from Ref.[177].

In addition to this, the effect of impurities, induced either by chemical substitution or by particle irradiation has been considered. Experiments [10; 27; 37; 271] show that the T_c suppression rates are generally more slow than the maximum rate expected for $s_{\pm}$ superconductivity, that is, supposing that the added impurities contribute to interband scattering only. Given the many uncertainties on the actual effect of impurities, which may not act simply as potential scatterers, but can also affect the electronic structure and the pairing interaction, experiments in which the disorder is systematically varied may not play a decisive role in the identification of the order parameter symmetry. This does not refrain one from studying, the effect of disorder, induced either by substitution or particle irradiation, with the pair-breaking model, *i.e.*, the generalization of the conventional Abrikosov-Gor'kov approach [151]. The presence of non-magnetic impurities in

conventional multi-band superconductors leads to quasi-particle scattering between bands or within the same band. This is sketched in Figure 3.9. In the case of a sign-changing multi-band system the intra-band scattering will average the gaps and can lead to some initial suppression of T_c, while, the inter-band scattering has a much more profound effect [1]. Namely, non-magnetic impurities with an inter-band component of the scattering potential have a pair-breaking effect and can suppress T_c to zero at a critical concentration. For the case of iron-based superconductors, related studies have been reported by several groups [14; 109; 259]. The suppression of T_c was further discussed in detail in terms of impurity scattering rates and the pair-breaking parameter in Ref. [60]. Recent experiments on the penetration depth and the thermal conductivity have provided some consensus on the evolution of the low-energy quasiparticle density over the phase digram of the "122" type materials. Even very early experiments evoked the possibility that variations between different samples of the same material can be explained by the effect of disorder [135]. The role of different experiments probing the gap structure and the effect of disorder on the low energy quasiparticle density of states will be outlined in the next paragraphs.

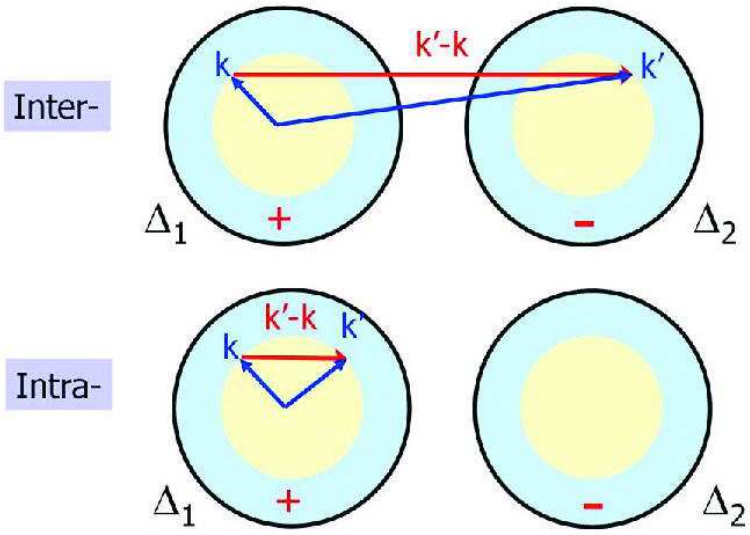

Figure 3.9 Schematic representation of two Fermi surface pockets with different superconducting gap signs. Top: inter-band scattering by impurities. Bottom: intra-band scattering states on each pocket. Taken from Ref.[177].

3.4 Experimental techniques as a probe for the gap symmetry and the nodal structure

3.4.1 Penetration depth measurements λ_L

Figure 3.10 shows an overview of magnetic penetration depth measurements performed on several iron-based superconductors by different techniques and groups. The temperature dependence of the low temperature penetration depth can be considered as a probe of the quasiparticle excitations, which sensitively depend on the gap structure, and therefore provides evidence for the presence of shallow gap minima, subgap states, or nodal structures. If a fit of λ_L to theory over the entire temperature range up to T_c is difficult for multi-band superconductors, the information related to the gap structure given by low temperature penetration depth measurement is unambiguous. The relation of different gap structure with power law T^2 in temperature, $\Delta\lambda_L = \lambda(T) - \lambda(0) \sim \mathrm{T}^n$, was pointed out by Gross *et. al.* [24; 71]. In fully gapped superconductors, at low temperature the temperature dependence of $\Delta\lambda_L(T)$ has an exponential behavior. This is the case in some iron-based materials, such as the members of the 1111 family [135], as well as K-doped $BaFe_2As_2$ [135]. However, $\Delta\lambda_L(T)$ can also commonly be fitted by a power law in T over some intermediate temperature range. Thus the low temperature behavior may not be straightforward to interpret. Only a linear dependence $\Delta\lambda_L \sim T$ may give the certitude concerning the presence of line nodes. Such a behavior of the penetration depth has been reported for both LaFePO [38] system and for isovalently substituted $BaFe_2(As_{1-x}P_x)_2$ [135] (see Figure 3.10). On the other hand, for the charge-doped "122" materials; $Ba(Fe_{1-x}Ni_x)_2As_2$ and $Ba(Fe_{1-x}Co_x)_2As_2$, a T^2 dependence is observed [34; 148]. It has been suggested that T^2 dependence is evidence for a $s_\pm$ state [33; 196; 204; 236]. Namely, in the $s_\pm$-state, the presence of disorder was argued to lead to a residual density of states induced at the Fermi level, and from there, to a T^2 dependence of the penetration depth at low temperatures. However, the critical temperatures of the materials at hand are still very high. Given the disorder levels necessary to attain the given behavior of the penetration depth and other thermodynamic parameters, superconductivity should be considerably suppressed. Another possibility, is that of a dirty (line) nodal state in parallel with the situation in the d-wave cuprate superconductors.

Experiments performed by Hashimoto *et. al.* in order to correlate the disorder to the low-temperature penetration depth [134] report a T-exponential dependence for a given sample, and a T^2 behavior for another, considered dirtier crystal. This was interpreted as due to the pair-breaking mechanism caused by inter-band scattering in an $s_\pm$ state. A similar analysis method was used by Kim *et. al.* to extract the low-energy density of states

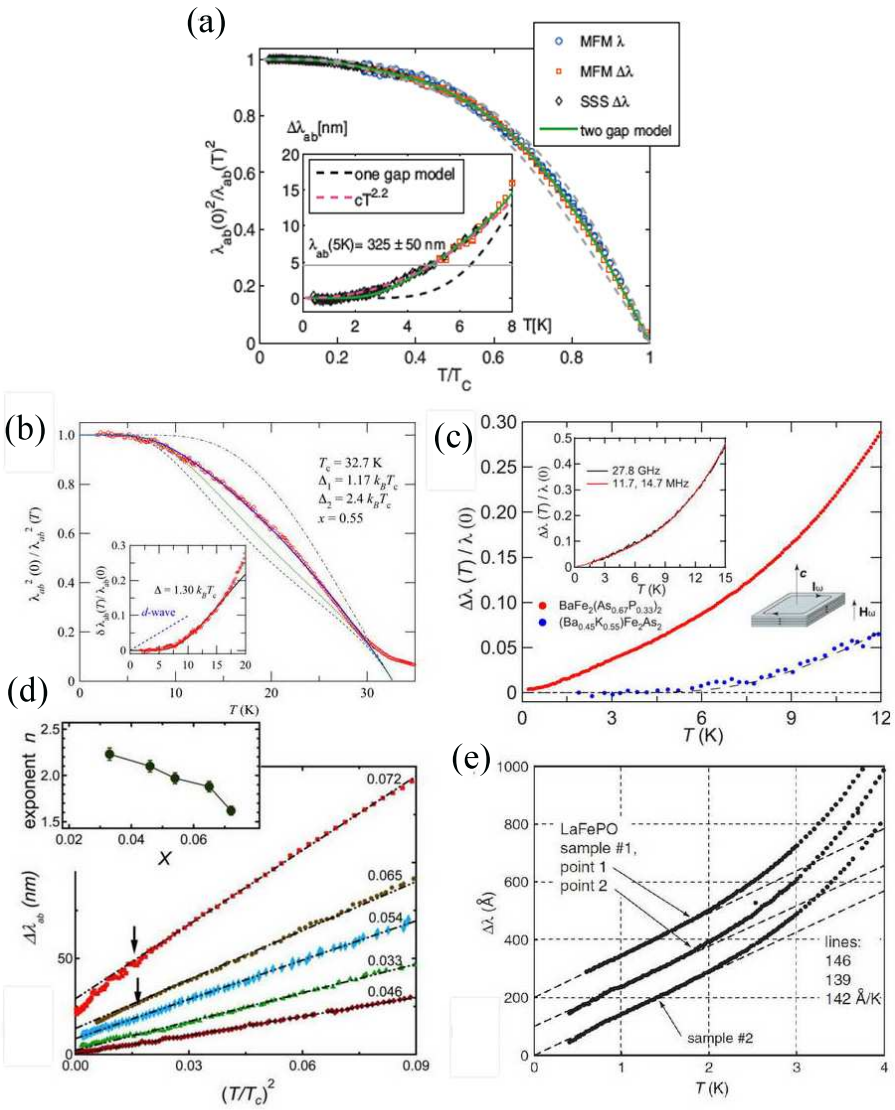

Figure 3.10 An overview of the temperature dependence of the London penetration depth, measured by different groups on different compositions of iron-based superconductors. (a) underdoped $Ba(Fe_{0.945}Co_{0.055})_2As_2$ [148], (b) optimally doped $Ba_{1-x}K_xFe_2As_2$ [135], (c) optimally doped $BaFe_2(As_{1-x}P_x)_2$ [132], (d) several doping levels of $Ba(Fe_{1-x}Ni_x)_2As_2$ [34] and (e) LaFePO [38].

caused by pair-breaking inter-band scattering and its effect on the temperature dependence of the penetration depth and the critical temperature T_c [91].

3.4.2 Specific heat C and thermal conductivity κ measurements

The measurements of the specific heat C

$$C/T = \gamma + \beta T^2, \tag{3.1}$$

where γ is the electronic specific heat coefficient and β is the coefficient of the phonon contribution, also probe the nodal structure of the superconducting gap. The first one is a $C \sim T^2$ dependence in the specific heat, which is indicative of line nodes in the gap. The latter is, however, very difficult to verify experimentally, due to large , other contributions to C, with other temperature dependences, such as shown for YBCO in Ref. [275].

The second way to probe the gap nodes is to measure the low temperature γ as a function of magnetic field. This, under the assumption that the system does not contain any magnetic impurities, since these latter obscure the magnetic field response of γ [208]. For a fully gapped symmetry, single gap-superconductor, γ will vary as H due to localized states in the vortex cores.

For d-wave superconductors (with line nodes), the theory of Volovik [84] predicts $\gamma \propto H^{1/2}$ at $H \ll H_{c2}$ as observed for YBCO by Moler *et. al.* in fields of up to 9 T [129]. For the case of disordered superconductors with line nodes, a $\gamma \sim \log H$ behavior is predicted [31]. Another explanation for the power law dependence, $\gamma \propto H^{\alpha}$, with $\alpha < 1$, is the changing size of the vortex cores, as observed experimentally in $NbSe_2$ in fields up to $0.3H_{c2}$ by Sonier *et. al.* [115]. Studies of γ vs H in superconductors often, reveal more complicated results than the simple, pure power law predictions. Volovik's theory is only valid in the low field limit, but the $\gamma \sim H^{1/2}$ law has been found at higher fields up to H_{c2}. An explanation for this sub-linear behavior in γ is the presence of two or more gaps.

The third way for the specific heat to probe the gap symmetry is to measure γ as a function of magnetic field angle in the nodal plane, where the minima will indicate directions of field that are perpendicular to the nodes. For perpendicularly applied magnetic field, this will give a $H^{1/2}$ dependence of γ. Due to its difficulties and the uncertainty in the experimental results, this technique has only begun to be employed, on the iron-chalcogenide [221]. Early measurements of the specific heat down to 2 K on both unannealed Ni and Co-doped $BaFe_2As_2$ [216] showed a residual $\gamma(T \to 0)$ of $\sim$10 mJ/moleK^2. Gofryk *et. al.* performed specific heat measurements on slightly overdoped, $x = 0.08$, and overdoped $x = 0.1$ Co-doped $BaFe_2As_2$, before annealing the samples. This gave values ranging from 3.7 mJ/mole K^2 to 14.6 mJ/mole K^2. The values decreased after annealing the samples to γ(T$\to$0)=1.3-3.8 mJ/mole K^2 [130].

Measurements of the thermal conductivity, κ,

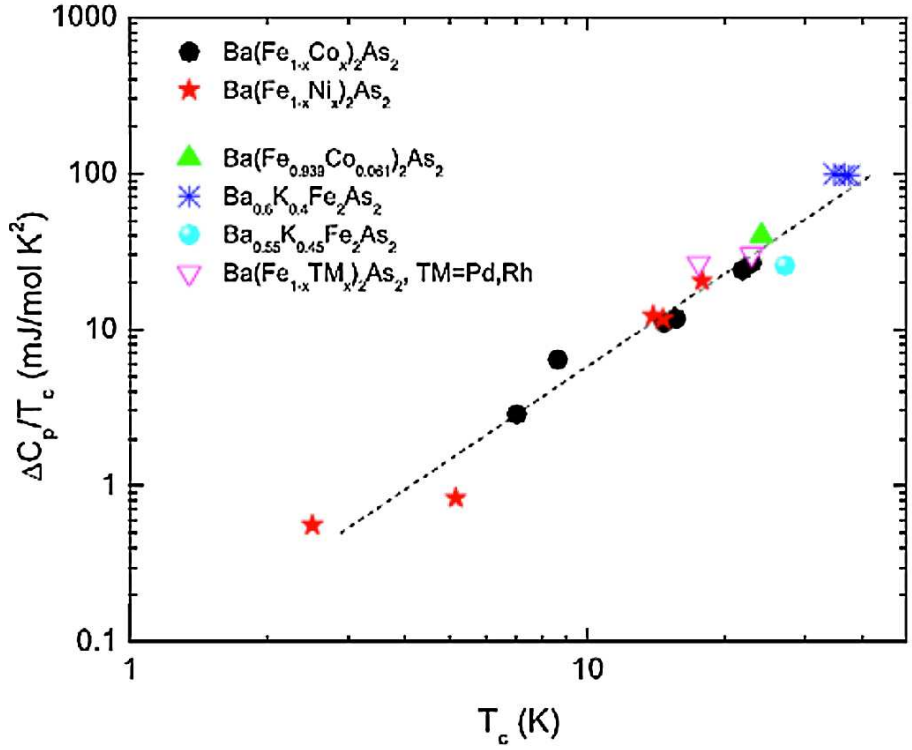

Figure 3.11 An overview of specific heat measurements at the critical temperature T_c showing the discontinuity in the specific heat as a function of T_c for different compounds of the "122" family. Taken from Ref. [216].

$$\frac{\kappa}{T} = a + bT^{\alpha-1}, \tag{3.2}$$

where the first term on the right comes from the conduction electrons and the second term is from phonons and magnons, were also performed on IBS compounds. Thermal conductivity is a similar probe to the specific heat in sensing the nodal gap structure: $\kappa/T \rightarrow 0$ as T$\rightarrow$0 indicates a fully gapped superconductor, while a finite value of κ/T may indicate either a nodal structure, or gapless behavior due to pair-breaking scattering. For the case of a nodal gap structure, the magnetic field dependence of the thermal conductivity $\kappa/T \sim H \log H$ is also similar to that found for the specific heat. Several publications on the thermal conductivity of iron-base superconductors have given clear evidence for fully gapped behavior [126]. Several measurements were performed especially on different compounds of the "122" family. Luo *et.al.* measured the zero magnetic field thermal conductivity on hole-doped $Ba_{1-x}K_xFe_2As_2$ (with $x = 0.25, 0.28$), which revealed

a negligible residual linear term in κ/T as $T \to 0$ [251]. They interpreted these results as showing the absence of zero-energy quasiparticles and nodes in the gap in the ab-plane. But they also showed that the application of a small magnetic field may induces a large κ/T, implying a minimum in the size of the superconducting gap somewhere on the Fermi surface. Similar measurements have been performed on several doping levels of charge-doped $Ba(Fe_{1-x}Co_x)_2As_2$ single crystals by Tanatar *et. al.* ($0.048 \leqslant x \leqslant 0.114$) and by Reid *et. al.* ($0.038 \leqslant x \leqslant 0.0127$). Tanatar *et. al.* reported similar results (*i.e.*, a negligible residual linear term in κ/T as $T \to 0$), interpreted as in the K-doped "122": there are no zero energy quasiparticles, hence the thermal current in the ab-plane has no electronic contribution [72; 153]. However, Reid *et. al.* found a finite residual κ/T as $T \to 0$ (implying sub-gap states and nodes in the gap) for a thermal currents along the c-axis in overdoped crystals.

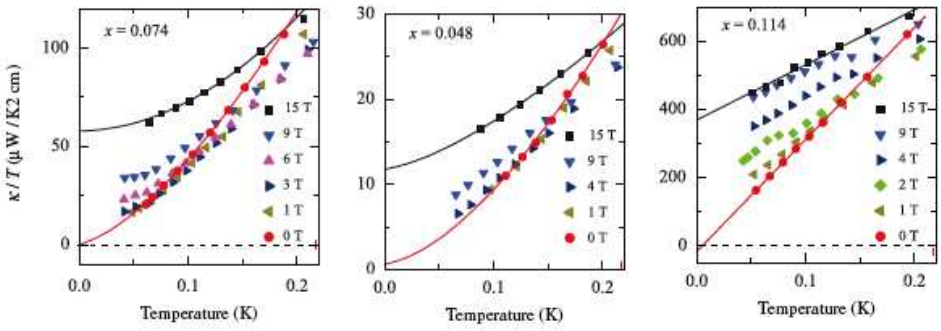

Figure 3.12 Thermal conductivity divided by temperature, versus T for three different doping levels of $Ba(Fe_{1-x}Co_x)_2As_2$, in various applied magnetic fields H_a as indicated, with the heat flow in the *ab*-plane ($\parallel$ to the FeAs layers). Taken from Ref. [153].

The application of a moderate field of $H_{c2}/4$ excites the quasiparticles that conduct heat along the *a*-axis just as well as nodal quasiparticles along the *c*-axis. This gives an indication of a small gap, also in regions of the Fermi surface that contribute to the in-plane conduction [126]. For optimally Co-doped $BaFe_2As_2$ the residual κ/T shows $\kappa \sim H$ for both directions. The appearance of quasiparticle thermal currents as one changes the doping level x implies the possibility of quasiparticle subgap states induced by impurity scattering, consistent with a sign changing $s_\pm$ symmetry. Similar measurements performed on the Ni-doped "122" system have given results consistent with a nodeless multigap symmetry [88]. For the isovalently substituted $BaFe_2(As_{1-x}P_x)_2$ single crystals, thermal conductivity measurements have been performed by Hashimoto *et. al.* in zero field down to 0.1 K. Measurements up to 12 T gave indications for a nodal gap [133], while the same

experiments on the same material as a function of angle and field have given indications for a the nodal s-wave symmetry [167].

3.4.3 ARPES

Low energy excitations, the existence of which is implied by the thermodynamic experiments described above, should in principle be observable by angle-resolved photoemission spectroscopy (ARPES). In fact, ARPES is the most direct probe of the superconducting gap structure. Its latests developments signify that this tool can both resolve the Fermi surfaces structure in momentum space and the spectra of the electronic states near the Fermi energy. The size, shape, and position in momentum space of the predicted Fermi surface pockets were measured by ARPES, allowing for the verification of the extent of Fermi surface nesting, which is very important for the role of spin fluctuations in superconducting pairing. ARPES data can also show the evolution of the Fermi surface pockets as a function of doping level. Brouet *et. al.* have reported a systematic ARPES study on the charge-doped $Ba(Fe_{1-x}Co_x)_2As_2$ compound [231]. Their study identified three different hole pockets, the outer one exhibiting a strong photon energy dependence. They have attributed this to a stronger 3D character of this band, in good agreement with band structure calculations. At large electron doping, 2D electron pockets, with rather circular shapes were observed. Mansart *et. al.* reported on an ARPES study of Co-doped $BaFe_2As_2$ across the superconducting phase transition [19]. They have performed ARPES study of the hole-like Fermi surface above and below the superconducting phase transition in optimally doped $Ba(Fe_{1-x}Co_x)_2As_2$ along high-symmetry directions in k space. Their analysis confirms that the superconducting gap is isotropic for the outer hole pocket β, while it shows slight anisotropies for the inner one, α. Their results are consistent with a $s_{\pm}$ order parameter.

There are also several works performed on the "1111" family using ARPES. Kondo *et. al.* reported the same fermiology for $NdFeAsO_{1-x}F_x$ and LaFePO as proposed for the "122" compounds and concentrate on measuring the gap magnitude [220].

3.4.4 Nuclear magnetic resonance (NMR)

Measurements of the temperature dependence of $1/T_1T$, where $1/T_1$ is the nuclear spin lattice relaxation rate in the superconducting state, give information on the presence or absence of a residual density of states. However, the applied magnetic field used to carry out the NMR measurements introduces vortices into the superconductor, and, thereby, a finite low-energy density of states related to quasiparticle states in the vortex cores. Methods to

avoid this field induced DOS is to measure $1/T_1$ as function of field, and extrapolate the data back to $H = 0$. Also, one may perform zero field nuclear quadrupole resonance (NQR) measurements of $1/T_1$. NMR measurements performed on $Ba_{1-x}K_xFe_2As_2$ by Fukuzawa *et. al.* gave similar results [89] as those found for $LaFeAsO_{0.9}F_{0.1}$, $1/T_1 \sim T^{2.6}$ [269]. These were interpreted as an indication of line nodes in the gap in an extended s-wave symmetry. Similar measurements have been performed on isovalently substituted $BaFe_2(As_{1-x}P_x)_2$ single crystals by Nakai *et. al.* They found a linear behavior response of $1/T_1$ in temperature, between 0.1 and 4 K, that constitutes evidence for a residual DOS at zero energy. In addition to this, the penetration depth and thermal conductivity measurements performed on the same compound confirm the existence of line nodes in the gap [270].

3.4.5 Neutron scattering

Neutron scattering is a very important tool to measure the dynamic susceptibility $\chi_s(\mathbf{q},\omega)$. For local interactions this parameter can be extracted in RPA from the electron-hole term $\chi_0(\mathbf{q},\omega)$,

$$\chi_s(\mathbf{q},\omega) = [I - U_s\chi_0(\mathbf{q},\omega)]^{-1}\chi_0(\mathbf{q},\omega), \tag{3.3}$$

Here I is a unit matrix in orbital space, and other quantities are matrices as well. For a given range of interactions entering the matrix U_s, $\mathrm{Im}\chi_0$=0, and the real part $\mathrm{Re}\chi_0$ leads a divergence in $\mathrm{Im}\chi_s(\mathbf{q},i\omega_m)$ according to Eq. 3.3. This increase in the spin susceptibility is called a "spin resonance". This resonance appears at the exact position Ω_{res}. The scattering between nearly nested hole and electron Fermi surfaces in iron-based superconductors produces a peak in the normal state magnetic susceptibility at, or close to, $\mathbf{q}$=$\mathbf{Q}$=(π,0).

In the superconducting state, for a uniform s-wave gap function, there is no resonance peak, while in the case of the sign changing $s_\pm$-state, the nesting vector $\mathbf{Q}$ connects different Fermi sheets bearing gaps of different signs. This fulfills the resonance condition for the interband susceptibility, hence a resonance peak is observed. The existence of a spin resonance peak in IBS was first predicted theoretically and later reported experimentally. A well defined spin resonance near (π,0) was reported in the "1111", "122" and "11" type IBS families [6; 59; 272]. These measurements observe a magnetic neutron scattering "spin resonance mode" in the superconducting state that has the same in-plane wavevector as the antiferromagnetic nesting vector in the normal state above T_c. In the case of the compounds of the "122" and "1111" family this wavevector is the same as the in-plane component of the long range antiferromagnetic order in the parent compound. Results on the Co-doped "122" gave $\Omega_{res}/2\Delta$=(0.79±0.15) [53; 54] which is close to the value 0.64 claimed to be a universal value for cuprates, heavy fermions and IBS. The temperature

dependence of Ω_{res} in $Ba(Fe_{1-x}Co_x)_2As_2$ is found to be BCS-like. Thus, inelastic neutron scattering measurements have constrained the order parameter symmetry in the doped (Ca,Sr,Ba)Fe_2As_2 and "11"-type compounds [193]. Recently it was argued that the theoretically predicted resonance peak for isotropic $s_{\pm}$-state is too sharp and too strong when compared to the maximum observed in experimental studies. Onari *et. al.* have proposed an explanation for the spin resonance in the case of the superconducting order parameter without sign change [213]. They reported that if there is a collapse in the scattering rate below the pair-breaking edge, the redistribution of the spectral weight when entering the superconducting phase can lead to an increase of the spin response below T_c as compared to the normal state. This response cannot be considered as a real spin resonance since it does not lead to a divergence in $Im\chi_s$. Also, similar experiments in cuprates gave sharper spin resonance response than IBS so there may be some doubt that scattering involves a sign-changing gap. The broadening of the spin excitation response may be due to several other reasons, such as a significant anisotropy of the $s_{\pm}$ gap. The exact effect of neutron scattering has been the subject of several debates [212; 268]. The fact that similar features of spin excitations are reported for all families of IBS would go against the possibility of an isotropic $s_{\pm}$- wave gap.

3.4.6 Andreev spectroscopy, tunneling, and Raman scattering

Andreev spectroscopy is a strong experimental probe of the superconducting order parameter. Point contact Andreev reflection (PCAR) spectra measured on a ballistic microconstriction between a normal metal and a superconductor consists of pure Andreev reflection and tunneling contributions, respectively [83]. At a normal metal/superconductor interface, the injected current at a bias voltage within the gap must first be converted into a supercurrent consisting of Cooper pairs of electrons with opposite spins. This can be accomplished by having the injected electron from one spin band accompanied by another electron from the opposite spin band. This is the well-known Andreev reflection process, which is equivalent to reflecting a hole back into the metal, thus doubling the conductance within the superconducting gap. Therefore, the first contribution yields a conductance within the voltage region $|V| < \Delta/e$ that is twice as large as the normal state conductance, or as the conductance at large bias at which the coupling via the gap is inefficient. The PCAR conductance can be compared to the predictions of the Blonder-Tinkham-Klapwijk (BTK) model, using as input parameters the energy gap Δ, the parameter z (a measure for the transparency of the interface barrier) and a parameter Γ for spectral broadening. The tunneling contribution reduces the conductance at zero bias due to the presence of the superconducting gap. In the absence of the Andreev reflection contribution expected

for high transparency junctions, two symmetrically located "coherence" peaks rise at the gap energy.

Measurements of the differential conductance $dI/dV(V)$, where I is the current, V is the bias voltage across the contact, and G is the conductance, were carried out on different iron-based superconducting compounds [181; 183]. A negative V is defined as that arising when electrons are injected from the tip into the superconductor. Andreev spectroscopy provides a sensitive and quantitative measurement of the gap structure of superconductors.

Andreev spectroscopy performed on K-doped $BaFe_2As_2$, has revealed a single gap, but strongly suggested that the measurement in the c-axis tunneling direction could be missing bands in the ab-plane [255]. Szabo *et. al.* reported, Andreev spectroscopy of the same compound, on two gaps in the ab-plane [183]. Recent work on Co-doped "122" [181] has reported a single gap, while a more recent study has found two gaps in the optimally doped material [165]. Andreev spectroscopy has also been performed on Co-doped thin film of the "122" material. This showed evidence of unconventional pairing, with a superconducting contribution to the conductivity, possibly due to fluctuations, to a temperature of up to $1.3T_c$. Several studies of Andreev spectroscopy have also been performed on the "111"-type materials. Evidence for a conventional single gap [224] or multiple gaps has been reported [49; 199] with possible unconventional behavior in one of the gaps. Scanning tunneling spectroscopy (STS) and STM performed on Co-doped "122" [75] and $NdFeAsO_{1-x}P_x$ [190] has revealed a single single gap.

Raman spectroscopy is also an important tool for probing the gap symmetry. Because the momentum and polarization of incoming and outcoming photons can be controlled in Raman scattering measurements, this technique is a useful to probe selectively different parts of the Fermi surface. Zhang *et. al.* performed Raman spectroscopy measurements on the single crystals of $K_{0.8}Fe_{1.6}Se_2$ [150] and found a large number of phonon modes which they analyzed consistently in terms of the Fe-vacancy ordering proposed by Bao *et. al.* [238]. One of the observed phonon modes showed a change in the frequency at the transition temperature indicating a connection between the superconductivity and phonon modes.

3.4.7 Quasiparticle interference (QIP)

Another experiment providing information on the gap structure is the so-called quasiparticle interference scattering (QIP). Any kind of impurity or defect in the metal is screened by the conduction electrons. This gives rise, for example, to the well-known Friedel oscillations of the charge and spin density around the imperfection. The Fourier transform of the electron density will reflect the charge susceptibility in reciprocal space. Scanning

tunneling spectroscopy can be used to map out this local electronic density at energies spanning the Fermi energy. In a scanning tunneling microscopy (STM) experiment on a metallic surface, taken at a given bias V, the differential tunneling conductance dI/dV is proportional to the electronic density of states at energy $\hbar\omega$ at the imaged position. The presence of impurities in the material leads to the scattering of the conduction electrons and ensuing interference of the refracted electronic wave functions, that can be probed by STM. A Fourier transform of the intensity image yields the main wave vectors q contributing to the scattering at the bias energy $\mathcal{E} = eV$. Hanaguri *et. al.* performed scanning tunneling microscopy (STM) in $FeSe_{1x}Te_x$ at 10 T and concluded as to an $s_{\pm}$-state [218].

For IBS, theoretical predictions for the dispersion $\mathcal{E}(q)$ of the QIP q-peaks have been made for models with electron and hole pockets in the presence of an $s_{\pm}$ order parameter, in the SDW state, and in the coexistence phase [226]. All gave different results, depending on the evolution of the quasiparticle energy on the various Fermi surfaces. Wang *et. al.* have pointed out that the Fourier transform of the STM (FT-STM) measurements can distinguish between $s_{\pm}$ and s_{++} pairing scenarios [80]. Chuang *et. al.* have performed QIP measurements in the magnetic phase of Ca-"122", slightly doped with Co that revealed strong breaking of the tetragonal symmetry, consistent with the observed SDW [121] and DFT calculations [226]. It was also pointed out that the scattering in this system may be due to impurity states around the dopant atom Co sites.

3.4.8 Disorder

Experiments such as the measurement of the low temperature T-dependence of the London penetration depth [132; 135; 198; 202; 203; 204; 236] and thermal conductivity [125; 126] can be used as probes of the low-energy quasi-particle density of states (QPDOS). The sensitivity to material disorder of the different physical parameters, such as the critical temperature, superfluid density, and the critical fields, in another indirect method to allow one to characterize the gap symmetry of the iron-based superconductors. In the case of a sign-changing order parameter, impurity scattering by point-like defects, generally present due to chemical substitution, or added artificially by irradiation, may lead to pair-breaking. In iron-based superconductors, quasi-particle scattering between electron–like and hole–like bands (with opposite sign of the order parameter) would lead to strong suppression of T_c [7; 94; 177; 211]. Superconductivity with a d–wave symmetry of the order parameter would be even more sensitive than the $s_{\pm}$ symmetry, because of the pair-breaking effect of both interband and intraband impurity scattering [60; 177]. As for now, the precise evolution of superconducting properties of the iron-based superconductors under the effect of increasing strength of disorder remains unknown. It is generally argued that the T^2 behavior of the

low temperature penetration depth $\lambda_{ab}(T)$ is indicative of a strong pair breaking [198; 202; 203; 204; 236]. Nevertheless, T_c of the material that show this behavior of the penetration depth is generally quite high. A more quantitative characterization of native disorder in iron based superconductors is therefore important. Also, the addition of artificial disorder by chemical substitution or energetic particle irradiation can be an invaluable tool to probe the evolution of superconducting parameters as function of increasing disorder strength.

Probing the sensitivity of iron-based superconductivity to disorder induced by chemical substitution has the major drawback that the latter also induces changes of the structure and of the chemical potential. It is therefore unclear in what sense the substitution experiments of Ref. [147] are to be interpreted. This caveat can be avoided by using energetic particle irradiation as a tool to controllably introduce disorder. Nakajima *et. al.* performed proton irradiation in optimally doped $Ba(Fe_{1-x}Co_x)_2As_2$ [271]. They reported that the critical current density under self-field increases by a factor of 2.5 at $T = 2\ K$ after irradiation. A significant T_c–reduction was observed, which was attributed to the interband scattering effect of the point defects and point defect clusters introduced by the proton irradiation. Tarantini *et. al.* reported that α-particle irradiation of NdFeAs(OF) also leads to a reduction of the critical temperature T_c [37]. From the Kondo-like excess resistance $\Delta\rho(\mathrm{T})\ln(T)$, observed over 2 decades in temperature above T_c, they argued that the α–irradiation caused both nonmagnetic and magnetic scattering. However, the critical density of magnetic irradiation defects which suppresses T_c completely is found to be much higher than for cuprates and multiband BCS superconductors. Tarantini*et al.* suggested that such anomalously weak pair breaking indicates that the magnetic scattering in pnictides is coupled with the spin fluctuations.

Li *et. al.* have reported on the evolution of superconductivity in $Ba_{0.5}K_{0.5}Fe_{2-x}M_{2x}As_2$ by different chemical substitutions (M=Mn, Ru, Co, Ni, Cu and Zn). They investigated the doping effect of magnetic as well as non-magnetic impurities. The superconductivity of the system was found to be robust against Ru-doping, but is weakened by the inclusion of Mn, Co, Ni, Cu and Zn impurities. However, the reported T_c suppression rate for all types of impurities is much lower that what is expected for $s_\pm$ pairing. The same group have also reported on Zn doping in $BaFe_{1.89-2x}Zn_{2x}Co_{0.11}As_2$. They have observed a depression rate in T_c (3.63 K/%) similar to what is expected for $s_\pm$-wave pairing. They interpreted their results as being more adequate for non-sign reversing s-wave pairing . Lin *et. al.* have studied the effect of Zn doping impurity on the Fe site in (Pr,Sr)FeAsO. As, in optimally electron doped "1111" LaFeAsO, they observed a negligible suppression of T_c by non-magnetic Zn impurities [253].

Material	impurity	k_F Å^{-1}	ξ_0 nm	n_d nm^{-3}	σ_{tr} Å^2	$n_d\xi_0^3$	$\sin\delta_0$	Γ meV
$PrFeAsO_{1-y}$	O vacancy	0.33	2.4	1.5	6.7	21	0.3(2)	10
$NdFeAsO_{0.9}F_{0.1}$ [41]	F	0.33	3.3	1.5	2.5	54	0.2	4
$Ba_{0.72}K_{0.28}Fe_2As_2$ [252]	K	0.4	2.4	2.8	1.5	38	0.1(4)	3
$Ba_{0.6}K_{04}Fe_2As_2$ [103; 127]	K	0.5	2.2	4	2.5 ± 1.3	43	0.2	8
$Ba_{0.45}K_{0.55}Fe_2As_2$ [44]	K	0.5	2.2	5.5	1.5	59	0.2	10
$Ba(Fe_{0.95}Co_{0.05})_2As_2$ [45]	Co	0.25	1.6	1	2.5	8	0.17	5
$Ba(Fe_{0.9}Co_{0.1})_2As_2$	Co	0.25	1.6	2	2.5	8	0.17	5
$Ba(Fe_{0.76}Ru_{0.24})_2As_2$ [158]	Ru	0.25	1.6	4.8	2.5	8	0.17	5
$BaFe_2(As_{0.67}P_{0.33})_2$	P	0.3 [97]	1.6	3.3	14	–	–	–

Table 3.1 Fundamental parameters and contribution of dopant disorder to elastic scattering parameters of various iron pnictide superconductors, such as estimated from the weak collective pinning contribution to the (flux pinning) critical current density, j_c^{coll}. Here, k_F is the Fermi wave-vector, ξ_0 is the Bardeen-Cooper-Schrieffer coherence length, n_d is the atomic point defect density, σ_{tr} is the transport scattering cross-section, δ_0 is the scattering phase angle [68; 69], and Γ is the scattering rate. From Ref. [29]

3.5 Vortices in iron-based superconductors

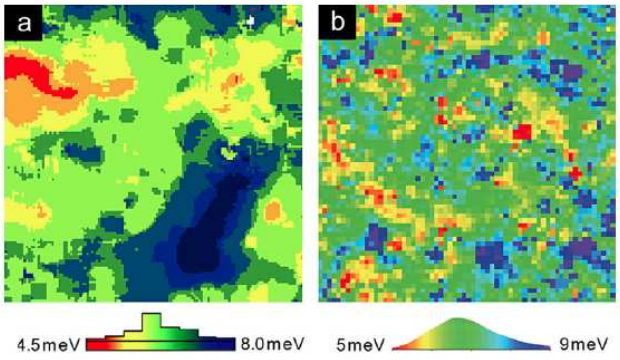

Figure 3.13 (a) Gap map recorded by Yin *et al.* over a 20×20 nm^2 area of $BaFe_{1.8}Co_{0.2}As_2$ at 6.25 K and (b) Massee *et al.* over a 18.9 ×18.9 nm^2 area of $BaFe_{1.86}Co_{0.14}As_2$ at 4.2 K. Taken from Ref. [277].

3.5.1 Vortex pinning

Pinning of vortices in iron-based superconductors is discussed by several groups, which have used different techniques such as magnetic measurements, magneto-optical imaging as well as different vortex imaging methods.

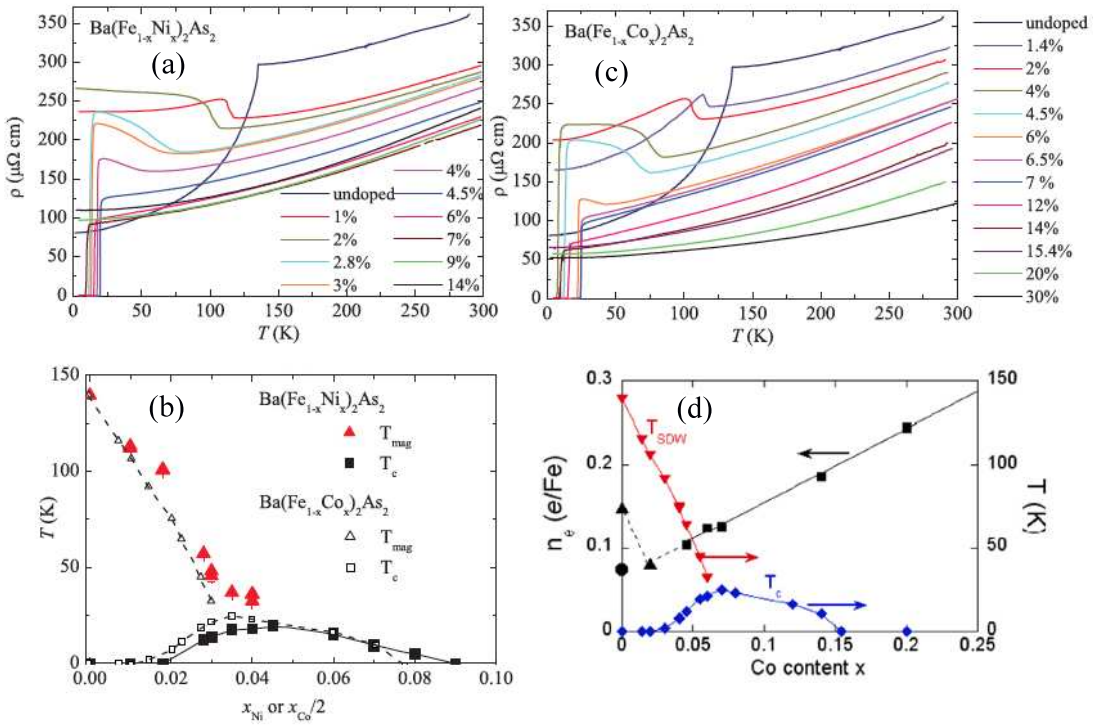

Figure 3.14 (a) Temperature dependence of the resistivity, and (b) Phase diagram indicating T_{mag} and T_c for both $Ba(Fe_{1-x}Ni_x)_2As_2$ and $Ba(Fe_{1-x}Co_x)_2As_2$ single crystals. In order to allow a comparison between the two families, the Co content was divided by 2. Lines are guides for the eye from Ref. [11]. (c) Resistivity as a function of temperature and (d)phase diagram for $Ba(Fe_{1-x}Co_x)_2As_2$ single crystals (from Ref. [77]).

The identification of different kinds of native disorder and their manifestation by vortex pinning in the mixed state of iron-based superconductors was the subject of Refs. [41; 44; 206] (see also Chapter 7 and Chapter 6). In their work on $PrFeAsO_{0.9}$ and $NdFeAsO_{0.9}F_{0.1}$ van der Beek *et. al.* have reported that both materials show significant spatial variations of T_c and the critical current density j_c. From local magnetic measurements of these system they concluded that the critical current density arises from two different contributions. The first is reported as being the weak-collective pinning by dopant atoms or vacancies. This pinning mechanism comes from mean-free-path variations in the vortex core ($\delta\kappa$ mechanism). However, the pinning contribution that predominantly manifests itself at lowest fields is the strong pinning theory for pinning by extended point-like defects. Typically, the critical current density j_c is maximum around zero field, and then drops off $j_c \sim B^{-1/2}$. The strong pinning contribution j_c^s to the critical current (see Fig. 9.9) was conjectured to

be due to nm-scale heterogeneity of the superconducting properties [45; 206].The strength of this strong pinning contribution allows one to estimate to what extent spatial variations in the doping level (of order of several dozen nm) occur. From there, it is induced that the absolute magnitude of the variations of the average dopant atom density, on the scale of 1 to 100 nm, is too small to allow for coexistence of the SDW and the superconducting phases due to chemical disorder [41]. From high-field magneto-transport and magnetization measurements on $Ba(Fe_{0.9}Co_{0.1})_2As_2$ single crystals, Yamamoto *et al.* suggest that there exists a dense vortex pinning nanostructure, that may result from the inhomogeneous spatial distribution of cobalt ions. They also concluded that the finite width of the resistive transition $R(T)$ in the measured single crystals most likely results from the T_c inhomogeneities due to the local variation of the dopant atoms density [15].

Later on van der Beek *et. al.* reported on the weak collective pinning mechanism in iron-based superconductors [44]. In their work, the authors suggested the origin of the weak-collective pinning contribution j_c^{coll} in iron-based superconductors to be the charged-dopant atoms. This is because the latter contribution is observed in the j_c curves (at fields above several tenths of a T to 1 T) of all charged-doped iron-based compounds, but is absent in the isovalently substituted $BaFe_2(As_{1-x}P_x)_2$. They suggested that charged-dopant atoms are responsible for the quasiparticle scattering in the Born limit. Estimations of the scattering rates $\gamma = n_d[\pi N(0)]^{-1} \sin^2 \delta_0$ of the doping impurities were obtained from flux pinning parameters n_d and δ_0 in Ref. [29] (see Table 3.1). This yields rather large values, which are again at odds with a superconducting ground state that would be sensitive to point-like disorder. The occurrence of the quasi-particle scattering contribution to flux pinning remarkably coincides with that of the T^2 behaviour of the penetration depth. On the other hand, it is conspicuously absent in clean materials with a T-linear dependence of λ_{ab}, such as in $BaFe_2(As_{1-x}P_x)_2$ [135; 205]. The authors of Ref. [44] suggested that the study of vortex pinning in the iron-based superconductors might be used as an alternate route to qualitatively and quantitatively assess both native and artificial disorder in these materials. This approach is to be explored in the chapters that make up this thesis.

Magnetic flux pinning and vortex penetration in $Ba(Fe_{1-x}Co_x)_2As_2$ single crystals has been also studied by Prozorov *et al.*, [196; 197] who reported on the irreversible magnetization and flux creep by magnetic relaxation measurements. The authors discuss the possibility of vortex pinning on intertwined orthorhombic/antiferromagnetic domains, notably for underdoped (x=0-0.054) single crystals, and suggested, from the study of the doping dependence of the critical current density, that structural domain walls may act as effective pinning centers. Magnetization and relaxation measurements on various doping levels of $Ba(Fe_{1-x}Co_x)_2As_2$ single crystals (with x = 0.06-0.15) have been performed by

Shen *et. al.* [21], who suggested that vortex pinning ought to be described within the collective pinning framework, but with the spatial fluctuation of the transition temperature (δT_c-mechanism) on a sub-nanometer scale being responsible for the elementary pinning force. Fang *et. al.* have reported recently on the systematic evolution of vortex pinning in isovalently substituted $BaFe_2(As_{1-x}P_x)_2$ single crystals [146]. Their study in different samples from optimally doped to overdoped showed that strong point pinning dominates the vortex behavior at low fields whereas weak collective pinning determines the behavior at higher fields.

Vortex imaging studies have been performed using different techniques by several groups for the understanding of the pinning mechanism in iron-based superconductors [18; 59; 90; 102; 144; 148; 152; 171; 172]. Different techniques agree on the absence of vortex lattice order in all studied iron-based materials. However, there is no clear consensus on the origin of this disorder and pinning. In Chapter 6 and 7, the different pinning mechanisms are identified by establishing a new vortex image analysis technique in iron-based superconductors, and by combining different experimental methods such as the Bitter decoration technique and magnetic measurements. Spatial variations of superconducting properties on the order of several dozen nm are identified as being at the origin of the strong pinning mechanism in iron based superconductors. For the particular case of $Ba(Fe_{1-x}Co_x)_2As_2$ (as well as several other compounds studied by different groups) the fingerprints of these spatial variations show up in the disposition of their vortex structure. A candidate for this kind of disorder in the vortex structure are the important superconducting gap variations reported by different groups (see Figure 3.13). These spatial variations of the superconducting parameters on a microscopic scale, such as observed in the gap maps, and on a macroscopic scale in the differential magneto-optical imaging (DMO) are suggested to be due to the large scale spatial variations of the dopant atom density. The same pinning mechanism is also studied in the isovalently substituted $BaFe_2(As_{1-x}P_x)_2$ compound. Contrary to what is reported by Fang *et. al.*, no weak-collective pinning contribution is found at any doping level of this material, from the under- to the overdoped region of the phase diagram. In this particular compound, the disorder level is, however, found to depend of the P-content in the crystal.

Chapter 4

The magneto-optical imaging technique and sample characterization

4.1 Introduction

Before performing further experiments we characterize our samples using the magneto-optical imaging method (MOI). The MOI technique notably allows one to discard samples with macroscopic defects as well as those exhibiting excessive chemical heterogeneity emerging from the crystal grown process. Selection is possible by using the so called "differential method" which allows one to obtain the spatial variation of T_c within a given crystal. In our set-up the MOI technique is limited by the electromagnet and the magnet power supply, which furnish applied fields of up to 50 mT. The technique is also limited by the saturation field of the utilized garnet films, which is, depending on the type of film, 90 or 200 mT. For magnetic measurements at higher fields, we have used the superconducting Quantum Interference Device (SQUID)-based magnetometer, as well as the Hall probe array magnetometry technique developed by M. Konczykowski in our laboratory[117].

In the framework of this thesis, we have characterized single crystals of several materials, including $Ba(Fe_{1-x}Co_x)_2As_2$, $Sr(Fe_{1-x}Co_x)_2As_2$, $Ba(Fe_{1-x}Ni_x)_2As_2$ and $BaFe_2(As_{1-x}P_x)_2$, for widely different doping levels x, as well as single crystals of the so-called (1111)- materials such as PrFeAsO. All of the samples were first checked in the magneto-optical imaging system. They were then usually cut using a wire saw in order to eliminate defective regions.

4.2 Magneto-optical imaging method

One main tool for investigation of electrodynamic properties of superconducting materials is the Magneto-Optical Imaging technique. This technique allows for the direct visualization of the spatial distribution of magnetic flux in the material, and allows one to obtain a number of superconducting parameters as the critical temperature T_c , the magnetic field of first penetration H_{c1}, or the critical current density J_c. Another interesting application of magneto-optical imaging technique is the non-destructive verification of the quality of superconducting samples.

4.3 Faraday effect

The Magneto-Optical imaging technique is based on the Faraday effect, discovered by Faraday in 1848. This consists of the rotation of the polarization plane of a linearly polarized wave traveling through an optically active material under a magnetic field, or with a non-zero spontaneous magnetization. This is illustrated in Figure 4.1. The rotation of the polarization plane obeys Faraday's law:

$$\theta_f = v \times H_{ext} \times d, \tag{4.1}$$

here θ_f is the Faraday rotation angle, v is the Verdet constant which is characteristic of the material, H_{ext} is the applied magnetic field and d is the thickness of the material. The Faraday rotation has a direct relation with the behavior of the electrons under the magnetic field and also with the magnetization of the optically active media. In a magnetic material, the Faraday rotation is proportional to the magnetization component parallel to the propagation direction of the light. Therefore, in a magnetic material with uniaxial anisotropy and light propagating along the anisotropy axis, the Faraday rotation angle $\theta_f \propto \arctan\left[H_\perp / \left(H_\parallel + H_k\right)\right]$. Here H_k is the anisotropy field of the magnetic material. For $H_{ext} > H_k$ the rotation angle θ_f saturates due to the total alignment of the magnetization M_s and the applied magnetic field. The Faraday rotation depends on the direction of the propagation of the light in the material with respect to its magnetic anisotropy axes.

In the case where the light traveling through the magnetic material is reflected from its outer interface, such as, in our experiments, the Al mirror layer deposited on the garnet indicator, the Faraday rotation angles of the impinging and reflected light are added,

$$\theta_f = \theta_{f,incident} + \theta_{f,reflected} \tag{4.2}$$

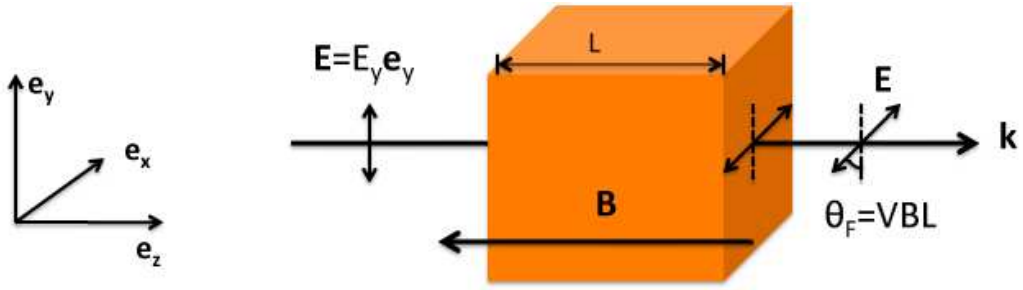

Figure 4.1 Illustration of the Faraday effect: a linearly polarized incident light traverses the medium (from the left to right) in the presence of an axial magnetic field **B** (along the z-axis). k denotes the wave vector of the light. Over the path spanning the medium, the direction of the electric field vector **E** is rotated over an angle $\theta_F = VBL$. This effect was discovered by M. Faraday in 1848.

From the fundamental mechanics law, the motion of the electrical charges in matter is

$$m\frac{\partial^2 r}{\partial t^2} = -m\omega_0^2\vec{r} - e(\vec{E} + \frac{\partial\vec{r}}{\partial t} \times \vec{B}). \tag{4.3}$$

Here m is the mass of the charged particle (ion, electron) set in motion, and e is its charge. In our case, m is the electronic mass, and e the electronic charge. The volume polarization $\vec{P}$ can be as $\vec{P} = -ne\vec{r}$. Writing the time-dependent electric field as $\vec{E} = \vec{E_0}exp(-i\omega t)$, we obtain

$$m(\omega_0^2 - \omega^2)\vec{P} = ne^2\vec{E} + i\omega eB\vec{P} \times \vec{e_z}. \tag{4.4}$$

We deduce that

$$\vec{E} = \frac{1}{\epsilon_0\chi_e}(\vec{P} - i\beta\vec{P} \times \vec{e_z}), \tag{4.5}$$

where $\chi_e = \left(ne^2/m\epsilon_0\right)\left(\omega_0^2 - \omega^2\right)^{-1} = \omega_p^2/\left(\omega_0^2 - \omega^2\right)$, and $\beta = \omega\omega_c/\left(\omega_0^2 - \omega^2\right)$, and ϵ_0 is the dielectric constant. ω_{pl} is the plasma frequency and ω_c is the cyclotron frequency. In tensor notation one wil have

$$\vec{E} = \frac{1}{\epsilon_0\chi_e}\begin{bmatrix} 1 & -i\beta & 0 \\ i\beta & 1 & 0 \\ 0 & 0 & 1 \end{bmatrix}\vec{P} = \frac{1}{\epsilon_0[\chi]}\vec{P}. \tag{4.6}$$

The electric susceptibility tensor can be expressed as

$$[\chi] = \begin{bmatrix} \frac{\chi_e}{1-\beta^2} & i\frac{\beta\chi_e}{1-\beta^2} & 0 \\ -i\frac{\beta\chi_e}{1-\beta^2} & \frac{\chi_e}{1-\beta^2} & 0 \\ 0 & 0 & \chi_e \end{bmatrix}, \tag{4.7}$$

while the relative dielectric constant can be written as a function of the electric susceptibility tensor as $[\epsilon_r] = [1] + [\chi]$. On the other hand, $\vec{\nabla} \cdot \vec{B} = 0$ implies that $\vec{k} allows for \vec{B} = 0$. In the absence of free charges $\vec{\nabla}.\vec{D} = 0$, so that

$$\vec{k}.[\epsilon_r]\vec{E} = 0 \tag{4.8}$$

and

$$([\epsilon_r]\vec{E})_z = (1 + \chi_{33})E_z = 0. \tag{4.9}$$

The fields $\vec{E}$ and $\vec{B}$ are transverse. Faraday's law andAmpère law can now be written out as

$$\vec{k} \times \vec{E} - \omega\vec{B} = 0 \tag{4.10}$$

and

$$\vec{k} \times \vec{B} + \frac{\omega}{c^2}[\epsilon_r]\vec{E} = 0; \tag{4.11}$$

hence, we have

$$\vec{k} \times \vec{k} \times \vec{E} = k^2\vec{E} = -\frac{\omega^2}{c^2}([\epsilon_r]\vec{E}) = -k_0^2([\epsilon_r]\vec{E}). \tag{4.12}$$

The equation $k^2\vec{E} = -k_0^2([\epsilon_r]\vec{E})$ has non-trivial solutions for the polarization $\vec{E} = E_x\vec{e_x} + E_y\vec{e_y}$ if the matrix determinant

$$\begin{bmatrix} 1 + \chi_{11} - n^2 & i\beta\chi_{11} \\ i\beta\chi_{11} & 1 + \chi_{11} - n^2 \end{bmatrix} \tag{4.13}$$

vanishes, *i.e.*

$$n_\pm^2 = 1 + \chi_{11} \mp \beta\chi_{11}. \tag{4.14}$$

Inserting $n_\pm^2$ in the wave equation, one obtains

$$(1 + \chi_{11} - n_\pm^2)E_x + i\beta\chi_{11}E_y = n^2E_x \tag{4.15}$$

and

$$E_y = \pm iE_x. \tag{4.16}$$

Here the minus sign - designates the left circularly polarized wave and the plus sign + represents the right circularly polarized wave. A polarized wave can be considered as the superposition of two circularly polarized waves of inverse direction of polarization. These waves will have their propagation velocities as c/n_+ and c/n_-. When these two waves traverse an optically active medium, their superposition yields a linearly polarized wave

with a polarization plane rotated by an angle θ_f. The latter angle is the Faraday rotation angle,

$$\theta_f = \frac{\omega d(n_- - n_+)}{2c}. \tag{4.17}$$

In non-magnetic media, the Faraday rotation angle is proportional to the magnetic field B, and to the distance travelled by the light in the media. $\theta_f = vBd$, where the Verdet constant v depends on the material, and on the wavelength. J. Larmor *et. al.* [122] proposed a relationship between the Verdet constant v, its dependence on the wavelength, and the refraction index of the media as ,

$$v = -\frac{e}{2mc}\lambda\frac{dn}{d\lambda}. \tag{4.18}$$

Here c is the light velocity, λ is the wave length. One may take into account the deviation observed in solids by introducing a proportionality constant C, so that

$$v = -C\frac{e}{2mc}\lambda\frac{dn}{d\lambda}. \tag{4.19}$$

The Verdet constant for most materials is extremely small. Therefore, the Faraday effect of magnetic materials, or "indicators", is used for magnetic measurements of superconductors which typically have small Verdet constant. The indicator film is placed on top of the superconductor under study. This indicator film allows one to detect the magnetic field at the surface of the superconductor. The Faraday active layer of the indicator film that I used for the experiments presented in this thesis is a ferrimagnetic bismuth doped Lutetium-iron garnet layer.

4.3.1 Magneto-optical indicators

The indicator films are 5μ m thick, and were grown by liquid-phase epitaxy on a transparent (paramagnetic) gadolinium-gallium-garnet (GGG) substrate. A 100 nm thick layer of Al, serving as a mirror, is evaporated on top of the garnet surface , to use it in the reflection mode. The mirror is covered by a thin protective Ti-TiN layer and an anti-reflective layer is deposited to the other surface of the substrate layer. A magnetic field applied at an angle α with respect to the normal to the garnet film will force the magnetization vector to turn out of the plane (see Figure 4.2). Here the applied field can be decomposed into the in-plane component $H_x = H\cos\alpha$, and the out of plane component $H_z = H\sin\alpha$. The Faraday rotation angle is given by $\theta_F = vdM_s\sin\theta$, where d is the thickness of the Bi:YIG layer.

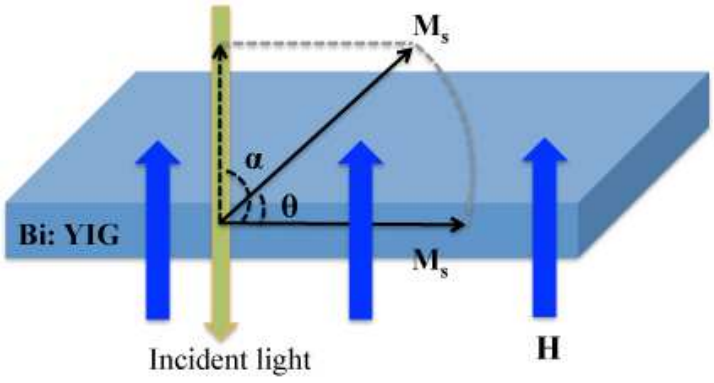

Figure 4.2 The perpendicular applied magnetic field **B** induces the rotation in the magnetization vector $\mathbf{M_s}$ and the perpendicular component of $\mathbf{M_s}$ produces the Faraday rotation.

The presence of a parallel magnetic field yields a reduced Faraday rotation angle. Considering the simplest form to find the equilibrium tilt angle θ, one has to minimize the total magnetic energy composed of the anisotropy energy $E_A(1-\cos\theta)$ and the dipolar energy,

$$E(H,\theta) = E_k(1-\cos\theta) + HM_s(1-\cos(\alpha_H-\theta)). \tag{4.20}$$

The condition $\partial E/\partial\alpha = 0$ yields

$$\tan\alpha = \frac{H_z}{H_k+H_x}; \tag{4.21}$$

here $H_k \equiv E_A/M_s$ is the anisotropy field. The Faraday rotation angle is proportional to the perpendicular component of M_s; therefore, one has

$$\theta_F \propto \arctan\left(\frac{H_z}{H_x+H_k}\right). \tag{4.22}$$

This describes both the reduced Faraday rotation angle θ_F and also its saturation for large H_z ($\sin\alpha \to 1$ for $H_z \gg H_k$). Under normal operating conditions for magneto-optical imaging, H_x should be small and the Faraday rotation angle is given by,

$$\theta_F = VdM_s\frac{H_z}{H_x+H_k}. \tag{4.23}$$

Therefore, for sufficiently small values of H_z, the relation between θ_F and H_z is linear.

4.4 Working principle of the magneto-optical imaging system

The magneto-optical imaging system consists of a polarized light microscope, below which a flow-type liquid Helium cryostat is mounted. The sample is glued (with n-nonadecane) on a small copper plate, which is then mounted on the cryostat sample holder. The sample holder is situated directly beneath the optical window of the cryostat; the indicator - to - window distance is about 1 mm. The linearly polarized light from the microscope first traverses the substrate, then the garnet film; after reflection by the Al layer, it passes the garnet film and the substrate a second time. Therefore, the total Faraday rotation angle is doubled with respect to Eq. (4.22). The luminous intensity of the reflected light is observed through an analyzing polarizer, rotated so as to be in a nearly perpendicular direction with respect to the initial polarization of the incoming light. The luminous intensity is observed using a 12 bit CCD camera mounted on the microscope (see Figure 4.3).

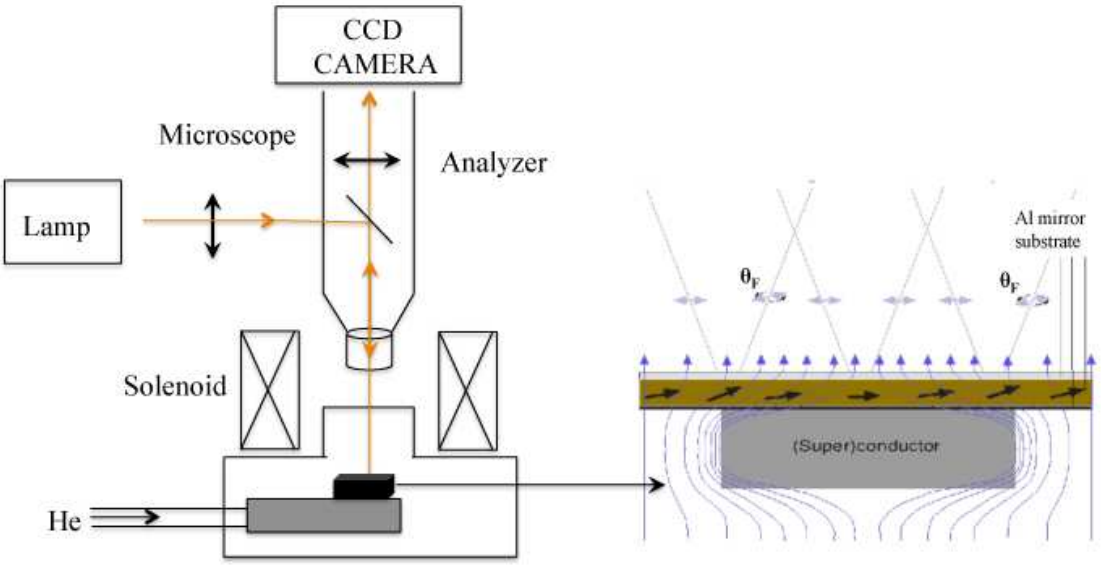

Figure 4.3 Schematic representation of the magneto-optical imaging system.

The magneto-optical garnet indicator is directly placed on top of the sample under study. A map of the luminous intensity is thus obtained on the sample surface, revealing the spatial distribution of the perpendicular component of the magnetic flux (see Figure 4.4). The dark areas on the image correspond to the absence of Faraday rotation, and therefore of any magnetic field (no Faraday rotation), while light areas correspond to the presence of a non-zero magnetic induction (a non-zero Faraday rotation).

Defining I_{in} as the incident light intensity, and I_r as the reflected light intensity on

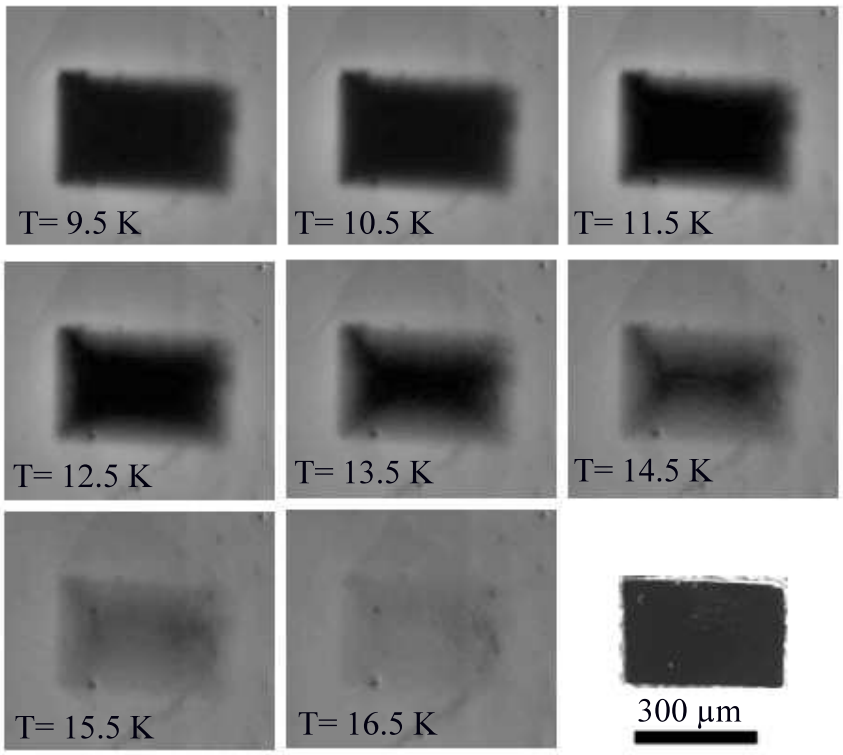

Figure 4.4 Magneto-optical images of the magnetic flux distribution on the surface of $Ba(Fe_{1-x}Ni_x)_2As_2$ single crystal ($x = 0.035$ #1.3) at an applied field of $H_a = 500$ Oe.

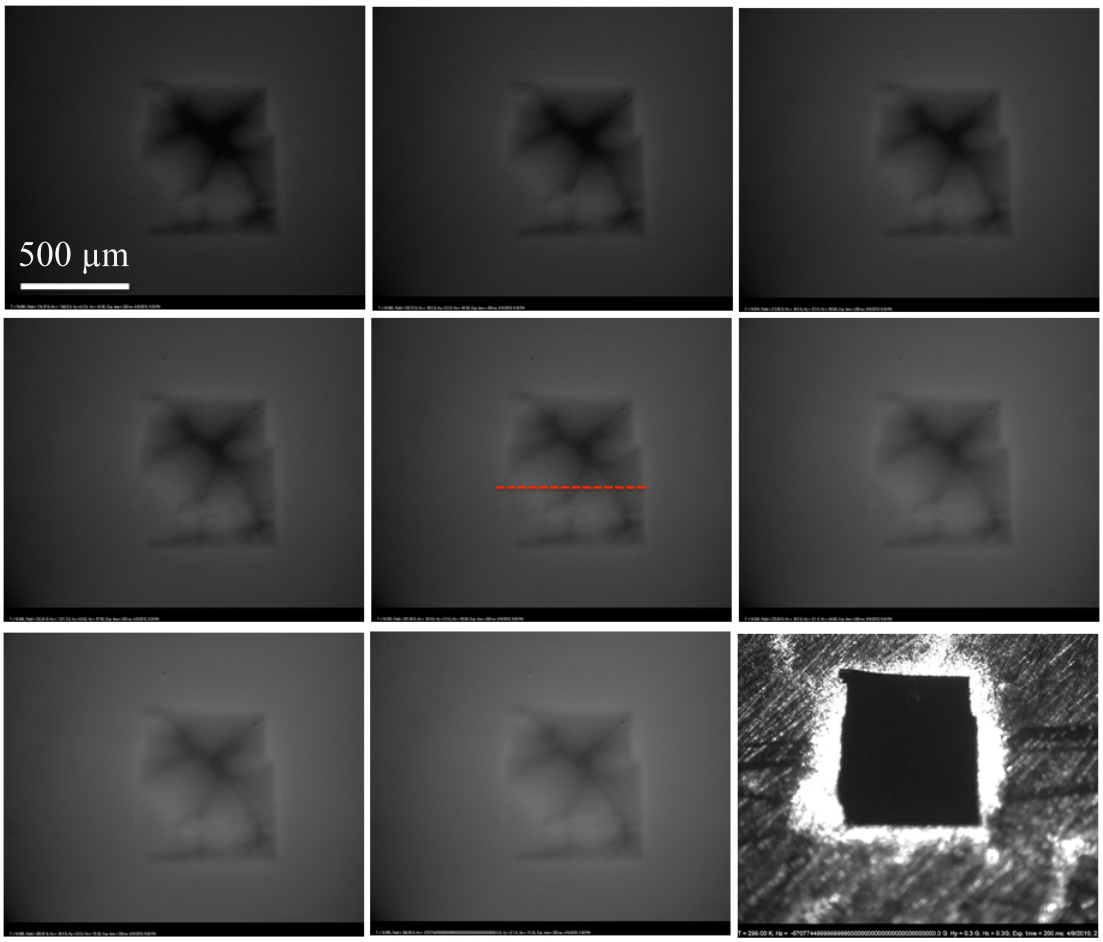

Figure 4.5 Magneto-optical images of the magnetic flux distribution on the surface of $Ba(Fe_{1-x}Co_x)_2As_2$ single crystal ($x = 0.065$ #2) at an applied field from $H_a = 170$ to 270 Oe at T=12 K. Example for crystal with macroscopic defect, the dashed red line denotes from where the crystal were cut in order to discard the defective region.

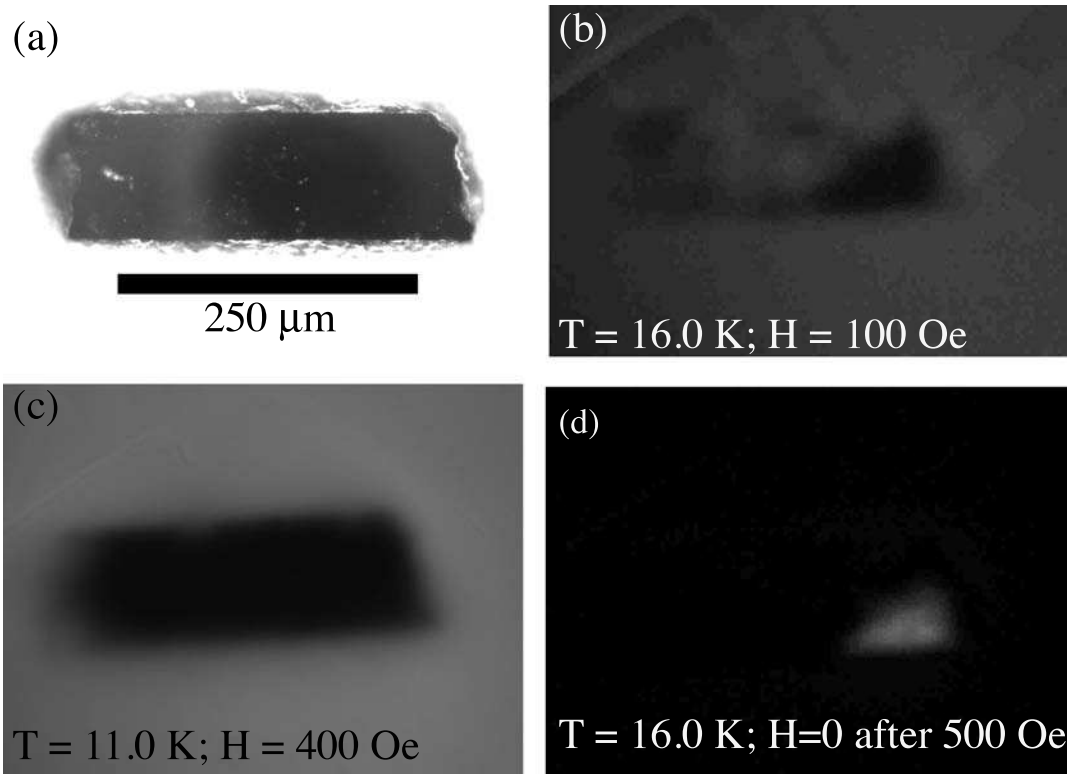

Figure 4.6 Magneto-optical images of the magnetic flux distribution on the surface of $BaFe_2(As_{1-x}P_x)_2$ single crystal ($x = 0.23$ #1) at an applied field from $H_a = 100$ to 500 Oe at different temperatures. Example for a crystal that has been totally discarded due to the macroscopic defect inside .

a magneto-optical indicator film with thickness d and absorption coefficient μ, one has $I_r = I_{in}e^{-2\mu d}$. The doubled Faraday rotation angle due to the reflection of the light across the garnet will be written as $\theta = 2\theta_F$, where $\theta_F = V_{MO}Hd$. Note also that the different components present in the optical path induce some depolarization effects. Using Malus' law, while taking into account depolarization effects by a parasitic luminosity K_0, one has for the light intensity,

$$I = K_0 + E_0^2 \sin^2(\theta), \tag{4.24}$$

where $E_0^2 = I_i e^{-2\beta d}$. Taking into account that the analyzing polarizer is not perfectly perpendicular to the polarization direction of the incoming light, but deviates from this by an angle α, one has

$$I = K_0 + E_0^2 \sin^2(\theta + \alpha). \tag{4.25}$$

The analyzer angle is adjustable on the system, the value of α can be optimized in order to get this term $E_0^2 \sin^2(\theta + \alpha)$ to be large, thus reducing the effects coming from the imperfections of the optical system. The variation of α is also used to augment the gain and the contrast of the images.

4.4.1 Experimental setup

The sample, glued on a OFHC (Oxygen-free high conductivity) copper plate using *n*-nonadecane, is fixed on the sample holder of the cryostat; the indicator film is directly placed on the sample surface. The Helium flow cryostat (Oxford Instruments MicrostatHe) provides temperatures as low as 5.5 K and has an optical access from above. Focusing on the image and the displacement in the x-y plane is possible using the adjustable XYZ-stage (see Figure 4.7). A split-coil magnet is wound on the Al lids of the cylindrical vacuum chamber is used to apply a magnetic field of up to 500 Oe perpendicular to the sample surface.

A transfer line links the liquid He dewar to the cryostat. The He flow is ensured with a small diaphragm pump. The copper sample holder houses two temperature probes: a Pt-sensor and an Allen-Bradley carbon sensor in order to measure the sample temperature. The different components of the applied magnetic field are measured using three Hall probes, these are positioned at 1 mm from the sample, on the opposite side of the sample holder. We use a Hamamatsu C4742-98 (CCD) camera for the acquisition of the MOI images, which are then acquired to the computer via a frame grabber and a Labview interface. The spatial resolution of our apparatus is about 5 -10 μm and is limited by the thickness of the indicator film, because the field contrast is attenuated when the distance from the sample surface increases.

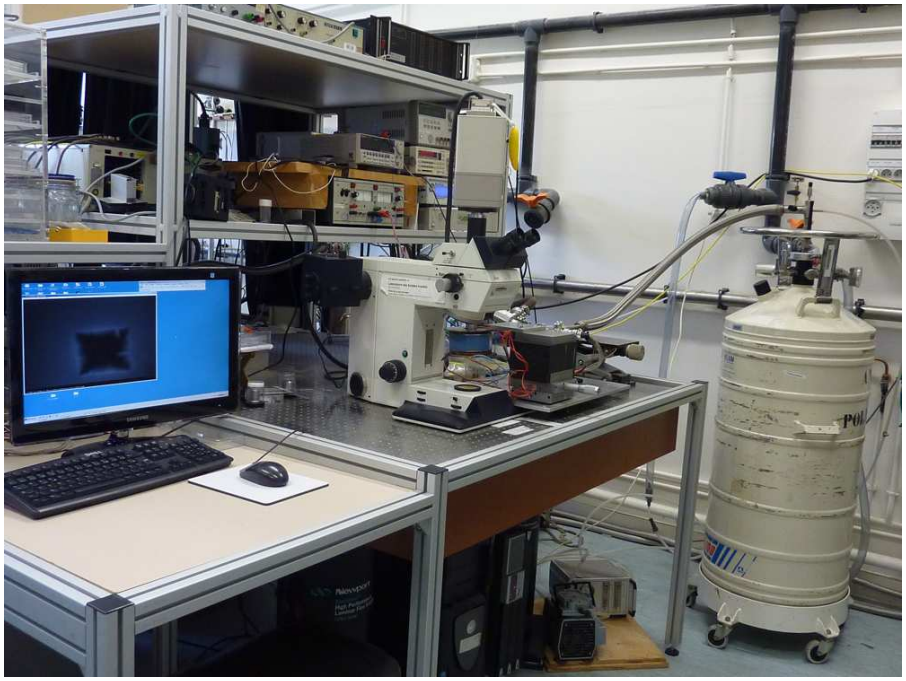

Figure 4.7 A photograph of the magneto-optical imaging system installed in our laboratory.

4.4.2 Magnetic flux penetration profiles

Profiles of the perpendicular flux density $B_y(x, y)$ at the surface and at the equatorial plane of bars with different thickness-to-width ratios in a perpendicular applied magnetic field were calculated by H. Brandt [62]. Figure 4.8 (a) shows the magnetic flux lines during the penetration of perpendicular flux into a strip with aspect ratio $b/a = 0.25$ for applied magnetic fields H_a/H_p= 0.2, 0.4, 0.8 and 1 where H_p= 0.374 j_ca. Here, H_p is defined as the field value at which in a gradually increasing applied filed H_a the magnetic flux has penetrated to the center and the current density has reached its saturation value j_c in the entire specimen. For the slabs and strips of rectangular cross section $2a \times 2b$ this field of full penetration in the parallel and perpendicular limits is given by $H_p \approx j_c a$,for $b \gg a$. The magnetic field component B_z parallel to the surface at the sample top and bottom surfaces $y = \pm b$ is shown Figure 4.8 (b) for various values of increasing B_a. This latter plot allows one to extract the calibration factor relating the magnetic flux density measured at the surface of a superconducting slab or elongated rectangular parallelepiped (with given aspect ratio) in a perpendicular magnetic field to the screening current density. The extracted screening current densities for various $Ba(Fe_{1-x}Co_x)_2As_2$ crystals are presented in Figure 4.11 , together with sustainable current density versus

temperature curves obtained on other crystals using Brandt's calculations in this manner

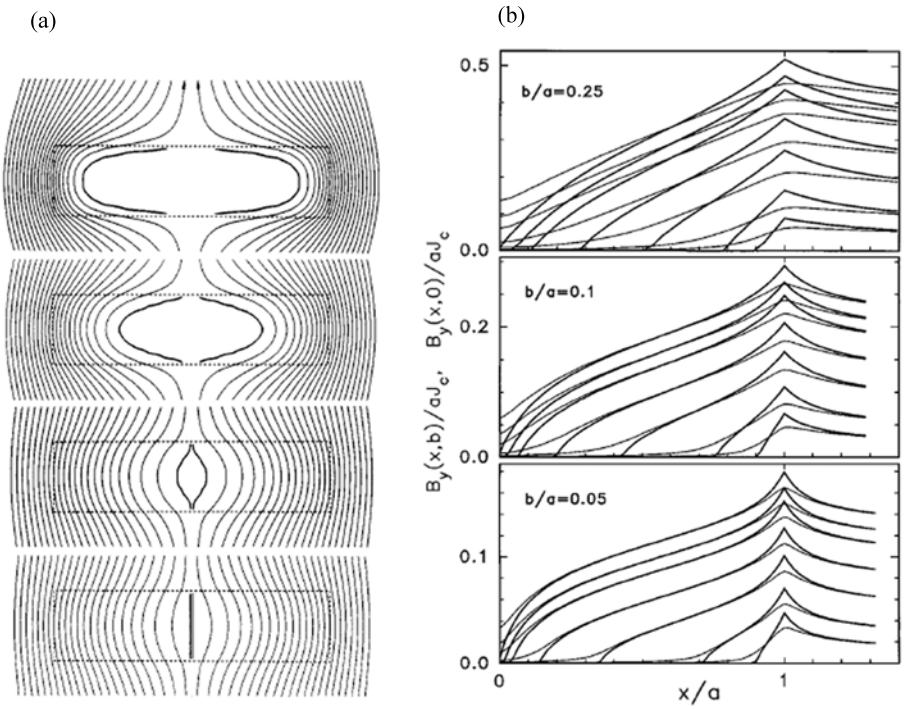

Figure 4.8 (a) Magnetic flux lines during penetration of perpendicular flux into a strip with b/a= 0.25 at applied fields H_a/H_p=0.2, 0.4, 0.8, and 1. Here, H_p= 0.374 j_ca . (b) Profiles of the perpendicular flux density $B_y(x, y)$ at the surface (thin lines, $y = \pm$ b) and equatorial plane (thick lines, y=0) of bars with side ratio b/a=0.25, 0.1, 0.05 at applied fields H_a/H_p=0.1, 0.2, 0.4, 0.6, 0.8, 0.9, and 1. Here for the field at the central plane one has $B_x(x, 0) = 0$ because of the symmetry. The central field profile for all aspect ratios b/a exhibits a sharp cusp at the sample edges and a sharp flux front inside which B is zero. These features are smeared out into the surface field, but for very thin strips this smearing is weak both fields profiles in the center and at the surface nearly collapse into one curve.From Ref. [62]

In the magneto-optical images presented in Figure 4.4, the light intensity outside the sample boundaries corresponds to the applied magnetic field, while the dark areas within the sample boundaries correspond to Meissner screening of the magnetic flux ($B = 0$); light areas along the sample boundaries correspond to the penetration of the magnetic flux (vortices) in the critical state. A calibration of the luminous intensity using the know values of the applied magnetic field allows one to obtain the profile of the penetration of the magnetic flux . The penetration profiles obtained from the regions indicated in Figure 4.9 are plotted in Figure 4.10. From the flux gradient $dB_\perp/dx$ of these profiles, one

can obtain the sustainable current density j_c of the crystal using the Bean model. In what follows, the thickness-to-width ratio of the sample under study is taken into account in the determination of the sustainable current density j. Figure 4.11 present the extracted current density as a function of temperature for a number of samples of different doping levels for $Ba(Fe_{1-x}Co_x)_2As_2$ single crystals.

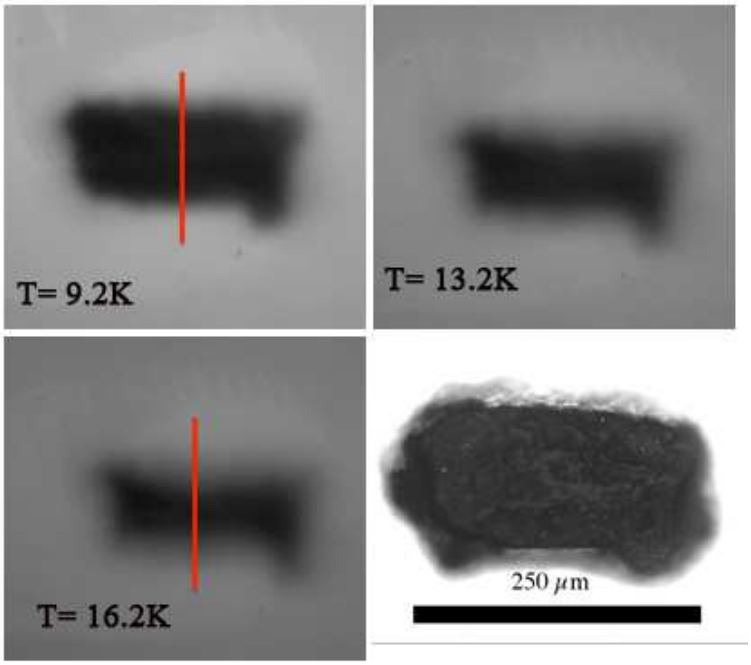

Figure 4.9 Magneto-optical images of the flux distribution on the surface of $BaFe_2(As_{1-x}P_x)_2$ single crystal ($x = 0.36$ #1) at an applied field $H_a = 400$ Oe.

4.4.3 Differential method

The Differential magneto-optical imaging technique is used to determine the spatial distribution of the critical temperature of our samples. In this method, the experiments are conducted after zero field cooling with a small field modulation $\Delta H_a = 1$ Oe. A field $H_a + \Delta H$ is applied and ten MOI images of the flux distribution above the sample are acquired and summed. The magnetic field is then reduced to H_a, whence ten other images are acquired and successively subtracted from the first sum. This procedure is repeated several times (twenty times in this case) ; the resulting images were averaged to produce the final DMO image. These images should be interpreted as representing the map of the local "permeability" of the sample. The grey level outside the sample represents

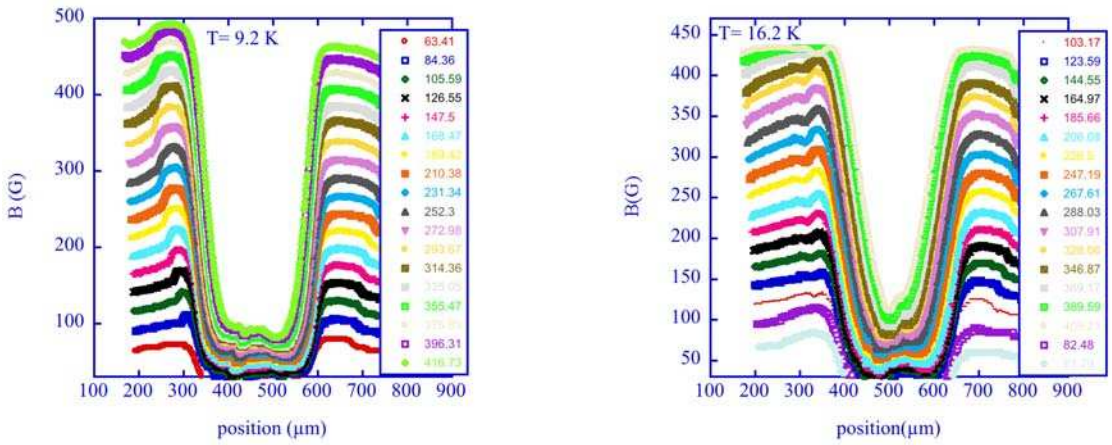

Figure 4.10 Magnetic flux penetration profiles obtained of $BaFe_2(As_{1-x}P_x)_2$ single crystal ($x = 0.36$ #1) from the regions indicated in Figure 4.9.

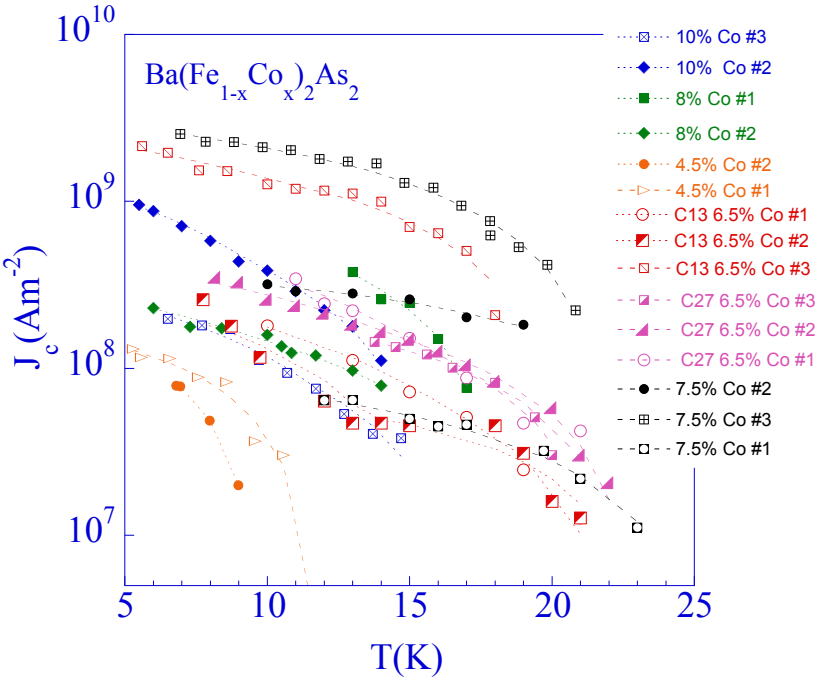

Figure 4.11 Sustainable current density $j_c(T)$ extracted from the MOI images for several crystals of $Ba(Fe_{1-x}Co_x)_2As_2$ single crystals over the whole phase diagram.

$\Delta B/\Delta H = 1$. In Figure 4.12 the zero intensity "black regions" represent diamagnetic screening, i.e. $\Delta B/\Delta H = 0$.

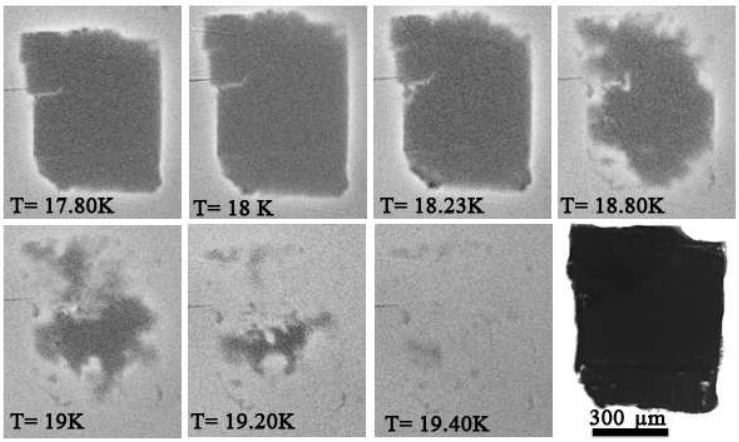

Figure 4.12 Differential magneto-optical images of $Ba(Fe_{1-x}Co_x)_2As_2$ crystal ($x = 0.1$ # 2) at an applied field $\Delta H_a = 1$ Oe.

From the obtained images one can determine quantitatively the width of the superconducting transition as well as the the spread of T_c within a given crystal. The T_c heterogeneity is in each location in the sample quantified by the local transmittivity

$$\mathcal{T}_H = \frac{[I(\mathbf{r},T) - I(\mathbf{r},T_c)]}{[I(\mathbf{r},T \gg T_c) - I(\mathbf{r},T \ll T_c)]}, \tag{4.26}$$

extracted from the luminous intensity $I(\mathbf{r},T)$ for different regions of a given crystal (see Figure 6.2).

4.5 Hall-probe array magnetometer

Some of the local magnetic measurements presented in this work were performed by the direct measurement of $B(r)$ using the micron size Hall probes developed by M. Konczykowski [117]. A typical measurement of the local gradient of the local induction B as a function of applied field is presented in Figure 4.13. In this technique, the sample under study is directly placed on a Hall probe or on a linear Hall probe array. The active area of these probes ranges from 2×2 to 10×10 μm^2. The measurement of the evolution of the magnetic

flux density at a given Hall probe location is complementary to the magneto-optical imaging technique, presented above. The information obtained using Hall probes, has a spatial resolution which is much more limited, however the sensitivity of Hall probes which can reach 10^{-7} T, is much better than for the magneto-optical imaging technique. With the

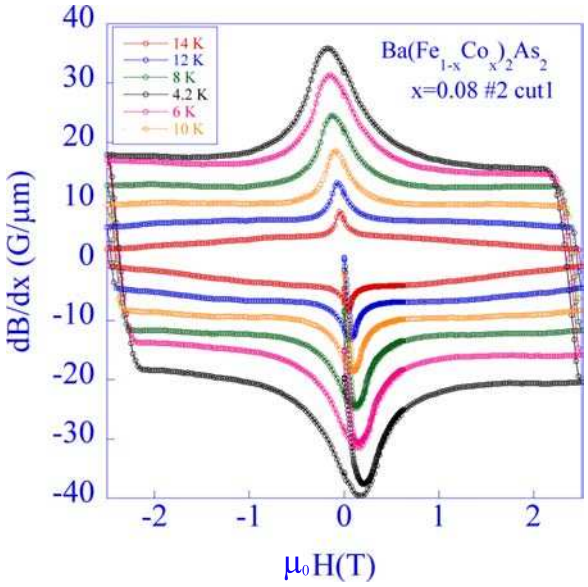

Figure 4.13 Hysteresis loop of the local gradient of the magnetic induction dB/dx as a function of applied magnetic field measured using a Hall probe array.

Hall-probe array magnetometry technique, measurements can be performed in dc mode or in ac mode. In ac mode, a periodic magnetic field of strength h_{ac} of the order of 10-100 μT is superposed with the static magnetic field. The frequency range of the ac field ranges between 0.5 Hz and 2 kHz. The measured periodic voltage $V_{ac}(f,T)$ on the Hall probe is proportional to the magnetic flux measured in the active area of the probe. For superconducting materials, the measured datas are, again, represented by the "transmittivity" ,

$$T_H = \frac{V_{ac}(f,T) - V_{ac}(f,T_c)}{V_{ac}(f,T_c) - V_{ac}(f,T_c)}. \tag{4.27}$$

which is directly proportional to the time periodic magnetic flux (at the fundamental frequency) which threads the sample at the probe location. One can also extract the transmittivity at the third harmonic of the frequency of the applied magnetic field,

$$T_{H3} = \frac{V_{ac}(3f,T)}{V_{ac}(f,T_c) - V_{ac}(f,T_c)}. \tag{4.28}$$

A non-zero signal at the third harmonic of the frequency signifies that the sample under study obeys non-linear electrodynamics at the given frequency and amplitude of the time-periodic component of the magnetic field, and at the particular temperature and static field under consideration. For superconducting materials, the relation between the voltage and current is non-linear due to the pinning of the magnetic flux lines by the defects present in the sample.

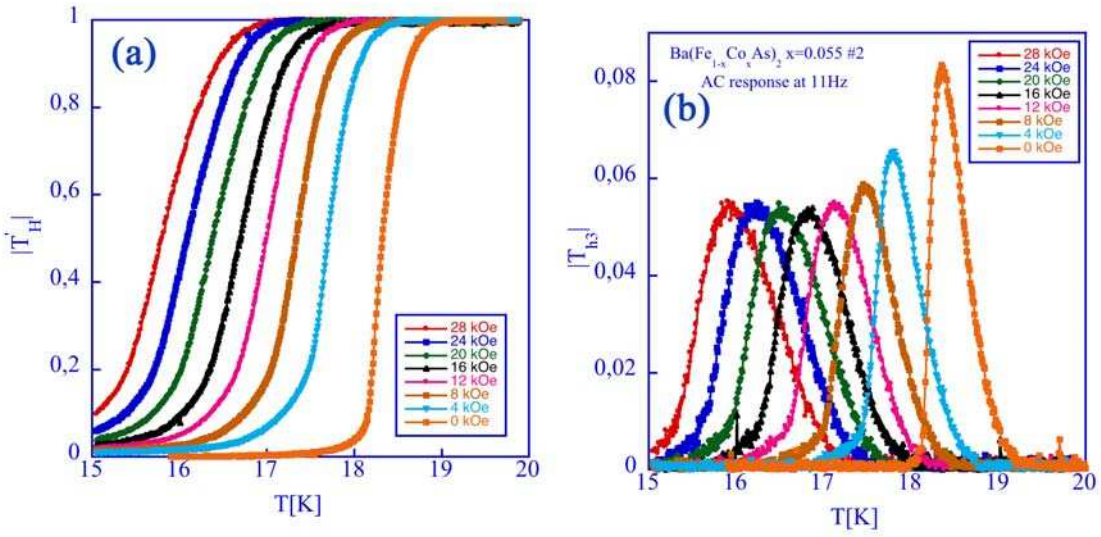

Figure 4.14 (a) Transmittivity T'_H measured on the crystal $Ba(Fe_{1-x}Co_x)_2As_2$ $x = 0.055$ #1 at an applied field of frequency 11 Hz. (b) norm of the third harmonics $\|T_{H3}\|$ for the same crystal.

Magnetic relaxation measurements performed by different groups [21; 196; 223], and the relaxation behavior of the magnetic flux penetration during the magneto-optical measurements entails the following distinction. The "true" critical current density j_c marks the crossover between the regimes of free flux flow and (exponentially slow) flux creep; at $j = j_c$ the current dependent activation barrier $U(j/j_c)$ for vortex escape from the minima of the pinning potential vanishes. The sustainable current density j experimentally measured in this work experimentally is always smaller than the critical current density j_c. Our measurements of the sustainable current density allow one to determine the usefulness of a particular superconducting material for current carrying applications. This measured sustainable current density is determined by the time window of the experiment Δt. It can be estimated from the logarithmic solution of the flux creep equation,$U(j/j_c) = k_B T \ln\left[(t + t_0)/\tau\right]$ [82]. Here $U(j/j_c)$ is the barrier for thermal activa-

tion and $\tau_0 \sim 10^{-5} - 10^{-7}$ s is the macroscopic characteristic time depends on the sample size and shape, t_0 describes the transient behavior at the onset of relaxation.

4.5.1 On the single crystalline iron-based superconductors studied in this thesis

Single crystals of $BaFe_2(As_{1-x}P_x)_2$ studied in this thesis were grown by S. Kasahara from the Research Center for Low Temperature and Materials Sciences in the Kyoto University in Japan. The single crystals were grown from a stoichiometric mixture of Ba and FeAs, Fe,P or FeP powders, placed in alumina crucible, and sealed in an evacuated quartz tube. The x values are determined using energy dispersive x-ray analysis [209].

The charge doped $Ba(Fe_{1-x}Co_x)_2As_2$ and $Ba(Fe_{1-x}Ni_x)_2As_2$ single crystals were grown by D. Colson and A. Forget of the Service de Physique de l'Etat Condensé of the CEA-Saclay. Single crystals of $Ba(Fe_{1-x}Co_x)_2As_2$ were grown by first mixing the reagents of high-purity Ba, FeAs and CoAs in the molar ratio $1 : (4 - x) : x$, loaded in alumina crucibles and then sealed in evacuated quartz tubes. For each doping level, chemical analysis by an electron probe was performed on several crystals, yielding the Co content to within 0.5% absolute accuracy. Chemical analysis was performed on several crystals of each batch, with a Camebax SX50 electron microprobe, on several spots of the surfaces. This technique gives a precision of typically 0.4% on the Ni content. The temperature dependence of the resistivity is shown in Figure 3.14 (a) for $Ba(Fe_{1-x}Ni_x)_2As_2$ single crystals and in Figure 3.14 (c) for $Ba(Fe_{1-x}Co_x)_2As_2$ single crystals. Superconductivity occurs for a Ni content in the range of $x = 0.02 - 0.09$. The resistivity goes to zero at T_c over a temperature span of no more than 0.5 K, which shows that the samples are very homogeneous. The optimum value of T_c is 19.5 ± 0.5 K, obtained for x = 0.045. For $x < 0.04$, the samples present a strong increase of the resistivity as T decreases, in the intermediate temperature range around 100 K. Similar behavior is observed for the other member of the "122" family [77]. This signals the occurrence of the structural and magnetic phase transitions. The phase diagram (T_c and T_{mag}) in Figure 3.14 obtained from the resistivity data, is compared to that of $Ba(Fe_{1-x}Co_x)_2As_2$ (indicated as empty symbols and dotted lines). In this plot, the Co concentration was divided by 2 accounting for the fact that only one electron is added to the electronic bands in this case.

The phase diagram of $Ba(Fe_{1-x}Co_x)_2As_2$ obtained from transport measurements is shown in Figure 3.14 [77]. The non-doped $BaFe_2As_2$ shows a transition; from a paramagnetic metal to a spin density wave (indicated on figure 3.14 as SDW) at a Néel temperature $T_{SDW} = 138$ K. When one dopes the system with Co, which substitutes for Fe, T_{SDW} decreases, before vanishing at x≈0.065. The superconducting phase is established at doping

levels 0.03⩽x⩽0.15. The maximum $T_c = 25$ K is reached for $x = 0.075$. The width of the superconducting transitions of $Ba(Fe_{1-x}Co_x)_2As_2$ single crystals are represented in Figure 3.14 (c). The qualitative features of the resistivity measurements are displayed for a series of samples, spanning the whole phase diagram. The drop of the resistivity at 135 K for the undoped parent compound, which signals the structural and SDW transitions is replaced by a an increase of ρ(T) when the Co is inserted into the system. With Co doping this transition occurs at lower temperatures and the superconductivity is observed between 0.03⩽x⩽0.15 doping levels.

Chapter 5

Bitter decoration technique

5.1 Historical overview

Magnetic decoration as a research technique has a relatively rich history. The starting point for the development of this technique was in 1931 when F. Bitter [70] proposed to use a suspension of tiny iron oxide particles to resolve inhomogeneities of the magnetic field in ferromagnetic alloys. If such a suspension was allowed to settle on the sample surface, the pattern of the deposited iron particles revealed the spots where intensity variations of the magnetic flux occur. Soon after its invention, the original Bitter decoration technique was improved by several researchers [30; 239]. The simplicity of the Bitter decoration method and its wide applicability to a large range of magnetic materials has made it a very useful tool in materials research. However, there are several limitations to the colloid-based method [57; 128; 131]. Notably, the sample surface was liable to become stained by prolonged contact with the colloid. Also, magnetic particles, when they are close to the sample surface, tend to agglomerate and lose their mobility. Another restriction for the resolution was set by the optical microscopes used for the observation of the decorated Bitter patterns.

The magnetic decoration technique as we know it today was introduced in 1965 by Hutchinson *et al.* [200], originally as a new method for the study of domain boundaries in ferromagnetic materials. They found that when iron is evaporated in a dilute atmosphere of a helium cloud, consisting of tiny magnetic particles is formed. If a ferromagnetic sample is placed in this atmosphere, the magnetic particles are deposited on the surface, preferentially at the domain boundaries, just as in the colloid-based decoration method. The Bitter pattern so formed can be examined optically, or, for higher resolution by scanning electron microscope (SEM). This new method did not required the sample to be immersed

in any liquid and provided better resolution.

Experiments on flux visualization on superconductors have been reported as early as 1956, when Schawlow [16], and independently, Sharvin and Balashova [23] used ferromagnetic powder to visualize the intermediate state in different materials. However only the application of the high-resolution decoration method of Hutchinson *et. al.* [200] made it possible to reveal the true complexity of the magnetic flux pattern in the superconducting samples. The pioneering work was done by Träuble and Essman [98], who decorated the domains of the intermediate state in type-I superconducting Pb, showing the peculiar structural variety at microscopic length scales. In 1967, Träuble and Essman [98] began their classic work on decoration of individual vortices in superconductors. They were the first to observe the vortex lattice with the decoration patterns on the surface of a superconducting sample. Until now, their work remains the most comprehensive source of information about vortex configurations in real samples. They made a classification of topological defects in the vortex lattice and demonstrated the analogy with defects in atomic lattices [99]. They studied how the vortex lattice sustains density gradients, and how it responds to material defects [99]. In 1969, they also showed a way to use the decoration technique for the study of the dynamics of magnetic flux. Several detailed reviews on decoration [56; 110; 149; 263] written in the last years give a broad overview of the contribution of this visualization technique, the better understanding of the behavior of vortex lattice in superconductors, and discuss the frontiers and new opportunities for the application of the method.

5.2 Bitter decoration:experimental setup and working principle

Ten years after the theoretical prediction by Abrikosov of the existence of vortex lines in type-II superconductors, the magnetic decoration technique was used by Essman and Träuble [98] to image the vortex structure in real space. These studies were crucial in order to provide irrefutable evidence for the existence of vortices and confirm that the magnitude of the vortex flux quanta $\Phi_0 = h/2e$.

The magnetic decoration working principle is based on the spatial modulation of the local magnetic induction inherent to the presence of vortices: $h(\vec{r})$ is maximum at the center of a vortex line. For bulk superconductors, it decays exponentially as a function of the distance to the vortex with a characteristic length λ [164]. As a result these are attracted towards the vortex core and decorate a region of size λ. When vortices are present in a superconducting sample they are responsible for the spatial variation of the

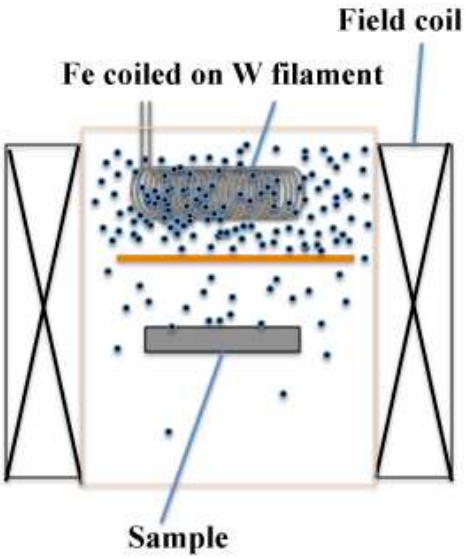

Figure 5.1 Schematic representation of the decoration chamber.

magnetic induction $h(\vec{r})$=$h(r,\vec{z})$. The local gradients of the magnetic induction exert the attractive force on the the pulverized iron clusters.

$$\vec{F} = \mid (\vec{M}.\vec{\nabla})\vec{h}(r) \mid . \tag{5.1}$$

Here $\vec{M}$ is the magnetic moment of the iron clusters. The agglomerated nano particles remain attached to the sample surface due to the van der Waals force. This allows for the observation of the vortex structure replica pattern at room temperature using SEM.

The spatial resolution of the Bitter decoration images is limited by the increasing magnetic field when the $h(\vec{r})$ of neighboring vortices overlaps. If we consider that the magnetic moment of an iron cluster is $M = \mu V$ where μ is the magnetization per unit volume. In order to decorate the vortex positions on the surface of the sample, the iron cluster volume must exceed the threshold value [30].

$$V_{th} = \frac{k_B T}{\Delta H \mu} = \frac{k_B T}{2H_{c1}\mu(1 - 2exp(\frac{-a}{2\lambda}))} \tag{5.2}$$

Here $\Delta H = h_{max} - h_{min}$, $h_{max} \approx 2H_{c1}$ the maximum contrast of the magnetic induction in the vortex core (approximated in the limit of low vortex densities) and $h_{min} \approx 4H_{c1}exp(\frac{-a}{2\lambda})$ [85; 169]. For a high magnetic field values the distance between vortices (iron cluster volume) will reach the threshold value $V_{th} \sim a^3(B)$ (a is the vortex

lattice parameter), and the imaging of individual vortices will be no longer possible.

In the experimental setup used for the vortex decoration in this thesis, the volume of the iron clusters inside the decoration chamber is controlled by the Helium pressure increasing as the pressure is increased. This makes the pressure the most important parameter to succeed in the imaging of individual vortices. For the decoration experiments presented in this thesis, a Helium pressure of 290 mTorr was typically used for a field of $B_a = 20$ and 200 mTorr for $B_a = 10\,G$.

The magnetic decoration experiment is performed by Joule evaporation of a magnetic material such as (Fe,Ni,Co), Fe in our case. An iron wire coiled on a W filament is prepared, and a copper shield is mounted between the filament and the sample holder such as represented in Figure 5.1. This is in order to avoid excess radiation and heating of the sample. The experimental procedure typically starts by the preparation of the sample surfaces. Since a very clean and smooth sample surface is required, the samples are cleaved just before the experiment. The freshly cleaved sample is then glued on top of the circular sample holder using a special glue (Figure 5.2) .

Figure 5.2 An image of crystal glued on Bitter decoration the sample holder designed in order to fit with the decoration chamber and with the SEM sample chamber. The arrow indicates the sample glued on the sample holder.

The sample holder, the filament and the copper shield are mounted in the decoration chamber and the setup is pumped vacuum. The magnetic field is applied on the longitudinal coil, and the system pre-cooled by putting it in a liquid nitrogen Dewar. The setup is transferred to the Helium Dewar; one continues pumping until a pressure of roughly 20 mTorr below the pressure value at which the decoration is performed is reached. Then, a current is applied on the W filament, and the decoration experiment is realized by Joule heating of the iron wire coiled on it.

Since the mean free path of the gas molecules at this pressure range is of the order

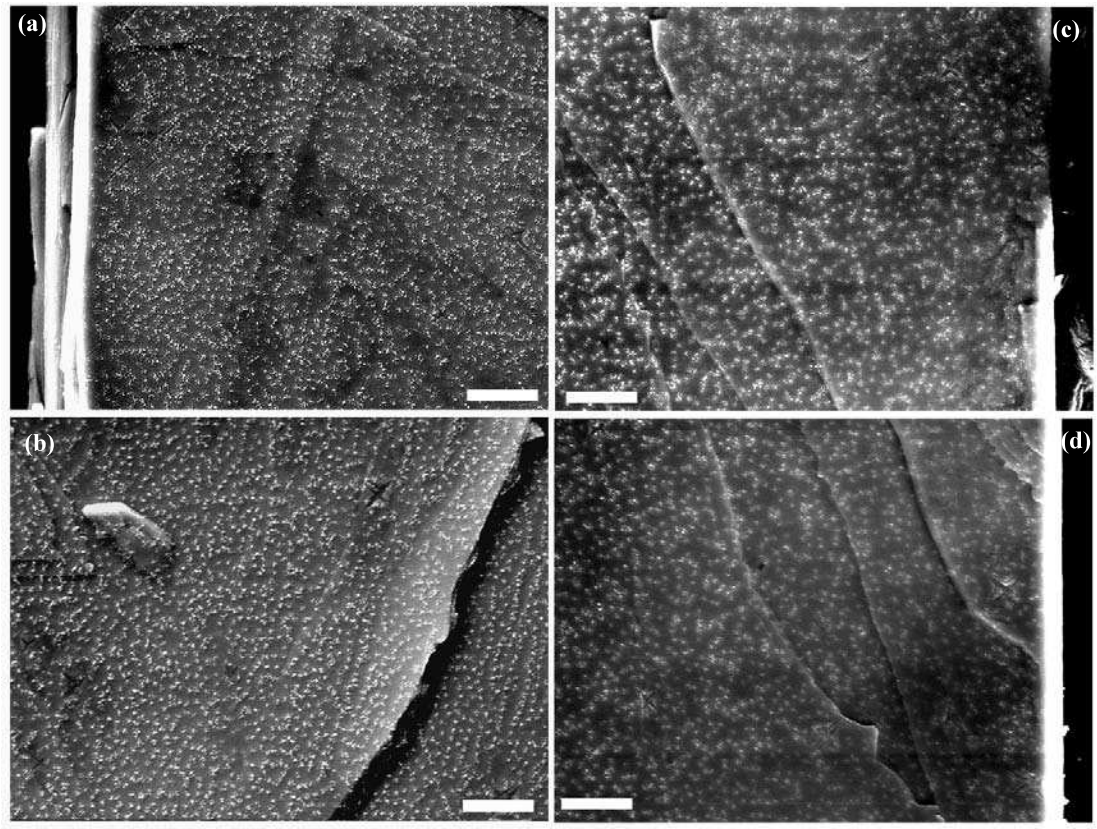

Figure 5.3 Bitter decoration images obtained of $Ba(Fe_{1-x}Co_x)_2As_2$ singles crystals (a) and (b) with x=0.1#1 , and (c) and (d) with x=0.075 # 2.1 Scale bars correspond to a length of 10 μm.

of micrometers, the Fe atoms scatter with the inert gas molecules during their diffusive spreading , thermalizing at the gas temperature, and forming clusters of roughly 50 nm in diameter. These clusters then diffuse in the decoration chamber, and at distances, from the sample, are attracted towards the vortex positions . The deposition of the clusters on the sample surface occurs during seconds. After the experiment one waits for the setup to warm up to room temperature whence the sample holder can be taken out of the decoration chamber. For better resolution, and in order to ensure a good conductivity a thin gold layer is sputter deposited on the decorated sample surface after this the decorated sample is imaged using SEM.

Chapter 6

Strong pinning and vortex energy distributions in $Ba(Fe_{1-x}Co_x)_2As_2$ single crystals

6.1 Vortex imaging in iron-based superconductors

Recent vortex imaging studies of iron-based superconductors performed by different groups and different techniques reveal highly disordered vortex arrangements for all studied compounds. In ideal superconducting samples without crystalline defects, the ground state vortex structure is the Abrikosov crystal, [3] a periodic lattice with triangular symmetry. In contrast, single crystals of iron based superconductors contain a large density of atomic point defects, nanometric [276] and mesoscopic [41] disorder, or twin domain boundaries [196] that pin the vortices and prevent the formation of an ordered lattice.

The imaging of the vortex structure in Type-II superconductors, in our case the iron-based compounds is very important, because the vortex configuration was directly related to the the flux line pinning. Vortex imaging was used to study phase diagrams of high-T_c superconductors. Using Bitter decoration method M. V. Marchevsky observed a pinning driven order-disorder transition in $Bi_2Sr_2CaCu_2O_{8+\delta}$ [174]. The author defined a displacement correlator $\mathbf{u}(\mathbf{r_i})$ for the presented vortex structure by generating a perfect lattice with a lattice parameter equal to the mean intervortex distances of the decoration image. The perfect lattice pattern was fitted to the real vortex structure with respect to translations, and rotations. A displacement vector $\mathbf{u}(\mathbf{r_i})$ is determined for each vortex with respect to the closest point $\mathbf{r_i}$ in the perfect lattice. From this, the correlator $< u^2(r) > \equiv < [\mathbf{u}(\mathbf{r}) - \mathbf{u}(\mathbf{0})]^{\mathbf{2}} >$ was computed. It is found that the displacement of the

vortex positions increases with decreasing magnetic field. The author suggests that the normalized average displacements at 2 mT $\sqrt{<\delta u_r^2>}/a_0$=0.12 is close to the expected value of Lindemann number c_L∼0.15 at which melting takes place [178]. From this, they argue that the observed vortex structure is in the proximity of a melting or order-disorder transition. Kim *et al.* have used the Bitter decoration technique for the visualization of the flux line lattice in $Bi_2Sr_2CaCu_2O_{8+\delta}$ single crystals with weak disorder at large scales (80-100 a_0). They realized decoration experiments up to 120 G, and obtained large scale dislocation-free images of the flux lattice, from which they extracted the displacement correlator B(r) [179]. Quantitative analyze of the translational order indicated that the flux lattice is in the random manifold regime, for length scales up to ∼80 a_0. They argued that large dislocation free regions in the vortex structure might be a signature of the existence of the Bragg glass [217].

Due to the availability of high quality single crystals of these compounds vortex imaging studies of iron pnictide superconductors have been mainly focused on the 122 family. Many different experimental methods have been applied to the visualization of vortices in iron based superconductors. Direct imaging methods at low field, such as Bitter decoration, [152; 171] scanning SQUID microscopy, [18] and magnetic force microscopy (MFM) [59; 148] have been complemented with methods useful at high fields such as scanning tunneling microscopy (STM), scanning tunneling spectroscopy (STS) [277] and small angle neutron scattering (SANS) [59; 171]. All these experiments have observed disordered vortex structures at all investigated fields. The Bitter decoration and small-angle neutron scattering (SANS) experiments were performed by Eskildsen, and Vinnikov *et. al.* [171] for vortex imaging in the optimally doped $Ba(Fe_{1-x}Co_x)_2As_2$ single crystals (with $x = 0.07$). Inosov, and Shapoval *et. al.* [59] imaged the vortices in overdoped $Ba(Fe_{1-x}Co_x)_2As_2$ single crystals (with $x = 0.095$) using SANS and magnetic force microscopy (MFM). Measurements carried out in magnetic fields of up to 9 T have revealed a vitreous vortex phase (vortex glass) with short range hexagonal order. The authors argued that pinning remains anomalously strong even in overdoped crystals where static magnetism is fully suppressed, and quantified the degree of disorder using a statistical analysis of multiple MFM images. [59]. Vortex imaging in iron pnictide single crystals of the 122 type including $Ba_{1-x}K_xFe_2As_2$ and $Sr_{1-x}K_xFe_2As_2$, as well as $SmAsO_{1-x}F_x$ (of the 1111 type) was performed by Vinnikov *et. al.* [152] using Bitter decoration in the magnetic field range from 0 to 200 Oe. They concluded that in all studied iron pnictide compounds, the disordered vortex structure exists and is independent of the crystal structure type, doping and synthesis method. They suggested the mechanism of strong pinning both in single crystals and polycrystalline samples to be the same but did not specify its origin. The only reported

ordering effect on the orientation of the vortex ensemble is that induced by twin-boundaries in $Ba(Fe_{0.949}Co_{0.051})_2As_2$ (with $x = 0.051$) reported by Kalisky *et. al.* This scanning Superconducting Quantum Interference Device (scanning SQUID) microscopy study shows that vortices avoid twin boundaries acting as a barrier for vortex motion [18] . Attempt to correlate vortex positions with material heterogeneity include the scanning tunneling spectroscopy (STS) and vortex imaging by Yin *et al*. STS and vortex imaging up to 9 T in slightly overdoped $Ba(Fe_{1-x}Co_x)_2As_2$ single crystals ($x = 0.1$) was performed by Yin *et. al.* [277] but the highly disordered vortex positions could not be correlated with surface impurities observed in the same work. Furthermore, scanning tunneling spectroscopy studies in different iron-based superconductors reveal nanoscale variations of the local superconducting gap [75; 261; 276]. In $Ba(Fe_{1-x}Co_x)_2As_2$, the length scale on which the deviations from the average gap value occur was claimed to be comparable to the average distance between dopant atoms [75]. Nevertheless, no correlation between the vortex positions and the superconducting-gap inhomogeneities or other defects has been found [277].

Hence, all techniques agree on the absence of vortex lattice order in the iron based materials. However, there is no clear consensus on the origin of this disorder and pinning. The aim of this work is the characterization of strong pinning. Below I present a quantitative analysis of the pinning energy and force distributions, which indicate that the key to understanding the disordered configurations is that these are arrested at temperatures very close to T_c, in crystals that show notable spatial variations of the superconducting parameters. The magneto-optical imaging technique is used to reveal the crystalline inhomogeneity before further experiments. The spatial variation of the transition temperatures ΔT_c for Co-doped crystals and the Co doping level dependence of the critical current densities j_c are presented in section 6.3.1. The configuration of vortices near surface steps is discussed in detail, this is used to extract the high temperature value of the penetration depth and the freezing temperature of the presented vortex ensembles is extracted from it (see section 6.4.1). Results on the vortex structure imaging are presented in section 6.4.2 a new method is developed to extract the pinning energies and pinning forces from the decoration images (section 6.4.2). This latter yields more information that classical analysis in terms of correlations functions of distance distributions because the typical quantities describing individual vortices are not integrated out. The analysis shows that there is a substantial local variation of the pinning energies and pinning forces in $Ba(Fe_{1-x}Co_x)_2As_2$ single crystals. The magnitude of these variation has at the origin the nanoscale spatial variations of T_c and/or the superfluid density due to an inhomogeneous distribution of the dopant atoms. By linking these results to the measured critical current densities it is shown that pinning in the low magnetic field regime is very likely due to heterogeneity of

the superconducting properties of the crystals, on the scale of several dozen nm.

6.2 Experimental details

The penetration of magnetic flux into selected crystals of thickness 30 μm was visualized by the magneto-optical imaging (MOI) method. A ferrimagnetic garnet indicator film with in-plane anisotropy is placed on top of the sample and a polarized light microscope is used to observe it. The Faraday rotation of the indicator allows for the detection of regions with non-zero perpendicular component of the magnetic flux density $B_\perp$, revealed as bright when observed through an analyzing polarizer. Dark regions correspond to $B_\perp \approx 0$. In order to characterize the inhomogeneity of the crystals in the vicinity of the critical temperature we use the differential magneto-optical method (DMO) [41]. Images acquired at applied fields $H_a + \Delta H_a$ and H_a are subtracted, and the differential images averaged by repeating the procedure 50 times. In the present experiments $\mu_0 \Delta H_a = 0.1\,\mathrm{mT}$ (with $\mu_0 \equiv 4\pi \times 10^{-7}$ Hm^{-1}).

The field dependence of the global critical current density of selected crystals was obtained from magnetization-loop measurements conducted using a Quantum Design SQUID magnetometer. The critical current densities were extracted using the Bean-critical state model. As discussed below, the assumption of this model is justified by the way flux penetrates into the crystals. Within the Bean model, $j_c = 3\mathcal{M}/Va$, where $\mathcal{M}$ is the magnetic moment, V is the sample volume, and $2a$ the sample width [63].

For the Bitter decoration experiments, [263] rectangles of dimension 200 μm $\times$ 300 μm were cut from larger crystals using a 20 μm wire saw and 1 μm SiC grit. Bitter decorations were only performed on crystals with $x = 0.055$, $x = 0.075$, and $x = 0.1$. The sample surfaces were freshly cleaved before the experiments. The experiments were carried out at liquid Helium temperature (4.2 K) and He-exchange gas at pressures of the order of 200 mTorr. The images shown here are the result of field-cooling experiments at a field $\mu_0 H_a = 1\,\mathrm{mT}$, applied parallel to the c-axis of the crystals. The decorated vortex arrangements were observed by scanning electron microscopy at room temperature.

6.3 Results

6.3.1 Magneto-optical imaging

Figure 6.1 (c) shows examples of magneto-optical images, here obtained at $T = 15$ K on single-crystal #2 of the composition with $x = 0.075$. The images reveal a globally homogeneous penetration of the magnetic flux into the sample obeying the Bean critical

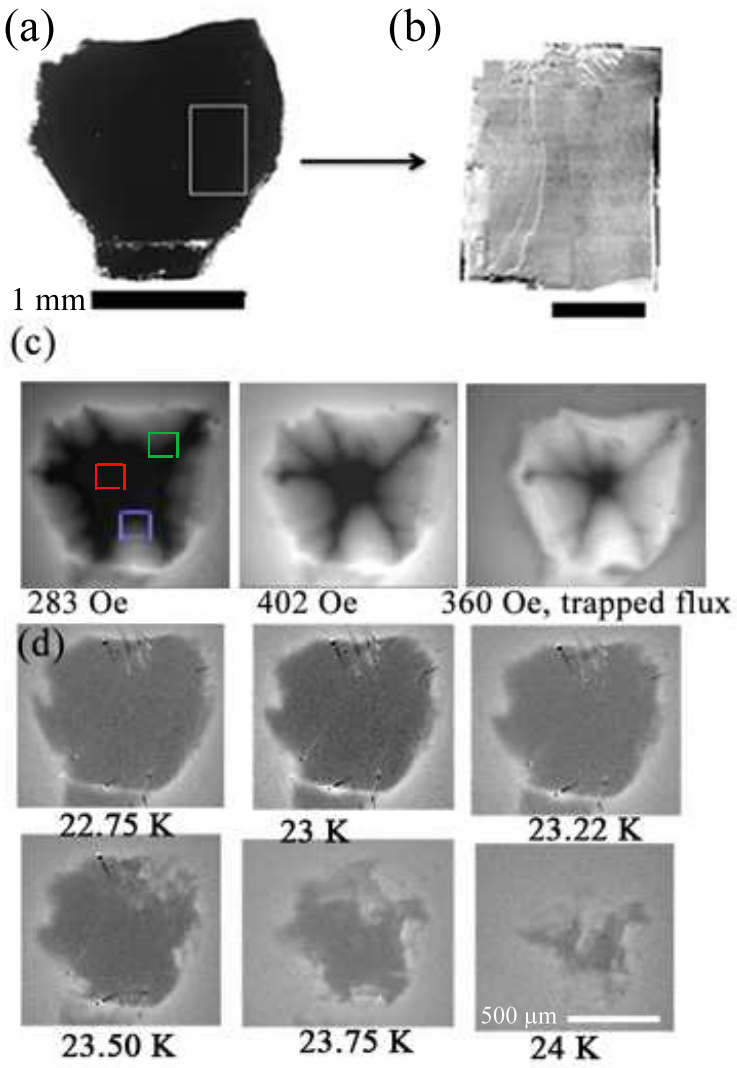

Figure 6.1 a) Photograph of $Ba(Fe_{0.925}Co_{0.075})_2As_2$ crystal # 2. (b) Scanning electron micrograph of the decorated sample #2.1 cut from the larger crystal #2. (c) Magneto-optical images of $Ba(Fe_{0.925}Co_{0.075})_2As_2$ crystal #2 at $T = 15\,\mathrm{K}$ and the indicated values of the applied magnetic field. (d) Differential Magneto-Optical (DMO) images in the vicinity of T_c, for $\mu_0 \Delta H_a = 0.1\,\mathrm{mT}$. The scale bar corresponds to a length of 100 μm unless indicated otherwise.

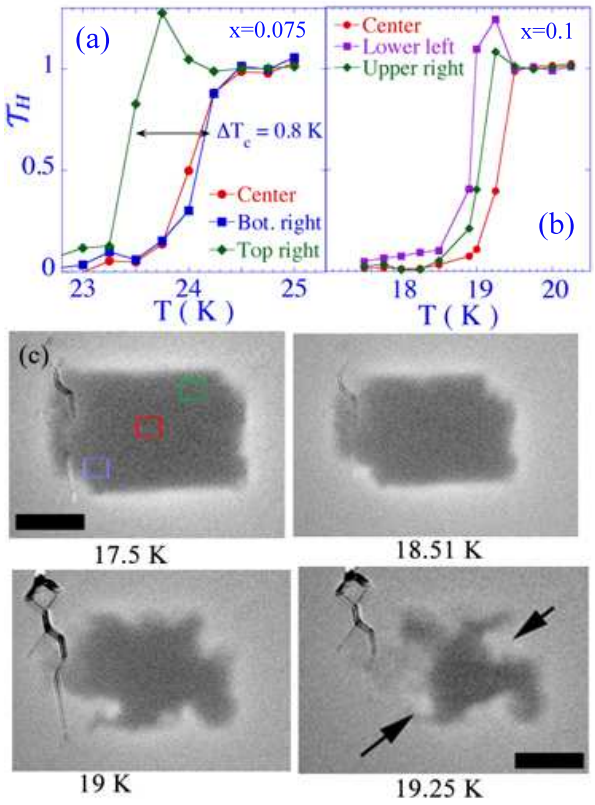

Figure 6.2 Local transmittivity $\mathcal{T}_H$ measured for three regions indicated in Fig. 6.1 (c) $Ba(Fe_{0.925}Co_{0.075})_2As_2$ crystal # 2 is concerned (a), and in panel (c) for $Ba(Fe_{0.9}Co_{0.1})_2As_2$ crystal #1 (b). (c) DMO images of $Ba(Fe_{0.9}Co_{0.1})_2As_2$ crystal #1, and the indications for the selected regions. Here the arrows indicate regions of paramagnetic transmittivity at the superconducting transition. Scale bars correspond to a length of 100 μ m.

state. [47; 66] We obtain the local value of the critical current density from $j_c \sim 6\ \partial B_\perp/\partial x$ (the factor 6 is estimated from Ref. [63] for a crystal aspect-ratio of 0.1).

The DMO images in Figure 6.1 (d), and 6.2 (c) reveal the same Bean-like flux penetration with an inhomogeneous j_c arising from the spatial variation of T_c. This inhomogeneity can be quantified using a plot of the local transmittivity, defined as the ratio $\mathcal{T}_H = [I(\mathbf{r},T) - I(\mathbf{r},T \ll T_c)]/[I(\mathbf{r},T \gg T_c) - I(\mathbf{r},T \ll T_c)]$ of the relative local luminous intensities $I(\mathbf{r},T)$ in the DMO images. The temperature-dependence of $\mathcal{T}_H$ measured on different regions of crystals #2 and #1 is depicted in Figure 6.2 (a),(b). The local variation of T_c-values within a given crystal is of the order of 0.5 – 1 K. In addition, regions of lower T_c give rise to a paramagnetic signal at the transition due to flux concentration by the

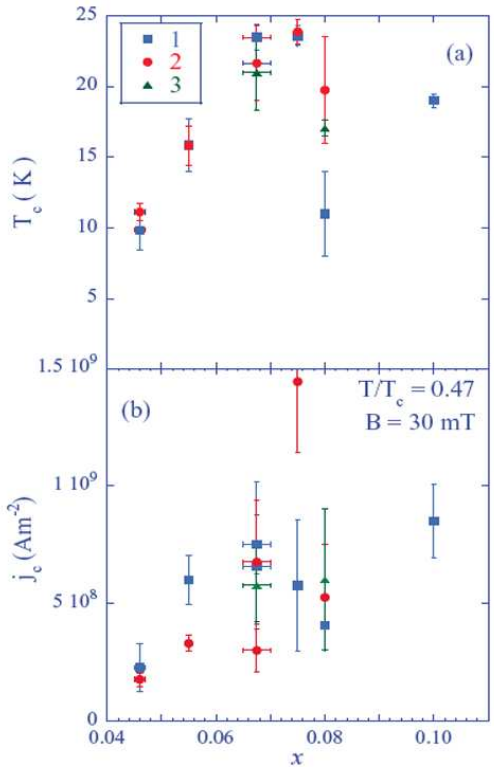

Figure 6.3 (a) Transition temperature, T_c, versus Co doping-level. The error bars denote the local spread of T_c values within a given crystal. For each doping level, #1, #2 and #3 denote different crystals. For $x = 0.075$ and 0.1, the numbering is the same as the decorated crystals. (b) Co doping-level dependence of the critical current density j_c measured by MOI at $B = 30\,\mathrm{mT}$ and a reduced temperature of $T/T_c = 0.47$.

surrounding superconducting parts of the crystal.

Figure 6.3 (a) summarizes the width of the T_c distribution for a large number of $Ba(Fe_{1-x}Co_x)_2As_2$ single-crystals of different doping levels. Figure 6.3 (b) shows the Co doping-level dependence of j_c for the same series of single-crystals at a reduced temperature of $T/T_c = 0.47$. A rather large sample-to-sample variation of the low–field ($B_\perp = 30\,\mathrm{mT}$) j_c is observed. Certainly, no clear doping-dependent trend appears, as proposed in Ref. [195]. The obtained critical-current values are comparable to those reported in the literature for the same material [197].

6.3.2 Vortex imaging in $Ba(Fe_{1-x}Co_x)_2As_2$ single crystals

The Bitter decoration technique [263] was used to observe vortex structures on three of the crystals used to compile Figure 6.3. These are crystal #1 of the composition with $x = 0.1$,

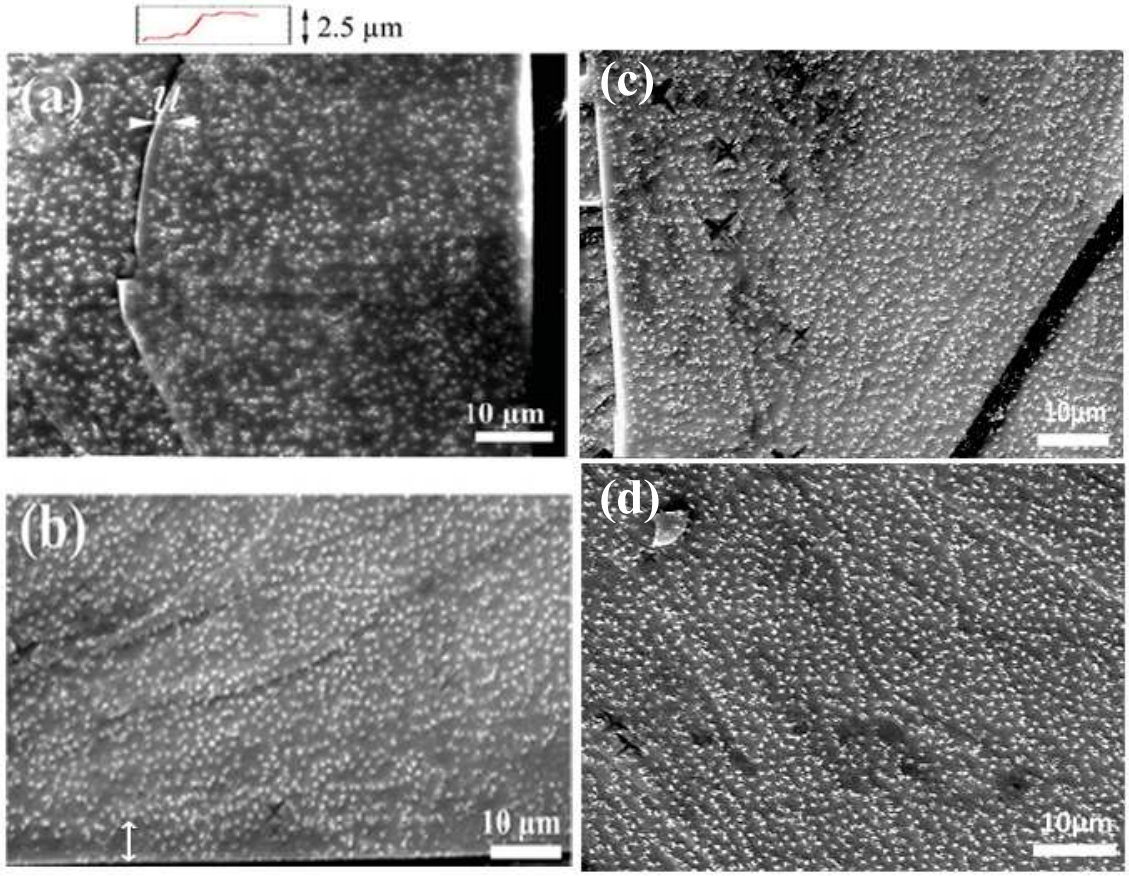

Figure 6.4 Bitter decoration image of $Ba(Fe_{1-x}Co_x)_2As_2$ single-crystal (a) with $x = 0.075$ #2.1, and in (b), (c) and (d) different images from the crystal with $x = 0.1$ #1. The white arrows indicate the vortex free regions near the surface step and/or at the edge of the crystal.

crystal #2 with $x = 0.075$, and on crystal #2 with $x = 0.055$. The decoration of crystal #2 with $x = 0.055$ was unsuccessful, presumably due to the large value of the penetration depth at this low doping level. The decorated patterns reveal highly-disordered vortex structures as in Refs. [18; 59; 148; 152; 171]. Figure 6.4 reveals regions of high and low vortex density, as well as the formation of vortex-free zones near the crystals edges and surface steps, due to the circulating Meissner current. These images are representative of those obtained on other regions of the crystal surfaces after different cleavage runs, and on other crystals. From the images, we extract the average value of the magnetic induction as $B_{int} = n_v\Phi_0$, where n_v is the vortex density and $\Phi_0 = h/2e$ is the flux quantum. For all images we obtain an average induction $B_{int} \approx 0.8\,\mathrm{mT}$, 20% smaller than the applied field $H_a = 1\,\mathrm{mT}$.

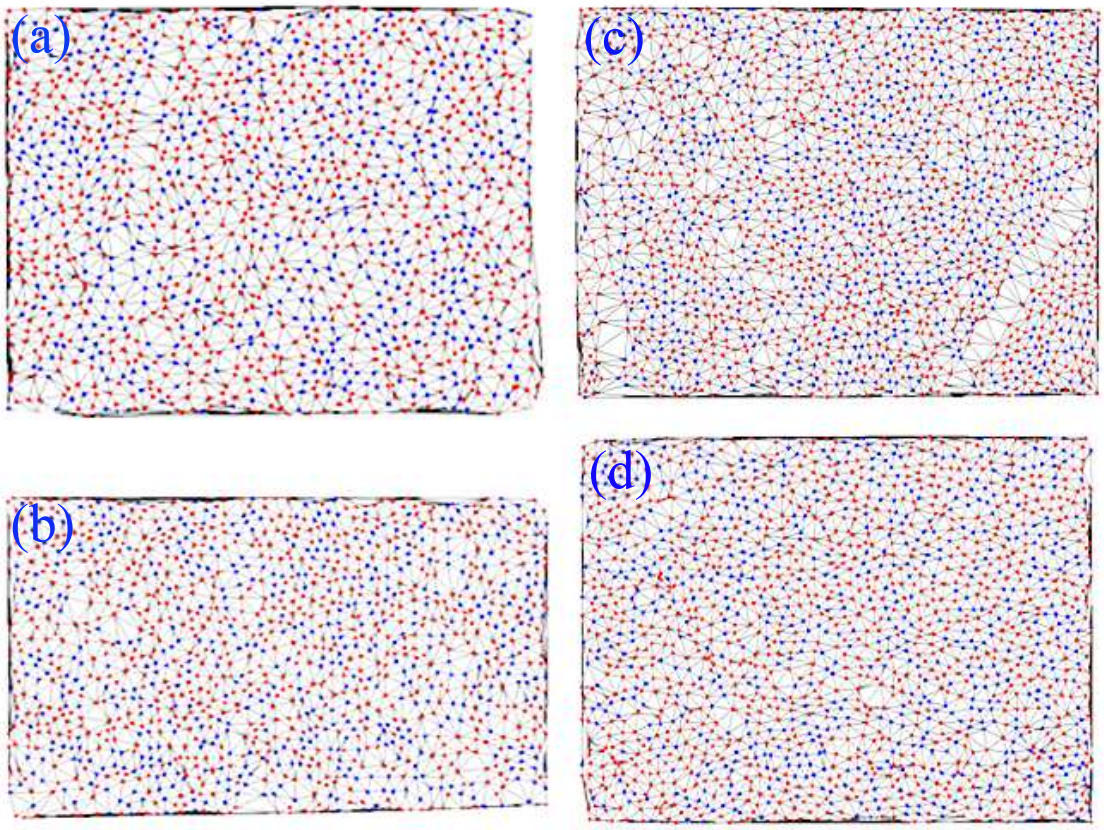

Figure 6.5 Delaunay triangulations of the images in Figure 6.4 respectively for single crystals (a) with $x = 0.075$ #2.1, and b), (c) and (d) with $x = 0.1$ #1. Here blue dots are the vortices with sixfold coordination number while red dots have a coordination number different than six.

Figure 6.5 presents the Delaunay triangulations of the images presented in Figure 6.4 for $x = 0.075$ and $x = 0.1$, respectively. Here, the blue dots represent vortices with sixfold coordination while the red dots represent vortices which have a different coordination number. Fourier transforms of the vortex positions in the images of Figure 6.4 are in the left hand panels of Figure 6.6 , while in the right-hand panels show the nearest neighbor distance distribution. The insets to Figure 6.5 show the distributions of the coordination numbers. All distance distributions have a mean value of $\sim$ 1.56 μm which corresponds to the triangular perfect lattice parameter $a_{\triangle} = 1.075\sqrt{\frac{\Phi_0}{B}}$ for an applied magnetic field $\mu_0 H_a$=0.1 mT. Distance distributions show a large deviation from the perfect lattice configuration, while the respective Fourier transforms of the vortex positions demonstrate the absence of any order in the vortex structure.

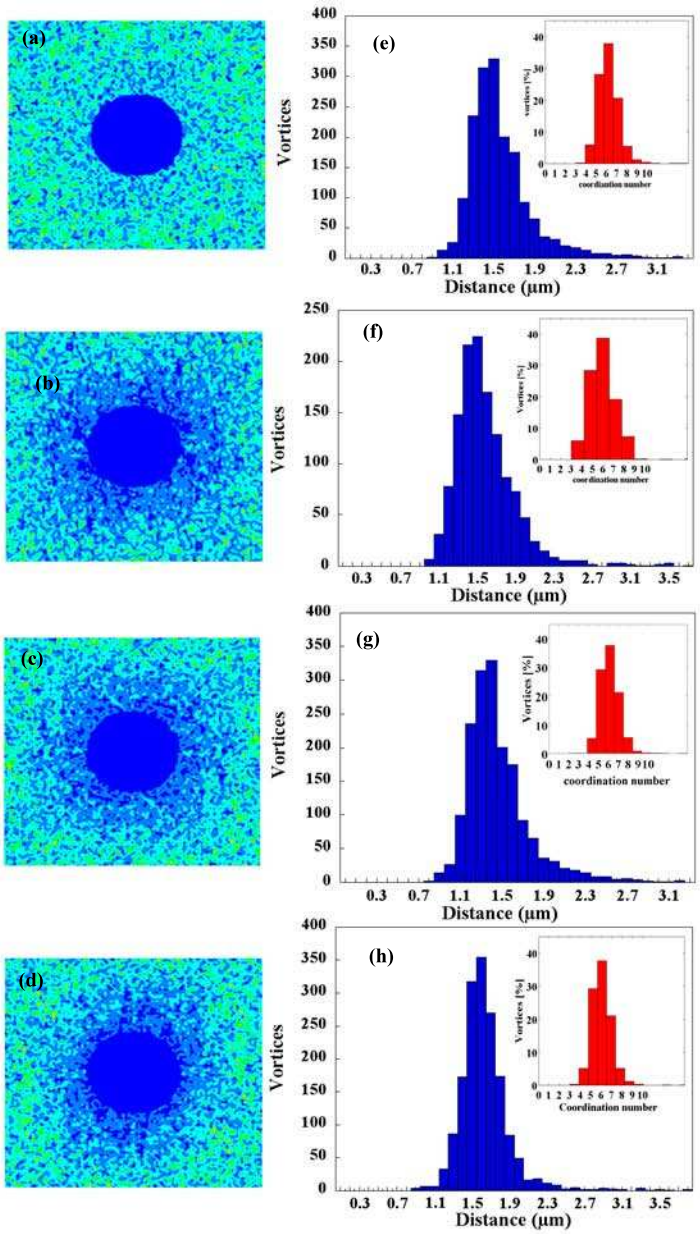

Figure 6.6 Fourier transforms of the vortex positions of the images presented in Figure 6.4 respectively for single crystals (a) with $x = 0.075$ #2.1, and b), (c) and (d) with $x = 0.1$ #1. In the right-hand panel were presented the histograms for the distribution of distances to nearest neighbors, the insets show the distribution of the coordination number belong to the histograms.

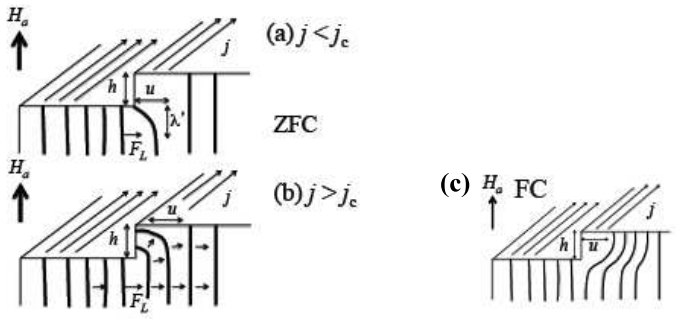

Figure 6.7 Representation of the behavior of vortex lines near a surface step under zero field-cooled conditions, for $j < j_c$ (a), and for $j > j_c$ (b), and under field cooled-conditions (c).

6.4 Discussion

6.4.1 Vortex configurations near surface steps

In what follows, the determination of the vortex pinning energies and forces from the decoration images will be attempted. The correct determination of the distribution of vortex pinning energies in the crystal and its interpretation requires knowledge of the temperature at which the vortex ensemble was frozen in the observed configuration. To determine this, we analyze the vortex distribution near the ubiquitous steps seen on the surfaces of the crystals. Such steps result from the repeated crystal cleavage performed during the Bitter decoration experiments. In zero-field cooled experiments, steps act as obstacles for vortex entry into the sample; they were described in Ref. [76] as "vortex diodes".

However, the present decoration experiments are carried out under field-cooled conditions and hence vortices nucleate in the sample at the temperature at which the mixed state becomes stable. As one cools down, the Meissner screening current running along the crystal edges, but also along the surface steps, increases as the penetration depth λ_{ab} for currents running in the ab–plane decreases. Thus, while cooling, vortices on the high-side of a surface step are progressively repelled by the increasing Meissner current density $j_M \sim H_a/\lambda_{ab}$. At the same time, the proximity of the step surface results in an attractive force that can be described by an image vortex segment. Finally, the vortex lattice elasticity tends to restore a homogeneous flux distribution near the step. The situation of a vortex segment close to a surface step is therefore similar to vortex entry or exit over a

surface barrier.

At the low fields of interest, the single vortex part of the tilt modulus dominates vortex elasticity,[13] so that the force balance can be written

$$\begin{aligned} \frac{B_{int}}{\lambda_{ab}}\left[H_a e^{-\upsilon} - \frac{B_{int}}{\mu_0}e^{-2\upsilon} - \frac{\varepsilon_\lambda^2\varepsilon_0}{\Phi_0}\ln\left(\frac{B_{c2}}{2B_{int}}\right)\frac{u\lambda_{ab}}{h^2}\right] &= \\ \frac{B_{int}}{\lambda_{ab}}\left[H_a e^{-\upsilon} - \frac{B_{int}}{\mu_0}e^{-2\upsilon} - \frac{\varepsilon_\lambda^2\Phi_0\upsilon}{4\pi\mu_0 h^2}\ln\left(\frac{B_{c2}}{2B_{int}}\right)\right] &= 0. \end{aligned} \tag{6.1}$$

Here, $\varepsilon_1 = \varepsilon_\lambda^2\varepsilon_0$ is the vortex line tension, $\varepsilon_0 = \Phi_0^2/4\pi\mu_0\lambda_{ab}^2$ is the vortex line energy, $\varepsilon_\lambda = \lambda_{ab}/\lambda_c$ is the penetration depth anisotropy, $\upsilon \equiv u/\lambda_{ab}$, represents the width of the vortex-free zone behind the step, u, normalized to λ_{ab}. The step running through Fig. 6.4 (a) has a height $h = 1.5\,\mu$m determined by a profilometer measurement, while the vortex-free region behind it has a width $u = 1.8\,\mu$m. Estimating the penetration depth anisotropy $\varepsilon_\lambda \approx 0.16$ from Refs. [196] and [120], and with all other parameters known, Eq. 6.1 can be solved graphically to yield $\upsilon \sim 1.5$, that is, $\lambda_{ab} \sim 0.6u \sim 1.2\,\mu$m. Combining this number with λ_{ab}(T)-data from Refs. [148] and [196], we conclude that the observed vortex pattern is frozen at $T_f \approx 0.9T_c$.

6.4.2 Pinning energies

The inter-vortex interaction energies are calculated from the vortex positions obtained from the decoration images. First of all, we proceed with the identification of the position of each vortex situated in each image with a program written in the C++ language, and provided by Y. Fasano. This program recognizes the vortex positions from the luminous intensity of the the iron clusters that decorate the vortex. Using the real SEM image the vortex positions extracted by the program were crosschecked by hand where this was found necessary.

A Matlab script was written to calculate the inter-vortex interaction energy (see Appendix 1),

$$\mathcal{E}_{int}^i = \sum_j 2\varepsilon_0 K_0\left(\frac{|r_{ij}|}{\lambda_{ab}}\right) \tag{6.2}$$

per unit length along the vortices' direction. Here $K_0(x)$ is the lowest-order modified Bessel function, and the vortex line energy $\varepsilon_0 = \Phi_0^2/(4\pi\mu_0\lambda_{ab}^2) \propto \lambda_{ab}^{-2}$ is proportional to the superfluid density. The script uses the position matrix as the input file to compute the distance r_{ij} from vortex i to all other vortices j. The calculation, takes into account all

vortices j situated at a distance smaller than $10\lambda_{ab}$ from vortex i. This cutoff radius was chosen after verifying that the interaction energy does not change significantly if greater values of j are considered. For the determination of the energy distribution histograms, only vortices situated away a distance larger than $4\lambda_{ab}$ from the edges of images were taken into account. The summing method was checked by calculating the interaction energy distribution of a perfect Abrikosov lattice, which should be a δ-function. After neglecting the contribution from the vortices situated less than $4\lambda_{ab}$ from the edges of the image,a well-defined δ-peak for the interaction energy distribution was indeed obtained for the perfect lattice. In the calculations the penetration-depth value at the temperature at which the vortex structure was frozen, $\lambda_{ab}(T/T_c = 0.9)$ was used (see Section 6.4.1).

A similar procedure yields maps of the pinning force acting on an individual vortex; per unit length,

$$\mathbf{f}_i = \sum_j \frac{2\varepsilon_0}{\lambda_{ab}} \frac{\mathbf{r}_{ij}}{|\mathbf{r}_{ij}|} K_1\left(\frac{|\mathbf{r}_{ij}|}{\lambda_{ab}}\right), \tag{6.3}$$

with $K_1(x)$ the first-order modified Bessel function. Since the system is stationary, Newton's third law requires the repulsive force exerted by neighboring vortices to be balanced by the pinning force. A map of the modulus $|\mathbf{f}_i|$ thus represents a map of the minimum pinning force acting on each vortex. In the case of a perfect lattice resulting, the sum Eq.(6.3) vanishes. We present our results by color-coded maps spanning the decoration images of Figure 6.4, and by histograms of the interaction energy distribution. The interaction energy maps with the energy-scale normalized by ε_0, are shown in Figure 6.8 (a,e) and Figure 6.9 (a,e). A granular structure of denser regions with larger interaction energy, and dilute regions with smaller $\mathcal{E}_{int}$ is clearly visible. This granularity is translates to broad vortex interaction-energy histograms, as shown in Figure 6.8 (b,f) and Figure 6.9 (b,f).

The histograms are reasonably well fitted by a Gaussian distribution. The standard deviations of these histograms are of the order of 23 %, in contrast to 50 % for the rather regular vortex structures [262] of the same density imaged in the high-T_c material $Bi_2Sr_2CaCu_2O_{8+\delta}$ (see Figure 6.10 (b)). However, as a result of the high reduced temperature T_f/T_c at which the vortex ensemble is frozen, the mean interaction energy (normalized by ε_0) is ten times larger in $Ba(Fe_{1-x}Co_x)_2As_2$ than in $Bi_2Sr_2CaCu_2O_{8+\delta}$. The histogram of the nearest-neighbor distance distribution in $Bi_2Sr_2CaCu_2O_{8+\delta}$ has a sharp peak at $r_{ij} = 1.56\mu m$, which corresponds to the triangular perfect lattice parameter $a_\triangle = 1.075\sqrt{\frac{\Phi_0}{B}}$, for $\mu_0 H_a = 0.1$mT. In order to compare the interaction energy distributions for $Bi_2Sr_2CaCu_2O_{8+\delta}$ and $Ba(Fe_{1-x}Co_x)_2As_2$ Figure 6.10 (b) presents the histogram for the distribution of the interaction energy of $Bi_2Sr_2CaCu_2O_{8+\delta}$ and $Ba(Fe_{1-x}Co_x)_2As_2$

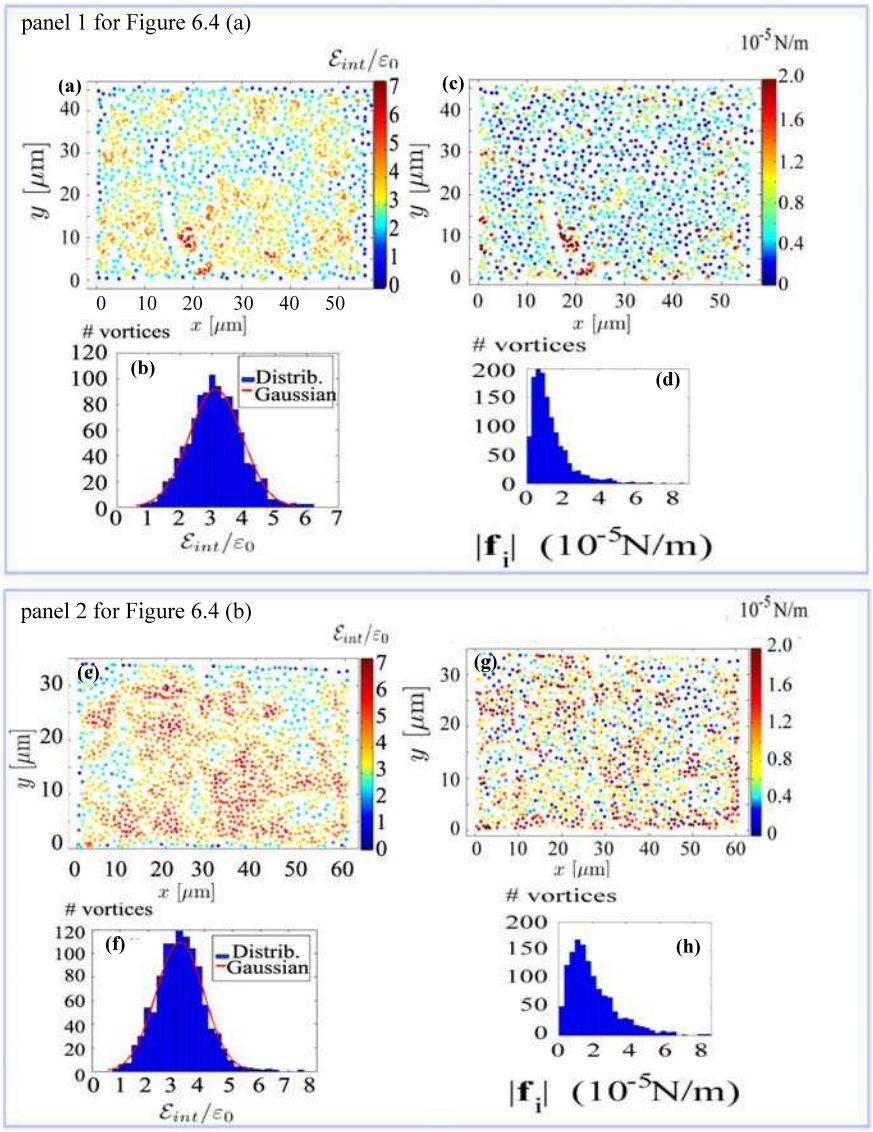

Figure 6.8 (a,e) Color-coded maps of the interaction energy normalized by ε_0 calculated from the images of Fig. 6.4 for $Ba(Fe_{1-x}Co_x)_2As_2$ single-crystals with (a)$x = 0.075$ and (b) $x = 0.1$. (c,g) Color-coded maps of the modulus of the individual vortex pinning force per unit length from the same images. The histograms of the distribution of the interaction energies and the modulus of the pinning forces are presented in (b,d), and (f,h) respectively.

with x=0.075 # 2.1 with the interaction energy calculated using the low temperature value of the penetration depth $\lambda_0(0) \sim 300$nm. The calculated distributions depend quite sen-

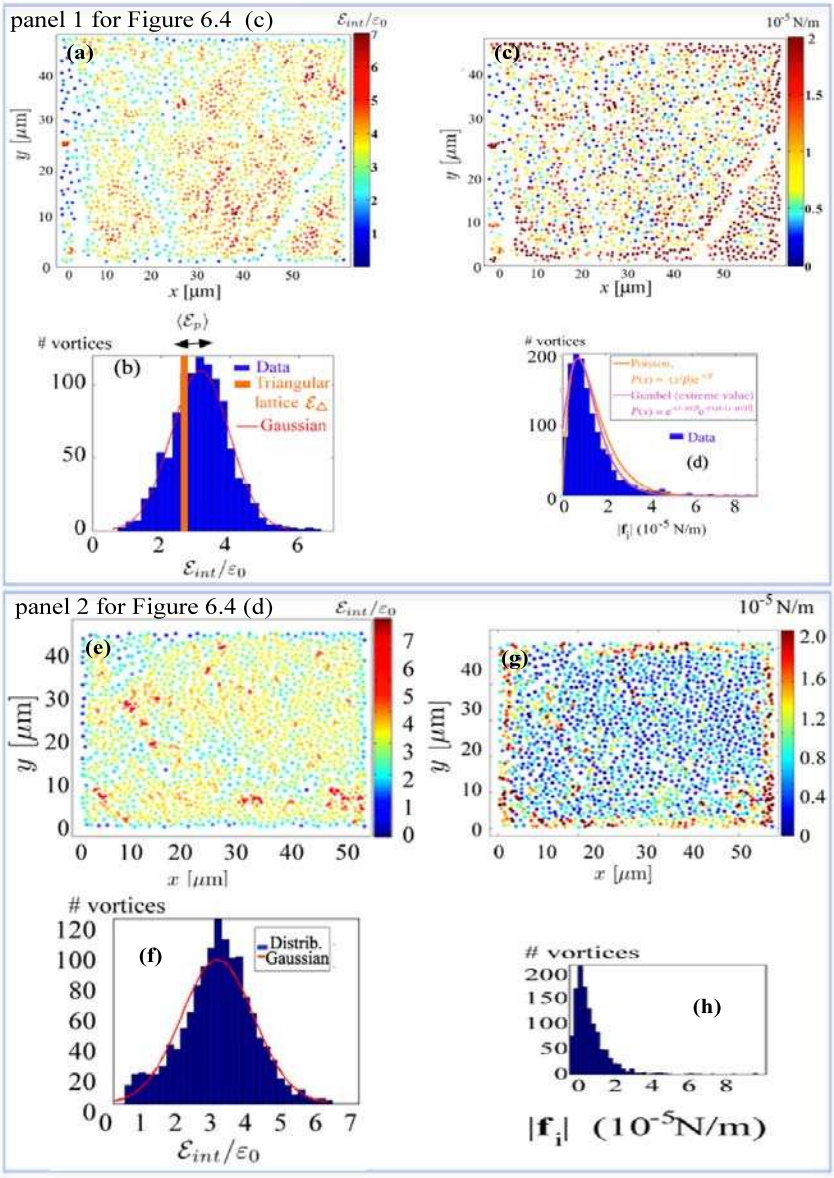

Figure 6.9 (a,e) Color-coded maps of the interaction energy normalized by ε_0 calculated from the images of Fig. 6.4 for $Ba(Fe_{1-x}Co_x)_2As_2$ single-crystals with (c,d) $x = 0.1$. (c,g) Color-coded maps of the modulus of the individual vortex pinning force per unit length from the same images. The histograms of the distribution of the interaction energies and the modulus of the pinning forces are presented in (b,d), and (f,h) respectively.

sitively on the value of λ_{ab}, and, by implication, on the temperature at which the vortex ensemble was frozen. A larger λ_{ab} yields a much larger energy scale as well as more sym-

metric distributions. Analyzing data on $Bi_2Sr_2CaCu_2O_8$ and $Ba(Fe_{1-x}Co_x)_2As_2$ using the same (low temperature) value $\lambda_{ab} = 300\,\mathrm{nm}$ [148] yields distributions that are three times broader for $Ba(Fe_{1-x}Co_x)_2As_2$, but with a mean value that is only 10% larger than for $Bi_2Sr_2CaCu_2O_{8+\delta}$. Figure 6.10 shows a Delaunay triangulation of $Bi_2Sr_2CaCu_2O_{8+\delta}$ single crystal decorated at $\mu_0 H_a = 0.1mT$ while Figure 6.10 (c) and (d) give us information on the vortex lattice homogeneity of the crystal. Figure 6.10 (c) shows the Fourier transform of the vortex positions from the Delaunay triangulation, and we present an histogram of the distribution of distances to the nearest neighbors in Figure 6.10 (d).

The reduced temperature T_f/T_c at which the vortex ensemble is frozen not only affects the deduced interaction energies, but also has a profound effect on the (orientational) order observed in the decorated vortex ensemble. Pardo *et al.* reported that in optimally doped $Tl_2Ba_2CuO_{6-\delta}$ superconductors with a broad magnetically reversible regime in the temperature-field phase diagram, and concomitantly low T_f/T_c, Bitter decoration yields a regular triangular lattice, while decorated vortex ensembles in the overdoped material with a narrow reversible temperature range (and high T_f/T_c) are amorphous [76]. At the origin of this effect is the high mobility of vortices just above T_f in materials with a wide reversible regime, such as $Bi_2Sr_2CaCu_2O_{8+\delta}$ or optimally doped $Tl_2Ba_2CuO_{6-\delta}$. On the other hand, the low mobility of the vortices just above T_f due to strong pinning in the vortex liquid phase in materials [such as, apparently, $Ba(Fe_{1-x}Co_x)_2As_2$ that have a narrow reversible regime yields an amorphous vortex ensemble.

Fig. 6.8 (c), and (g), and Fig. 6.9 (c), and (g) show maps of the modulus of the pinning force of individual vortices per unit length of the vortex lines. The pinning energy shows some correlation with the interaction energy at the local scale: regions of large (small) $\mathcal{E}_{int}$ generally correspond to regions of large (small) $|\mathbf{f}_i|$. There is noticeable inhomogeneity on scales smaller than the apparent grain size. If the granularity would be due to microscopic (μm scale) inhomogeneity of superconducting parameters such as the superfluid density one would expect a larger pinning force at the interface only. In the images, fluctuations of the pinning force within grains of similar $\mathcal{E}_{int}$ are observable. Therefore,inhomogeneity of the superconducting parameters exists not only on the μm scale of the images, but also on smaller length scales. It is interesting to note that the rendered pinning forces are simply related to a metastable current density $\mathbf{j}_i$, *running through each vortex*, as $\mathbf{f}_i = (\Phi_0/|\mathbf{B}|)\mathbf{B} \times \mathbf{j}_i$. The average pinning force per unit length of $5 \times 10^{-6}\,\mathrm{N/m}$, with local maxima of up to $6 \times 10^{-5}\,\mathrm{N/m}$, imply local currents of the order of $2.5 \times 10^9\,\mathrm{A\,m^{-2}}$. Maximum currents concentrated on vortex rich areas are of the order $3 \times 10^{10}\ \mathrm{A\,m^{-2}}$, comparable to the low-temperature value of the critical current density in Figure 6.11.

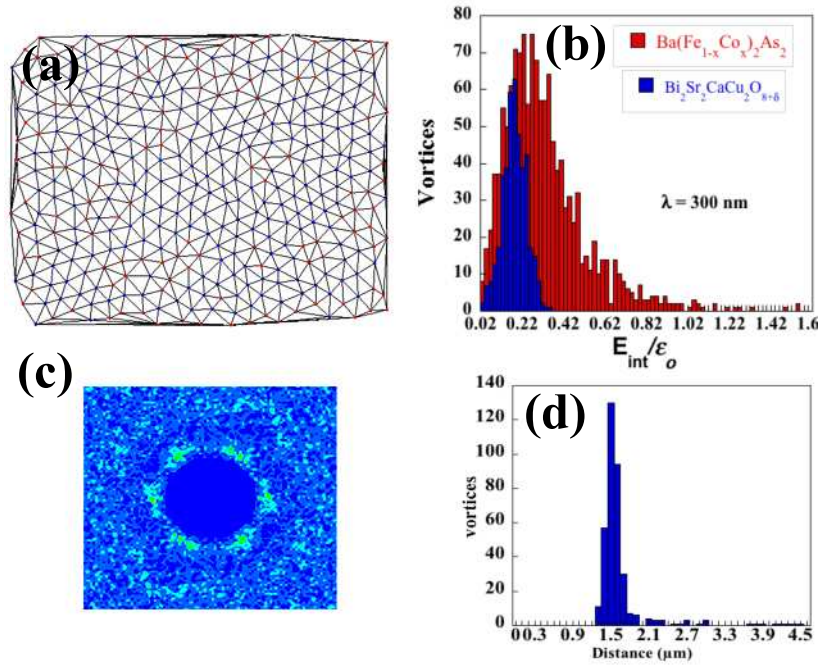

Figure 6.10 (a) Delaunay triangulation for $Bi_2Sr_2CaCu_2O_{8+\delta}$ single crystal, (b) comparative graph with the histograms of the interaction energy distribution of $Bi_2Sr_2CaCu_2O_{8+\delta}$ and $Ba(Fe_{1-x}Co_x)_2As_2$ with x=0.075 # 2.1. (c) The Fourier transform of the vortex positions , and (d) histogram of the distribution of distances to the nearest neighbors.

6.4.3 Effect of the spatial variations of T_c

Since the vortex locations result from the balance between inter-vortex repulsion and the interaction $\mathcal{E}_p$ of individual vortices with the pinning impurities, one has, at T_f, $\mathcal{E}_{int} = \mathcal{E}_p$. The position of the maximum and the width of the interaction-energy distributions in Figures 6.8 (b,f), and in Figures 6.9 (b,f) are therefore determined by, respectively, the mean and the standard deviation of the pinning energies, at T_f, of the individual vortices in a given image. In particular, the displacement of the maximum of the distribution with respect to the position of the δ-peak energy-distribution of a perfect vortex lattice of the same density is a measure of the mean pinning energy. As far as the vortex densities of Figure 6.8, and Figure 6.9 are concerned, the average $B_{int} = 0.8\,\mathrm{mT}$ would yield a δ-peak-maximum at $\mathcal{E}_{int} = 2.5\varepsilon_0$ for the triangular perfect lattice.

By comparison, the maxima of the distributions for both investigated crystals in Figure 6.8 (b,f), and in Figure 6.9 (b,f) occur at $\mathcal{E}_{int} \approx 3.2\varepsilon_0$. The average pinning energy per unit length is therefore $\mathcal{E}_p \sim 0.7\varepsilon_0$, while the variance in pinning energy is given by the width of the distribution, $(\langle \mathcal{E}_p^2 \rangle - \langle \mathcal{E}_p \rangle^2)^{1/2} \sim 0.5\varepsilon_0$. Note that $3.2\varepsilon_0$ corresponds to the

interaction energy of a triangular vortex lattice with $\Phi_0 n_v = 1\,\mathrm{mT}$, *i.e.* the external field applied during the experiments. This means that the average interaction energy is determined by vortex-rich areas, with $\Phi_0 n_v \gtrsim 1\,\mathrm{mT}$. However, the vortex density also presents vortex-poor areas so that the average $B_{int} = 0.8\,\mathrm{mT}$.

The large absolute values of the inferred pinning energies can be understood if one combines the notion that the crystals show local variations both of the critical temperature $T_c = T_c(\mathbf{r})$ and of the line energy $\varepsilon_0 = \varepsilon_0(\mathbf{r}, T)$, and that $T_f/T_c \lesssim 1$. As the crystal is cooled below T_c, vortices will avoid regions of higher T_c and ε_0, and accumulate in regions with lower values of these parameters.

They will remain trapped in such regions as the temperature is lowered below T_f. The large absolute values and variances of the pinning energies revealed by the decoration experiment are caused by the local variations of $T_c(\mathbf{r})$, which manifest themselves through the temperature dependence of the line energy, $\varepsilon_0(\mathbf{r}, T) = \varepsilon_0(\mathbf{r}, 0)[1 - T/T_c(\mathbf{r})]$. More specifically, the width of the inferred pinning-energy distribution (Figure 6.8 (b,f), and Figure 6.9 (b,f))should correspond to the width $\Delta\varepsilon_0(T_f)$ of the line energy distribution,

$$0.5\varepsilon_0(0)(1 - T_f/T_c) \sim \Delta\varepsilon_0(T_f). \tag{6.4}$$

Near to the critical temperature, $\Delta\varepsilon_0(T) = \varepsilon_0(0)T\Delta T_c/T_c^2$ is determined mainly by the width ΔT_c of the distribution of local $T_c(\mathbf{r})$. Solving Eq. (6.4) then yields $T_f = T_c/[1 + \Delta T_c/0.5T_c]$. Taking $T_c = 24$ K, and estimating $\Delta T_c \approx 0.8$ K from the DMO data of Fig. 6.2, one obtains a freezing temperature $T_f = 0.94T_c$ for $x = 0.075$; the same exercise with $T_c = 19\,\mathrm{K}$ and $\delta T_c = 0.5\,\mathrm{K}$ yields and $T_f = 0.95T_c$ for the crystal with $x = 0.1$. Thus, the analysis of the inhomogeneous and disordered vortex distribution, as well as the vortex distribution near steps and edges, is fully consistent with the observed patterns having been frozen between $T = 0.9$ and $0.95T_c$. We can draw the same conclusion from the local variations of the vortex density. For example, for the crystal #2 with $x = 0.075$, the largest local vortex gradient correspond to $0.15\,\mathrm{mT}/\mu\mathrm{m}$ or $1 \times 10^8\,\mathrm{A\,m^{-2}}$. This value is consistent with the critical current density of $Ba(Fe_{0.925}Co_{0.075})_2As_2$ crystal #2 at 23 K. In the case of $Bi_2Sr_2CaCu_2O_{8+\delta}$ single crystals whith a wide reversible regime in their phase diagram where the freezing temperature of the vortex structure is $T_f \sim T_{irr} \ll T_c$. The T_c variations are completely irrelevant since vortices have high mobility just above T_f.

6.4.4 Critical current density j_c

At low temperatures, the spatial variations of the magnitude of the line energy $\varepsilon_0(\mathbf{r}, 0)$ are dominant for pinning. These correspond to the variations in space of the superfluid

density, [18] and are responsible for the non-zero low-T pinning force associated from spatial inhomogeneity. A spatially homogeneous superfluid density would imply a vanishing (or logarithmically weak) pinning energy at low T, at odds with the existence of a large critical current density (see, *e.g.* , Figure 6.11).

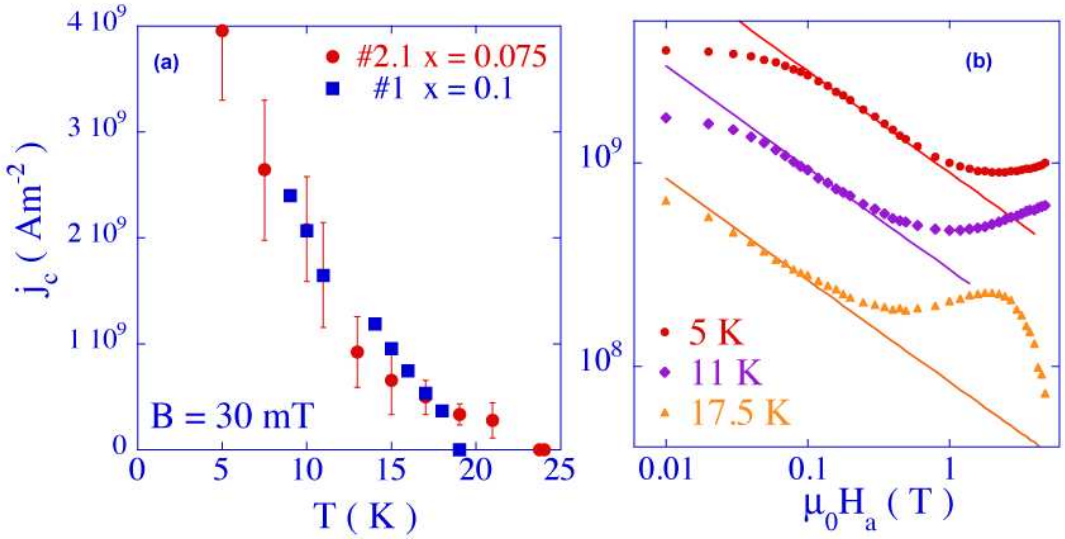

Figure 6.11 Critical-current densities in our $Ba(Fe_{0.925}Co_{0.075})_2As_2$ crystals. (a) Temperature-dependence of the low-field j_c of crystals #1 ($x = 0.1$) and #2.1 ($x = 0.075$), as obtained from MOI. Error bars represent the dispersion of j_c within a given crystal. (b) Field-dependence of j_c for crystal #2.1, obtained from magnetic hysteresis measurements using a SQUID magnetometer. Straight lines indicate fits with Eq. (6.6), see section 6.4.

As in all charge-doped single-crystalline iron-based superconductors, the critical current of $Ba(Fe_{1-x}Co_x)_2As_2$ is composed of a contribution from strong, extrinsic pins, and from a contribution from pinning by atomic sized-point pins. The latter dominates at high fields (above 1 T at 5 K, and above 0.2 T at 17.5 K), see Figure 6.11 (b) [41] while the former contribution manifests itself as a low-field plateau [41; 43]

$$j_c = \pi^{1/2} \frac{f_p}{\Phi_0 \varepsilon_\lambda} \left(\frac{U_p n_i}{\bar{\varepsilon}_0} \right)^{1/2} \qquad (B \ll B^*) \tag{6.5}$$

followed by a power-law in the flux density B,[41; 43]

$$j_c(B) = \frac{f_p}{\Phi_0 \varepsilon_\lambda} \left(\frac{U_p n_i}{\varepsilon_0} \right) \left(\frac{\Phi_0}{B} \right)^{1/2} \qquad (B \gg B^*). \tag{6.6}$$

The crossover field B^* is that above which the number of effective pins per vortex is limited by the intervortex repulsion, f_p is the maximum pinning force exerted by a single strong pin, n_i is the pin density, and $U_p/[\mathrm{J}]$ is the pinning energy gained by a vortex line traversing such a pin. The measurement of the low-field critical current density $j_c(0)$ and the slope $\partial j_c(B)/\partial B^{-1/2}$ allows one to eliminate n_i and to obtain $f_p = \pi \Phi_0^{3/2} \varepsilon_\lambda \left\{ j_c^2(0)/[\partial j_c(B)/\partial B^{-1/2}] \right\}$ from experimental data without further assumptions. We find that, at 5 K, $f_p \approx 3 \times 10^{-13}\,\mathrm{N}$ for both $Ba(Fe_{0.925}Co_{0.075})_2As_2$ crystal #2.1 and $Ba(Fe_{0.9}Co_{0.1})_2As_2$ crystal #1.

The identification of the strong pins with regions of lower $\varepsilon_0(T)$ means that f_p should be interpreted in terms of the local maxima of the position-dependent force $f(\mathbf{r}) = \int_{\delta z} \nabla \varepsilon_0(\mathbf{r}) dz$ experienced by vortices as they move through the sample. Here δz is the maximum extent of a region of low $\varepsilon_0(T)$ along the field direction. We approximate

$$f_p \sim \Delta\varepsilon_0 \left(\frac{\delta z}{\delta \varrho} \right), \tag{6.7}$$

where $\delta\varrho$ is the length scale characterizing the disorder in the direction perpendicular to the field, and $\Delta\varepsilon_0$ is the standard deviation of the $\varepsilon_0(\mathbf{r})$ distribution in the crystal. The pinning energy $U_p \sim f_p \delta\varrho$. A comparison of Eq. (6.7) with the value of f_p obtained from j_c yields $\Delta\varepsilon_0 \sim 3 \times 10^{-13}\ \mathrm{J\,m^{-1}}$ for a unit aspect ratio $\delta z/\delta\varrho$.

In a next step, we evaluate the ratio of $f_p/|\bar{\mathbf{f}}_i|$; this yields the average distance between effective pins, $\bar{\mathcal{L}} = 60$ nm. Using Eq. (17) of Ref. [43], which has $\bar{\mathcal{L}} = (\varepsilon_1/\pi n_i U_p)^{1/2}$, one finds $(n_i \delta z)^{-1/2} \sim 60\,\mathrm{nm}$. With all parameters known, the low-field value of the critical current density is reproduced as

$$j_c \approx \pi^{1/2} \frac{\Delta\varepsilon_0}{\Phi_0 \varepsilon_\lambda} \sqrt{n_i \delta z} \frac{\delta z}{\delta\varrho} \sqrt{\frac{\Delta\varepsilon_0}{\bar{\varepsilon}_0}} = 8 \times 10^9\,\mathrm{A\,m^{-2}}, \tag{6.8}$$

in fair agreement with the data of Fig. 6.11 (a). The investigated features of vortex pinning in $Ba(Fe_{1-x}Co_x)_2As_2$, including the disordered vortex patterns and the critical current density, are therefore consistently described by the presence of spatial variations of the superfluid density on the scale of *several dozen* nanometers, in agreement with the conjecture of Ref. [15].

Note that the observed spatial structures at the macroscopic (Figure 6.1) and meso-

scopic (Figure 6.4) levels are not those responsible for the critical current. The random vortex positions observed in the decoration experiments are determined by the underlying nanoscale disorder, an observation consistent with the fact that disordered vortex structures have been observed up to high fields.[59; 171]

One may speculate about the possible link between the existence of nm-sized regions of reduced superfluid density, the local variation of the dopant atom density, and the effect of the overall doping level. For instance, one would expect the fluctuations of the Co density to be more important at lower doping levels, yielding larger local fluctuations of ε_0. However, given the much larger values of the penetration depth at low doping, we have not been successful in performing Bitter decorations on the relevant crystals. Recent STS studies have reported substantial variations of the value of the superconducting gap on a scale of 10 to 20 nm.[75; 277] These local variations of the gap magnitude should correspond to the variations of the critical temperature and therefore lead to vortex pinning. Although it is tempting to relate our results to the nanoscale disorder observed in the STS gap-maps, it should be remarked that the spatial scale of the variations in the gap maps is a factor of 3-6 smaller than that found from the analysis of the data presented here. This would correspond to a concomitantly larger j_c in the samples used in Refs. [75; 277].

6.5 Conclusion

Bitter-decoration imaging of the disordered vortex distribution in superconducting $Ba(Fe_{1-x}Co_x)_2As_2$ single-crystals with $x = 0.075$ and $x = 0.1$ reveals a substantial local variation of pinning energies and pinning forces. The magnitude of these fluctuations is suggested to stem from nanoscale spatial variations of T_c and/or the superfluid density due to an inhomogeneous distribution of dopant atoms. The spatial scale of the variations is inferred from the correlation of the features of the vortex distributions with global and local critical current density measurements. The macroscopic spatial variations of the critical temperature observed using magneto-optical imaging give an idea of the magnitude of the T_c variations in the crystals, but are unrelated to the measured pinning properties. The same can be said for mesoscopic disorder structures observed by single-vortex imaging. An important corollary of our work is the fact that the observed vortex distributions are frozen, at a length scale of the lattice spacing, at a high temperature close to T_c.

6. STRONG PINNING AND VORTEX ENERGY DISTRIBUTIONS IN $BA(FE_{1-X}CO_X)_2AS_2$ SINGLE CRYSTALS

Chapter 7

Disorder, critical current, and vortex pinning energies in isovalently substituted $BaFe_2(As_{1-x}P_x)_2$

7.1 Introduction

Recent vortex imaging studies performed on iron pnictide superconductors show evidence of nanoscale inhomogeneity [46; 206] as being at the origin of the highly disordered vortex structures in these materials [18; 59; 90; 102; 144; 148; 152; 171; 172]. Notably, in $Ba(Fe_{1-x}Co_x)_2As_2$, the critical current density j_c and vortex distributions imaged by Bitter decoration could be reconciled provided that spatial heterogeneity of both the critical temperature T_c and the vortex line energy ε_0, on a scale of several dozen nm, is taken to be responsible for flux pinning. [206] At higher magnetic fields, of the order of several tenths of T, nano-scale heterogeneities are no longer thought to be responsible for pinning of flux lines. The critical current density is then most likely determined by the scattering of quasiparticles in the vortex cores associated with the presence of atomic-size defects in the crystal. [46] A good candidate for these defects are the dopant atoms themselves. [41; 44; 46; 206] The nature of the dopant atom is essential for this mechanism; charged defects lead to different scattering than uncharged defects. [44] The latter so-called "weak collective pinning" contribution to the critical current density manifests itself as a plateau-like behavior in a $j_c(B)$ plot at higher magnetic field. It is present in all charge doped iron-based superconductors, as well as in $Ba(Fe_{1-x}Ru_x)_2As_2$. [46; 206]

On the other hand, in isovalently substituted $BaFe_2(As_{1-x}P_x)_2$ there is no indication of this contribution, which qualifies the material as "clean" with respect to charge-doped

iron-based superconductors.[44] Thus, it is interesting to see whether the absence of weak collective pinning has any impact on the spatial configuration of vortices, in particular, given recent claims of more ordered vortex configurations than previously observed [18; 59; 90; 148; 152; 171; 172]. Vortex imaging in hole-doped $Ba_{1-x}K_xFe_2As_2$ (with $x = 0.28$ and $x = 0.4$) by Yang *et al.* using magnetic force microscopy (MFM) at magnetic fields up to 100 Oe have lead to the claim of more ordered vortex configurations in that compound than in, *e.g.* $Ba(Fe_{1-x}Co_x)_2As_2$. [206] The authors of Ref. [102] argue that this is due to weaker pinning. In fact, using the same analysis method as Ref. [206], they found pinning forces that are, on average, one order of magnitude smaller. They even observed some local triangular vortex order in the optimally doped $Ba_{1-x}K_xFe_2As_2$, as well as remarkable vortex chains, both in the underdoped ($x = 0.28$) and optimally doped ($x = 0.4$) samples. They related the presence of chains in the underdoped compound to pinning of vortices near the twin boundaries arising from the orthorhombic structure. Furthermore, neutron scattering experiments on the vortex lattice in isovalently substituted $BaFe_2(As_{1-x}P_x)_2$ were performed at $T = 2$ K by Kawano-Furukawa *et al.* [144]. No Bragg spots were found for the optimally substituted compound. However, after annealing the samples at 500°C, a distorted triangular vortex lattice was observed; this became more ordered as the applied magnetic field was increased from 0.7 to 7 T. [144] Thus, the study of vortex pinning in $BaFe_2(As_{1-x}P_x)_2$ is of interest because it casts light on the nature of crystalline disorder, which, in turn is relevant for the understanding of the nodal structure of the order parameter [167; 258] and that of possible phase coexistence [209; 219].

In this chapter we present and analyze critical current density measurements, magneto-optical imaging, and Bitter decoration experiments performed on $BaFe_2(As_{1-x}P_x)_2$ single crystals with different x. The spatial configuration of vortices in isovalently substituted $BaFe_2(As_{1-x}P_x)_2$ is found to be more homogeneous (less density fluctuations) than was observed in charge-doped $Ba(Fe_{1-x}Co_x)_2As_2$ single crystals.[206] Nevertheless, there is still no evidence for any triangular order in the vortex structure. At the same time, the quantitative analysis of the vortex configurations in terms of the pinning energy leads to the conclusion that disorder is less effective in $BaFe_2(As_{1-x}P_x)_2$ with respect to $Ba(Fe_{1-x}Co_x)_2As_2$, and that it depends on the P-content x. The cross-correlation of the pinning energies, pinning forces, and the critical current density with P-content is discussed. The analysis of the critical current density yields an estimate of the pin density that is in remarkable agreement with that extracted from Bitter decoration. The pin density clearly decreases upon increasing the P-content. The results also suggest that the pinning energy is proportional to the vortex line energy, implying that local variations of the superfluid density might be at the origin of the critical current density j. In contrast to what is reported in the

literature [146] we find no weak collective pinning contribution or "fishtail effect" in $j(B)$, in magnetic fields up to 5 T.

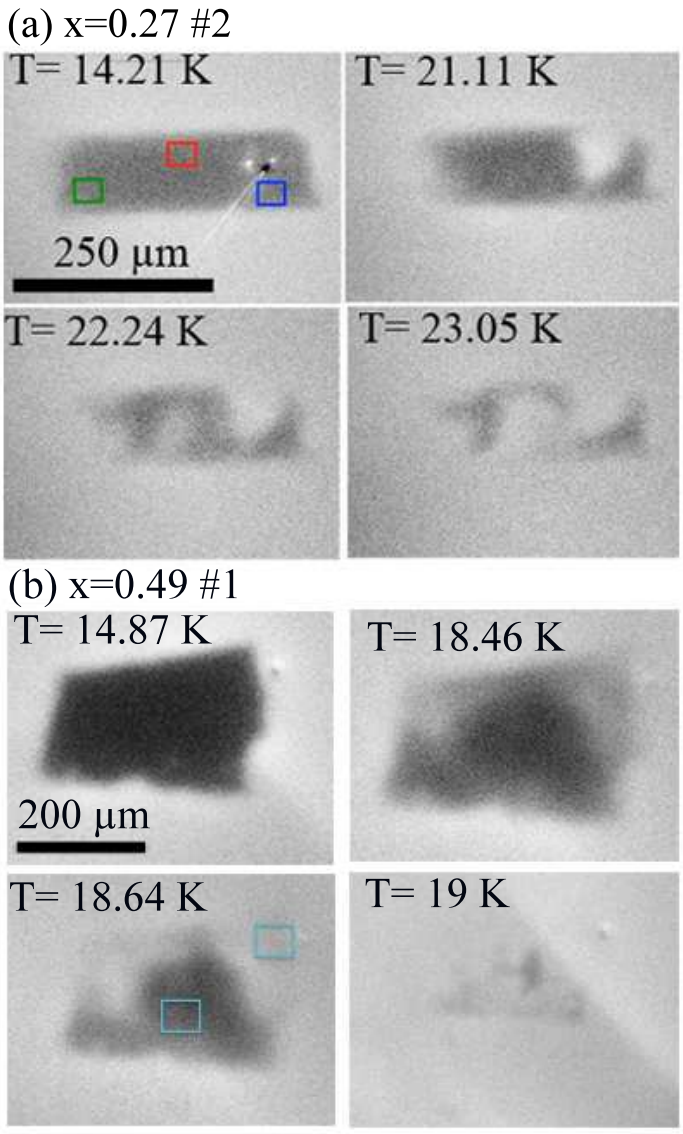

Figure 7.1 Differential magneto-optical images of screening of a magnetic field of $H_a = 1$ Oe by $BaFe_2(As_{1-x}P_x)_2$ single crystals (a) $x = 0.27$ # 2 , and (b) $x = 0.49$ #1. Squares in (a) indicate the regions over which the local transmittivity data of Figure 7.2 (b) are determined. The frames in (b) indicate the regions where the decoration images presented in Figure 7.12 (b,d) are situated.

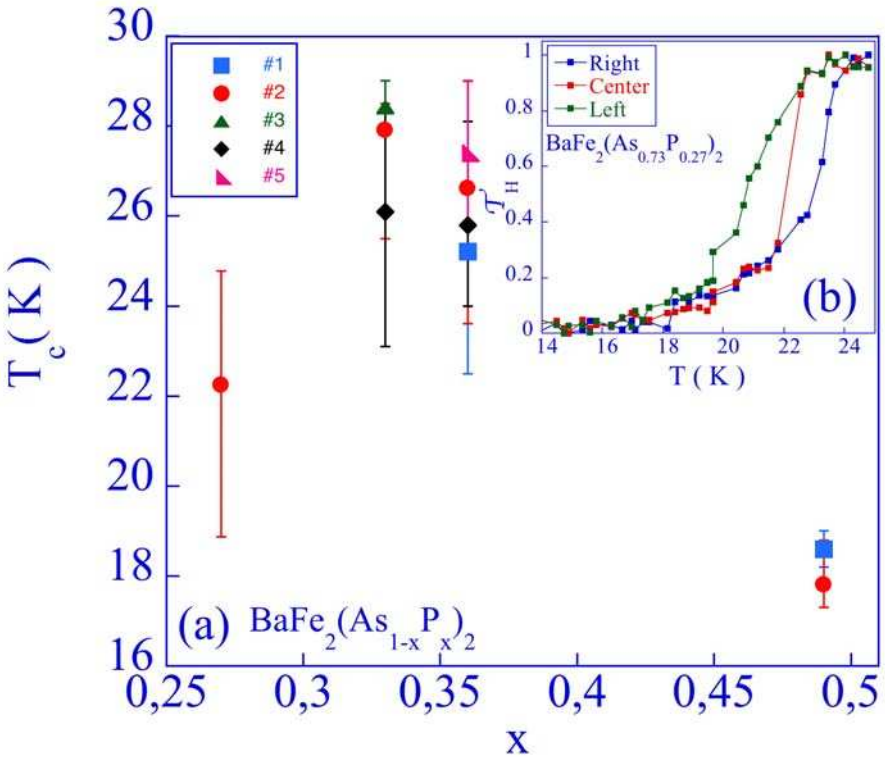

Figure 7.2 (a) Transition temperatures T_c and transition widths versus P doping level. The errors bars indicate the local spread of T_c inside a given crystal. For each doping level, the numbering # 1, #2,... denotes different crystals from the same batch. (b) $\mathcal{T}_H$ measured on the three regions of the crystal with $x = 0.27$ #2 indicated in Fig. 7.1.

7.2 Experimental details

Experiments have been performed on $BaFe_2(As_{1-x}P_x)_2$ single crystals grown by the self-flux method, [209] and characterized using Energy Dispersive X-Ray Spectroscopy (EDX) and EDX mapping in a scanning electron microscope (SEM). Crystals with manifest chemical heterogeneity were discarded from further study. The crystals described below present no impurity phases, within the experimental limits of accuracy $\lesssim \%1$.

Magnetic flux penetration in crystals with different doping levels ($x = 0.27 - 0.49$) was characterized using the magneto-optical imaging (MOI) method [41; 46; 145] (see Chapter 4) before further experiments. The MOI technique notably allows one to discard samples with macroscopic defects, and also, to extract calibrated flux density profiles. The sustainable current density j for magnetic fields up to $H_a = 500\,\mathrm{Oe}$ was obtained from the gradient of the local magnetic flux density B perpendicular to the crystal surface, using the Bean model [47; 66] (see Figs. 7.6,7.7). Given the thickness-to-width ratio of these crystals, $d/w \sim 0.25$, one has $j \sim 3\,dB/dx$. [62] The crystal inhomogeneity, and notably the local distribution of T_c was characterized using the differential magneto-optical (DMO) method. [12; 41] Measurements in higher magnetic fields were performed using micron-sized Hall probe arrays,[157] tailored in a pseudomorphic GaAlAs/GaAs heterostructure, as well as using a Superconducting Quantum Interference Device (SQUID)- based magnetometer. In what follows, individual crystals will be identified as (x = doping level, sample number #). Bitter decoration experiments at an applied field of H_a= 20 G were performed on $BaFe_2(As_{1-x}P_x)_2$ single crystals at several doping levels ($x = 0.33 - 0.58$).

7.3 Results

7.3.1 Spatial variations of the critical temperature T_c

Figures 7.1 (a) and (b) presents DMO images of the exclusion of an applied field $H_a = 1$ Oe as one crosses the superconducting to normal transition of $BaFe_2(As_{1-x}P_x)_2$ single crystals ($x = 0.27\,\#2$) and ($x = 0.49\,\#1$) respectively. These images reveal that T_c is spatially inhomogeneous. While spatial heterogeneity of T_c is especially pronounced in the underdoped samples, see crystal ($x = 0.27\,\#2$), it is also present in the overdoped crystals. A link between the heterogeneity observed in the underdoped samples and the possible coexistence of superconductivity with the antiferromagnetic phase, and/or the coexistence of orthorhombic and tetragonal structural domains is therefore not obvious. The T_c heterogeneity is quantified by the local transmittivity $\Im_H = [I(\mathbf{r},T) - I(\mathbf{r},T \ll T_c)] \,/\, [I(\mathbf{r},T \gg T_c) - I(\mathbf{r},T \ll T_c)]$ extracted from the luminous intensity $I(\mathbf{r},T)$, in the different regions indicated in the DMO

images of Fig. 7.1. The result is presented in the Inset to Fig. 7.2 for crystal ($x = 0.27\,\#2$). The width of the superconducting transition obtained for various crystals is presented in Fig. 7.2 (a), where the error bar indicates the spread of T_c in a given crystal, and the data points give the temperature value at which half the superconducting crystal has transited.

Element	K-ratio	Zaf	Elm. wt %	Norm wt %	At. %	At. prop.	Nom.%
P	0.0619	1.6952	10.49	4.76	11.60	13.30	10.8
As	0.2883	2.1698	62.55	28.38	28.58	32.80	29.2
Fe	0.6528	0.9723	63.47	28.79	38.91	44.64	40
Ba	0.7747	1.0831	83.90	38.07	20.91	24	20
Total			220.41	100.00	100.00	114.74	
P	0.0696	1.7002	11.83	4.60	11.21	12.89	10.8
As	0.3385	2.1619	73.18	28.43	28.67	32.95	29.2
Fe	0.7685	0.9717	74.68	29.01	39.24	45.10	40
Ba	0.9022	1.0832	97.72	37.96	20.88	24	20
Total			257.41	100.00	100.00	114.94	

Table 7.1 Chemical analysis over the surface of the crystal $BaFe_2(As_{1-x}P_x)_2$ with $x = 0.27\,\#1$ were presented as shown in Figure 7.3 obtained for the selected regions 1 and 2 respectively using EDX with accelerating voltage: 15.00 keV and takeoff angle 30 degrees.

In order to investigate the link between chemical heterogeneity and spatial inhomogeneity of T_c revealed by the MO images, quantitative chemical analysis was performed using the EDX mapping over the sample surface in a scanning electron microscope. Surfaces of samples under study were etched chemically using an aqueous solution of 1.769 g KI in 6.09 g of deionized water. The etching rate of such a solution as a function of time is given in Ref. [240] as 256 Å/min. In our case the etching process takes 10 minutes. The effect of the etchant on a superconducting YBCO film was also studied; after a 10 minute exposure to the etchant, any physical attack on the films occurs at a rate less than about 30 Å/min. Figure 7.3 shows maps of chemical composition, obtained on the underdoped crystal with x=0.27 # 1. In the color maps, the intensity of blue represents the occurrence of the corresponding element (Ba, Fe, As, or P). The global spatial distribution seems homogeneous, however some heterogeneity might exist in a smaller scale than the resolution of the figure. Chemical analysis was performed on selected regions on the surface of the underdoped crystal (x=0.27 # 1). The surface maps and chemical analysis results are shown in Figure 7.3 and in Table 7.1.

Table 7.1 shows small fluctuations on the atomic percentage of the dopant atom P exist between different regions selected for chemical analysis. One also observes spatial heterogeneity of the chemical analysis maps , but this kind of heterogeneity is due to the surface roughness and/or surface state (dirt, steps). More particularly, we have observed

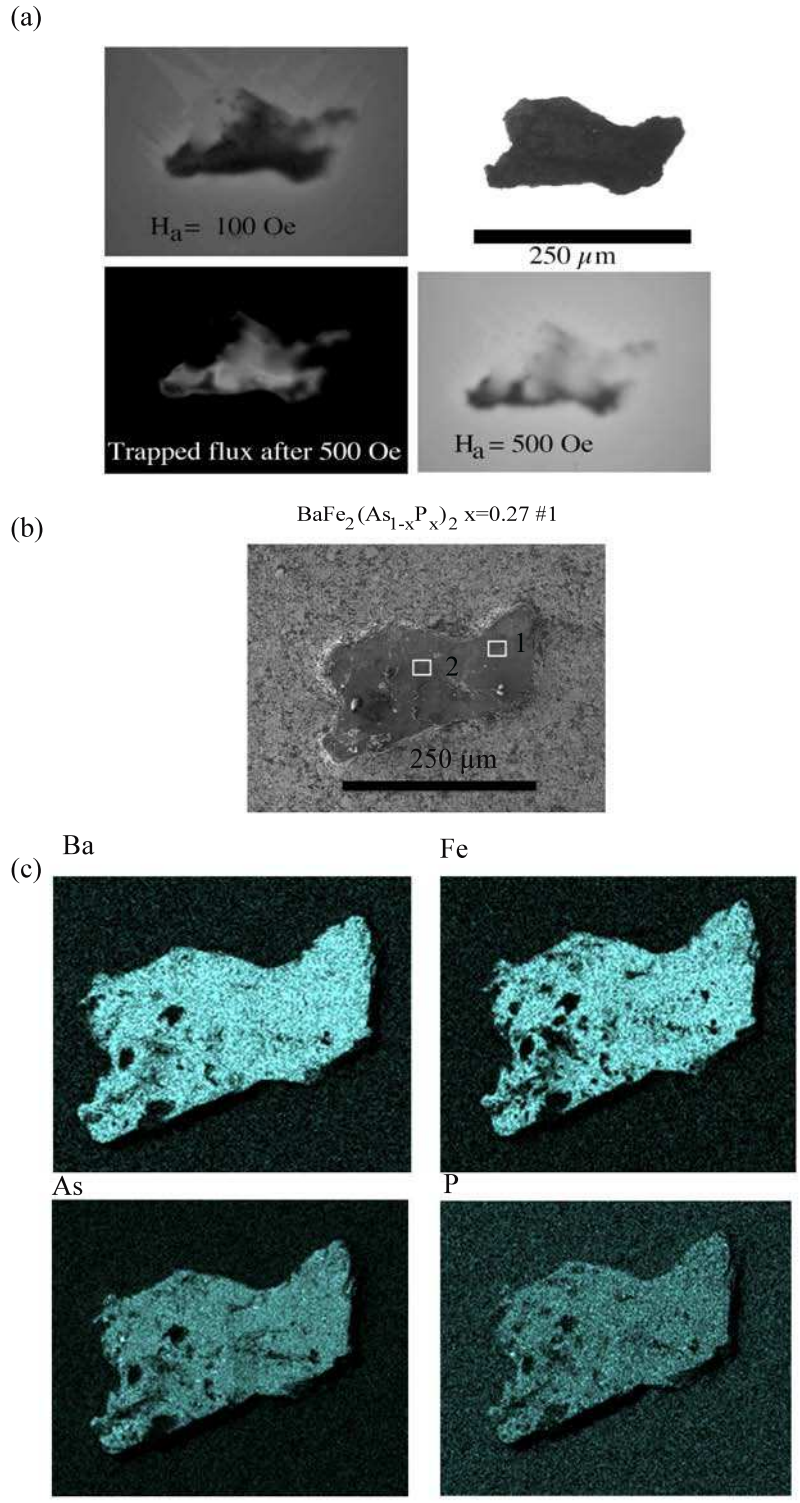

Figure 7.3 (a) DMO images of the crystal that reveal the spatial heterogeneity. (b) SEM image of the crystal with x=0.27 # 1. Regions selected for chemical analysis are indicated with squares on the crystal image.(c) Maps of chemical analysis for each element, performed using EDX on the surface of the crystal with x=0.27 # 1.

an slight excess of P (% 29) and a deficit of As on the surface of the crystal with $x = 0.27$ # 1(see Table 7.1). In order to see whether this heterogeneity has a chemical origin or exists only in the underdoped samples, similar analysis was performed on an optimally doped sample with x=0.36 # 2 (see Figure 7.4). In Table 7.2 one can see the chemical analysis results for this optimally doped sample that there is a deficit of P (% 31) on the surface of the crystal with $x = 0.36$ # 1 . One can argue that the spatial heterogeneity observed separately on the MOI images are supported by the spatial variations of the chemical composition from nominal values on the sample surfaces.

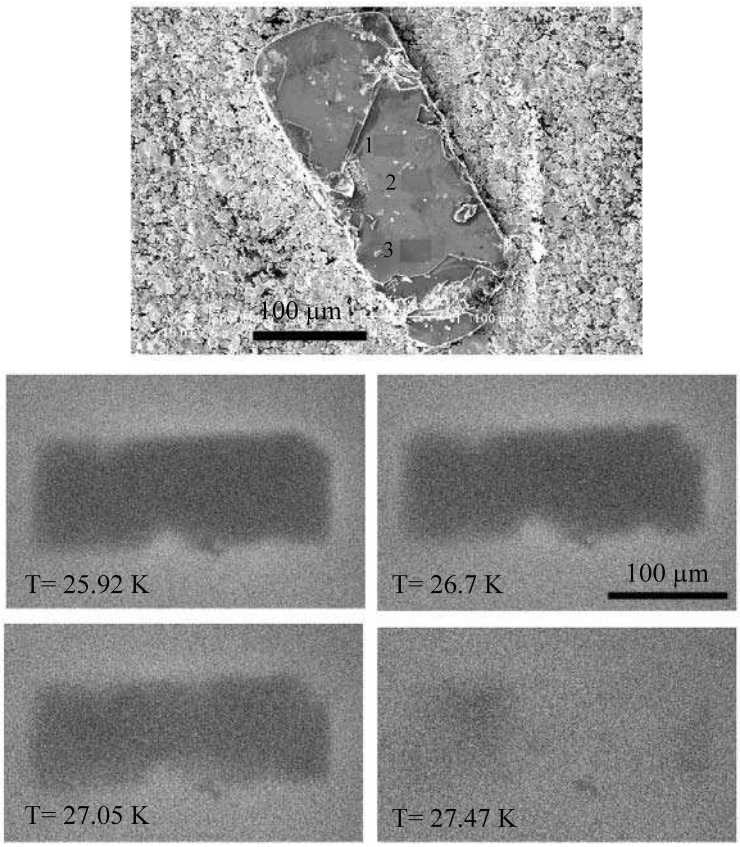

Figure 7.4 SEM image and DMO images of the crystal with x=0.36 # 1. Regions selected for chemical analysis are indicated with numbers on the crystal image.

Element	K-ratio	Zaf	Elm. wt %	Norm wt %	At. %	At. prop.	Nom.%
P	0.0328	1.6778	5.50	5.21	12.53	24	14.4
As	0.1265	2.1951	27.78	26.34	26.15	50.11	25.6
Fe	0.3321	0.9743	32.35	30.67	40.86	78.30	40
Ba	0.3679	1.0833	39.85	38.78	20.47	39.22	20
Total			105.48	100.00	100.00	191.63	
P	0.0327	1.6799	5.49	5.27	12.68	24	14.4
As	0.1268	2.1890	27.75	26.65	26.50	50.18	25.6
Fe	0.3229	0.9742	31.45	30.21	40.29	76.30	40
Ba	0.3640	1.0835	39.44	37.87	20.54	38.90	20
Total			104.13	100.00	100.00	189.38	
P	0.0329	1.6781	5.52	5.30	12.74	24	14.4
As	0.1252	2.1937	27.47	26.37	26.22	40.39	25.6
Fe	0.3241	0.9743	31.58	30.32	40.43	76.18	40
Ba	0.3655	1.0833	39.59	38.01	20.61	38.84	20
Total			104.16	100.00	100.00	188.41	

Table 7.2 Chemical analysis over the surface of the crystal $BaFe_2(As_{1-x}P_x)_2$ with $x = 0.36\,\#1$ as shown in Figure 7.4 obtained for the selected regions using EDX with accelerating voltage: 15.00 keV and takeoff angle 30 degrees.

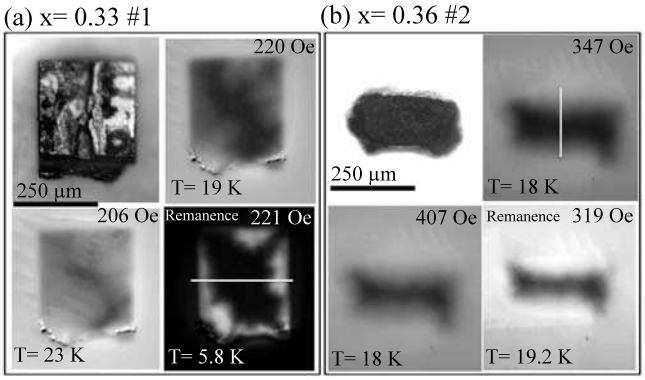

Figure 7.5 Magnetic flux density distribution in the $BaFe_2(As_{1-x}P_x)_2$ single crystals (a) ($x = 0.33\,\#1$), and (b) ($x = 0.36\,\#2$), for the indicated temperatures and applied magnetic fields H_a. The top left of each subfigure is the image of the crystal. White bars represent the lines along which the profiles in Figs. 7.6 are extracted.

7.3.2 Sustainable current density j

Figure 7.5 presents MOI of the magnetic flux penetration (after zero-field cooling) into superconducting $BaFe_2(As_{1-x}P_x)_2$ single crystals with different doping levels, ($x = 0.33\,\#1$) and ($x = 0.36\,\#2$) respectively. The former crystal is characterized by very weak bulk pinning and, as a result, a large influence of geometrical [64] and surface barriers [35]. The

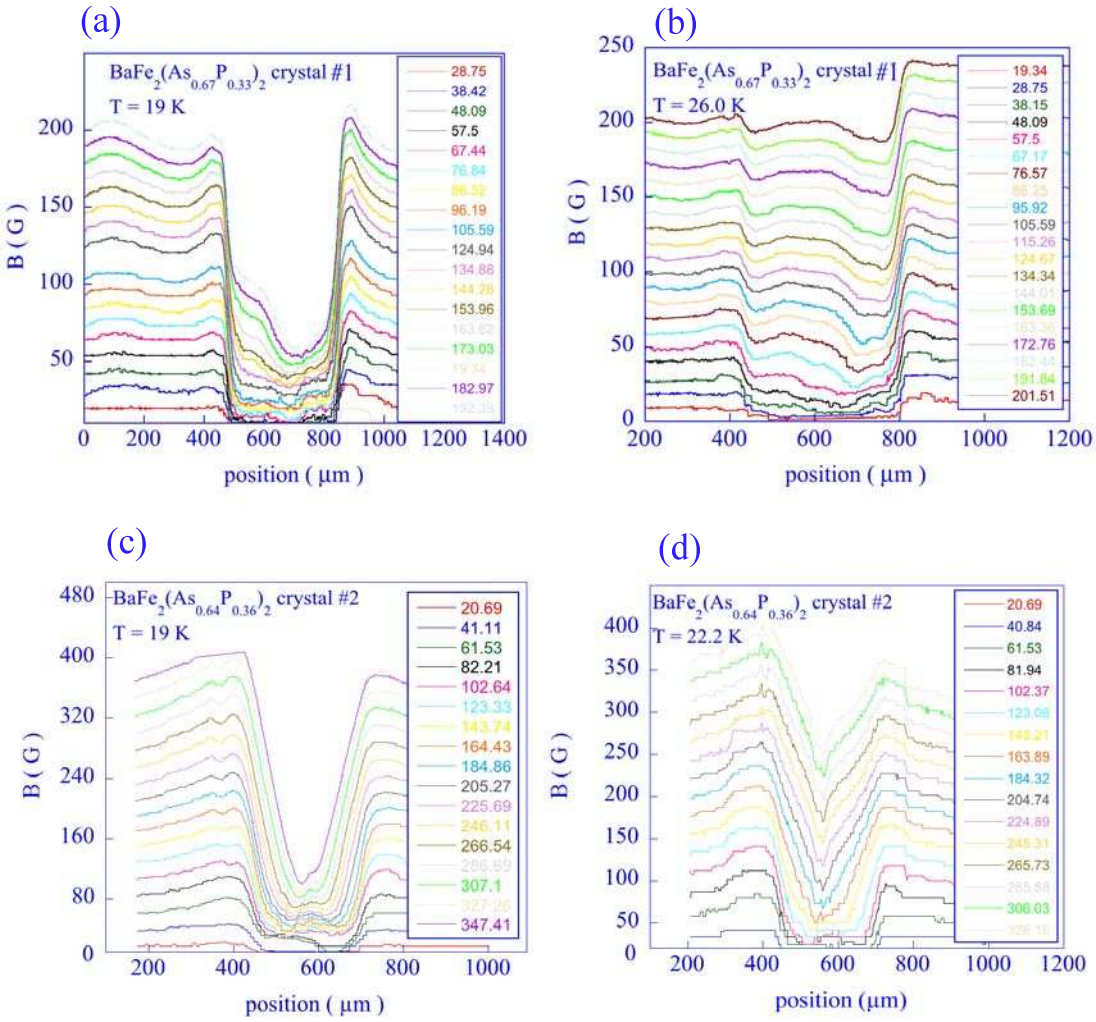

Figure 7.6 Magnetic flux profiles in $BaFe_2(As_{1-x}P_x)_2$ single crystals ($x = 0.33\,\#1$) at $T = 19$ K and 26 K (a,b), and ($x = 0.36\,\#2$) at $T = 19$ K and 22.2 K (c,d). The Bean–like profiles in (c,d) are obtained from the MOI images of Figure 7.5 (b). The profiles presented in (a,b) are influenced by a surface barrier and are obtained from images on the crystal in Fig. 7.5 (a).

influence of the surface screening current leads to an inhomogeneous flux density distribution as presented in Figure 7.5 (a). In contrast, crystal ($x = 0.36\,\#2$) shows regular flux penetration, in accordance with the Bean critical state model. The influence of a surface barrier, present for both flux entry and flux exit, is also revealed by Hall probe array measurements.

The flux density profiles across the same crystals ($x = 0.33\,\#1$) and ($x = 0.36\,\#2$),

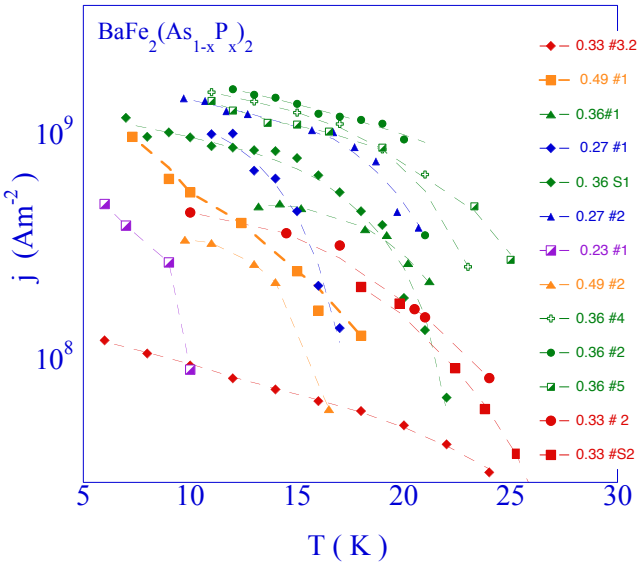

Figure 7.7 Temperature dependence of the sustainable current density $j(T, B = 30\,\mathrm{mT})$ determined from t flux density profiles as obtained from MOI images for each presented sample, for doping levels varying from $x = 0.23$ to $x = 0.49$. Dashed lines are guide for eyes.

depicted in Figure 7.6 (a,b) and (c,d) respectively, were extracted from the calibrated luminous intensities of the magneto-optical images in Figure 7.5. One sees that, even for the same or comparable doping levels, very different flux density profiles can be obtained. Figure 7.6 (c,d) shows the Bean-like penetration of the magnetic flux inside the crystal with ($x = 0.36\,\#2$), with no clear influence of a surface barrier, while the flux profiles for crystal ($x = 0.33\,\#1$) in Figure 7.6 (a,b) show, apart from inhomogeneity, a large discontinuity in the magnetic induction at the sample edge, characteristic of a surface barrier. Given the very different behavior for nearly the same sample composition, the origin of the bulk critical current density in $BaFe_2(As_{1-x}P_x)_2$ must be extrinsic. This is underscored by the temperature dependence of the sustainable current density $j(T, B = 30\,\mathrm{mT})$ of the studied samples, shown in Fig. 7.7 . The absolute value of $j(T)$ is widely disperse, even for crystals with the same doping level.

In spite of the disparity, the flux pinning mechanism in all crystals is the same. Fig. 7.8 shows hysteresis loops of the local gradient of the magnetic induction dB/dx in fields of up to 2 T, obtained on crystals of different doping levels, all clearly showing Bean-like critical state flux profiles, using the Hall probe–array magnetometry technique [157]. The hysteresis loops were measured at 6 K, at which flux creep has only a moderate

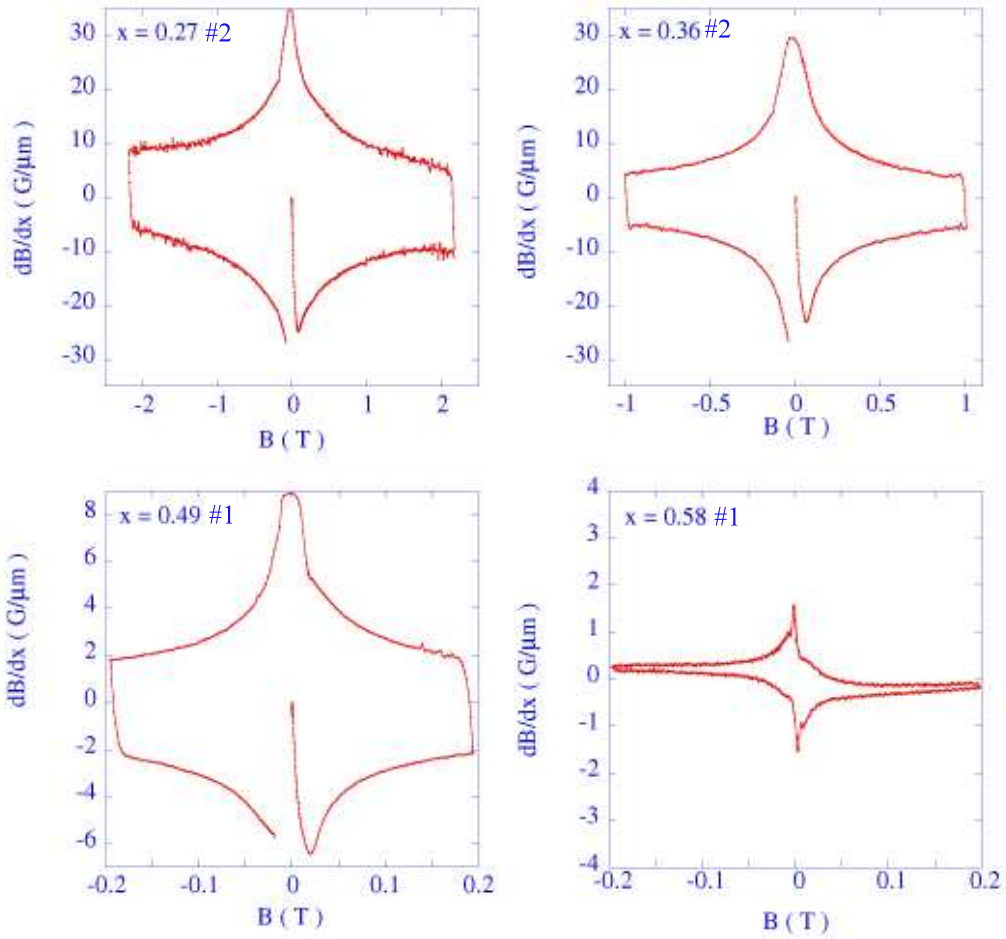

Figure 7.8 Hysteresis loops of the spatial gradient of dB/dx the local magnetic induction measured at $T = 6$ K, in $BaFe_2(As_{1-x}P_x)_2$ single crystals of different doping levels ($x = 0.27 - 0.58$) using the Hall probe magnetometry technique .

influence. For all crystals, of all doping levels, one has the ubiquitous central peak at zero field, believed to be due to strong pinning by nm-scale disorder.[41] The magnetic field dependence of the sustainable current density $j(B)$ was extracted from the width of the measured hysteresis loops. Figure 7.9 shows the $j(B)$ curves for optimally doped single crystal ($x = 0.36$ # 2) at the indicated temperatures. Here the $j(B)$ curve at the lowest temperature in Figure 7.9 is representative of the critical density j_c. At larger temperatures and fields the curves are even more affected by flux creep.

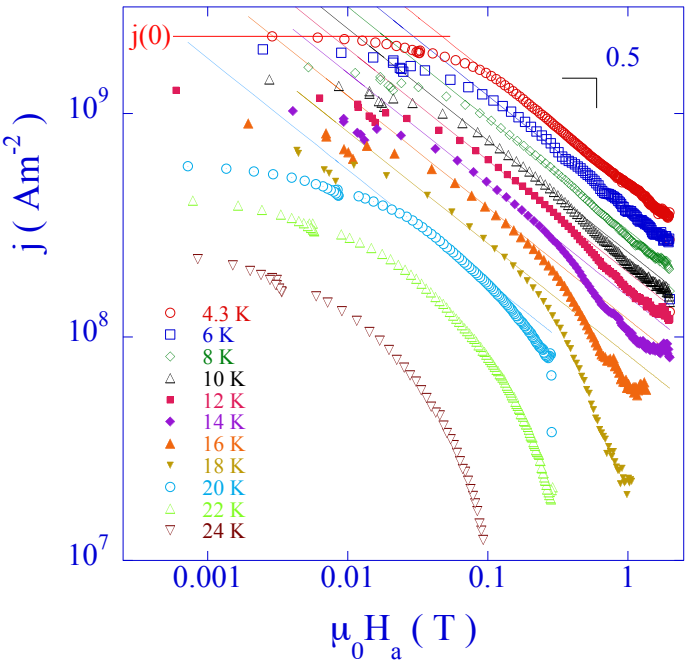

Figure 7.9 Magnetic field dependence of the sustainable current density j for the crystal with x=0.36 # 2, obtained from magnetic measurements of the hysteresis loops using the Hall probe magnetometry method [157]. Above $\mu_0 H_a$=0.1 T, the low temperature data follows $j\ B^{-1/2}$.

7.3.3 Effect of flux creep

The influence of flux creep is assessed using relaxation measurements of the local flux density using the Hall probe magnetometry technique. Typical examples shown in Fig. 7.10(a) show that the creep rate $S \equiv d\ln(dB/dx)/d\ln t$ is typically less than 1%. Nevertheless, the sustainable screening current density j is significantly affected, such that it is given by the

equality $U(j) = k_B T \ln\left[(t_0 + t)/\tau\right]$ rather than by the critical current density j_c [43; 235]. Here, t_0 is a time describing transient effects at the onset of relaxation, and τ is a normalization time related to the sample inductance.[43; 235] The dependence of the flux creep barrier can be extracted using various methods, including those of Maley *et al.* [170] and Abulafia *et al.* [156; 257]. Applying the latter, we find [see Fig. 7.10(b)] that the creep barrier in optimally doped $BaFe_2(As_{1-x}P_x)_2$ follows

$$U(j) = U_c \left(\frac{j_c}{j}\right)^{\mu}, \tag{7.1}$$

with values of the exponent $\mu \sim 1.5-2$. Therefore, the time– and temperature dependence of the screening current density is described by

$$j = j_c \left[\frac{k_B T}{U_c} \ln\left(\frac{t + t_0}{\tau}\right)\right]^{-1/\mu}. \tag{7.2}$$

The impact of flux creep on the temperature dependence of the sustainable current is depicted in Fig. 7.10(c), which shows $j(B,T)$–curves for crystal ($x = 0.33$) #2). The curve in zero applied field is little affected by creep, and roughly follows the expected temperature dependence of the depairing current, $j(0,T) \sim \varepsilon_0(T)/\Phi_0\xi(T)$. Here, the vortex line energy, $\varepsilon_0(T) = \Phi_0^2/4\pi\mu_0\lambda_{ab}^2$ is evaluated using the data for the in–plane penetration depth $\lambda_{ab}(T)$ of Ref. [135] ($\Phi_0 = h/2e$ is the flux quantum). The curves in non-zero field can then be well described by taking the creep barrier prefactor $U_c(T) \propto \varepsilon_0(T)$, $j_c(B,T) \propto j(0,T)B^{-1/2}$, $\mu = 1.6$, and $\ln\left[(t + t_0)/\tau\right] = 20$ [156] .Therefore, the temperature dependence of the screening current in fields larger than 0.1 T is essentially determined by flux creep.

7.3.4 Extraction of pinning parameters

We now analyze the $j(B)$–curves measured at low temperature, which bear the hallmarks of strong pinning. These are the plateau at low magnetic field, [41; 43]

$$j_c(0) = \pi^{1/2} \frac{f_p}{\Phi_0 \varepsilon_\lambda} \left(\frac{U_p n_i}{\varepsilon_0}\right)^{1/2} \qquad (B \ll B^*), \tag{7.3}$$

followed by a power-law decrease as a function of the the flux density B,[41; 43] which can be described as

$$j_c(B) = \frac{f_p}{\Phi_0 \varepsilon_\lambda} \left(\frac{U_p n_i}{\varepsilon_0}\right) \left(\frac{\Phi_0}{B}\right)^{1/2} \qquad (B \gg B^*). \tag{7.4}$$

$B^* = (\Phi_0/\pi)(U_p n_i/\varepsilon_0)$ is the crossover field above which the intervortex repulsion limits the number of effective pins per vortex, and f_p is the maximum pinning force exerted by a

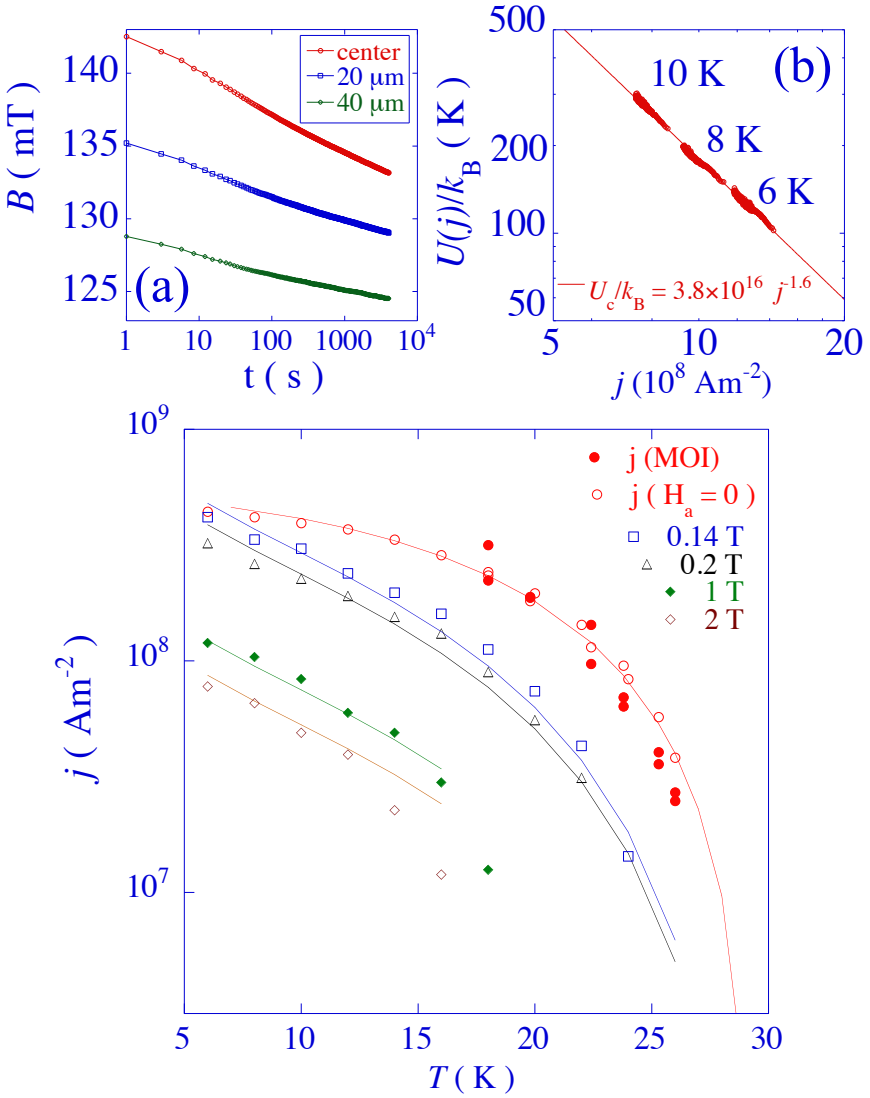

Figure 7.10 Magnetic relaxation in $BaFe_2(As_{1-x}P_x)_2$ crystal ($x = 0.33$ #2) measured using the Hall-probe array technique. (a) shows the relaxation of the magnetic flux density at the center of the crystal surface, and positions 20 and 40 μm from the center, respectively. Data were taken at 10 K, after field cooling in 200 mT and reducing the applied field to zero. (b) Activation barrier versus shielding current density, as obtained using the method outlined in Refs. [156; 257]. (c) Temperature dependence of the sustainable current density in zero applied field, and applied fields of 0.14, 0.2, 1, and 2 T. Measurements using the Hall probe-array technique (open symbols) were obtained from the width of the magnetic hysteresis loops such as those in Fig. 7.8 , while data from MOI are obtained from the flux-profile gradient. The lines depict fits to the depairing current density (H_a=0) and to Eq. 7.2, taking the activation energy $U_c(T) \propto \varepsilon_0(T)$, and $j_c(B,T) j_c(0,T) B^{-1/2}$ ($H_a \neq 0$).

single strong pin. $U_p/[J]$ is the pinning energy of a single strong pin, n_i is the pin density, and ε_λ is the penetration depth anisotropy. The contribution to $j(B)$ due to weak collective pinning of the vortex lines by atomic sized point pins, observed in all charge-doped iron based superconductors as well as in $Ba(Fe_{1-x}Ru_x)_2As_2$, is clearly absent in Figure 7.9. Furthermore, no second peak feature of the critical current, such as this was reported by Fang *et al.* [146], was observed, in fields up to 5 T. The $BaFe_2(As_{1-x}P_x)_2$ system can therefore be seen as an typical strongly pinning superconductor.

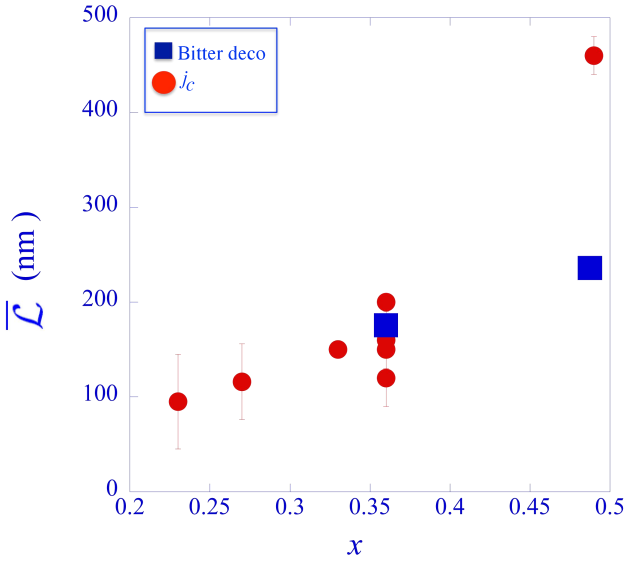

Figure 7.11 Average distance $\overline{\mathcal{L}}$ between effective pins versus the P doping level, at $T = 5$ K (●), and as determined from Bitter decoration (■).

Equations (7.3) and (7.4) show that the pinning force of a single strong pin is given as $f_p = \pi\Phi_0^{3/2}\varepsilon_\lambda\{j_c^2(0)/[\partial j_c(B)/\partial B^{-1/2}]\}$ and can therefore be obtained from the experimentally measured low temperature, low-field critical current density $j_c(0)$, and the slope $\partial j_c(B)/\partial B^{-1/2}$. Reserving our attention to the crystals used in the Bitter decoration experiments presented below, we obtain, for an estimated $\varepsilon_\lambda = 0.15$,[196] $f_p \approx 8\times10^{-13}$ N for both crystals, ($x = 0.36\#2$) and ($x = 0.49\#1$). This value is twice larger than that measured in $Ba(Fe_{1-x}Co_x)_2As_2$.[206] An evaluation at the highest measurement temperature of $0.8T_c$ yields $f_p = 2\times10^{-14}$ N; however, this value is likely to be overestimated due to creep. One can also extract a "pinning efficiency" $(U_p n_i/\varepsilon_\lambda\varepsilon_0) = (1/\pi\Phi_0)\left[(\partial j(B)/\partial B^{-1/2})/j(0)\right]^2$ in units $[m^{-2}]$. This number, involves a simple ratio of the slope $\partial j(B)/\partial B^{-1/2}$ and the zero–field $j(0)$, and should not be affected by material anisotropy. It is directly related to the mean distance between effective pins in the low–field single–vortex regime of strong

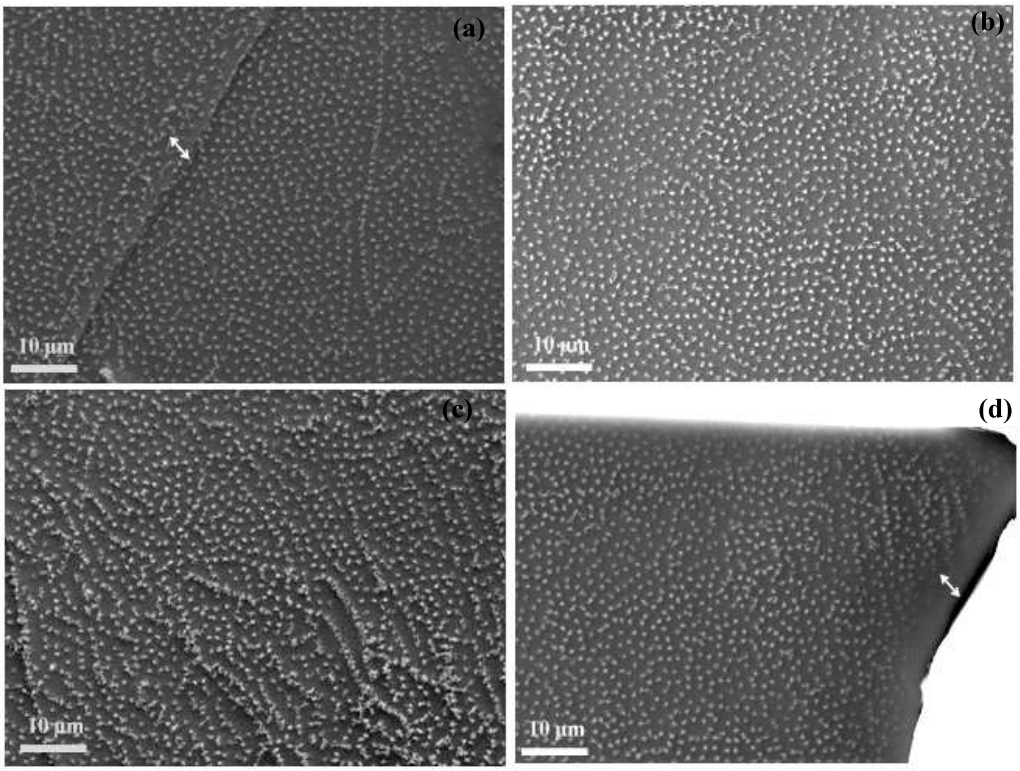

Figure 7.12 Bitter decoration images of $BaFe_2(As_{1-x}P_x)_2$ single crystal ($x = 0.49\,\#1$), (a) and (c) and ($x = 0.36\,\#2$), (b) and (d). The white arrows indicate the vortex-free Meissner belt observed (a) near a surface step and (d) at the edge of crystal ($x = 0.49\,\#1$).

pinning, $\overline{\mathcal{L}} = (\pi U_p n_i/\varepsilon_\lambda \varepsilon_0)^{-1/2}$.[43] Figure 7.11 shows that the latter distance is of the order of several dozen to several hundreds of nm, in accordance with the strong pinning hypothesis. Moreover, the distance between effective pins clearly increases as function of the doping x.

7.3.5 Vortex imaging by Bitter decoration

The Bitter decoration technique [206] was used to image the vortex ensemble in $BaFe_2(As_{1-x}P_x)_2$ single crystals with three different doping levels ($x = 0.33$, $x = 0.36$, $x = 0.49$). The experiments were realized under field cooled (FC) conditions at a field $H_a = 20$ G applied parallel to the c-axis of the crystals. The decoration experiment for the crystal with $x = 0.33$ was not successful, presumably due to the high value of the penetration depth.[132; 209] The vortex configurations shown in Fig. 7.12 for samples ($x = 0.36\,\#2$), and ($x = 0.49\,\#1$) are representative of what is observed over the entire crystals. From

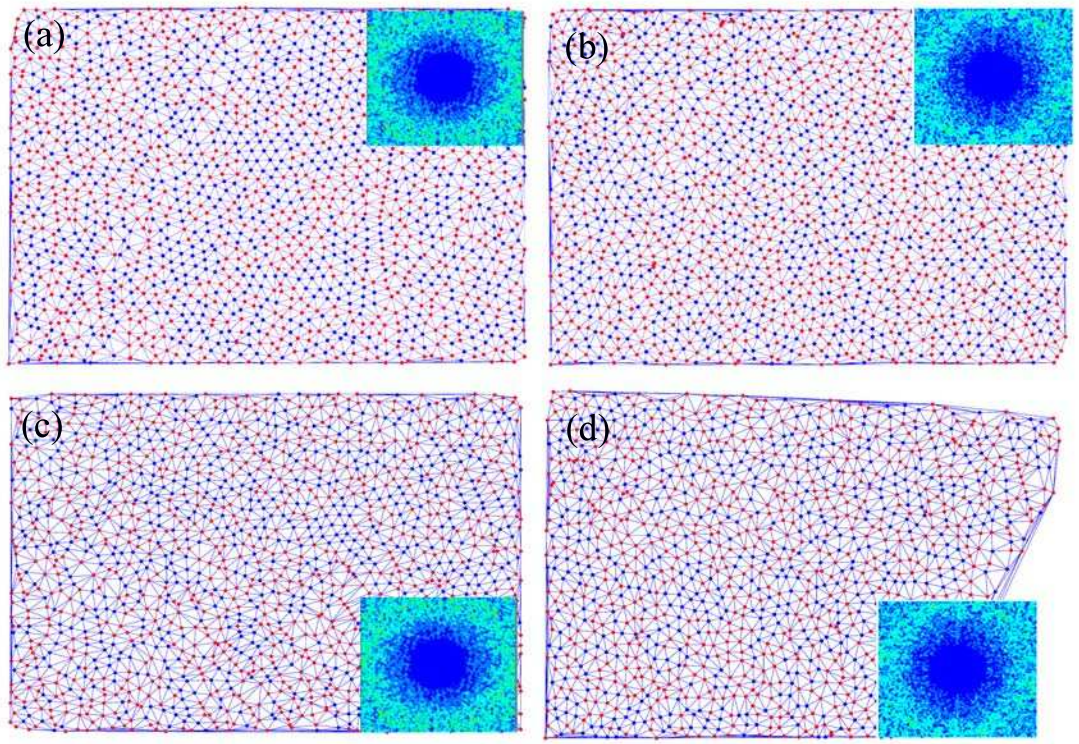

Figure 7.13 Delaunay triangulation of vortex ensembles presented in Fig. 7.12 for $BaFe_2(As_{1-x}P_x)_2$ single crystals ($x = 0.36\,\#2$), (a,c) and ($x = 0.49\,\#1$), (b,d). Blue dots represent vortices with sixfold coordination, while red dots represent differently coordinated vortices.

the decoration images, we obtain, for both crystals, the average value of the magnetic induction as $B_{int} = n_v\Phi_0 \approx 19$ G (with n_v the vortex density). This is 1 G smaller than the applied field during the experiment. In contrast to Ref. [194], there is therefore evidence for Meissner exclusion of the magnetic flux. Moreover, the Meissner current manifests itself as a vortex-free “Meissner belt" along the edges of the decorated crystal ($x = 0.49\,\#1$) as well as near the surface steps indicated with arrows in Figure 7.12. These appear during preliminary cleavage of the samples. Long vortex chains reminiscent of those observed in Ref. [102] are observed in the decoration images of both doping levels, however, these are more pronounced in the crystal ($x = 0.36\,\#2$).

The spatial distribution of vortices in both crystals appears to be more homogeneous than was observed for the Co-doped compound,[206] but there is no evidence for true vortex lattice order. This is brought out by the insets to Figure 7.13 (a,c) and (b,d), which represent the Fourier transforms of the vortex positions in the respective images. The

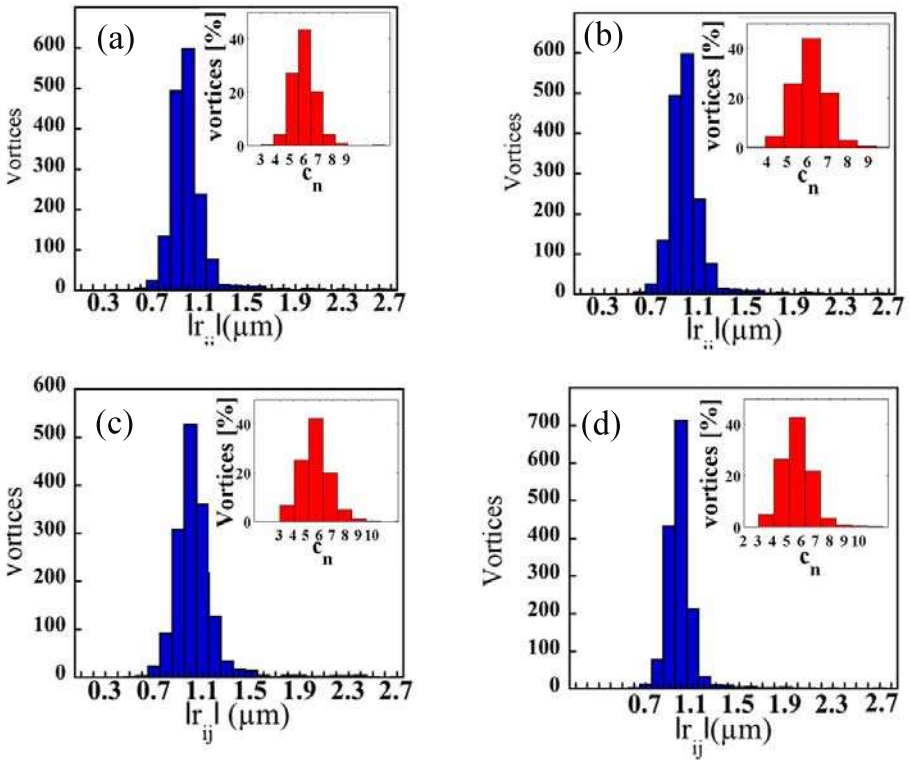

Figure 7.14 Distributions of the nearest neighbor distances in the respective triangulations presented in Fig. 7.13 for $BaFe_2(As_{1-x}P_x)_2$ single crystals ($x = 0.36\,\#2$), (a,c) and ($x = 0.49\,\#1$), (b,d). The insets represent the distribution of the coordination number c_n.

main panels of Fig. 7.13 (a,c) and (b,d) present the Delaunay triangulations of the vortex ensembles in Figure 7.12. The blue dots represent vortices with sixfold coordination, while red dots represent vortices which have a different coordination number. One can see that the vortex structure contains some “ordered" regions with sixfold coordination number. The insets to Figure 7.14 (a-d) reveal that almost half of the vortices have coordination number $c_n = 6$ (46% for the crystal with $x = 0.49\,\#1$, and 43% for crystal $x = 0.36\,\#2$). The main panel represents the distributions of nearest neighbor distances for each vortex. These have a mean value $r_{ij} = 1$ μm, while the lattice parameter for a triangular perfect lattice of the same density is $a_\triangle = 1.075\sqrt{\Phi_0/B} = 1.12$ μm. This shift indicates that vortex pinning induces vortex density fluctuations. Note that the presence of chain-like structures of more closely spaced vortices accentuates the decrease of the mean vortex spacing with respect to what is expected for the triangular lattice.

7.4 Discussion

7.4.1 Pinning energies

In that follows, we adopt the procedure of Ref. [206] to determine the vortex interaction energy. For this, one needs to know the value of λ_{ab} at the temperature T_f at which the vortex ensemble is frozen. As in Ref. [206], we use the information that can be obtained from vortex lines situated near surface steps.[206] Such steps may act as barriers, but, due to the circulation of the Meissner current, they also prevent vortex lines from being situated right at their edge. Inserting the height of the surface step in Fig. 7.12 (a), $h = 1.3$ μm, and the width of the vortex free region close to the step, $u = 1.2$ μm, in Eq. (1) of Ref. [206], the value of the penetration depth at the freezing temperature is graphically estimated as $\lambda_{ab}(T_f) \approx 700$ nm. Using the temperature dependence of λ_{ab}(T) from Ref. [135], this yields the freezing temperature of the vortex ensemble as $T_f \approx 0.87T_c$. Even though vortices are frozen at a relatively high temperature, T_f is lower than the value of 0.95 T_c found in $Ba(Fe_{1-x}Co_x)_2As_2$.

Using the estimated value $\lambda_{ab}(T_f) \approx 700$ nm and the vortex positions extracted from the SEM images in Fig. 7.12, we calculate the vortex interaction energy as

$$\mathcal{E}^i_{int} = \sum_j 2\varepsilon_0 K_0 \left(\frac{|r_{ij}|}{\lambda_{ab}} \right). \tag{7.5}$$

Here $K_0(x)$ is the lowest-order modified Bessel function, and $|r_{ij}|$ is the distance from vortex i to vortex j. For each vortex i, only the neighbors j contained within a radius of $10\lambda_{ab}(T)$ are taken into account. This cutoff radius was chosen after verifying that the interaction energy $\mathcal{E}^i_{int}$ does not change significantly if greater values of j are considered.

Figure 7.15 (a) and Figure 7.16 (a) present the vortex interaction energies as color-coded maps with energy scale normalized by $\varepsilon_0(T_f)$, for the decoration images of Fig. 7.12 (a-d), respectively. The maps show a globally homogeneous distribution, however a number of denser regions exist. The histograms of the interaction energies for maps drawn in Figure 7.15 (c) and 7.16 (c) . Note that the presence of chain-like features with a denser vortex arrangement adds to the width of the histograms for $BaFe_2(As_{1-x}P_x)_2$ single crystal ($x = 0.36\,\#2$). In spite of this, the energy distributions are considerably narrower than those found in $Ba(Fe_{1-x}Co_x)_2As_2$.[206] Furthermore, all distributions are centered about the average $\overline{\mathcal{E}}_{int} \approx 3.5\varepsilon_0$, which corresponds to the interaction energy value (δ-peak) of the Abrikosov lattice for this particular vortex density. Therefore, in contrast to $Ba(Fe_{1-x}Co_x)_2As_2$,[206] no pinning-induced shift of the average value of the energy distribution histogram with respect to the δ-peak value is observed. The large shift found in

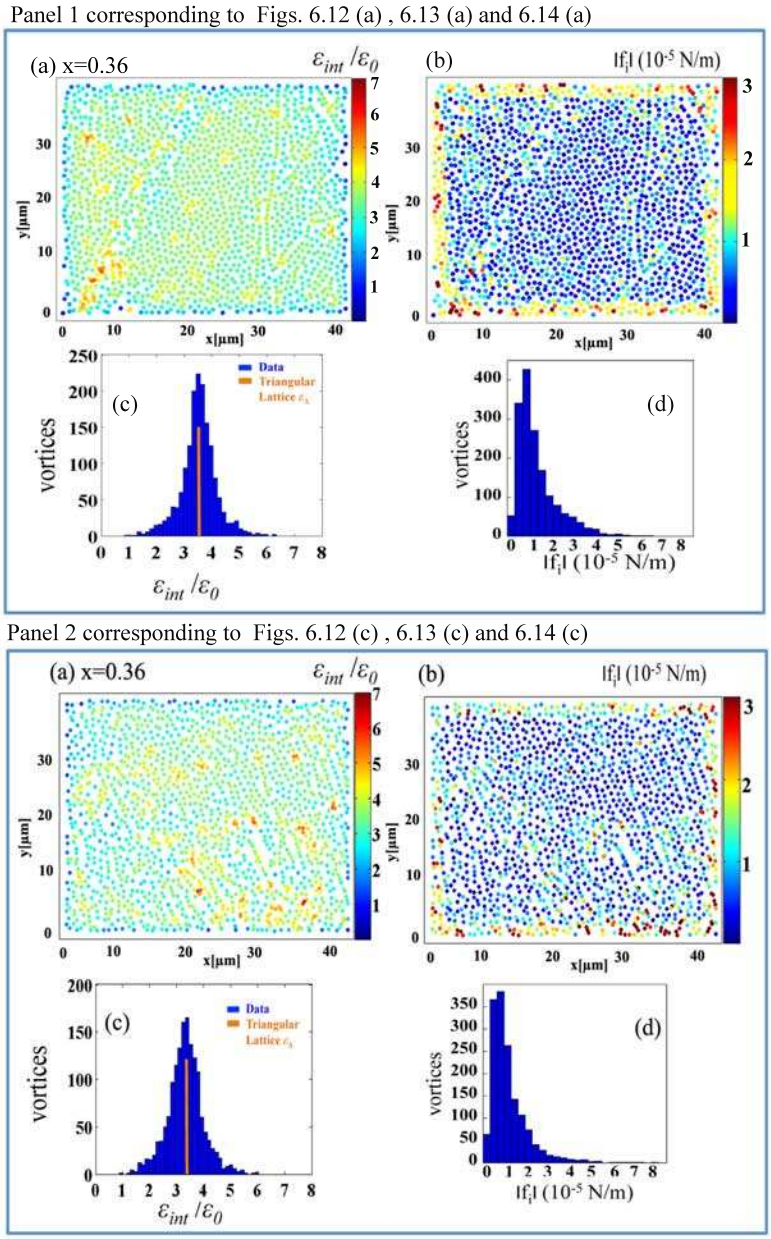

Figure 7.15 $BaFe_2(As_{1-x}P_x)_2$ single crystal ($x = 0.36\,\#2$) (a) Normalized color-coded maps of the vortex interaction energy calculated from the images of Fig. 7.12 (a,c) using Eq. (7.5) , and (b) the modulus of the pinning force (per unit length), calculated from the images of Fig. 7.12 (b,d) using Eq. (7.6). (c) Normalized interaction energy distributions for $BaFe_2(As_{1-x}P_x)_2$ crystals ($x = 0.36\,\#2$). The interaction energy per vortex of the triangular lattice (δ-function) is represented by the central beam in each histogram. (d) Pinning force distributions .

Ref. [206] was interpreted in terms of a large average pinning energy in the vicinity of T_c, which can only be a result of T_c heterogeneity. The absence of such a shift in isovalently substituted $BaFe_2(As_{1-x}P_x)_2$ means that spatial inhomogeneity of T_c is irrelevant for vortex pinning in this material. This can be due to a smoother temperature dependence of the pinning potential, *e.g.* $U_p \propto (1-T/T_c)^2$, or to a larger mobility of vortices due to more pronounced flux creep. Figure 7.17 (a) shows the different temperature dependence of the superfluid density for both the Co and P doped "122" compounds. It is seen that upon approaching T_c, the dependense $n_s(T)$ for P-substitution $BaFe_2As_2$ is much smoother. If $\varepsilon^i_{int} \propto \varepsilon_0 \propto n_s$, this smoother T-dependence in $BaFe_2(As_{1-x}P_x)_2$ explains not only the lack of pinning-induced shift in ε_{int} distribution but also the lower $T_f \sim 0.87 T_c$. The sketch in Figure 7.17 (b) depicting the mean vortex line energy for vortices situated in low T_c and high T_c regions of the crystal that illustrates the situation even large spatial variations of T_c at T_f approaching connot affect the vortex disposition (see Figure 7.17). In fact, the T_c heterogeneity observed within the decorated areas does not lead to qualitatively different vortex arrangements in different parts of the crystal [see Figure 7.1 (b)].

Maps of the modulus of the pinning force for each individual vortex, calculated from

$$\mathbf{f}_i = \sum_j \frac{2\varepsilon_0}{\lambda_{ab}} \frac{\mathbf{r}_{ij}}{|\mathbf{r}_{ij}|} K_1\left(\frac{|\mathbf{r}_{ij}|}{\lambda_{ab}}\right) \tag{7.6}$$

following a similar procedure as used for the determination of $\mathcal{E}^i_{int}$, are shown in Fig. 7.16 (b) and Fig. 7.15 (b) . Here $K_1(x)$ is the first order modified Bessel function. Since the rendered vortices in Fig. 7.12 are in a stationary state at the freezing temperature T_f, the calculated intervortex repulsive force must be balanced by the pinning force. The maps of Fig. 7.16 (b) and Fig. 7.15 (b) therefore represent the minimum local pinning force for each vortex, $\mathbf{min}(|\mathbf{f}_i|)$. The distributions of these, shown in Fig. 7.16 (d) and Fig. 7.15 (d) , allow one to estimate the average pinning force per unit length of vortex. We obtain $|\bar{\mathbf{f}}_i| \sim 3.5 \times 10^{-6}$ Nm^{-1} for crystal ($x = 0.49$ #1) and $|\bar{\mathbf{f}}_i| \sim 4.5 \times 10^{-6}$ Nm^{-1} for crystal ($x = 0.36$ #2). These (high temperature) values are comparable to those found in $Ba(Fe_{1-x}Co_x)_2As_2$.[206] The moduli of the pinning forces mapped in Figure 7.16 (b) and Fig. 7.15 (b) , are reasonably correlated with the interaction energy maps, with the respective probability distributions, shown in Figs. 7.15 (d) and 7.16 (d), being clearly broader for the lower doping level $x = 0.36$.

As in Ref. [206], the ratio of the elementary pinning force per pin f_p, extracted from the $j(B)$ curves in section 7.3.1, and $|\bar{\mathbf{f}}_i|$ obtained from Bitter decoration, allows one to evaluate an upper bound on the average distance $\bar{\mathcal{L}}$ between effective pins in an independent manner. Using the low-temperature value $f_p \sim 8 \times 10^{-13}$ N, our analysis yields $\bar{\mathcal{L}} = 180$

Panel 1 corresponding to Figs. 6.12 (b) , 6.13 (b) and 6.14 (b)

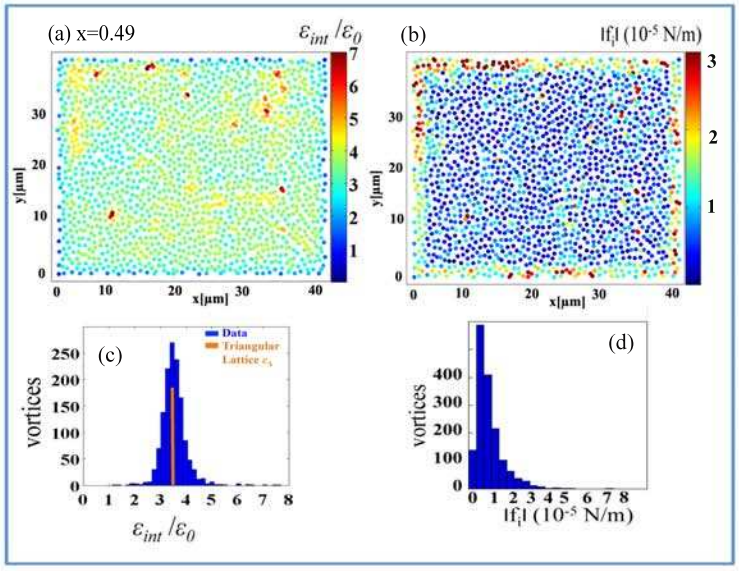

Panel 2 corresponding to Figs. 6.12 (d) , 6.13 (d) and 6.14 (d)

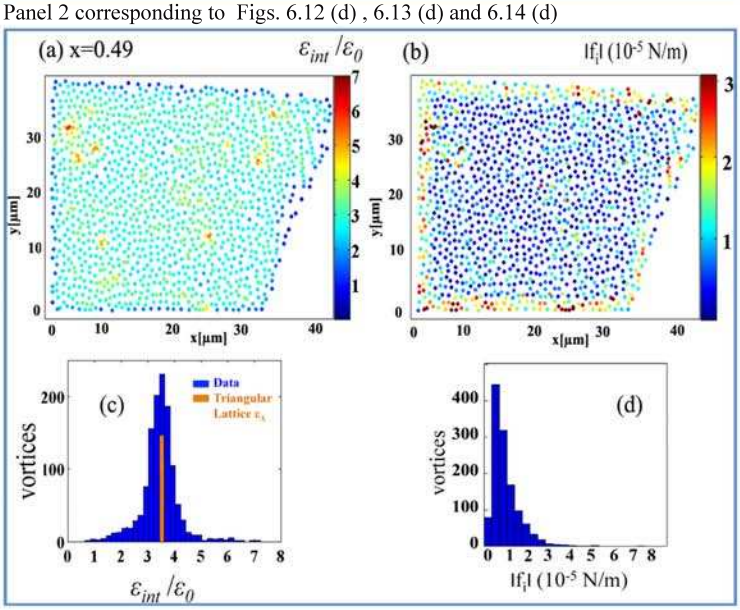

Figure 7.16 $BaFe_2(As_{1-x}P_x)_2$ single crystal ($x = 0.49\,\#1$) (a) Normalized color-coded maps of the vortex interaction energy calculated from the images of Fig. 7.12 (b,d) using Eq. (7.5) , and (b) the modulus of the pinning force (per unit length), calculated from the images of Fig. 7.12 (b,d) using Eq. (7.6). (c) Normalized interaction energy distributions for $BaFe_2(As_{1-x}P_x)_2$ crystals ($x = 0.49\,\#1$). The interaction energy per vortex of the triangular lattice (δ-function) is represented by the central beam in each histogram. (d) Pinning force distributions .

nm for crystal ($x = 0.36\,\#2$) and $\bar{\mathcal{L}} = 230$ nm for crystal ($x = 0.49\,\#1$). Figure 7.11 shows that these numbers correspond reasonably to those extracted from the pinning efficiency.

The increase with doping x of the distance $\overline{\mathcal{L}} = (\varepsilon_\lambda \varepsilon_0/\pi U_p n_i)^{1/2}$ between effective pinning centers is quite remarkable. Among the three possible reasons, one can first invoke the increase with doping of the vortex line energy, due to the decrease of the London penetration depth with increasing x [132]. More rigid vortices that are less able to take advantage of the pinning centers in the material. Second, the density n_i of pinning centers decreases as the doping x increases. If the pinning would be directly linked to the P dopant atoms, this would be rather surprising: usually, disorder levels upon alloying increase, with maximum disorder being attained at 50 % substitution. Nevertheless, the evolution with x is reminiscent of that of the mean free path values extracted by Shishido *et. al.* from de Haas-van Alphen oscillations of the magnetization [97] They reported that the mean free path for the β orbits in $BaFe_2(As_{1-x}P_x)_2$ single crystals increases from $l \sim 170$ Å to 800 Å when P content varies from $x = 0.41$ to 1. Last but not least, the penetration depth anisotropy ε_λ^{-1} decreases as function of x, leading to stiffer vortex lines and less pinning. This hypothesis follows from the doping-dependent evolution of the Fermi surface.[97] Another possible origin of disorder might be the different pnictogen height (P, As) upon increasing the doping level x as reported by Rotter *et. al.* [161]. Given the heterogeneity observed in DMO for all investigated x, and the inconsistence of the evolution of $\overline{\mathcal{L}}(x)$ with the increase in P dopant–induced disorder, we surmise that the main trends in the doping–dependent pinning force and critical currents in $BaFe_2(As_{1-x}P_x)_2$ (see Figs. 7.8 and 7.11) are due to the evolution of the intrinsic superconducting parameters such as the superfluid density $n_s(x) \propto \lambda_{ab}^{-2}(x)$ and the anisotropy parameter $\varepsilon_\lambda(x)$.

The question concerning the origin of strong pinning in $BaFe_2(As_{1-x}P_x)_2$ remains. The irrelevance of T_c–heterogeneity and the incompatible trend with increasing dopant disorder argues against a major role of the P-atoms. We can ascertain that the relevant pinning defects are of extrinsic origin, and have a size and separation on the scale of, perhaps, several to several dozen nm. From Furukawa *et al.*,[144] we know that the disorder can be readily annealed. This qualifies nanoscale defects structures such as vacancy clusters or dislocation loops as possible pinning defects.

One can also compare rendered pinning energy distributions to the high-T_c material $Bi_2Sr_2CaCu_2O_{8+\delta}$ of the same density imaged using Bitter decoration. Figure 7.18 presents a decoration image of the vortex lattice in $Bi_2Sr_2CaCu_2O_{8+\delta}$ at H_a=20 Oe , the Delaunay triangulation of the vortex positions and their Fourier transform. The rendered vortex structure of $Bi_2Sr_2CaCu_2O_{8+\delta}$ appears to be more homogeneous than that presented previously in Fig. 6.10. This is due to the higher value of the applied magnetic field during the

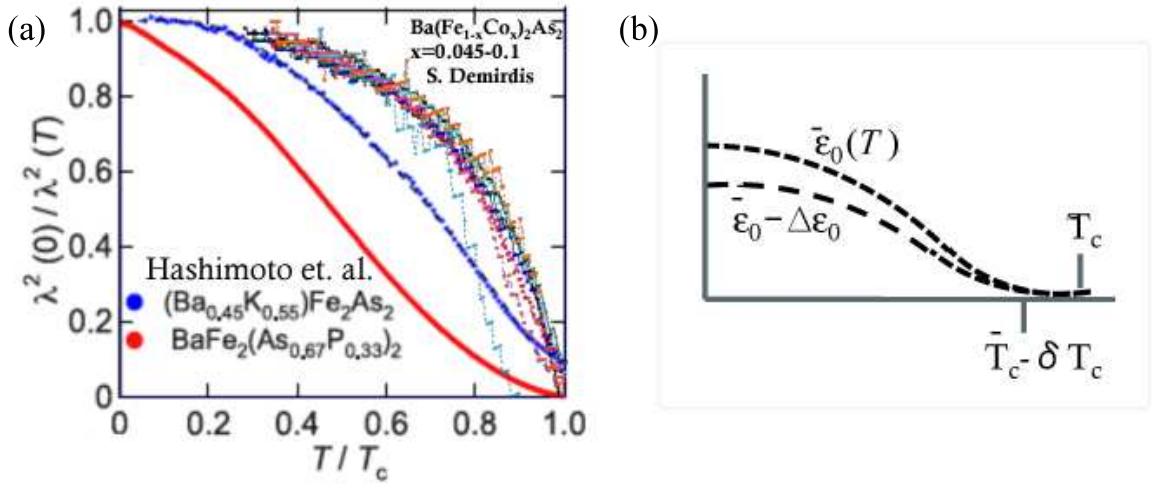

Figure 7.17 (a) Temperature dependence of the superfluid density for $BaFe_2(As_{1-x}P_x)_2$ and $Ba_{1-x}K_xFe_2As_2$ single crystals from Ref. [135] and $Ba(Fe_{1-x}Co_x)_2As_2$ single crystals (see Chapter 8). (b) Sketch of the temperature dependence of mean vortex line energy when approaching T_c.

decoration experiment. The corresponding Fourier transform of the vortex positions shows perfect Bragg spots of the triangular lattice. One can compare the interaction energy distributions of the studied compound $BaFe_2(As_{1-x}P_x)_2$ and $Bi_2Sr_2CaCu_2O_{8+\delta}$ calculated using the low temperature value of the penetration depth $\lambda_L(0) \sim 300$ nm. The comparison of the interaction energy distributions are shown in Figure 7.19. The calculated distributions depend on the value of λ_{ab}, and also on the freezing temperature value of the vortex ensembles. In spite of the lower of T_f/T_c of the vortex ensemble in $BaFe_2(As_{1-x}P_x)_2$ as compared to $Ba(Fe_{1-x}Co_x)_2As_2$, the distributions calculated the sam low temperature value λ=300 nm are still 3-4 times wider than for $Bi_2Sr_2CaCu_2O_{8+\delta}$ at the same field. The mean value of the calculated interaction energies for $BaFe_2(As_{1-x}P_x)_2$ ($x = 0.36$ # 2 and $x = 0.49$ #1) are found to be $\overline{\varepsilon}_{int} \approx 0.6\varepsilon_0$, which is twice that in $Bi_2Sr_2CaCu_2O_{8+\delta}$.

Finally, one can address the clear presence of the chain-like structures in the Bitter decoration images. Since the latter are obtained after field–cooling, and since the $BaFe_2(As_{1-x}P_x)_2$ under consideration show Meissner expulsion, a certain fraction of vortices must exit the material before the vortex ensemble is frozen at T_f. A possible interpretation of the chains is in terms of flow channels for these exiting vortices, the flux in intermediate areas remaining pinned. Indeed, it was shown numerically [40] that, for a

strongly pinned vortex system, vortex flow occurs along only a few preferential paths.

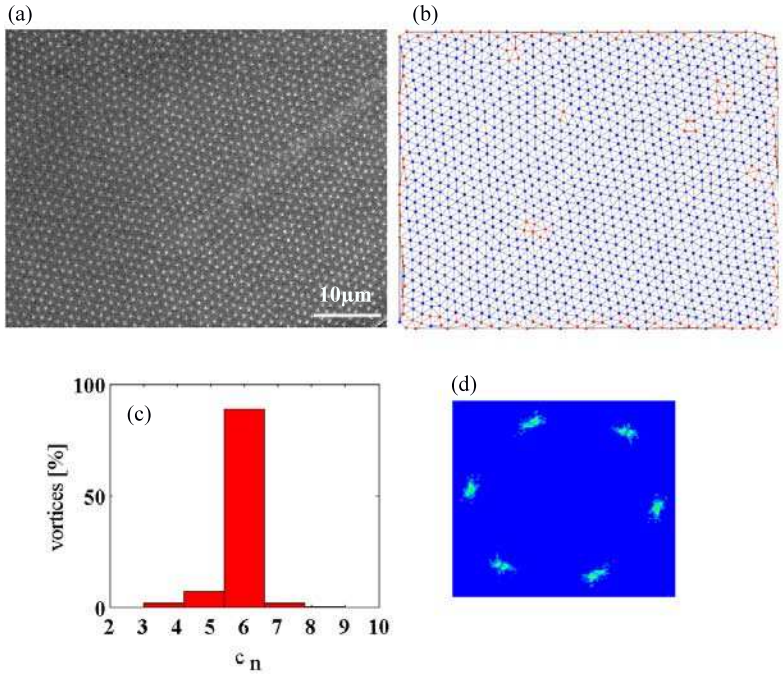

Figure 7.18 (a) Bitter decoration image of $Bi_2Sr_2CaCu_2O_{8+\delta}$ for an applied field H_a=20 G. (b) Delaunay triangulation of the vortex positions. (c) Distribution of the coordination number of vortices, and (d) Fourier transform of the vortex positions.

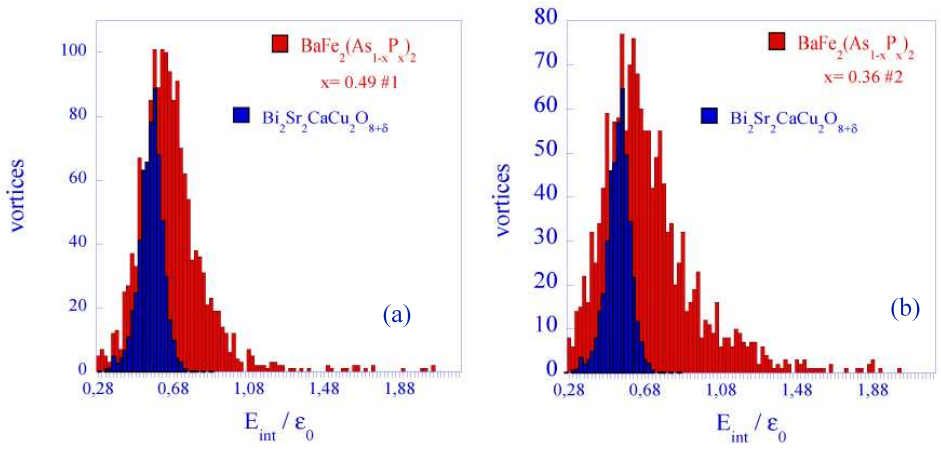

Figure 7.19 Comparaison of the interaction energy distributions calculated using $\lambda(0)$=300nm of $Bi_2Sr_2CaCu_2O_{8+\delta}$ and $Fe_2(As_{1-x}P_x)_2$ with (a) $x = 0.49$ # 1 , (b) $x = 0.36$ # 2.

7.5 Conclusion

We have presented an overview of vortex pinning in single crystals of the isovalently substituted iron-based superconductor $BaFe_2(As_{1-x}P_x)_2$ single crystals, in which we have attempted to correlate the screening (critical) current density as function of temperature, field, and doping x, with vortex lattice structures observed using Bitter decoration. The critical current density in $BaFe_2(As_{1-x}P_x)_2$ is, overall, very well described by the strong pinning scenario of Ref. [43], which allows one to extract elementary pinning forces (of the order of 10^{-13} N) and the distance between effective pins. The latter are of the order of 100 nm, and increase as a function of doping level x. Contrary to Ref. [146], we find no contribution of weak collective pinning to the critical current. Critical current data are rather significantly affected by flux creep, which prohibits one from drawing definite conclusions concerning temperature dependence of pinning.

The decoration images reveal rather less density fluctuations in the vortex ensemble with respect to what was observed in the charge doped $Ba(Fe_{1-x}Co_x)_2As_2$ material. Also, pinning energy and force distributions in $BaFe_2(As_{1-x}P_x)_2$ are much narrower than those in $Ba(Fe_{1-x}Co_x)_2As_2$, and are not shifted with respect to the interaction energy of a triangular vortex lattice of the same density. These observations exclude a role of T_c–variations in determining the frozen vortex state obtained upon field–cooling, and pinning in general. This observation is underscored by the doping–dependence of our results, which seems to be determined by the variation of intrinsic superconducting parameters, rather than by a major role of the P-dopant atoms.

Finally, chain-like vortex configurations were observed in both studied doping levels; we propose that these are due to heterogeneous vortex flow during Meissner expulsion of part of the flux.

7. DISORDER, CRITICAL CURRENT, AND VORTEX PINNING ENERGIES IN ISOVALENTLY SUBSTITUTED $BAFE_2(AS_{1-X}P_X)_2$

Chapter 8

Cavity perturbation technique

8.1 Microwave electrodynamics of superconductors

The loss of the resistance and the Meissner effect in superconductors were first united in a phenomenological picture by the London brothers [73]. Their model proposed the existence of superconducting carriers, with density number n_s, whose electromagnetic response is governed by the London equations. The generalized two fluid model, built on the London model, supposes that besides the superconducting electrons there are normal charge carriers obeying Ohm's law. It assumes that the electromagnetic response of a superconductor can be divided into two components, that due to normal and to superconducting electrons n_n, and n_s respectively. The results of the two fluid model roughly describe the temperature dependence of electromagnetic response but imply that losses vanish at T=0 or ω=0. Further details cannot be deduced from this model. The shortcoming of the two-fluid model were remedied by the theory of Pippard which takes into account the non-local electrodynamics of superconductors in microwave regime, and by the BCS theory which derives the electromagnetic response taking into account the superfluid, but also the quasiparticle excitations across the superconducting gap Δ.

8.1.1 Complex conductivity- Two fluid model

To understand the behavior of an ordinary conductor exposed to electromagnetic fields, the permeability μ and the conductivity σ must be known. A useful form of the conductivity can be obtained from the Drude model, which considers the equation of motion of an electron in an applied electric field:

$$m\dot{\mathbf{v}} = -\frac{m^*\mathbf{v}}{\tau} - e\mathbf{E}. \tag{8.1}$$

The term $-m\mathbf{v}/\tau$ characterizes the electrical resistance through τ, the relaxation time or scattering time, which is the average interval between scattering events for the electron within the conductor. Solving Equation (8.1) for a steady state driving force $-e\mathbf{E}e^{i\omega t}$, noting that the local current density $\mathbf{J}$=-$en\mathbf{v}$ where n is the electron density gives

$$\mathbf{J} = \frac{ne^2\tau}{m}\frac{1-i\omega\tau}{1+\omega^2\tau^2}\mathbf{E}. \tag{8.2}$$

The complex conductivity is identified as,

$$\sigma(\omega) \equiv \sigma_1 - i\sigma_2 = \sigma_0\frac{1-i\omega\tau}{1+\omega^2\tau^2} \tag{8.3}$$

with real and imaginary parts,

$$\sigma_1 = \sigma_0\frac{1}{1+\omega^2\tau^2} \tag{8.4}$$

$$\sigma_2 = \sigma_0\frac{\omega\tau}{1+\omega^2\tau^2}, \tag{8.5}$$

and a dc conductivity σ_0=$ne^2\tau/m^*$. Integrating $\sigma_1(\omega)$ over all frequencies gives a result that is independent of both τ and ω:

$$\int_0^\infty \sigma_1(\omega)\,\mathrm{d}\omega = \frac{\pi}{2}\frac{ne^2}{m^*}. \tag{8.6}$$

Equation (8.6) is a very general oscillator strength sum rule, and is derived from a Kramers-Krönig transformation relating the imaginary and real parts of the response function $\sigma(\omega)$. In the generalized two fluid-model, the total conductivity can be written as coming from two parallel and independent sources, one due to the normal electrons, and other one due to the superconducting electrons:

$$\sigma(\omega) = [\sigma_{1n}(\omega) - i\sigma_{2n}(\omega)] + [\sigma_{1s}(\omega) - i\sigma_{2s}(\omega)]. \tag{8.7}$$

The total electron density ne^2/m^* is temperature independent, and equal to the sum of the normal fluid density n_ne^2/m^*, and the superfluid density n_se^2/m^*. In reality the "normal" conductivity arises from the quasiparticle excitations. In the clean limit, all of the charge carriers are assumed to condense into the superconducting ground state at T=0 such that:

$$\frac{ne^2}{m^*} = \frac{n_se^2}{m^*}(T=0) = \frac{n_ne^2}{m^*}(T) + \frac{n_se^2}{m^*}(T). \tag{8.8}$$

Allowing τ in the superconducting state to go to infinity, one finds from Equation (8.4) that σ_{1s} becomes a δ-function at zero frequency. The δ-function represents the dc conductivity

of the superconductor, and its coefficient is set by Equation (8.6):

$$\sigma_{1s}(\omega) = \frac{\pi}{2}\frac{n_s e^2}{m^*}\delta(\omega). \tag{8.9}$$

At nonzero frequency, σ_s is strictly determined by σ_{2s}. In the same $\tau \to \infty$ limit, σ_{2s} becomes:

$$\sigma_{2s} = \frac{n_s e^2}{m^*\omega} = \frac{1}{\mu_0 \omega \lambda_L^2(T)}, \tag{8.10}$$

which is the same London penetration depth obtained from the second London equation, but now related to σ_{2s}. Remembering the definition of the magnetic penetration depth $\lambda^2 = 1/\mu_0\omega\sigma_2$ reveals that the measurement of λ will differ from $\lambda_L^2 = 1/\mu_0\omega\sigma_{2s}$ if there is a significant contribution to σ_2 from σ_{2n}. Provided $\sigma_{2s} \gg \sigma_{2n}$, a measurement of the magnetic penetration depth yields the superfluid density:

$$\frac{n_s e^2}{m^*\omega} \approx \frac{1}{\mu_0}\frac{1}{\lambda^2(T)}. \tag{8.11}$$

When this is the case, the normal fluid plays a role in screening electromagnetic fields, and cannot be experimentally distinguished from the superfluid. The total integrated quasiparticle conductivity σ_{1n} is again a measure of the normal fluid density n_n:

$$\frac{n_s e^2}{m^*\omega} = \frac{2}{\pi}\int_0^\infty \sigma_{1n}(\omega, T)\,\mathrm{d}\omega. \tag{8.12}$$

8.1.2 Plane waves in superconductors: surface impedance

We will examine the electromagnetic properties of superconductors, by using Maxwell's equations for periodically varying fields, and observing that a wave equation can be develop from them. From the wave equation, a propagation constant and impedance can be extracted. These parameters will then be examined using complex conductivity. For a sinusoidal time dependence and in a region in the space free of static charges, Maxwell's equations are:

$$\vec{\nabla} \times \vec{B} = \mu\left(\vec{J} + j\omega\epsilon\vec{E}\right) \tag{8.13}$$

$$\vec{\nabla} \times \vec{E} = -j\omega\vec{B} \tag{8.14}$$

$$\vec{\nabla}.\vec{B} = 0 \tag{8.15}$$

$$\vec{\nabla}.\vec{E} = 0 \tag{8.16}$$

Taking the curl of Equation (8.14), and one obtains

$$\vec{\nabla} \times \vec{\nabla} \times \vec{E} = -j\omega\vec{\nabla} \times \vec{B} \tag{8.17}$$

Substituting Equation (8.13) , and introducing the complex conductivity σ one has

$$\vec{\nabla} \times \vec{\nabla} \times \vec{E} = -j\omega \left(\sigma + j\omega\epsilon\right) \vec{E} \tag{8.18}$$

where σ is complex in the case of a superconductor. Using the vector identity

$$\vec{\nabla} \times \vec{\nabla} \times \vec{E} = \vec{\nabla}(\vec{\nabla}.\vec{E}) - \Delta\vec{E} \tag{8.19}$$

where $\vec{\nabla}(\vec{\nabla}.\vec{E}) = 0$ (no free charges), and Equation (8.15) , one has

$$\vec{\nabla} \times \vec{\nabla} \times \vec{E} = -\Delta\vec{E} \tag{8.20}$$

Substitution into Equation (2.7) gives

$$\Delta\vec{E} = j\omega\mu(\sigma + j\omega\epsilon)\vec{E}, \tag{8.21}$$

the wave equation for the electric field. A similar equation exists for $\vec{H}$ and is calculated in a similar way. This equation can be rewritten as

$$\Delta^2\vec{E} = \gamma^2\vec{E}, \tag{8.22}$$

where γ is the propagation constant. This equation is very general, and will be used to obtain a better understanding of the propagation of electromagnetic waves in superconductors. This will now be simplified by assuming the case of plane waves.

For a plane wave traveling in the z direction the simplest expressions for the electromagnetic fields are

$$E_x = E_x^0 e^{-j(k_z z - \omega t)} e^{-\gamma z} \tag{8.23}$$

$$H_y = H_y^0 e^{-j(k_z z - \omega t)} e^{-\gamma z}. \tag{8.24}$$

Here the electric field is directed in the x direction and the magnetic field at a right angle to this in the y direction. The variation with time is $e^{i\omega t}$, but this has been dropped to simplify the expressions. To verify that these equations are solutions to the wave equation, they can be substituted into Equation (8.21) If this is done, it can be easily shown that

the propagation constant is given by

$$\gamma = \sqrt{k_z^2 + j\omega\mu(\sigma + j\omega\epsilon)} \tag{8.25}$$

This expression can be written as

$$\gamma = -j\beta \tag{8.26}$$

Defining the propagation constant in this manner allows separate consideration of the losses (real part) and the phase (imaginary part) of the electromagnetic wave. It is interesting to note that $\vec{E}$ and $\vec{H}$ are independent for the plane waves under consideration, and are connected through Faradays law. For plane waves, Faraday's law becomes

$$-j\omega\mu H_y = \frac{\partial E_x}{\partial z} \tag{8.27}$$

Substituting $\vec{E_x}$ and $\vec{H_y}$ gives

$$Z_s = \frac{E_x}{H_y} = \frac{j\omega\mu}{\gamma} = \sqrt{\frac{j\omega\mu}{\sigma + j\omega\epsilon}} \tag{8.28}$$

This is the intrinsic impedance or surface impedance of the material, which is very general and can be considered to be any material at the moment. Intrinsic impedance is used for any material, while the surface impedance is usually used for good conductors. In the case of superconductors, σ has to be replaced by the complex conductivity $\sigma_1 - j\sigma_2$, and $k_z = \omega/c$. Hence the propagation constant becomes:

$$\gamma = \sqrt{\omega\mu\sigma_2\left(1 + j\frac{\sigma_1}{\sigma_2} + \frac{\epsilon}{\mu\sigma_2}\right)} \tag{8.29}$$

We will now assume $\omega\epsilon/-\sigma_2$ to be very small which is the situation when the displacement current is much less than the super-current in a superconductor. This is always true in a superconductor at low temperature because of the high conductivity. If one assumes that at temperatures below the transition temperature $\sigma_2 \gg \sigma_1$, a series expansion gives, for the expression of the propagation constant

$$\gamma = \sqrt{\omega\mu\sigma_2(1 + j\frac{\sigma_1}{2\sigma_2})}. \tag{8.30}$$

The real part of γ is the attenuation coefficient, which can be written as

$$\gamma = \sqrt{\omega\mu\sigma_2}. \tag{8.31}$$

This represents the decay of the amplitude of the electromagnetic wave as it travels in a superconductor. This characteristic depth is equivalent of the skin depth for superconductors and is again given by the penetration depth

$$\lambda = \frac{1}{\sqrt{\omega\mu\sigma_2}} \tag{8.32}$$

The imaginary part of the propagation constant from Equation (8.30) is ,

$$\beta = \sqrt{\frac{\omega\mu\sigma_1^2}{4\sigma_2}}. \tag{8.33}$$

Hence the velocity of an electromagnetic wave can be calculated as ,

$$c = \frac{\omega}{\beta} = \sqrt{\frac{4\omega\sigma_2}{\mu\sigma_1^2}}. \tag{8.34}$$

Now, using the expression for the surface impedance for a superconductor given by Equation (8.28), and by substituting σ by the complex conductivity $\sigma_1 + j\sigma_2$, one gets

$$Z_s = \sqrt{-\frac{\omega\mu}{\sigma_2}}\left(-\frac{\sigma_1}{j\sigma_2} + 1 - \frac{\omega\epsilon}{\sigma_2}\right)^{-1/2} \tag{8.35}$$

As described above the displacement current term can be neglected in the quasi-static limit $\omega\epsilon \ll \sigma_2$, i.e. $\frac{j\omega\epsilon}{-j\sigma_2}$. If we also consider $\sigma_2 \gg \sigma_1$ we get

$$Z_s \approx \sqrt{\frac{\omega\mu}{\sigma_2}}\{j + \frac{\sigma_1}{2\sigma_2} + ...\} \tag{8.36}$$

Starting from this expression it is possible to separate the surface impedance in terms of resistive

$$R_s = \frac{\sigma_1}{2\sigma_2}\sqrt{\frac{\omega\mu}{\sigma_2}} \qquad = \frac{\omega^2\mu^2\sigma_1\lambda^3}{2} \tag{8.37}$$

and reactive parts

$$X_s = \sqrt{\frac{\mu\omega}{\sigma_2}} \qquad = \omega\mu\lambda \tag{8.38}$$

8.2 BCS theory: penetration depth $\lambda(T)$ and surface resistance R_s

The BCS theory [111] provides the quantum description of the superconducting state needed for a microscopic understanding of superconducting properties such as the surface impedance. The BCS theory describe the correct condensate wave function, which is a linear combination of two electron states , or Cooper pairs of electrons linked with opposite spin and momenta. This coherence between Cooper pairs exists over a distance $\xi_0 = \hbar v_F/\pi\Delta(0)$, called the BCS coherence length. As a consequence of the condensated state, there is an energy gap $2\Delta(T)$ in the one electron excitation spectrum. The single electron excitations are called quasiparticles, and their density of energy is illustrated in Figure 8.1 . The density of thermally excited quasiparticles of energy ε is proportional to the density of states times the Fermi distribution function $f(\varepsilon) = 1/(e^{\varepsilon/kT} + 1)$.

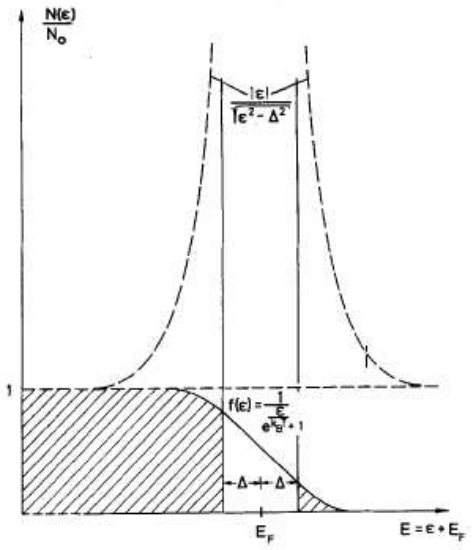

Figure 8.1 The normalized density of states $N(\varepsilon)$ of a superconductor versus the energy ε referred to the Fermi energy $E_F(\varepsilon = E - E_F)$, $\Delta = \Delta(T)$ is the gap parameter. [119]

8.2.1 Penetration depth

Below we use the description of the condensed state and quasiparticle excitation spectrum to describe the surface impedance. Since the complex conductivity $\sigma(\omega)$ in the two fluid model is an approximation, the description is restricted to frequencies well below the energy gap frequency ω_g. In the BCS description, the complementary regime where ω

is comparable to the gap frequency ω_g is taken into account. On the basis of the BCS theory, one can directly obtain the expressions for the interaction of a superconductor with a transverse electromagnetic field is represented by the vector potential $\mathbf{A}$. The kinetic particle momentum represented by $\mathbf{p}$, is, in an electromagnetic field, supplemented as $\mathbf{p}$=$\mathbf{v}$+$e\mathbf{A}$. One can describe $\mathbf{A}(\mathbf{r})$ in terms of spatial Fourier components $\mathbf{a}(\mathbf{q})$, where $\mathbf{q}$ is the wave vector. Since we are interested in weak fields, i.e., in the linear response, it is sufficient to expand the operator for the kinetic energy, $(\mathbf{p} - e\mathbf{A})^2$ to first order in field. This yields the interaction Hamiltonian

$$H = \frac{e\hbar}{m} \sum_{k,q} \mathbf{k}.\mathbf{a}(\mathbf{q}) c^*_{k+q,\sigma} c_{k,\sigma}; \tag{8.39}$$

the corresponding operator for the current density is given by

$$\mathbf{J} = -\frac{ne^2}{m}\mathbf{a}(\mathbf{q}) - \frac{e\hbar}{m} \sum_{k} \mathbf{k}.c^*_{k-q} c_k. \tag{8.40}$$

Equation (8.40) can be evaluated in terms of $\mathbf{a}(\mathbf{q})$ to yield a generalized current-field relation,

$$\mathbf{J}(\mathbf{q},\omega,T) = \frac{-1}{\mu_0} K(\mathbf{q},\omega,T).\mathbf{a}(\mathbf{q},\omega). \tag{8.41}$$

Since the electric field E is given by $\mathbf{E} = -i\omega\mathbf{A}$, both the conductivity σ, and the surface impedance Z_s can be expressed in terms of the kernel K:

$$\sigma = \sigma_1 - i\sigma_2 = \frac{-i}{\omega\mu_0} K(\mathbf{q},\omega,T) \tag{8.42}$$

$$Z_s = R_s + iX_s = \frac{i\omega\mu_0}{[K(\mathbf{q},\omega,\mathbf{T}]^{\mathbf{1/2}}} \tag{8.43}$$

The London penetration depth can be obtained from the response kernel $K(\mathbf{q},\rightarrow 0,\omega = 0,T)$ for fields varying slowly in space. The first term in Equation (8.40) then reduces to the London equation with the notation $K_L(0) = 1/\lambda_L^2$; according to our earlier results, $\sigma_2 = 1/\omega\mu_0\lambda_L^2$, and $X_s = \omega\mu_0\lambda_L$. The temperature dependence of the penetration depth (and equivalently that of σ_2) is therefore determined by $K(T) = 1/\lambda_L^2(T)$. Following the analysis given in [164], resulting in the the local limit

$$\frac{\lambda_L^2(0)}{\lambda_L^2(T)} 1 - 2\int_{\Delta}^{\infty} dE \frac{N_s(E)}{N(0)} \left(-\frac{\partial f(E)}{\partial E}\right). \tag{8.44}$$

In the BCS theory for s-wave superconductors, the gap Δ(T)=Δ can be considered constant in the sense that i.e. if does not depend on the direction in the reciprocal space. At temperatures T<T_c/2, the integral Equation (8.44) can be simplified, giving for the reduced change in the penetration depth [119]. One finds that the low temperature dependence of λ is determined by the topology of the possible nodes of the superconducting gap function.

$$\frac{\lambda(T)-\lambda(0)}{\lambda(0)} \propto \begin{cases} \sqrt{\frac{\pi\Delta}{2k_BT}}\exp\left(-\frac{\Delta}{k_BT}\right) & \text{nodeless gap function} \\ T & \text{line node and 3D Fermi surface} \\ T^2 & \text{point node and 3D Fermi surface} \end{cases}$$

The exponential temperature dependence uniquely reflects the singularity in the BCS density of states, which is convoluted in the integral in Equation (8.44) with the bell shaped weight function $\partial f/\partial E$.

The expressions above are correct only for the case of a s-wave superconductor. However the penetration depth in general also depends on the specifities of the crystal anisotropy and/or the superconducting gap $\Delta(k)$ anisotropy. Chandrasekhar *et.al.* [24] derived the complete expression for the superfluid density by taking into account these two possible anisotropies,

$$\rho_{Si}(T) = \frac{\mu_0 e^2}{2\pi^3\hbar}\left\{\oint dS_F \frac{\vec{v_{Fi}}.\vec{v_{Fi}}}{v_F} - \oint dS_F \frac{\vec{v_{Fi}}.\vec{v_{Fi}}}{v_F}\int_{\Delta_k}^{\infty} dE_k \left(-\frac{df(E_k)}{dE_k}\right)\frac{E_k}{(E_k^2-\Delta_k^2)^1/2}\right\}. \tag{8.46}$$

In this expression above the first term corresponds to the total electronic density in the i direction, from which one subtracts the excitations above the superconducting gap Δ. In order to understand the signification of the "total electronic density" one considers the plasma frequency ω_{Pi} (in cgs units),

$$\omega_{Pi}^2 = \oint dS_F \frac{\vec{v_{Fi}}.\vec{v_{Fi}}}{v_F} = \frac{4\pi\rho_S e^2}{m_{ii}}. \tag{8.47}$$

This gives the anisotropy of the electronic transport, and therefore, the effect of the anisotropy via the plasma frequency, while the gap anisotropy is in the term Δ_k.

8.2.2 Surface resistance

Mattis and Bardeen, and independently Abrikosov, Gorkov, and Khalatnikov derived analytical expressions for the complex conductivity within the framework of the BCS theory

[55] on the basis of Equations (8.40), and (8.4), in the low frequency limit, $\hbar\omega \ll \Delta$,

$$\frac{\sigma_1}{\sigma_n} = \frac{2}{\hbar\omega}\int_{\Delta}^{\infty} dE \frac{[E(E+\hbar\omega)+\Delta^2]|f(E)-f(E+\hbar\omega)|}{\sqrt{E^2-\Delta^2}\sqrt{(E+\hbar\omega)^2-\Delta^2}} \tag{8.48}$$

and

$$\frac{\sigma_2}{\sigma_n} = \frac{1}{\hbar\omega}\int_{\Delta-\hbar}^{\Delta} dE \frac{[E(E+\hbar\omega)]|1-2f(E+\hbar\omega)|}{\sqrt{\Delta^2-E^2}\sqrt{(E+\hbar\omega)^2-\Delta^2}}. \tag{8.49}$$

These latter two equations are only valid in the dirty ($l/\xi_0 \ll 1$) or the extreme anomalous ($\lambda_L/\xi_0 \ll 1$) limits [164], but the expressions seem to contain qualitatively the main features characteristic of all BCS superconductors.

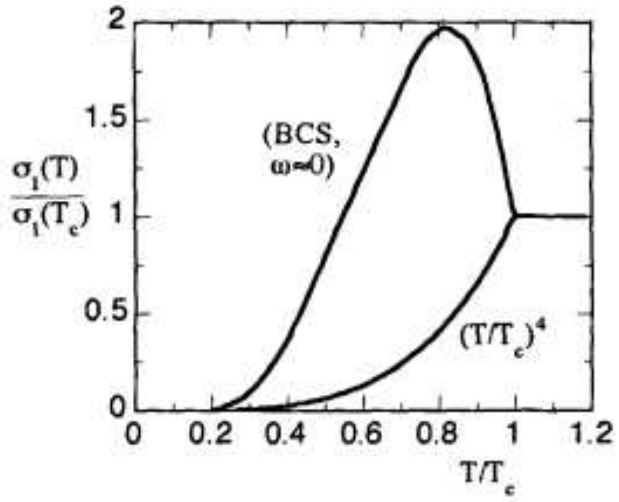

Figure 8.2 Temperature dependence of the quasiparticle conductivity $\sigma_1(T)/\sigma_1(T_c$ evaluated from BCS theory, in comparison with the expectation from the two fluid model [164].

Physically the conductivity peak in Figure 8.2 results from the phase coherent superposition of the occupied quasiparticle states due to the pair interaction:The scattering, creation or annihilation of quasiparticles reflects the coherence in the scattering, creation or annihilation of the pair constituents. This coherence is not contained in the two fluid model, resulting in the obvious difference represented in Figure (8.2) . When the temperature decreases below T_c, more and more quasiparticle condensate in the superconducting state. The conductivity $\sigma_1(T)$ vanishes, as discussed in Ref. [119] for $T < T_c/2$ on the

basis of the following expression,

$$\sigma_1 \propto \frac{1}{k_B T} ln(\frac{4k_B T}{\hbar\omega}) exp(-\frac{\Delta}{k_B T}). \tag{8.50}$$

Comparing Equation (8.2) with the two fluid formulation, the exponential term can be regarded as a Boltzmann factor, which describes the vanishing number x_n on unpaired charge carriers as the thermal energy drops below the gap energy. However , the phase coherence of the quasiparticles violates the two fluid assumption $x_n + x_s = 1$ at temperatures close to T_c.

8.3 Experimental setup and working principle

For the surface resistance measurements by the cavity perturbation technique we realized the conception of a new cryostat. The superconducting Nb cavity was fabricated in the IFPAN (Institute of Physics, Polish Academy of Sciences) in Poland was and provided to us by Dr. Gierloswki. All the RF (wave guides, coaxial cables) and the cryogenic components were realized in LSI, in collaboration with the technical team specialized in low temperatures. The details related to the realization of the entire cryostat are given in Appendix B.

Figure 8.3 shows a drawing of the cryostat, realized in our laboratory, that I used for the cavity perturbation measurements. The SRP-052A model Sumimoto Heavy Industries (SHI) pulsed-tube refrigerator mounted on the cryostat provides the necessary power to cool down the entire system. In Figure 8.3 the copper braid connections between the two cold stages of the pulse tube and the 50 K, and 4 K plates of the cryostat are represented. The cryostat is cooled down sequentially from 300 K to 50 K and then to 4.2 K; each stage is protected from thermal radiation by gilded shields. Therefore it is possible to reach 4.2 K on the inner plate of the cryostat, hosting the He gas switch assembly, the sample holder, and the Nb cavity . The gas switch assembly is the most important part of the cryostat where the proper cavity perturbation measurement process and the cooling process necessary for it take place. This process is described in details in the following section. A cylindrical cavity made out of the conventional superconductor niobium is used. The sample is inserted into the cavity using a sapphire rod, which also serves as a thermal connection to the Cernox thermometer and the heater mounted on the sample holder. Figure 8.7 shows the cylindrical Nb cavity used for the measurements presented in this work. The microwave cavity can be considered as a two port system, where microwaves are sent down transmission lines (coaxial cables, and wave guides) which couple to the

microwave cavity. The interaction of the superconducting sample with the cavity field leads to changes in the response of the system. We consider perturbations from the temperature changes of the sample. In this case the changes in the surface impedance are easily related to the changes in the center frequency f_0, and the quality factor Q_0, of the cavity.

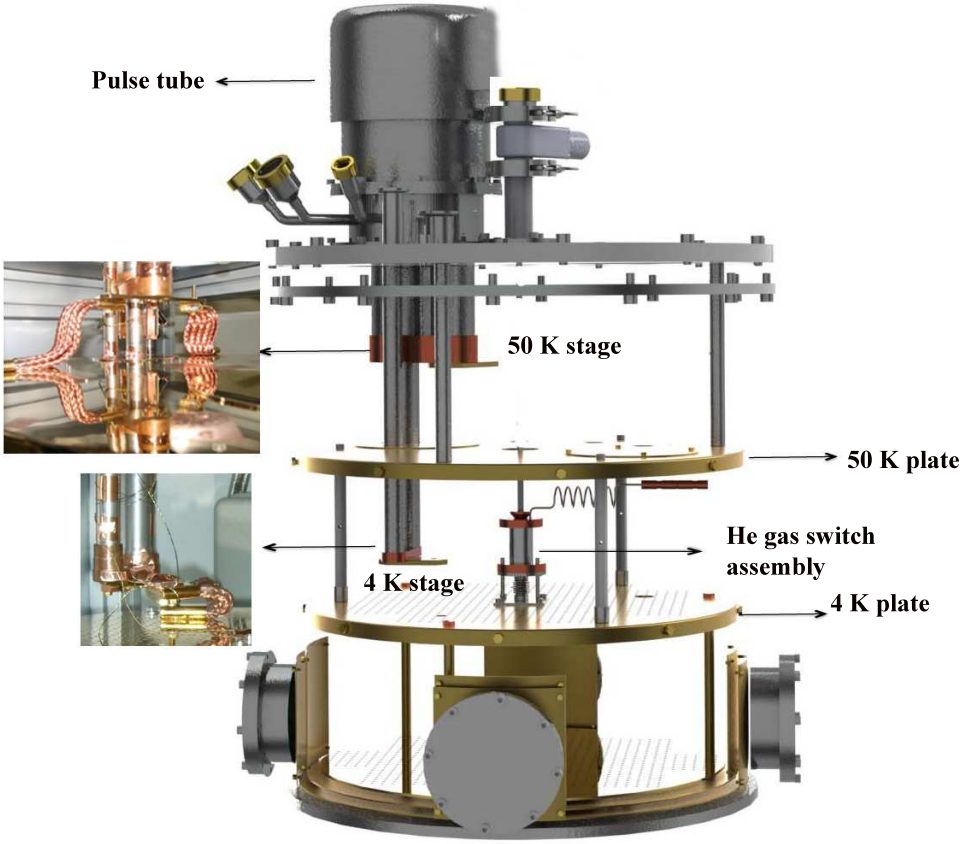

Figure 8.3 A drawing of the cryostat used for the cavity perturbation measurements.

8.4 He gas switch

The He gas switch assembly is represented in Figure 8.4. Its function is to couple or decouple thermally the sample holder from the Nb cavity. In particular one needs to be able to cool down the sample to 5 K, and to heat it without heating the cavity. The switch is typically composed of two homocentric stainless steel tubes with two copper ends, and a charcoal pump which adsorbs and desorbs the He gas as a function of temperature. A heater is mounted on the charcoal pump to provide the necessary amount of power to

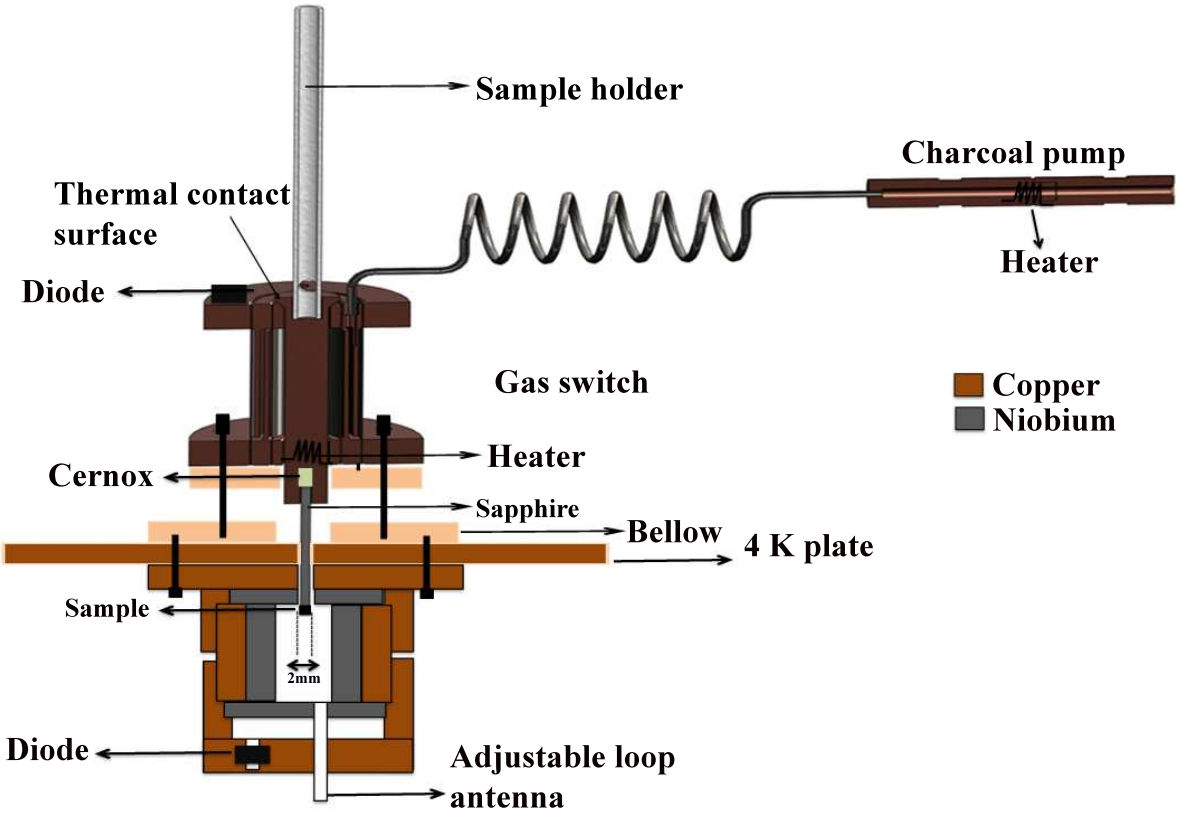

Figure 8.4 Drawing of the assembly, the gas switch, the sample holder, and the Nb cavity.

desorb the He gas. The top copper end of the switch has a conical shape in order to accommodate the sample holder, which needs a perfect thermal contact. The bottom part of the switch perfectly fits with the bellows mounted between the switch and the 4 K plate (see Figure 8.5). The bellow is screwed to the Nb cavity through the 4 K plate, thus keeping the bottom part of the switch at low temperature. For this, copper braids are mounted between the 4 K plate and the bottom of the switch (see Figure 8.5) .

A schematic representation of the Nb cavity (T_c= 9 K) is shown in Figure 8.4. The cavity has a cylindrical shape, and is made of copper and niobium pieces. The dark brown pieces shown in that figure are made of copper and the gray parts are of niobium. The length of the coupling microwave antenna is adjustable. The sapphire end of the sample holder is inserted into the cavity through a 2 mm diameter hole situated in the top cover of the cavity. This is the side which is connected to the 4 K plate (see Figure 8.5). The conduction through the inner stainless steel tubes, and/or the He gas is discussed in the

Appendix B.

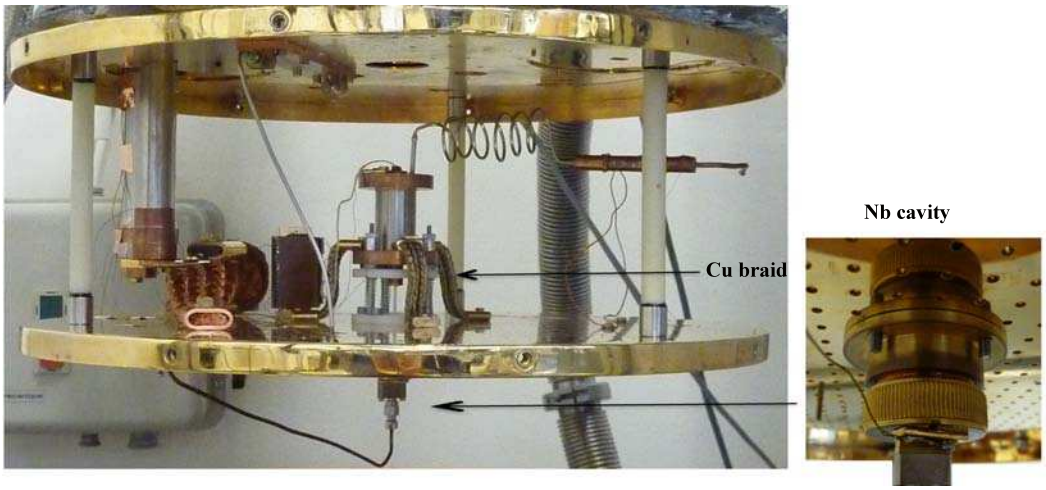

Figure 8.5 A photo of the real ensemble of the gas switch mounted on the 4K plate inside the cryostat

The realized configuration allows one attain 4.2K at the bottom of the gas switch. Our goal in this design is to reach the lowest temperature at the end of the sample holder, which is in thermal contact with the top of the switch (see Figure 8.6). When the He gas switch is in the "off mode" (without He gas), the sample , through conduction through the stainless steel tubes can only reach a temperature of 11 K. In order to reach lower temperatures, one needs to go to the "on mode". He gas is then desorbed from the charcoal pump into the space between two cylindrical walls of the switch. The charcoal pump, which is connected to the switch via a thin stainless steel tube, contains small grains of active charcoal which have the property to absorb He gas at low temperatures and desorb it when is heated above 20K (see Figure 8.5). In our conception, we need to use both properties of the active charcoal. Therefore we thermalize the pump on the 4 K plate by connecting it with copper wires and we install an heater on it for the desorption of He gas above 20K. By using the switch "on mode" of our design, one reaches 6 K at the sapphire end of the sample holder. From this temperature we use the heater mounted on the sample holder in order to sweep the whole temperature range necessary for a measurement.

Figure 8.6 shows a photograph of the sample holder. One can see the upper conical shape which fits snugly with the top part of the switch, the Cernox thermometer mounted close to the sapphire rod on which we glue the sample, and the heater that we use to increase the temperature above 6 K. Calculations related to the design of the He gas switch are discussed in the Appendix B.

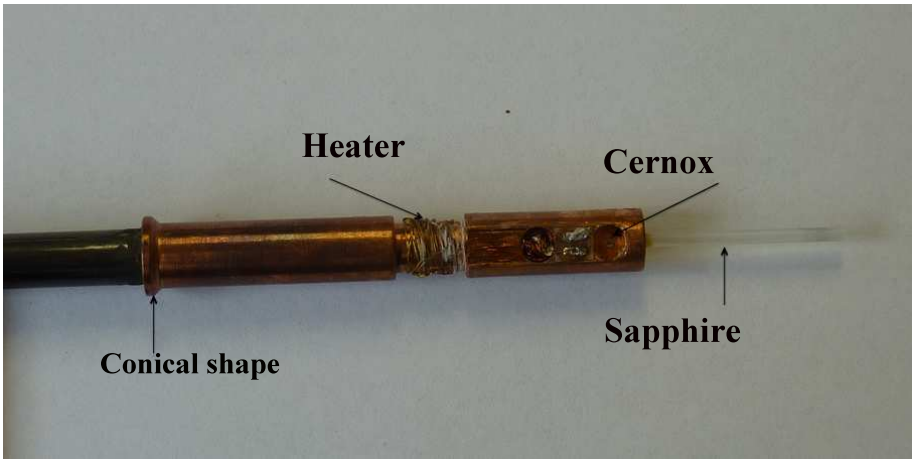

Figure 8.6 A photograph of the sample holder

8.4.1 Cavity measurement process

We start the measurement process typically by pumping the system vacuum to $p = 1 \times 10^{-3}$ mbar, whence we launch the cryocooler. After 10 hours, a vacuum of $P = 3 \times 10^{-7}$ m bar, is reached due to i.e. the low temperature conditions required for the measurement. The second step is to put the switch to switch "on mode" (He gas inside) by applying a voltage of 1.5 volt on the heater of the charcoal pump (see Figure 8.8). The latter process takes half an hour to cool down the sample to 6 K.

The experiments at 26 GHz were performed using the cavity shown in Figure 8.7. The coaxial lines, and the wave guides were used to couple inductively through the adjustable cavity antenna. The cylindrical Nb cavity is operated in the TE_{011} mode, and has superconducting Nb inner surfaces as shown in Figure 8.7, which yield high quality factor Q. The sample, glued on the sapphire rod using with n-nonadecane, is inserted into the cavity up to the distance where optimum coupling is established (the maximum of the amplitude of the magnetic field). This location gives the maximum shift in the quality factor and the resonance frequency if the temperature of the sample is varied. The sample temperature is controlled using a Lakeshore 340 temperature controller and the heater on the sample holder (see Figure 8.8). The measurements are performed in the one-port S_{11} reflection mode. A schematic view of the measurement procedure is represented in detail in Figure 8.8. The reflected power (wave) is received by the network analyzer HP 8510C, where the resonance tracé is represented. All the datas points of the resonance loop recorded for each temperature are saved on the computer hard disk via a Labview interface for the network analyzer (see Figure 8.8).

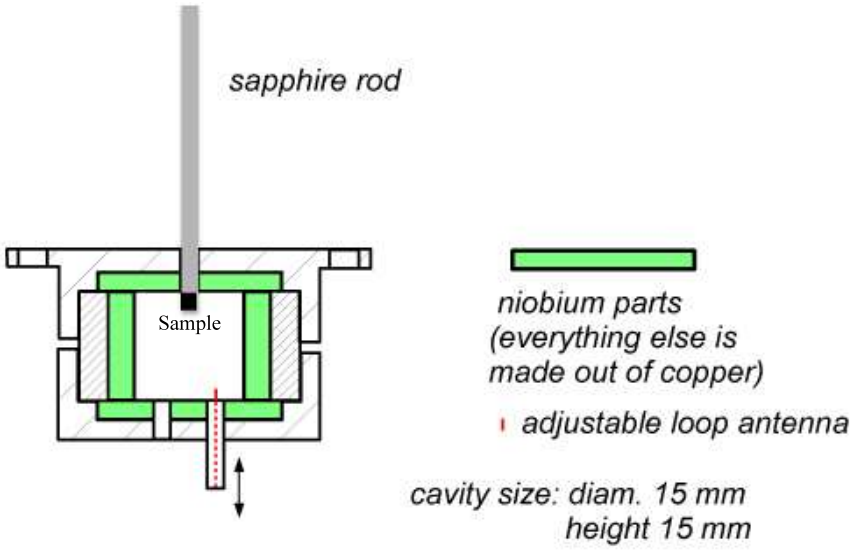

Figure 8.7 Schematic representation of the Nb cavity, and the sapphire rod.

8.5 Superconducting microwave cavity perturbation

The cavity perturbation technique exploits the manner in which the introduction of a sample changes the resonant properties of a cavity. This method depends on the shape of the cavity which supports the resonant electromagnetic modes. A cylindrical electromagnetic cavity can supports a number of electromagnetic resonant modes, the nature and the frequency of which depend on the size and the shape of the cavity. One typically distinguishes the transverse electric modes (TE), in which the microwave electric field in parallel to the cavity equator, and transverse magnetic modes (TM), in which the magnetic field is parallel to the equator. The mode indices indicate the number of nodes in the vertical and azimutal directions. When we operate in the TE_{011} mode, there is an electric field node and a magnetic field antinode along the central axis of the cavity. At a given mode all electromagnetic (EM) energy fed to the cavity is stocked in the cavity. Therefore the cavity appears as an EM sink in a reflection measurement. The width Δf of the absorption dip, as function of frequency is a measure of the cavity quality factor (Q-factor) which is given by,

$$Q = 2\pi \frac{\text{peak energy stored}}{\text{energy dissipated per cycle}} = \frac{f}{\Delta f} \tag{8.51}$$

where, for a transmission geometry, Δf is the full width at half maximum of the

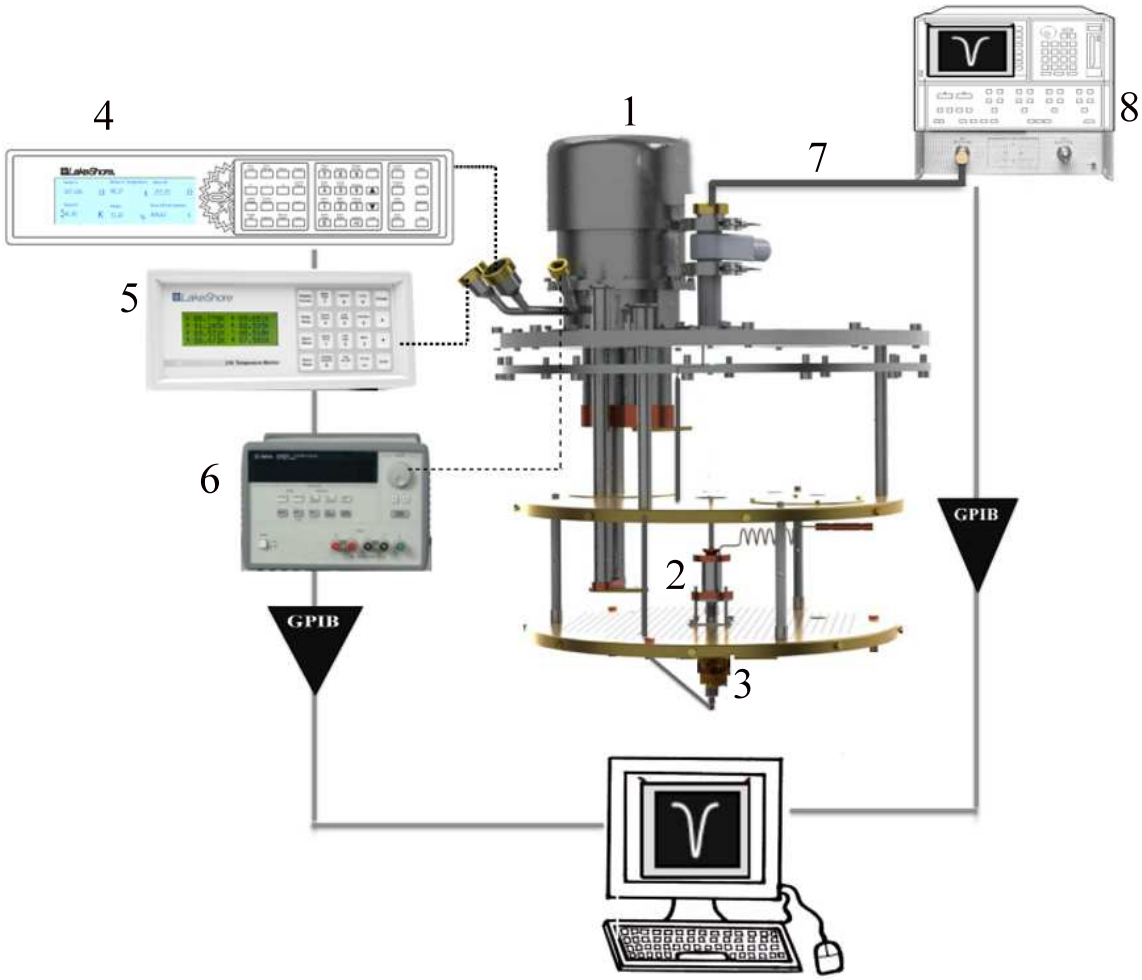

Figure 8.8 Schematic representation of the cavity measurement system: 1. cryostat , 2. switch assembly , 3. Nb cavity , 4. Lakeshore 340 temperature controller for monitoring the sample temperature , 5. Lakeshore 218 temperature monitor for monitoring the temperature at different stages of the cryostat , 6. Agilent dc power supply for the switch , 7. Rf coaxial cable , 8. HP 8516A network analyzer. Two wave guides are situated on the 50 K, and 4 K plate to ensure the coaxial cable connection for the microwave transmission line.

transmitted power. For an empty cavity, the energy dissipated per cycle is primarily due to the dissipation of energy by the currents in the cavity walls. To maximize the cavity Q, the copper cavity walls are coated with Nb. This is a conventional superconductor with a transition temperature $T_c = 9$ K. In our cavity measurement the walls should be made of

a very low resistance material.

Now consider a superconducting sample that is introduced into the cavity. Because of screening effects, the microwave magnetic field is expelled from the interior of the sample, apart from a sheet of thickness the penetration depth λ. The expulsion of magnetic field from the sample reduces the effective volume of the cavity and shifts the resonance to a higher frequency $f + \delta f$. The sample also absorbs some of the microwave magnetic field causing a broadening of the resonance width from Δf_0 to $\Delta f > \Delta f_0$. For a thin film conductor of thickness d, the change in the resonance frequency and quality factor Q of the cavity are given by [186]

$$\frac{\delta f}{f} = \frac{1}{2}\frac{V_s}{V_r}\left[1 - \mathrm{Re}\left\{\frac{\tanh(Kd/2)}{Kd/2}\right\}\right], \tag{8.52}$$

$$\delta\left(\frac{1}{Q}\right) = \frac{V_s}{V_r}\mathrm{Im}\left\{\frac{\tanh(Kd/2)}{Kd/2}\right\}. \tag{8.53}$$

Here K is the propagation constant of the electromagnetic field inside the sample, V_s is the sample volume, V_r is the effective volume of the resonator (effective cavity volume-sample volume). For a normal metal $K = (1+i)/\delta$ and for a superconductor $K = 1/\lambda$. Furthermore, in a superconductor $c \gg \lambda$ except very close to T_c and for most normal metals at microwave frequencies $d \gg \delta$. When $d \gg \lambda$, δ, the hyperbolic tangents of Eqs. (8.52) and (8.53) are good approximation equal to one, so that:

$$\frac{\delta f}{f} = \frac{1}{2}\frac{V_s}{V_r}\left(1 - \frac{\delta}{c}\right) \text{ metallic}, \tag{8.54}$$

$$\frac{\delta f}{f} = \frac{1}{2}\frac{V_s}{V_r}\left(1 - \frac{2\lambda}{c}\right) \text{ superconducting}. \tag{8.55}$$

If the sample temperature can be changed independently of the cavity temperature, thus one can determine changes in δf caused by changes in λ as a function of temperature. The frequency shift Δf from a base temperature T_0 can be defined as,

$$\Delta f \equiv \delta f(T) - \delta f(T_0) = -\frac{fA}{V_r}\Delta\lambda(T), \tag{8.56}$$

where $A = V_s/c$ is the sample area and $\Delta\lambda(T) \equiv \lambda(T) - \lambda(T_0)$. The measurement of the cavity frequency shift as a function of temperature is therefore directly proportional to the change in the magnetic penetration depth. Furthermore, the sensitivity of the measurement is determined by the cavity filling factor V_s/V_r [249; 250].

The dissipation in the walls of the resonant cavity can be described in terms of surface

resistance for both the normal and the superconducting states [113]. The power dissipation takes place within a very thin layer near the cavity surface. The power lost per unit area, p, is related to the surface resistance of the measured sample according to the following expression,

$$p = \frac{1}{2} R_s H_t^2 \tag{8.57}$$

where H_t is the peak value of the applied RF magnetic field tangential to the surface. For a good conductor in the normal state, currents flow near the surface with a characteristic skin depth, and surface resistance R_s at angular frequency ω is then given by

$$R_s = \mu_0 \omega \delta = (\frac{\omega \mu_0}{2\sigma})^{1/2} \tag{8.58}$$

where σ is the electrical conductivity and μ_0 is the permeability of the vacuum. The surface resistance in the superconducting state may be understood qualitatively in terms of the London-two fluid model [241]. According to this model, as the temperature of the metal is lowered below T_c, a fraction n_s(T) of the conduction electrons condense into Cooper pairs and move together through the lattice without dissipation. The penetration depth of electromagnetic fields in a superconductor is given by the London penetration depth λ

$$\lambda = (\frac{m^*}{4 n_s e^2 \mu_0})^{1/2} \tag{8.59}$$

where m^* is the effective mass of electron, e is the charge of the electron, and n_s the density of superconducting electrons. For a BCS s-wave superconductor, the frequency and temperature dependence of the superconducting surface resistance is described rather well by the following simple formula

$$R_s \propto \frac{\omega^2}{T} exp(-\frac{\Delta(T)}{kT}) \tag{8.60}$$

where 2Δ, corresponds to the energy needed to break into quasiparticles. The frequency dependence can be explained as follows. The internal electric field induced by the change of the current is

$$E_{int} \propto \frac{dH}{dt} \propto \frac{di_{sc}}{dt} = \omega i_{sc} \tag{8.61}$$

where i_{sc} is the supercurrent density. The dissipated power by the quasiparticles will be

$$p_d \propto E_{int} \tag{8.62}$$

where

$$i_{qp} = \sigma_{qp} E_{int} = \frac{n_{qp} e_{qp}^2}{m_{qp}} E_{int}. \tag{8.63}$$

Here, n_n is the quasiparticle density, and i_{qp} is the quasiparticle current density. The power dissipated may be thus expressed as

$$p_d \propto E_{int}^2 n_n = \omega^2 i_s^2 n_{qp} \tag{8.64}$$

so that

$$R_s \propto \omega^2 n_{qp}. \tag{8.65}$$

The number of electrons thermally excited above the gap, 2Δ, is given approximately by the Boltzmann factor, $e^{-\Delta/kT}$. For niobium at T<T_c/2, Δ=1.9 T_c. The surface resistance can be obtained from a measurement of the unloaded quality factor of the cavity $Q(Q_0)$, a geometrical factor Γ determined by the shape, and the mode of the cavity. In what follows, I shall describe how the surface impedance may be obtained from such a measurement.

8.5.1 Data analysis

The principle at the basis of the data analysis obtained from the cavity perturbation technique, is the representation of experimental set-up as as resonant circuit and to consider the possible losses. For a typical resonant circuit, these are the intrinsic losses $Q_0 = \omega W_{max}/P_0$, $Q_{rad} = \omega W_{max}/P_{rad}$ due to the the radiated power, and the coupling losses $Q_{ex} = \omega W_{max}/P_{ext}$. Here W_{max} is the energy stored per cycle and P_0 is the power dissipated per cycle. One has to take these losses into account in order to extract the supplementary losses due to the presence of the sample inside the cavity.

Therefore, the total losses can be written as $P = P_0$+P$_{rad}$+P$_{ext}$+P$_{sample}$ i.e., for the loaded quality one has ,

$$\begin{aligned} \frac{1}{Q_L} &= \frac{1}{Q_0} + \frac{1}{Q_{sample}} + \frac{1}{Q_{rad}} + \frac{1}{Q_{ext}} \\ &= \left(\frac{1}{Q_0} + \frac{1}{Q_{sample}}\right) + \frac{1}{Q_{rad}} + \frac{1}{Q_{ext}} \\ &= \left(\frac{1}{Q}\right)_{measured} + \left(\frac{1}{Q_{rad}} + \frac{1}{Q_{ext}}\right). \end{aligned} \tag{8.66}$$

Here the last term in brackets is corrected by calibration. Nevertheless, radiation losses are usually negligible: they depend on the size of any apertures that may be present in the

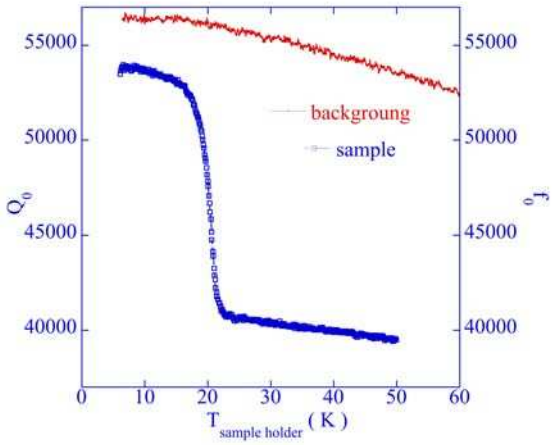

Figure 8.9 Typical signal obtained for a superconducting sample (in blue) compared to the background signal of the cavity with empty sample holder inserted on it (in red).

cavity walls. Part of the cavity losses are accounted for by a "calibration" or "correction" of the coupling coaxial line leading to the cavity using a calibrated open load,short current to impedance. The measured loaded quality factor after calibration contains the information as the surface impedance of the sample. The background signal due to different losses has to be subtract from the measured signal of the sample. Test measurements have been performed in order to extract the background signal of the sample holder (see Figure 8.9).

If the power dissipated by the sample is bigger, one will have a bigger $(1/Q)_{measured}$ and so smaller Q_L. One now has to take into account the sample shape, its position inside the resonant cavity, and the effective volume of the resonant cavity to extract the surface impedance of the sample. The most adequate way for the data treatment of the cavity perturbation method in the literature is suggested by M. R. Trunin [160]. In the case of sample sizes which are relatively small compared to the inner wall of the resonant cavity, to calculate the field distribution for sample with sharped edge geometry is not trivial. Trunin *et. al.* proposed to consider rounded edge geometry for a slab-like sample, since under this assumption the calculation of the field distribution can be quite possible by taking into account the sample aspect ration and the dimensions. Following a similar procedure, the author presented the measurements of the real $R_s(T)$ and imaginary $X_s(T)$ parts of the surface impedance for a superconducting sample as derived from the experimental datas of $Q_i(T)$ and $\Delta f_i(T)$ obtained using a cylindrical cavity. These are described as the following

relations:

$$R_s(T) = \Gamma_s \left[\frac{1}{Q(T)} - \frac{1}{Q_0(T)}\right]$$
$$X_s(T) = -\frac{2\Gamma_s}{f_0}\left[\Delta f(T) - \Delta f_0(T)\right] + X_0 \tag{8.67}$$

where Γ_s is the sample geometrical factor and X_0 is an additive constant. In order to overcome the difficulty of the calculation of the field distribution at the sharp edges of the sample an assumption is made for the calculation of Γ_s. The sample is considered to be a plate with rounded edges, and the corresponding geometrical factor is given by

$$\Gamma_s = \frac{2\pi f \mu_0 V}{4\gamma_0 A} \frac{1}{\ln\left(\frac{b}{c}\right) + 1}. \tag{8.68}$$

Here, A is the sample area, V is the cavity volume, and γ_0 is a constant determined by the field configuration of the resonant mode of the cavity [36]. In the following we will use a similar procedure by taking into account the sample geometry.

If the simple transverse orientation (Figure 8.10) , the sample which has usually the shape of a plate, is placed on the end of the sapphire rod, with that the crystal c-axis is aligned with the microwave magnetic field. Then the high frequency currents which determine the sample microwave response circulate in the ab-planes such as depicted in Figure 8.10.

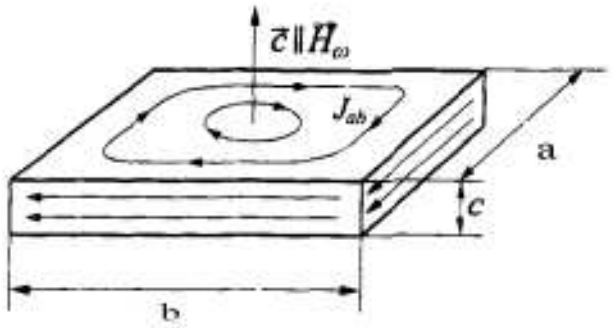

Figure 8.10 Transverse orientation of a sample with respect to the microwave magnetic field H_ω ∥ c-axis , arrows on the surface and side edges of the sample show the directions of the microwave currents. Figure adapted from [160].

We will assume that the sample is placed inside the cavity at the maximum of the

magnetic field, and that the frequency is sufficiently high for the sample response to ben in the skin depth regime. Then, the dissipated power by the sample is given by

$$\begin{aligned} P_{sample} &= P_0\chi'' = P_0\frac{\delta}{a} \\ &= P_0\left(\frac{\rho}{\mu_0 f a^2}\right)^{1/2} = P_0\frac{R_s}{\pi\mu_0 f a}. \end{aligned} \tag{8.69}$$

We will use the expression with the susceptibility $\chi'' = \delta/a$ in the skin-effect regime where the skin depth is given by $\delta = (\rho/\mu_0 f)^{1/2}$. Here ρ is the resistivity, f is the resonance frequency, a is the sample width and $R_s = \pi\mu_0 f\delta$ is the surface resistance of the sample. Therefore one can obtain the surface resistance of the measured sample by subtracting the Q_0 of the cavity as following,

$$\left(\frac{1}{Q}\right)_{measured} - \left(\frac{1}{Q}\right)_{cavity} = \frac{\omega W_{max}}{P_{sample}} = \frac{\omega W_{max}}{P_0}\frac{R_s}{\pi\mu_0 f a}, \tag{8.70}$$

from here one obtains,

$$R_s = \left[\frac{\Delta(\frac{1}{Q})_{measured}}{\Delta(\frac{1}{Q_0})_{cavity}}\right] \times (\pi\mu_0 f a). \tag{8.71}$$

If one would take into account the sample geometrical factor and the cavity dimensions,

$$\begin{aligned} Q_{measured} &= \frac{\mu_0 H^2 f}{\mu_0 H^2 f\chi''}\frac{V_{cavity}}{V_{sample}} \\ &= \frac{1}{\chi''}\frac{V_{cavity}}{V_{sample}} \end{aligned} \tag{8.72}$$

from this one obtains,

$$\begin{aligned} \Delta\left(\frac{1}{Q}\right) &= \chi''\frac{V_{cavity}}{V_{sample}} \\ &= \frac{\delta}{\sqrt{ac}}\frac{a^2 c}{V_{cavity}}. \end{aligned} \tag{8.73}$$

From above expressions one get for the skin depth ,

$$\delta = \Delta\left(\frac{1}{Q}\right)\frac{\sqrt{ac}}{a^2 c}V_{cavity} \tag{8.74}$$

inserting this into R_s=$\pi\mu_0 f\delta$, one obtains for the surface resistance the following expression:

$$R_s = \pi\mu_0 f \frac{V_{cavity}}{a^{3/2}c^{1/2}}\Delta\left(\frac{1}{Q}\right) \tag{8.75}$$

where the geometrical factor is defined as $\Gamma_s = \pi\mu_0 f \frac{V_{cavity}}{a^{3/2}c^{1/2}}$.

For the imaginary part X_s of the surface impedance we proceeded as following;

$$X_s = B\Gamma_s\left(\frac{\Delta f}{f_0}\right) = AB\Gamma_s - B\Gamma_s\left(\frac{\Delta f}{f_0}\right) \tag{8.76}$$

here the first term corresponds to X_0 additional constant, and the prefactor of the second term gives $2\Gamma_s$, where $\Gamma_s = \pi\mu_0 f_0 a$.

Chapter 9

Electron irradiation of iron-based superconductors

The discovery of superconductivity in the iron-based superconductors and the subsequent increase of the critical temperature up to 55 K in this family of compounds raised the fundamental question of the superconductivity mechanism. Early studies have revealed that electron-phonon interaction based superconductivity is not likely in these systems; subsequently, a spin-fluctuation mediated pairing has been proposed [107; 138]. The nesting between disconnected pockets of the Fermi surface is for itinerant anti-ferromagnetism and the associated spin fluctuations. These can be at the origin of the superconducting pairing. The ensuing gap has s-wave symmetry, but changes sign between different Fermi surface sheets. This state is labelled s± or sign reversing s-wave as introduced by Mazin *et. al.* [107].

Experimental studies, such as angle resolved photoemission (ARPES) [88; 142; 222], muon spin relaxation (μ SR) [115] and penetration depth [132; 135] measurements showed results consistent with fully gapped s-wave symmetry and sign reversing order parameter. The sign reversing s-wave symmetry is also consistent with neutron scattering measurements , that observed a resonance peak. On the other hand, the relatively small effect on T_c of doping by transition metal atoms [17; 147; 207; 214] has cast some doubt on the reality of a sign reversing gap function. On the other hand, theoretical studies have shown that these experiments do not necessarily contradict the s± pairing [51; 215].

It has been widely suggested [7; 10; 27; 101; 153; 161; 162] that the charged atom doping effects cannot be reduced to a shift of the Fermi level. It is also suggested by different groups [7; 211] that the dopant atoms act as scattering impurities, which maybe pair-breaking due to admixture of quasiparticle excitations on different Fermi surface sheets,

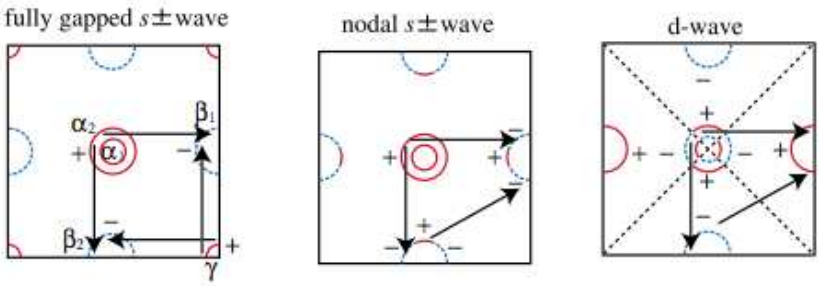

Figure 9.1 Representation of the fully gapped s wave top panel,the nodal s wave middle, and the d-wave gap bottom. The solid red dashed blue curves represent positive negative sign of the superconducting gap function. The arrows indicate the dominating nesting vectors. From Ref. [138]

and henceforth cause the decrease in T_c in the overdoped region of the phase diagram [236]. Onari *et. al.* studied the effect of impurities in iron pnictides, and by treating the multi-orbital effect they revealed that the Anderson's theorem is violated for $s_\pm$ symmetry due to inter-band scattering. This fact means that the fully gapped sign-reversing s-wave state, which is predicted by spin fluctuation theories, is very fragile against impurity scattering [211]. Glatz *et. al.* who showed that scattering between different bands by impurities has a pair-breaking effect and introduces considerable spectral weight inside the gap. They studied the statistics of disorder-induced sub-gap states in $s_\pm$ superconductors due to collective effects of impurities [7]. van der Beek *et. al.* proposed that charge dopant atoms act as scatterers in iron-based superconductors, while isovalent substitutions do not. They used the vortex pinning as a probe of impurities. In electron-doped $PrFeAsO_{1-y}$, $NdFeAsO_{1-x}F_x$ and $Ba(Fe_{1-x}Co_x)_2As_2$ as well as in the hole-doped $Ba_{1-x}K_xFe_2As_2$, the critical current density j_c at fields above 1 Tesla can be described by collective pinning due to the spatial fluctuations of the quasiparticle mean free path [28**?**]. They found that the impurity density accounting for pinning corresponds to the dopant atom concentration.

Another manifestation of the disorder apart from the different pinning regimes in iron-based superconductors is the temperature dependence of the magnetic penetration depth λ_L. This sense the low-energy quasiparticle density of states (DOS) and is a probe for the determination of the superconducting gap structure (see Figure 9.2), but also for the effect of disorder. In particular, inter-band scattering of quasiparticles by point-like disorder was predicted to lead to the appearance of a peculiar T^2 dependence of the London penetration depth at low temperature [198]. Other scenarios for superconductivity predict accidental

gap nodes either in an s or d-wave symmetry, with the nodes being lifted in the presence of inter-band scattering [60; 234]. In what follows the effects of electron irradiation of iron-based superconductors on their physical properties such as the critical temperature T_c , the critical current density j_c as well as the surface resistance R_s is discussed. The introduction of controlled disorder by irradiation is a powerful tool for the characterization of the nature of superconductivity. In particular, sensitivity of superconductivity to point-like defects introduced by energetic electron irradiation (at the SIRIUS Accelerator of the LSI) may reveal the presence or not of exotic superconductivity (with a sign-reversing order parameter). Figure 9.3 presents the photograph of the Pelletron accelerator installed in LSI where the electron irradiation up to 2.5 MeV on iron-based superconductors were performed.

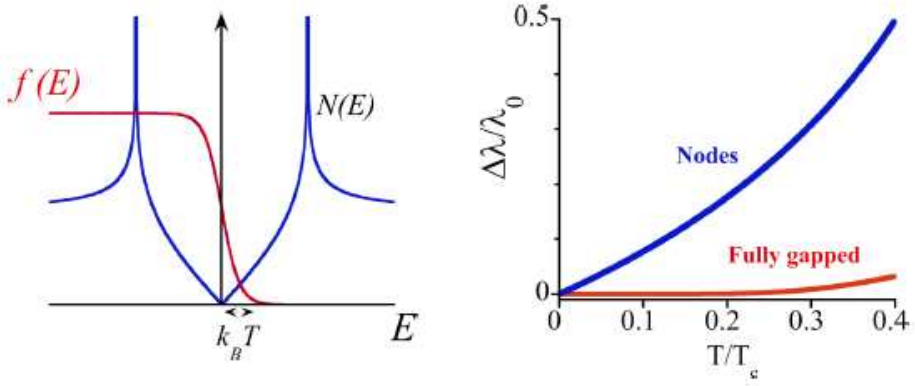

Figure 9.2 Schematic representation of the theoretical temperature dependence of the magnetic penetration depth explaining the gap structure for different dependence law. From Ref.[5]

In order to test the sensitivity to disorder, the introduction of different kinds of point-like defects were performed, this is possible either by chemical doping [123; 124; 175], or by irradiation [37; 271]. Substitution of magnetic ions, which suppresses T_c rather more effectively than non-magnetic substitutions was performed by Chen *et.al.* [124; 175]. Tarantini *et al.* reported on T_c–suppression by α–particle irradiation of NdFeAs(O,F); However it was argued that it induces magnetic impurities and defect clustering. The 3 MeV proton irradiation experiments performed by Nakajima *et al.* on $Ba(Fe_{1-x}Co_x)_2As_2$ leads to a monotonous T_c–depression as the residual resistivity increases and the authors provided estimates for the critical pair-breaking parameter as $\Gamma/2\pi T_c \sim 4-7$ and $\Gamma/2\pi T_c \sim$

Figure 9.3 A photograph of the SIRIUS Accelerator of the LSI. On the right-hand side the cryostat used for the irradiation at low temperature is presented.

1.5−2.5, as one goes from underdoped to overdoped [271]. Apart from point defects, proton and neutron irradiation are known to induce, *in situ*, point defect cascades and clusters, which may play a different role than that of simple scatterers.

In this chapter, the effect of 2.5 MeV electron irradiation on differently substituted $BaFe_2As_2$ such as $Ba(Fe_{1-x}Co_x)_2As_2$, $Ba(Fe_{1-x}Ni_x)_2As_2$, and $BaFe_2(As_{1-x}P_x)$ single crystals is compared. It is known from earlier studies that electron irradiation of high-T_c superconductors at low temperature with electrons of 2.5 MeV produces a random distribution of Frenkel pairs (vacancies and intersitials) and provides a sound basis for the interpretation of irradiation effects. Warming the irradiated samples even without continuing irradiation there is some defect mobility from 100 K upwards [100]. Early studies reported in the literature for high-T_c superconductors revealed that, a few exceptions like NbN, all metallic superconductors exhibit a gradual decrease of the critical temperature T_c upon electron irradiation. This was interpreted as a result of the pair-breaking mechanism. In the high-T_c cuprates, electron-irradiation defects are known to be strong unitary scatterers, comparable to Zn substitution. Therefore, they are responsible for the suppression of the critical temperature [78; 79; 182], and the appearance of a T^2–temperature dependence of the penetration depth [182].

For the electron irradiation of $Ba(Fe_{1-x}Co_x)_2As_2$, $Ba(Fe_{1-x}Ni_x)_2As_2$, and $BaFe_2(As_{1-x}P_x)$, similar suppression of T_c is observed. For the case of the charged-doped $Ba(Fe_{1-x}Co_x)_2As_2$ the decrease in T_c is larger in the underdoped crystals than it is in the optimally doped one. A monotonic increase in the resistance was observed for range of intermediate electron dose applied in this work. The temperature dependence of the superfluid density shows very little or no change for all studied doping levels

of charge-doped $Ba(Fe_{1-x}Co_x)_2As_2$, $Ba(Fe_{1-x}Ni_x)_2As_2$ single crystals. While, in charge-doped $Ba(Fe_{1-x}Co_x)_2As_2$ clear increase of the weak collecting pinning contribution to j_c is observed, this contribution absent at all doping levels of pristine material appears clearly in the isovalently substituted $BaFe_2(As_{1-x}P_x)$ after electron irradiation. In these above materials, the finding of the weak collective pinning contribution allows one to estimate the density of the produced defect per unit irradiation fluence. In $Ba(Fe_{1-x}Ni_x)_2As_2$ an important suppression of j_c is observed.

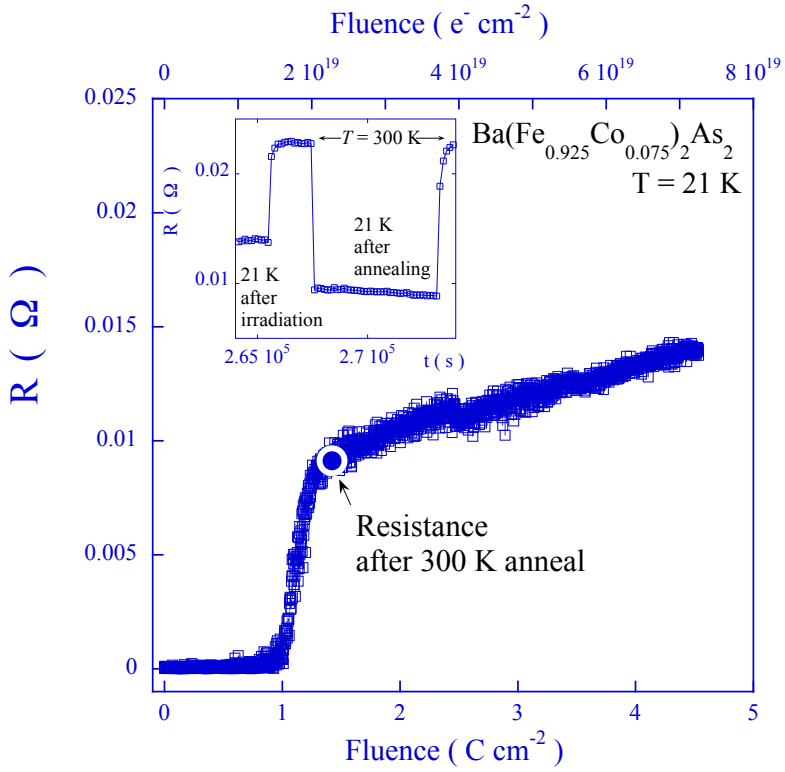

Figure 9.4 $Ba(Fe_{0.925}Co_{0.075})_2As_2$: Resistance as function of dose of 2.5 MeV electrons, measured at 21 K. The sample transits to the normal state after a dose of 1.2 Ccm^{-2}, after which the resistance increases at a rate of $\Delta R/R = 0.14[Ccm^{-2}]^{-1}$. The Inset shows the effect of annealing. The resistance of the crystal is represented as function of time. The protocol comprises initial measurements at 21 K following irradiation with 4.6 Ccm^{-2} 2.5 MeV electrons. The crystal is then warmed to 300 K, cooled to 21 K, and heated once again to 300 K. After the first anneal at 300 K, the resistance drops back to the value reached after low-temperature irradiation with only 1.4 Ccm^{-2} (white circle on the curve in the main panel).

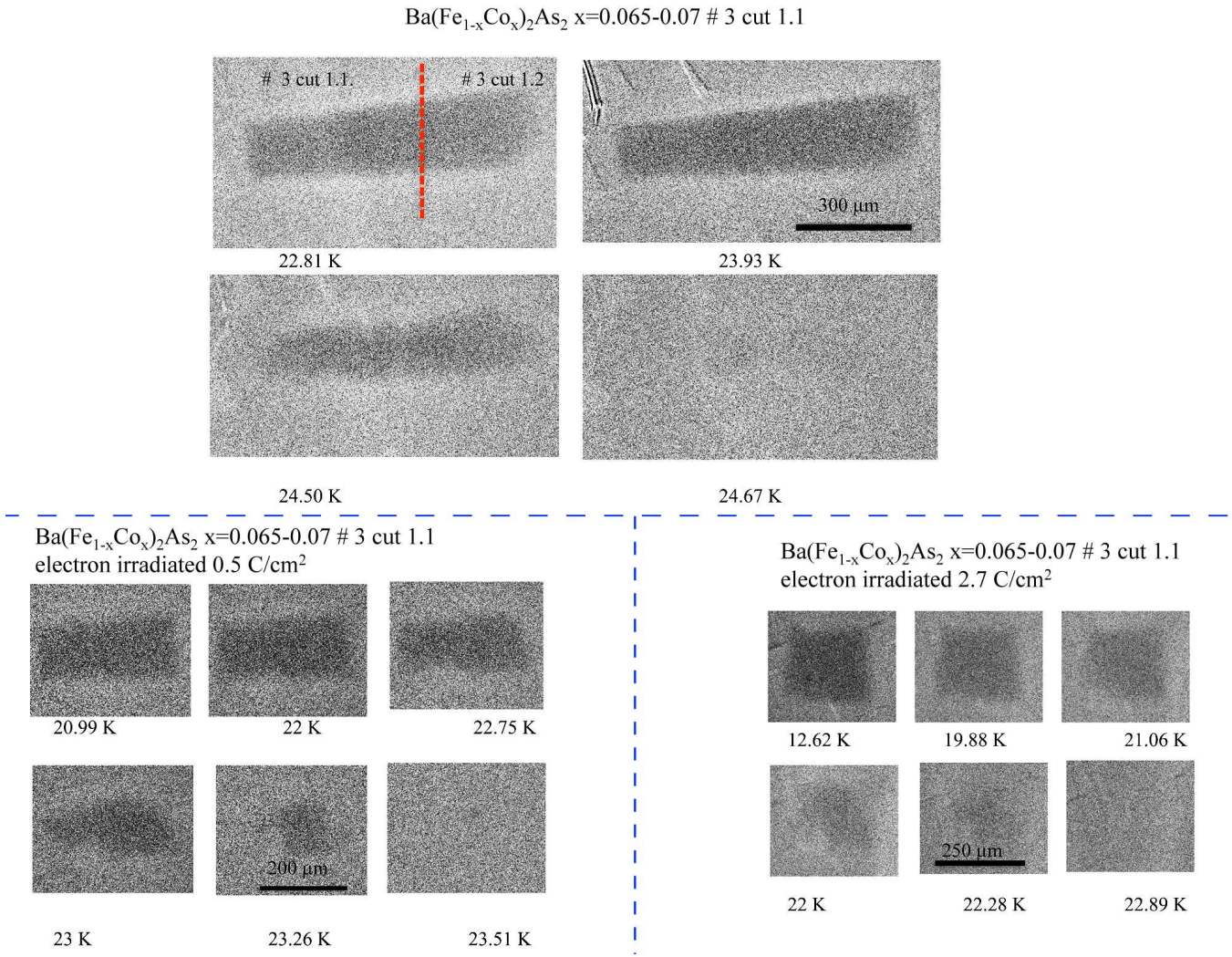

Figure 9.5 Differential magneto-optical images (a) of pristine $Ba(Fe_{1-x}Co_x)_2As_2$ single crystal with $x = 0.065 - 0.07$ # 3 cut 1, (b) $Ba(Fe_{1-x}Co_x)_2As_2$ single crystal with $x = 0.065 - 0.07$ # 3 cut 1.1 2.5 MeV electron irradiated with 0.5 C/ cm^2 and (c) $Ba(Fe_{1-x}Co_x)_2As_2$ single crystal with $x = 0.065 - 0.07$ # 3 cut 1.2 2.5 MeV electron irradiated with 2.7 C/ cm^2 . The images (a,b,c) show the progressive admission of an ac magnetic field of magnitude 1 Oe, applied perpendicularly to the sample surface, as the temperature is raised. In these flux density maps, areas of high luminous intensity I correspond to the value of the applied field, while dark areas correspond to zero field, (*i.e.* full screening). Crystals shown in (b,c) were cut out from the big crystal shown in (a) with a dashed line. Here the squares represent the regions where the data is selected for the transmittivity curves presented in Figure 9.6 .

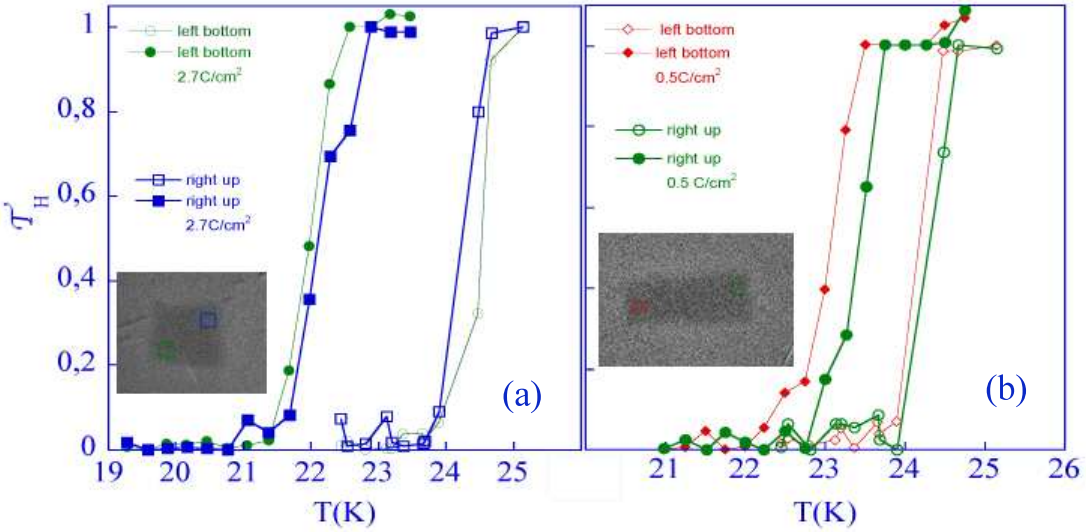

Figure 9.6 Local "transmittivity" (or "local ac susceptibility") curves defined as $[I(T) - I(T \ll T_c)]/[I(T \gg T_c) - I(T \ll T_c)]$ depicted in (a,b) determined from the regions indicated as squares in Figure 9.5 on the pristine crystal with with $x = 0.065 - 0.07$ # 3 cut 1 and as a inset in (a,b) on each irradiated cut pieces. The shift of the curves after irradiated with respect to the x-axis determine the local variation of the transition temperature for the indicated regions. Here open markers represent data for pristine samples while, filled markers were used to represent datas for the irradiated samples.

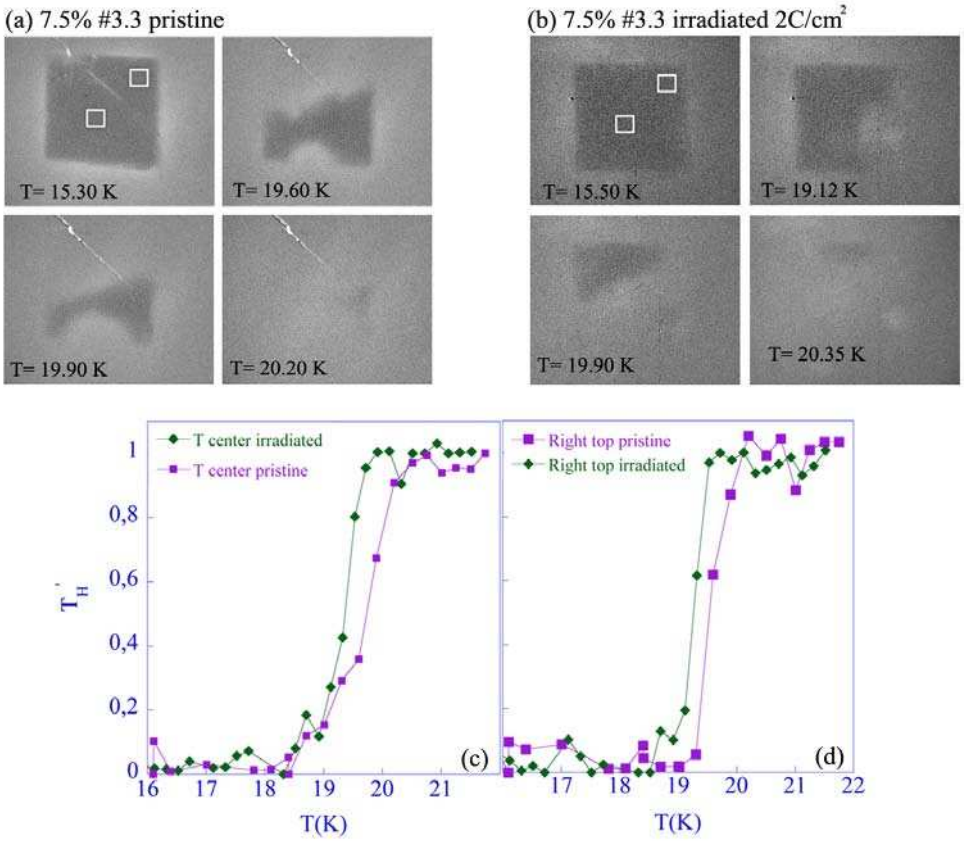

Figure 9.7 Transition from the superconducting to the normal state of a $Ba(Fe_{0.925}Co_{0.075})_2As_2$ single crystal before (a,c) and after irradiation with 2.1 Ccm^{-2} 2.5 MeV electrons (b,d), as imaged by the differential magneto-optical imaging (DMO) technique Ref. [206]. The images (a,b) show the progressive admission of an ac magnetic field of magnitude 1 Oe, applied perpendicularly to the sample surface, as the temperature is raised. In these flux density maps, areas of high luminous intensity I correspond to the value of the applied field, while dark areas correspond to zero field, (*i.e.* full screening). The dark rectangle in the upper left hand panels of (a) and (b) correspond to the sample outline, *i.e.*, full Meissner expulsion of the magnetic field at the lowest temperature. The white squares indicate the positions at which the "transmittivity" (or "local ac susceptibility") defined as $[I(T) - I(T \ll T_c)]/[I(T \gg T_c) - I(T \ll T_c)]$ depicted in the lower panels (c,d) was determined.

9.1 Electron irradiation

Controlled point-like disorder is induced into $Ba(Fe_{1-x}Co_x)_2As_2$, $Ba(Fe_{1-x}Ni_x)_2As_2$ and $BaFe_2(As_{1-x}P_x)$ single crystals using the SIRIUS Pelletron facilty of the Laboratoire des Solides Irradiés (LSI) at the Ecole Polytechnique in Palaiseau, France [106] (see Figure 9.3). Samples of different composition irradiated to the same dose, were mounted together and irradiated simultaneously with the 2.5 MeV electron beam. The irradiation experiments were carried out in a liquid H_2 bath ($T = 20$ K) using the cryostat installed on the beam line. The irradiation is performed at low temperature in order to prevent *in-situ* defect migration, recombination, and clustering. In–situ resistance measurements were carried out on the $Ba(Fe_{1-x}Co_x)_2As_2$ material in order to measure the increase of the residual resistivity as a function of defect density at low temperature, as well as the effect of room-temperature annealing. Figure 9.4 shows *in-situ* resistance measurements of the irradiated sample and the measurement of the same sample after annealing at room temperature.

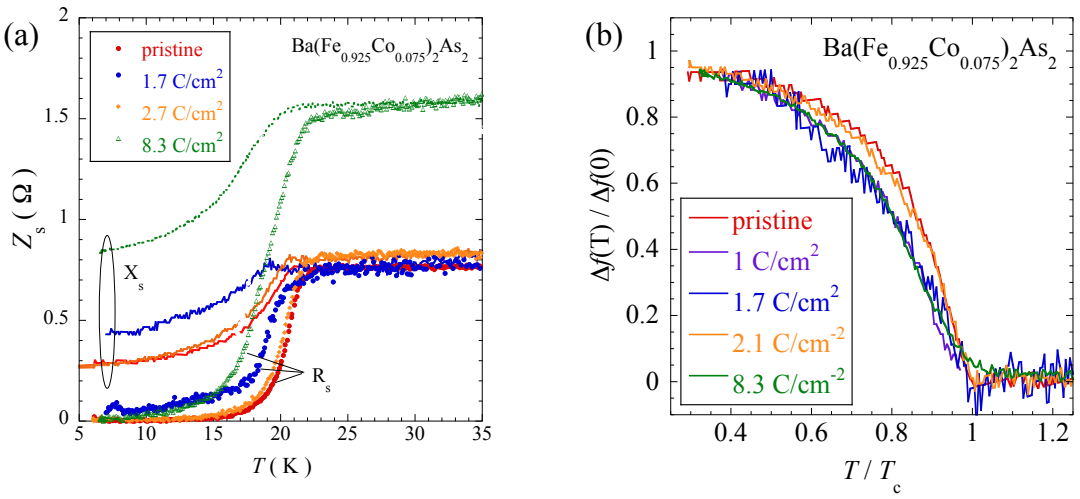

Figure 9.8 Surface impedance Z_s of $Ba(Fe_{0.925}Co_{0.075})_2As_2$ crystals before and after various low–temperature irradiation runs with 2.5 MeV electrons, and subsequent annealing at 300 K. Data points and thin lines show the surface resistance R_s and reactance X_s respectively, for various electron doses. (b) Shift $\Delta f(T)$ of the resonant frequency of the superconducting Nb cavity, as function of temperature, normalized with respect to the low–temperature extrapolated $\Delta f(0)$, for $Ba(Fe_{0.925}Co_{0.075})_2As_2$ crystals irradiated with various fluences of 2.5 MeV electrons.

9.2 Measurements of T_c and the surface impedance Z_s

We have studied the effects of electron irradiation on the charge-doped $Ba(Fe_{1-x}Co_x)_2As_2$, $Ba(Fe_{1-x}Ni_x)_2As_2$ and isovalently substituted $BaFe_2(As_{1-x}P_x)_2$ single crystals. Several samples of different doping levels were irradiated, and each doping level was irradiated at various irradiation fluence. Experiments discussed below are generally performed on the same crystal before and after irradiation, if not on different pieces cut from a crystal. We have first characterized each sample using the Magneto optical imaging method, in order to measure the exact T_c and its spatial distribution within each crystal. This is done in order to identify the effective changes in the critical temperature T_c for each sample after irradiation process. However, even this precise method for the determination of the exact change of T_c turned out to be not very adequate. Namely the T_c changes in $Ba(Fe_{1-x}Co_x)_2As_2$ are generally of order of the spatial variation of T_c over the whole pristine crystal. In order to overcome this problem we have proceeded to the extraction the local transmittivity T_H curves before and after irradiation from the same region of the sample under study; this gave us more adequate results (see Fig. 9.7).

The change in T_c was further quantified using (*ex-situ*) measurements of the temperature dependent microwave surface impedance $Z_s = R_s + iX_s$. These were performed using the superconducting Nb cavity, cooled to 5 K using a 0.5 W cryocooler cold head, this measurement technique has been previously described in details in Chapter 8. From the temperature dependent resonance frequency f and unloaded quality factor Q_0, the surface resistance R_s and reactance X_s were determined as

$$R_s = \mu_0 f G \left[\frac{1}{Q_0(T)} - \frac{1}{\tilde{Q}_0} \right] \tag{9.1}$$

and

$$X_s(T) = \mu_0 G \left[f(T) - f(0) \right] + X_0 \tag{9.2}$$

respectively. Here $f(0)$ and $\tilde{Q}_0$ are the resonance frequency and the unloaded quality factor in the absence of the sample, and the geometrical factor $G = V/4\pi w\sqrt{wd}$, with V the inner volume of the cavity, d the thickness of the platelet-like single crystal sample, and w its smaller width. The additive constant X_0 was adjusted so that $R_s = X_s$ in the normal state.

9.3 Critical current density and its analysis

The critical current density for the $Ba(Fe_{1-x}Co_x)_2As_2$ and $Ba(Fe_{1-x}Ni_x)_2As_2$ single crystals as function of the applied magnetic field H_a were extracted from the magnetization measurements performed using a commercial SQUID magnetometer. From the the width $\Delta M(H)$ of the magnetic hysteresis loops, the field and temperature dependence of the sustainable current density $j = \frac{3}{2}\Delta M/w$ was determined using the Bean model. The prefactor $\frac{3}{2}$ is estimated from calculations of E.H. Brandt for rectangular bars of similar aspect ratio as the measured crystals [62]. Data on $BaFe_2(As_{1-x}P_x)_2$ were acquired using the local Hall probe magnetometry technique [156; 157] (see Chapter 4). The gradient dB/dx (in G/μm) measured by Hall sensors is directly proportional to the sustainable screening current j, with $dB/dx \sim \frac{1}{6}j$ for a crystal aspect ratio of ~ 0.1 [62].

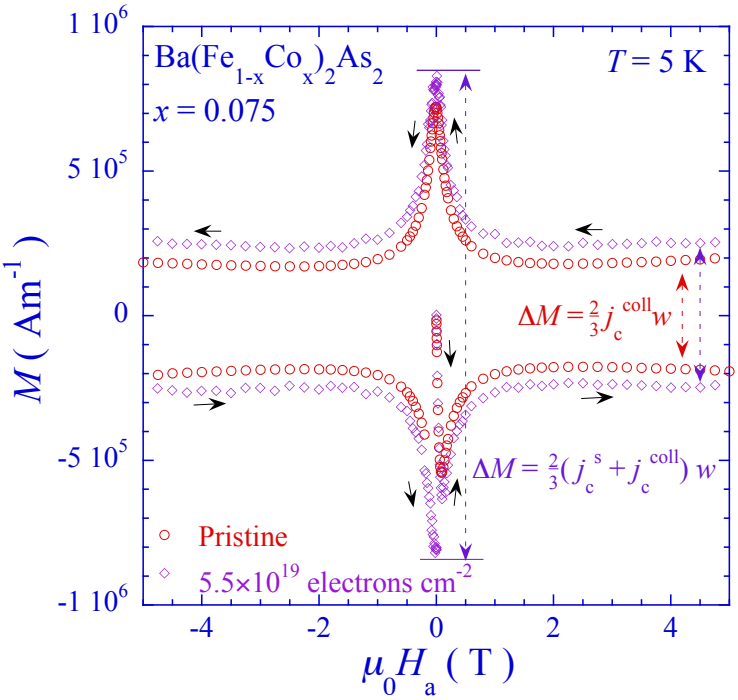

Figure 9.9 Single crystalline $Ba(Fe_{0.925}Co_{0.075})_2As_2$ # 2 : Hysteresis loops of the irreversible magnetization at 5K, before and after irradiation with 5.5 $\times 10^{19}$ cm^{-2} 2.5 MeV electrons. Closed arrows depict the direction in which the loop is traversed upon cycling the magnetic field. Dotted double arrows depict the width of the magnetization loop in the low-field, strong pinning regime, and in the higher field regime in which only the weak collective pinning contribution j_c^{coll} is relevant.

For further analysis we will take into account only the lowest temperature (5 K) measurements for j to be representative of the critical current density, since at higher temperature, the measured current density can be significantly lower than the pinning critical current density because of flux creep [156; 205]. The critical current density is further analyzed along the lines of Refs. [41; 44]. The two main contribution to the critical current density in all charge–doped iron-based superconductors from vortex pinning is exemplified by Fig. 9.9.

The typical central peak observed in the hysteresis loops in Fig. 9.9 , at low applied fields, is the indication of the first contribution j_c^s to the critical current from vortex pinning called the strong–pinning contribution , while the constant contribution at higher fields comes from "weak collective pinning" by the dopant atoms. These contributions can be also identified on the critical current density - versus magnetic field plot (see Fig. 9.11 and Fig. 9.14): the strong pinning contribution is responsible for the low–field plateau and the subsequent $j_c \propto B^{-1/2}$ decrease, while the collective pinning contribution yields the high–field constant j_c. It can be written in terms of superconducting parameters, defect density n_d, and the elementary pinning force f_p of a single defect, as

$$j_c^{coll} = j_0 \left(\frac{n_d \langle f_p^2 \rangle \xi_{ab}^3}{\varepsilon_\lambda \varepsilon_0} \right)^{2/3} . \tag{9.3}$$

Here, j_0 is the depairing current density, ξ_{ab} and λ_{ab} are the ab–plane coherence length and penetration depth respectively, $\varepsilon_0 \equiv \Phi_0^2/4\pi\mu_0\lambda_{ab}^2$ is the vortex line energy, ε_λ is the penetration depth anisotropy [46] , and $\Phi_0 = h/2e$ is the flux quantum. The averaging $\langle \ldots \rangle$ is performed over the vortex core.

The magnitude of j_c^{coll} is compatible with scattering of the quasi-particles in the vortex cores as being at the origin of the weak collective pinning contribution in pristine iron-based superconductors, provided that the dopant atoms are the scattering defects. This gives rise to [68; 69]

$$f_p = 0.3 g(\rho_D) \varepsilon_0 \left(\frac{\sigma_{tr}}{\pi \xi_{ab}^2} \right) \left(\frac{\xi_0}{\xi_{ab}} \right) \tag{9.4}$$

which depends not only on the Gor'kov dirt parameter $\rho_D = \hbar v_F / 2\pi T_c l = \xi_0 / l$, but also on the transport cross-section $\sigma_{tr} = (2\pi/k_F^2) \sin^2 \delta_0$ (δ_0 is the scattering phase angle, and k_F the Fermi wavevector). The analysis of the intermediate field critical current density of several common iron based superconductors allows one to estimate the scattering parameters compiled in Table 3.1. The weak collective pinning contribution is absent in isovalently doped $BaFe_2(As_{1-x}P_x)_2$ for all doping levels x [see Ref. [205] and Fig. 9.17 (b), Fig. 9.14 (b)]; surprisingly, it is present in $Ba(Fe_{1-x}Ru_x)_2As_2$ [158] and LiFeAs [157].

9.4 Results

9.4.1 $Ba(Fe_{1-x}Co_x)_2As_2$

Electron irradiation of $Ba(Fe_{1-x}Co_x)_2As_2$ single crystals of different doping level at several doses were performed. The evaluation of some superconducting properties such as the transition temperature T_c, the sustainable current density j and the surface resistance R_s is discussed below. Fig. 9.4 shows the *in-situ* resistance measurement of an optimally doped $Ba(Fe_{0.925}Co_{0.075})_2As_2$ single crystal, performed during exposure to the 10 μA, 2.5 MeV beam, at $T = 21$ K. The superconducting-normal state transition takes places at at a fluence of 1.2 Ccm^{-2}, after which the resistance increases at a rate of $\Delta R/R = 0.14[Ccm^{-2}]^{-1}$. The electron irradiation was stopped once we reach a fluence of 4.6 Ccm^{-2} and the sample holder was taken out of the cryostat. When the sample was heated to 300 K, its resistance is measured again. Then the sample holder is put back into the cryostat and the crystal was subsequently cooled down once again to 21 K, and the resistance measured again (Inset to Fig. 9.4). After this cycle, 21 K(e^- irradiated)–300 K–21 K, it appears that the resistance has dropped to the value first measured after irradiation with a fluence of 1.4 Ccm^{-2}. This shows that a large annealing effect exists whence the irradiated samples are heated up to room temperature. Heating leads to the annihilation and clustering of the point defects produced by the irradiation, with a resulting drop of the irradiation–induced resistance change of 65 % . Since all data presented in the following sections concern *ex-situ* experiments performed after heating the crystals to 300 K, the effect of annealing should be taken into account.

The evolution of the reduced critical temperature T_c/T_{c0} with electron fluence (after 300 K annealing) is shown for various Co-doping levels x in Fig. 9.10(a). Here, T_{c0} is the critical temperature of the crystal before irradiation. Given that the T_c changes are very modest and that there is an important dispersion of T_c even in pristine crystals similarly grown samples, as well as from the same batch,it is the relative change of T_c that is to be compared.

Fig. 9.10(b) shows the same data, as function of the product of the induced change in the scattering rate $\delta\Gamma/2\pi T_c$ and the electronic effective mass enhancement $z = m^*/m_e$. Here, $z\delta\Gamma = e\rho/R_H m_e$ (with m_e is the free electron mass, e the electronic charge, and m^* the effective mass) is estimated from the resistive change after annealing, $\delta R/R \sim 0.05$ $[Ccm^{-2}]^{-1}$, together with the published data for the resistivity ρ and the Hall coefficient R_H published in Ref. [77]. However, the resistivity change with electron dose depends on x, and that, in order to produce the *simulated* $\delta\Gamma$ values presented in Fig.9.10(b), we used the data measured $in-situ$ on crystals with different x. Estimates of the scattering rate

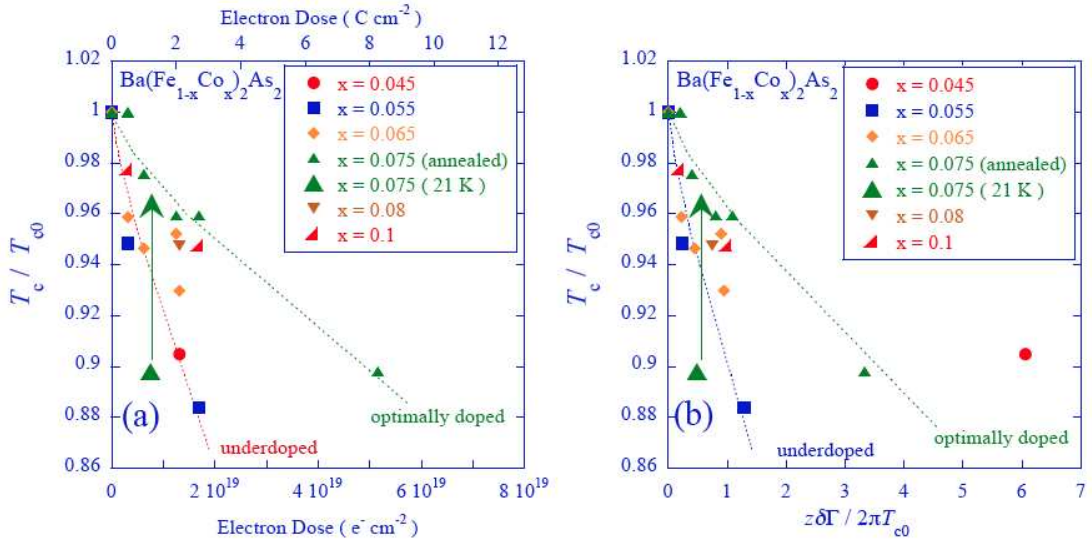

Figure 9.10 $Ba(Fe_{1-x}Co_x)_2As_2$: evolution of T_c (normalized by the initial critical temperature T_{c0}) as function of (a) the fluence of 2.5 MeV electrons (b) the estimated normal state scattering rate $\delta\Gamma$ (normalized by T_{c0}), for different doping levels x. The small data points show the T_c–values after annealing at 300 K. The large green triangle shows the drop of T_c following low-temperature irradiation of optimally doped $Ba(Fe_{0.925}Co_{0.075})_2As_2$, the arrow shows the effect of annealing at 300 K.

from critical current measurements (see below) yield qualitatively similar results.

The surface impedance of optimally doped $Ba(Fe_{1-x}Co_x)_2As_2$ before and after electron irradiation was measured using the cavity perturbation method (see Chapter 8) and is depicted in Fig. 9.8. We have observed a monotonous increase of the surface resistance after electron irradiation; even though in this series of experiments, the increase was not linear as function of fluence. In particular, the crystal irradiated with 2.1 Ccm^{-2} electrons did not conform to the general trend. We have extracted the temperature dependence of the superfluid density $n_s \propto \lambda_{ab}^{-2}$ of our superconducting crystals, from measurements of normalized frequency shift of the Nb cavity before and after irradiation for various Co-doping levels x. This showed little change to a less marked temperature dependence, if any. The observed trend is similar to that observed by Hashimoto *et al.* in $Ba_{1-x}K_xFe_2As_2$ crystals with varying degrees of disorder [135], but is much less marked here.

The low–temperature critical current density of single crystalline $Ba(Fe_{0.925}Co_{0.075})_2As_2$ was measured before and after irradiation with electrons. Fig. 9.11 shows an increase in the field-independent part of the critical current density above 1 Tesla, this increase indicates that the weak collective pinning contribution j_c^{coll} that is enhanced, presumably

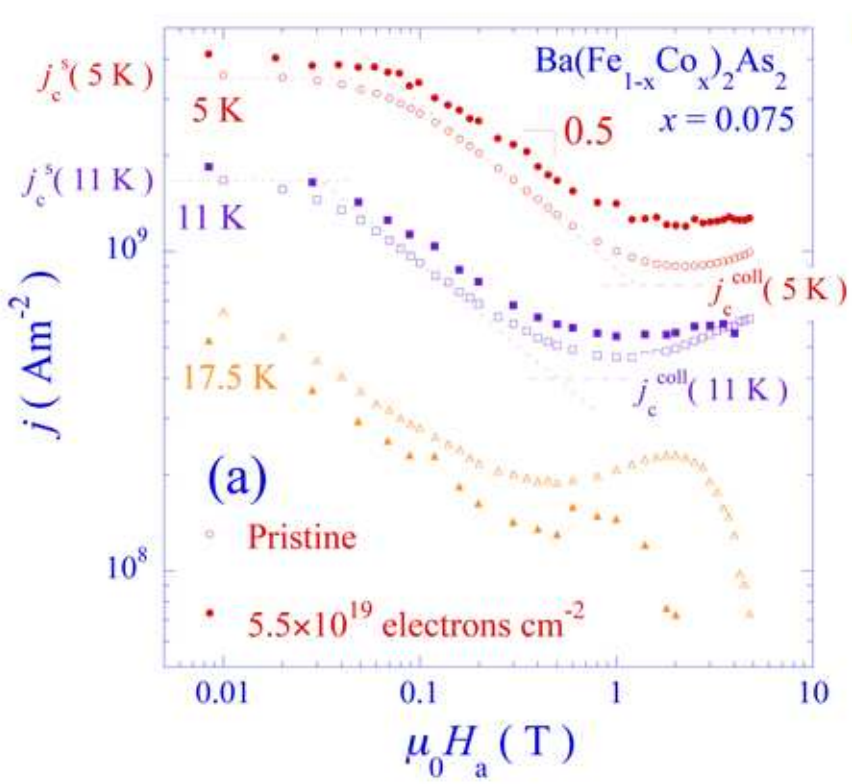

Figure 9.11 Sustainable current density j of optimally doped $Ba(Fe_{1-x}Co_x)_2As_2$ ($x = 0.075$) before (open symbols) and after irradiation at 21 K with 5.5×10^{19} cm^{-2} 2.5 MeV electrons (closed symbols). The measurements were performed at 5 K, 11 K and 17.5 K.

by atomic-sized point defects introduced by the irradiation. The magnitude of the j_c^{coll} part of the critical current density allows one to estimate the defect numbers created by electron irradiation. It is known that the electron irradiation creates some vacancies and interstitials and these are generally the defects caused by the atom with lowest atomic weight. Assuming that the created defects are Fe vacancy-interstitial pairs, one can estimate $\sigma_{tr} \sim \pi D_{Fe}^2 \sim 2.6$ Å^2, from the the ionic radius of Fe^{2+} $D_{Fe}^2 = 0.92$ Å. The increase of the critical current density is consistent, through Eqs. (9.3) and (9.4), with 0.006 dpa Fe / Ccm^{-2}. The increase of the low–temperature critical current density and the concomitant decrease of T_c after irradiation implies a steeper decrease of j_c with temperature, and a crossing of j_c–values of the pristine and the irradiated crystal at an intermediate temperature.

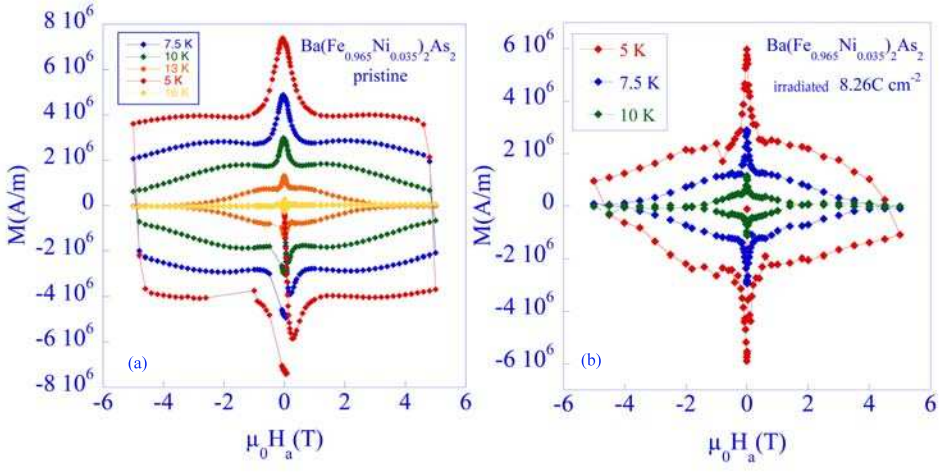

Figure 9.12 Single crystalline $Ba(Fe_{0.965}Ni_{0.035})_2As_2$: Hysteresis loops of the irreversible magnetization at 5K, 7.5 K, 10 K, 12.5 K, 17 K (a) before and (b) after irradiation with 5.5 $\times 10^{19}$ cm^{-2} 2.5 MeV electrons. Decrease of the width of the magnetization loop in low-field, strong pinning regime and in higher field regime is observed after electron irradiation.

9.4.2 $Ba(Fe_{1-x}Ni_x)_2As_2$

Surface impedance measurements , SQUID measurements and DMO imaging were performed on three different Ni-doping levels ($x = 0.006-0.0045-0.0035$) of $Ba(Fe_{1-x}Ni_x)_2As_2$ crystals before and after irradiation. The irradiated $Ba(Fe_{1-x}Ni_x)_2As_2$ crystals show a more rapid depression of T_c with dose than in $Ba(Fe_{1-x}Co_x)_2As_2$. The depression rate in T_c for the Ni-doped compounds were comparable to that found in underdoped $Ba(Fe_{1-x}Co_x)_2As_2$ (see Fig. 9.20). The critical current density of the $Ba(Fe_{1-x}Ni_x)_2As_2$ crystals were extracted from the SQUID measurements of the hysteretic loops of magnetization as a function of applied field (see Figure 9.12 and Fig. 9.13). The extracted critical current densities and the width of the magnetization loops show a strong suppression after the irradiation for both measured doping levels as such can be seen in Fig. 9.14 and Figs. 9.13 9.12. This is partially because the reduced measurement temperatures are lower in $Ba(Fe_{1-x}Ni_x)_2As_2$ than in its Co-substituted counterpart, but mainly because the suppression of the prefactor $j_0 \propto n_s e(\Delta/\hbar k_F)$ in Eq. (9.3) outweighs the increase in n_d (Δ is the superconducting gap amplitude). The surface impedance measurements performed on the optimally Ni-doped crystal before and after electron irradiation with 5.5×10^{19} cm^{-2}

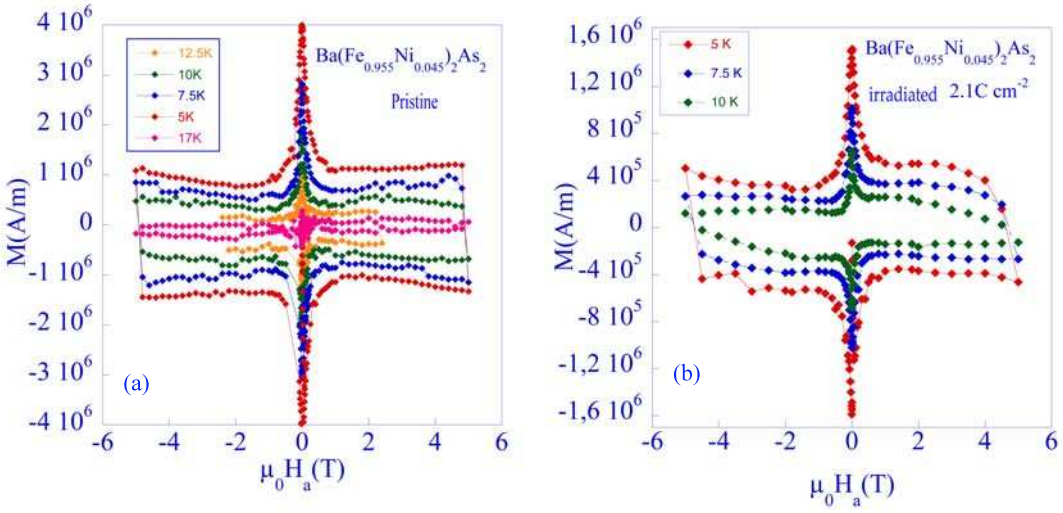

Figure 9.13 Single crystalline $Ba(Fe_{0.965}Ni_{0.045})_2As_2$: Hysteresis loops of the irreversible magnetization at 5 K, 7.5 K, 10 K, 13 K, 16 K (a) before and (b) after irradiation with 1.3 $\times 10^{19}$ cm^{-2} 2.5 MeV electrons. Decrease of the width of the magnetization loop in low-field, strong pinning regime and in higher field regime is observed after electron irradiation.

2.5 MeV electrons are depicted in Figure 9.15. As in $Ba(Fe_{1-x}Co_x)_2As_2$, the temperature dependence of the superfluid density of $Ba(Fe_{1-x}Ni_x)_2As_2$ changes little or not at all, even at the largest irradiation dose of 5.5×10^{19} electrons cm^{-2}.

9.4.3 $BaFe_2(As_{1-x}P_x)_2$

For comparison, magnetic measurements up to 2 Tesla for pristine and electron irradiated $BaFe_2(As_{1-x}P_x)_2$ single crystals were performed using Hall probe magnetometry technique by M. Konczykowski (see Chapter 4). The Inset to Fig. 9.16 shows an example of flux density gradients measured on a $BaFe_2(As_{0.64}P_{0.36})_2$ single crystal irradiated with 0.9×10^{19} electrons cm^{-2}, after zero field cooling and the application of an external field of 100 mT. The temperature dependence of the flux density gradient obtained after field-cooling in 400 mT, reduction of the applied field to the indicated target value, and subsequent warming is shown in the main panel of the Figure. Fig. 9.16 (b) shows the shift on the irreversibility line after irradiation with various electron doses.

The critical temperatures after electron-irradiation were determined as the extrapolation to zero of the "irreversibility field" $H_{irr}(T)$ above which the nonlinearity of the

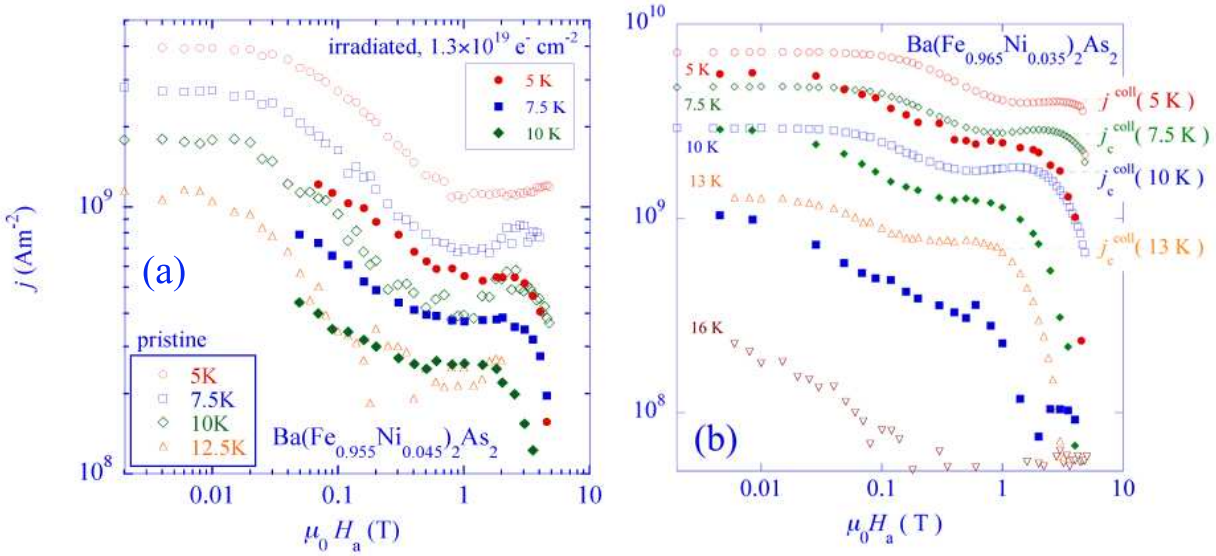

Figure 9.14 Sustainable current density j of (a)slightly overdoped $Ba(Fe_{1-x}Ni_x)_2As_2$ ($x = 0.045$) and (b) optimally doped $Ba(Fe_{1-x}Ni_x)_2As_2$ ($x = 0.035$) before (open symbols) and after irradiation at 21 K with 1.3×10^{19} cm^{-2} 2.5 MeV electrons (closed symbols) for (a) and with 5.5×10^{19} cm^{-2} 2.5 MeV electrons (closed symbols) for (b). The measurements were performed at 5 K, 7.5 K , 10 K , 11 K , 13 K , 16 K, and 17.5 K .

current-voltage characteristic – and therefore the critical current density – vanishes. Details on the determination of H_{irr}, can be found in, *e.g.*, Ref. [156]). In all cases, the $H_{irr}(T)$ values depend vary very little on the frequency of the ac field used to investigate the screening by the superconducting sample; the corresponding $T_{irr}(H)$ lie very close to the temperatures at which the dc screening current vanishes in Fig. 9.16. The T_c–values resulting from the extrapolation of $H_{irr}(T)$ to zero are gathered in Fig. 9.20. The T_c–depression as function of electron fluence is comparable to that in $Ba(Fe_{1-x}Ni_x)_2As_2$. Note that the resistivity increase of the irradiated $BaFe_2(As_{1-x}P_x)_2$ crystals corresponds to $\Delta R/R \sim 0.16$ [Ccm^{-2}]$^{-1}$, three times higher than $Ba(Fe_{1-x}Co_x)_2As_2$.

The hysteresis loops of the local flux density gradient measured on the pristine $BaFe_2(As_{0.77}P_{0.33})_2$ single crystal ad the same scystal irradiated at 23 K with 1.8×10^{19} electrons cm^{-2} is shown in Figure 9.17. The magnetic hysteresis loops for the pristine crystal shows the typical behavior for a strongly pinning superconductor with a central peak at zero field. After electron irradiation, the hysteresis loops open up due to the appearance of the field–independent collective pinning contribution from atomic-sized point defects (see Figure 9.18 (b)). The flux density gradient is directly proportional to the

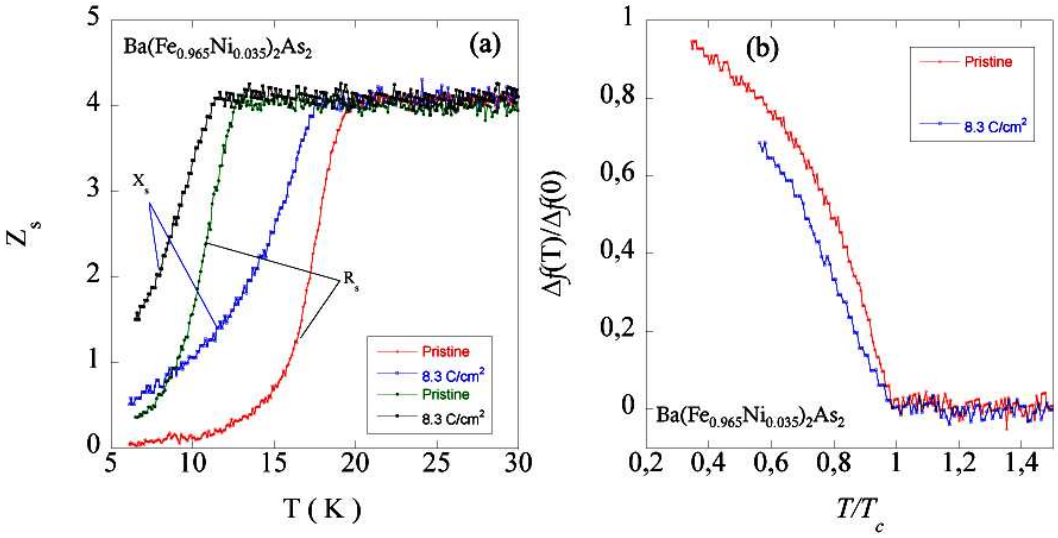

Figure 9.15 Surface impedance Z_s of $Ba(Fe_{0.965}Ni_{0.035})_2As_2$ crystal before and after irradiation runs with 2.5 MeV electrons 5.5×10^{19} e^- cm^{-2}, and subsequent annealing at 300 K. Data points show the surface resistance R_s and reactance X_s respectively. (b) Shift $\Delta f(T)$ of the resonant frequency of the superconducting Nb cavity, as function of temperature, normalized with respect to the low–temperature extrapolated $\Delta f(0)$, for $Ba(Fe_{0.965}Ni_{0.035})_2As_2$ crystal before and after irradiation.

sustainable current density j. As in $Ba(Fe_{1-x}Co_x)_2As_2$, the screening current in the irradiated crystal exceeds that of the pristine crystal at low temperature, but drops below it at higher temperature, due to the decrease of T_c. Fig. 9.19 shows the monotonic increase (at low temperatures) of j_c^{coll} as a function of irradiation dose, which allows one for a direct comparison with the theory for quasi-particle scattering mediated collective vortex pinning. Here we will assume again that the created defects by electron irradiation are Fe-vacancies. In this case the only unknown parameter, σ_{tr} will be the ionic cross–section of a Fe-vacancy, using this value in Eq. (9.3) yields a defect density of 0.0035 dpa / Ccm^{-2}. This number is taken as more precise than that obtained for $Ba(Fe_{1-x}Co_x)_2As_2$ in subsection 9.4.1, in which only two points were available. Note that the hypothesis of simple voids (non-scattering point defects) would necessitate an unphysical 1 dpa / Ccm^{-2} to explain the magnitude of the critical current density change. Measurements performed in Kyoto university on the isovalently substituted $BaFe_2(As_{1-x}P_x)_2$ single crystals show an appearence of a T^2 dependence of the absolute value of the London penetration depth

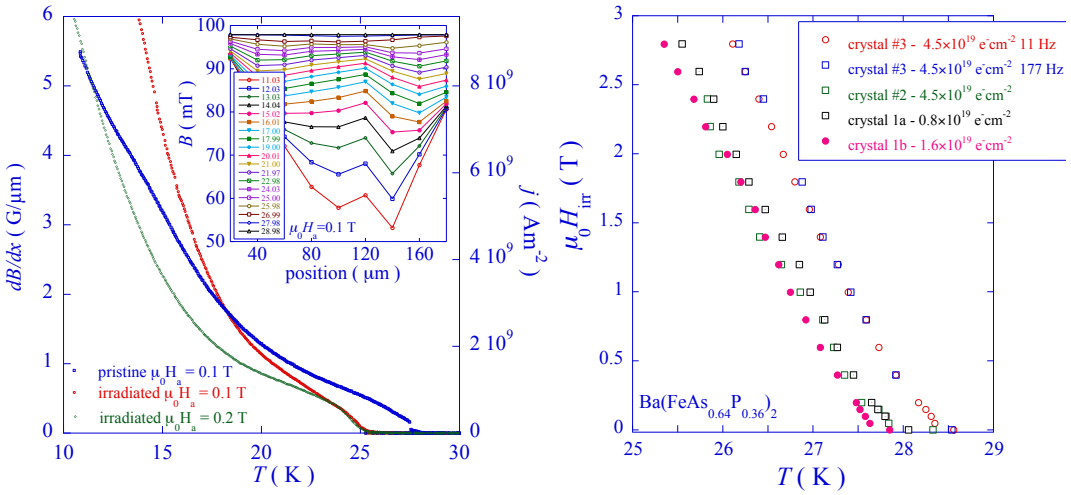

Figure 9.16 Temperature dependence of the flux density gradient dB/dx in a $BaFe_2(As_{0.64}P_{0.36})_2$ single crystal before and after irradiation with 0.8×10^{19} electrons cm^{-2}. Inset: Flux density profile across the crystal after zero-field cooling, application of the applied field $\mu_0 H_a = 100$ mT, and subsequent warming.

as a function of electron dose after electron irradiation. This is another indication of the controlled introduction of point like disorder into this system.

9.5 Discussion

The observed modifications after electron irradiation in the critical current density of the charge-doped $Ba(Fe_{1-x}Co_x)_2As_2$ and isovalently substituted $BaFe_2(As_{1-x}P_x)_2$ lead to the conclusion that the contribution to j_c apparent at high fields above 1 Tesla is indeed due to collective pinning by atomic-sized point defects [207]. We have estimated the defect generation of the electron beam at 0.35% dpa / Ccm^{-2}. In a first approximation we assume that the most relevant produced defects by electron irradiation are Fe vacancies, and that these vacancies are responsible for quasi-particle scattering mechanism which is at the origin of the weak collective pinning contribution to j_c. Our assumption is supported by the fact that scattering rates estimated for $Ba(Fe_{1-x}Co_x)_2As_2$ single crystals from the *in-situ* resistivity measurement are comparable to $\Gamma = n_d/[\pi N(0)]/\sin^2\delta_0$ estimated from the current density (see Table 3.1). It also turns out that scattering cross-section for Fe vacancies is comparable to that of Co and Ru impurities. Electron–irradiation of $Ba(Fe_{1-x}Co_x)_2As_2$ and $Ba(Fe_{1-x}Ni_x)_2As_2$ does not lead to important changes of the temperature dependence

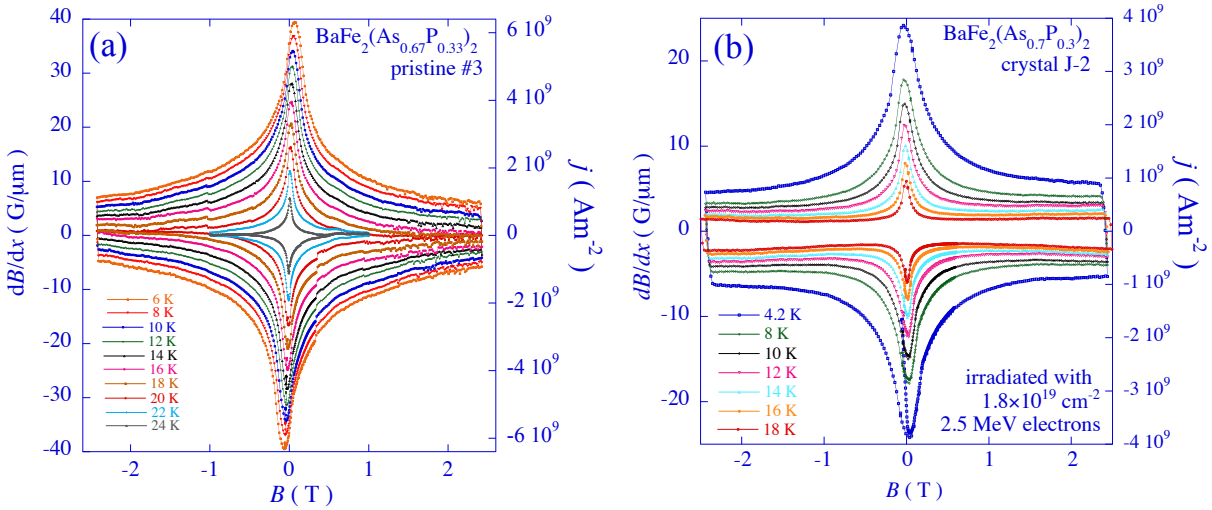

Figure 9.17 (a) Hysteretic loops of the local flux density gradient versus local induction B, measured on the surface of a pristine $BaFe_2(As_{0.67}P_{0.33})_2$ single crystal, at various temperatures (indicated). The astroid-shaped hysteresis loops are determined by the sole strong-pinning contribution to the critical current. (b) *ibid*, measured on the surface of a $BaFe_2(As_{0.7}P_{0.3})_2$ single crystal irradiated at 23 K with 1.8×10^{19} electrons cm^{-2}, at the indicated temperatures. The opening of the loops at higher flux densities reveal the emergence of a weak collective pinning contribution by the atomic–sized point defects introduced by the irradiation.

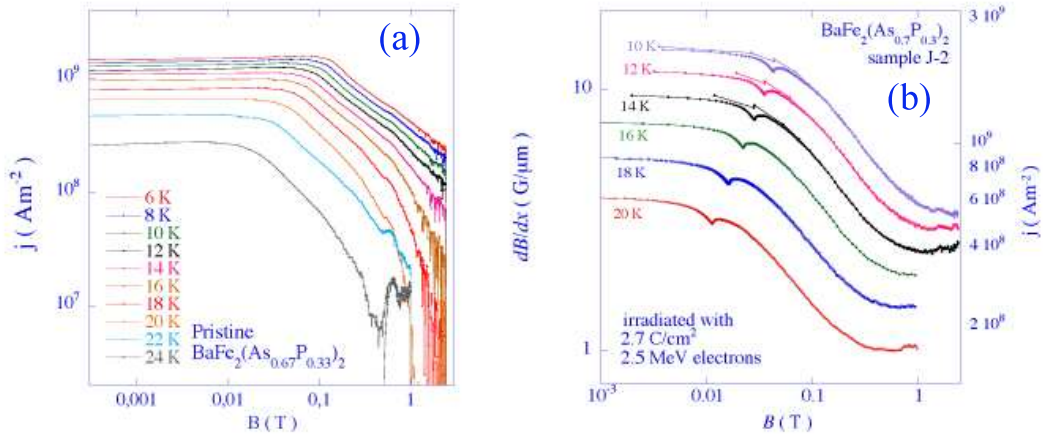

Figure 9.18 Sustainable current density as a function of applied field at various temperature (a) of pristine $BaFe_2(As_{0.67}P_{0.33})_2$ single crystal and (b) of $BaFe_2(As_{0.67}P_{0.33})_2$ single crystal # J-2 irradiated with electrons 2.5 MeV at 2.7 C/cm^2. Apparition of the in the the weak collective pinning contribution j_c^{coll} at higher field regime due to the introduction of point-like impurities by irradiation. The sustainable current density curves shown here were extracted from the hysteretic loops of the local flux density gradient shown in Figure 9.17.

of the superfluid density shown in the surface impedance experiments of those materials, which suggests that the effect of the dopant impurities overwhelms that of the defects added by the irradiation. For the exact confirmation of this hypothesis , larger electron doses are needed for further experiments.

The T_c suppression after irradiation on the underdoped $Ba(Fe_{1-x}Co_x)_2As_2$, $Ba(Fe_{1-x}Ni_x)_2As_2$ and $BaFe_2(As_{1-x}P_x)_2$ for a given dose are similar, while for the optimally doped $Ba(Fe_{1-x}Co_x)_2As_2$ the decrease is about twice less (see Figure 9.20). These observations leads to the question of possible nodal structure of the order parameter in the charge-doped $Ba(Fe_{1-x}Ni_x)_2As_2$, and, possibly, $Ba(Fe_{1-x}Co_x)_2As_2$, as it is known for the $BaFe_2(As_{1-x}P_x)_2$. The possibility was raised by different authors that nodal lines might exist on the α– (hole–like) sheet, at finite k_z [34; 126]. As it is mentioned above, controlled point-like impurities can be used to test this premise by particle irradiation or by chemical doping. Wang *et. al.* reported on the evolution of T_c in $Ba_{1-x}K_xFe_2As_2$ for Co-doping [147]. The suppression of T_c after electron irradiation of our optimally doped $Ba(Fe_{1-x}Co_x)_2As_2$ samples is comparable to that found for Co-doping reported by Wang

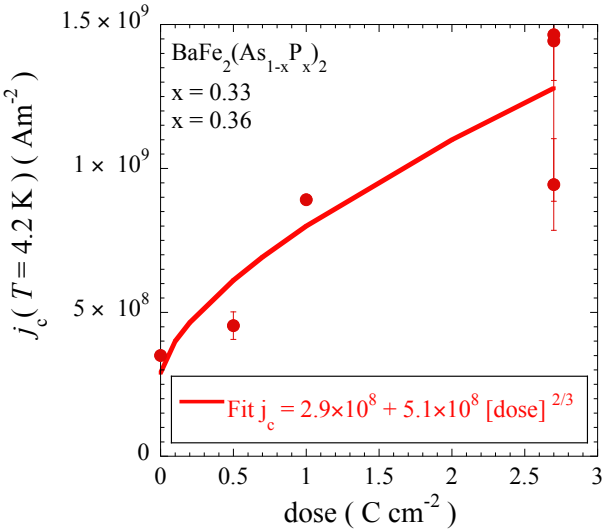

Figure 9.19 $BaFe_2(As_{1-x}P_x)_2$ (with $x = 0.33$, $x = 0.36$): Electron-fluence dependence of the weak collective pinning contribution j_c^{coll} to the critical current density. The drawn line denotes a fit to Eqs. (9.3,9.4). Assuming that the point defects most relevant for quasi-particle scattering are Fe vacancies induced by the irradiation, the parameter value 5.1×10^8 would correspond to 0.0035 dpa / Ccm^{-2}.

et. al., it is much less than that obtained by Co-doping of KFe_2As_2 studied by the same authors. A comparison with chemical doping gives the conclusion that the suppression in T_c for the underdoped $Ba(Fe_{1-x}Co_x)_2As_2$, $Ba(Fe_{1-x}Ni_x)_2As_2$, and $BaFe_2(As_{1-x}P_x)_2$ is similar to the Cu and Zn doping by those authors. Even if the comparison with chemical doping is tenuous, the observed trend clearly indicates a much weaker sensitivity of the materials studied here than what is expected for the scenario of $s_\pm$ superconductivity with strong interband scattering, and sets the three materials even further from the d-wave scenario. A comparison with the previous irradiation studies reveals that T_c–suppression after electron irradiation is somewhat weaker than the results obtained by Nakajima by 3 MeV proton irradiation of optimally doped $Ba(Fe_{1-x}Co_x)_2As_2$ [37] , and much weaker than in the α–particle irradiation of NdFeAs(O,F) by Tarantini *et al.* [37].

9.6 Conclusions

$Ba(Fe_{1-x}Co_x)_2As_2$ crystals of different doping levels x, as well as $Ba(Fe_{1-x}Ni_x)_2As_2$ and $BaFe_2(As_{1-x}P_x)_2$ crystals, have been irradiated with high energy (2.5 MeV) electron at low temperature (21 K). Annealing of created defects by electron irradiation is observed

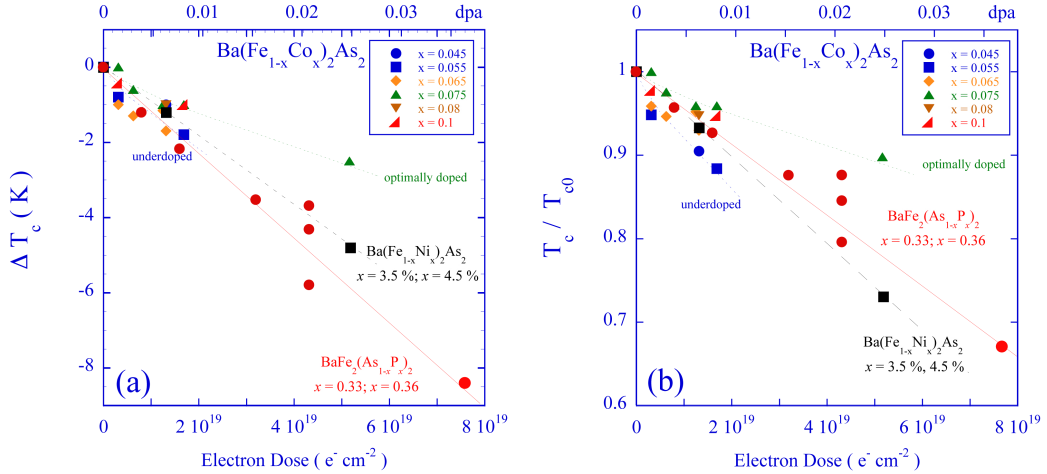

Figure 9.20 (a) Dose–dependence of the T_c–change of $Ba(Fe_{1-x}Co_x)_2As_2$, $Ba(Fe_{1-x}Ni_x)_2As_2$, and $BaFe_2(As_{1-x}P_x)_2$, after irradiation with 2.5 MeV electrons and annealing at 300 K. The upper scale shows the density of point defects (presumably Fe vacancies) added by the irradiation, such as determined from the dose-dependence of the critical current density of $BaFe_2(As_{1-x}P_x)_2$ (see Fig.9.19). (b) Dose dependence of T_c/T_{c0}, where T_{c0} is the critical temperature of the pristine crystal.

during the *in-situ* resistivity measurements performed on a $Ba(Fe_{1-x}Co_x)_2As_2$ single crystal. The enhancement of the weak-collective pinning contribution after irradiation in $Ba(Fe_{1-x}Co_x)_2As_2$ and its appearance in the isovalently substituted $BaFe_2(As_{1-x}P_x)_2$ in which it is absent in the pristine material, demonstrate that the irradiation produces atomic-sized point defects. These latter are at the origin of the collective pinning contribution to the critical current density due to quasi-particle scattering in the vortex cores. The increase in the magnitude of the weak collective pinning contribution is consistent with pinning by Fe vacancies created by electron irradiation. In charge-doped $Ba(Fe_{1-x}Co_x)_2As_2$ and $Ba(Fe_{1-x}Ni_x)_2As_2$ the introduction of point-like impurities does not lead to a significant difference in the temperature dependence behavior of the superfluid density suggesting that the pre-existing point-like disorder due to the dopant atoms in these systems counterbalances the artificially introduced point-like impurities. For the case of isovalently substituted $BaFe_2(As_{1-x}P_x)_2$, an induced T^2 behavior by electron irradiation is observed on penetration depth measurements performed by Shibauchi *et. al.* in parallel to the work presented in this thesis.

Surprisingly, the critical temperature is similarly suppressed in all three materials. This, in spite of the fact that the order parameter in $BaFe_2(As_{1-x}P_x)_2$ is thought to have line nodes, while this possibility is much less certain in the other two materials. The

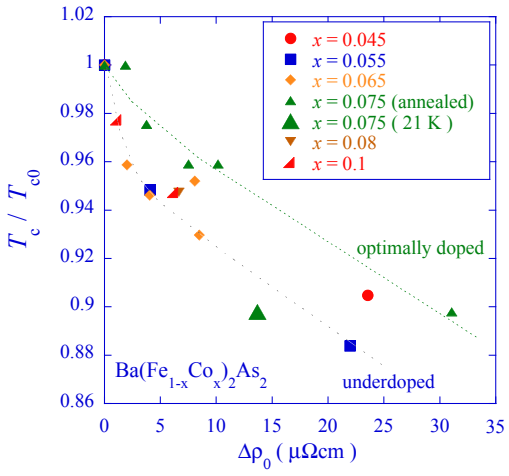

Figure 9.21 Reduced critical temperature versus disorder induced resistivity change for different crystals of $Ba(Fe_{1-x}Co_x)_2As_2$.

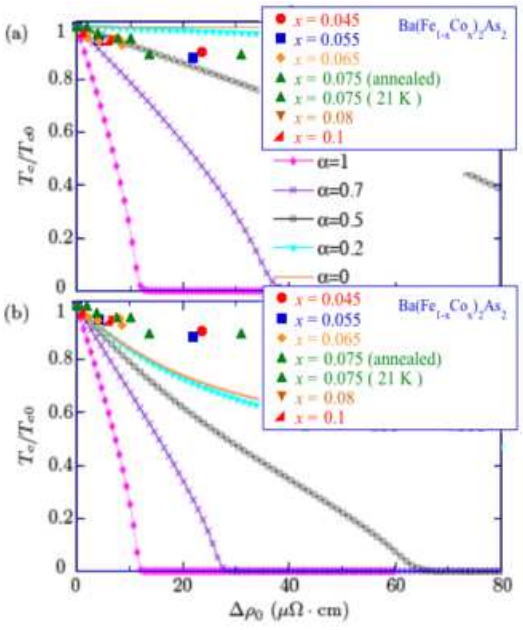

Figure 9.22 (a) Normalized critical temperature T_c/T_{c0} vs. disorder-induced resistivity change $\Delta\rho_0$ for isotropic $s_\pm$ wave paring for various values of the inter-/intraband scattering ratio α (b) for anisotropic (nodal) $s_\pm$ wave paring.

results therefore lend credence to evidence for line nodes obtained from c-axis penetration depth [34] and thermal conductivity measurements [126]. Figure 9.21 presents the reduced critical temperature change versus disorder induced resistivity change for different crystals of $Ba(Fe_{1-x}Co_x)_2As_2$. We have compared these results to the theoretical work [274] of Wang *et. al.* where they discussed how it is possible to distinguish the $s_{\pm}$ gap structure from s_{++} gap structure in iron based superconductors. In Fig. 9.22 is presented the fit of our results shown in Fig. 9.21 with the results proposed by Wang *et. al.* for the case of a nodeless $s_{\pm}$ gap symmetry and nodal $s_{\pm}$ gap symmetry. Our results are in consistence with the case of nodeless $s_{\pm}$ gap symmetry with a ration to intra-inter band scattering of α=0.5.

Chapter 10

Summary

In order to characterize the disorder in iron-based superconductors, several experimental techniques have been used in this thesis. The first one, introduced in Chapter 4, is the magneto-optical imaging technique which allows one to identify the spatial heterogeneity of the critical current density; this cannot be neglected for an accurate interpretation of further experimental results. Using the magneto-optical imaging technique in the differential mode, maps of the magnetic flux distribution were established from the low temperature to the critical temperature T_c. This work, performed on single crystals of $Ba(Fe_{1-x}Co_x)_2As_2$, $Ba(Fe_{1-x}Ni_x)_2As_2$, $Sr(Fe_{1-x}Co_x)_2As_2$ and $BaFe_2(As_{1-x}P_x)_2$, allows one to also establish the spatial distribution of T_c.

The guiding principle in this manuscript is the characterization of flux pinning for the identification of the type of disorder. The Bitter decoration technique, described in Chapter 5, is used for the imaging of the vortex ensemble in different compounds of the 122-type family.

In Chapter 6, a study of the flux pinning properties in charge-doped $Ba(Fe_{1-x}Co_x)_2As_2$ is presented. The highly disordered vortex ensembles observed in the Bitter decoration images is studied using a novel data analysis technique, that takes into account the interaction of individual vortices with their neighbors. In the latter, the pinning energies and pinning forces of each vortex are extracted from distribution the of vortices at small magnetic fields. We then correlated our Bitter decoration datas with critical current measurements. The spatial heterogeneity of T_c revealed in the DMO images of the decorated samples allows one to pinpoint the origin of the amorphous vortex structure in single crystalline $Ba(Fe_{1-x}Co_x)_2As_2$. Heterogeneity of the superconducting properties is found to explain these ensembles, with inhomogeneity on the nm scale the origin of the strong pinning mechanism at the origin of the low-field critical current. Namely, the low-field value of the critical current density can be explained as being due to the same material inhomogeneity

that gives rise to the disordered vortex configurations [46; 206].

In Chapter 7, we present a systematic study of the flux pinning, using the same data analysis procedure, in the isovalently substituted $BaFe_2(As_{1-x}P_x)_2$. Vortex ensembles with less vortex density fluctuations are observed in this compound. The pinning forces and pinning energies extracted from the Bitter decoration images are analyzed. It is found that they can be analyzed to yield a mean distance between effective pins of about 90 nm, that increases when one increasing the P content x. This result is found in nice agreement with the work of Shishido *et. al.* on the influence of the disorder o the normal state properties of the same material. Namely, they reported that the mean free path of the β orbits increases from $l \sim 20$ nm to 80 nm when the P content x varies from $x = 0.41$ to 1 [97].

The "weak collective pinning" contribution is also considered for all studied compounds. This pinning mechanism was proposed to arise from the quasiparticle in the vortex cores; it manifests itself as a second plateau, at magnetic fields above a few tenths of a T to 1 T. In the attempt to link the flux pinning properties in this regime to the quasi-particle scattering rate, a new experimental set-up based on the cavity perturbation technique described in Chapter 8 is established for the measurements of surface resistance R_s. In addition to this, additional atomic-sized point like defects are introduced using high-energy 2.5 MeV electron irradiation with the Pelletron accelerator SIRIUS [106] of the Laboratoire des Solides Irradiés. The introduction of such atomic sized point-like defects (vacancies,interstitials) by this kind of particle irradiation is shown to, indeed, enhance the weak collective pinning contribution to the critical current, at least in $Ba(Fe_{1-x}Co_x)_2As_2$.

In Chapter 9, we present a study on the evolution of different superconducting properties under the effect of electron irradiation for $Ba(Fe_{1-x}Co_x)_2As_2$, $Ba(Fe_{1-x}Ni_x)_2As_2$, and $BaFe_2(As_{1-x}P_x)_2$ single crystals. An important annealing effect (70% of defects) is revealed for $Ba(Fe_{1-x}Co_x)_2As_2$ when the crystals are heated to 300 K after low-temperature irradiation. The critical temperature is found to decrease similarly as function of dose for all investigated materials, namely, 5% dpa induces a decrease of T_c by approximately 30 %. From the increase of the weak collective pinning contribution, the number of defects created by the irradiation (Fe vacancies) is estimated. In isovalently substituted $BaFe_2(As_{1-x}P_x)_2$, the initially absent weak collective pinning contribution appears after irradiation. The measured surface impedance for Co and Ni-doped 122 compounds before and after electron irradiation increases . These results allows one to confirm the role of the atomic sized point-like defects as scatterers in iron-based superconductors, as well as the hypothesis that these defects are at the origin of the weak collective pinning contribution to j_c.

Appendix A

I include here the Matlab codes used for the calculation of the interaction energy and the pinning force.

```
close all
clear all

cd '/Users/sultandemirdis/DATAS/Bitter Decoration/2011/datas DECOS/COMP
BSCCO/IM 30'
lambda1=0.3; %en µm
lim=6*lambda1;

M=load('30A.txt'); %matrice en µm ordonnée sur la 2eme colonne
E=[];
Dist=[];
B=[];

figure(1)
plot(M(:,1),M(:,2),'.');

for i=1:size(M,1)
    Xc=M(i,1);
   Yc=M(i,2);


J1=find(M(:,2)<Yc+lim);
J2=find(M(:,2)>Yc-lim);
J=[J2(1):J1(end)];

Mo=[M(J,1),M(J,2)];

[Mor1,H]=sort(Mo(:,1));

Mor=[Mor1,Mo(H,2)];


I1=find(Mor(:,1)<Xc+lim);
I2=find(Mor(:,1)>Xc-lim);
I=[I2(1):I1(end)];

M1=[Mor(I,1),Mor(I,2)];

% hold on
% plot(M1(:,1),M1(:,2),'.r');


D=[];

for k=1:size(M1,1)

    d=sqrt((Xc-M1(k,1))^2+(Yc-M1(k,2))^2);% en µm

    D=[D,d];

end
x=find(Dist>0);
Dist=Dist(x);
Dist=[Dist,D];



y=find(D>0);
D=D(y);

phi=2.067*10.^-15;
mu=4*pi*10^-7;
lambda=0.3*10^-6
eint=phi^2/(2*pi*mu*lambda^2)*besselk(0,D./lambda1);
b=besselk(0,D./lambda1);
```

```
%figure(2)
%hold on
%plot(D,b*0.1278,'.');
%hold off

Eint=sum(eint);
E=[E,Eint];
end



%Nor = E-min(E); %normalize E entre 0 et 1
%Enorm = Nor./max(Nor);

Mf=[M,E'];
save(['XYEint.txt'],'Mf','-ascii','-double', '-tabs')
E0=1.69*10.^-12
figure(3)
colormap(jet(100));
scatter(M(:,1),M(:,2),30,E/E0,'filled')
colorbar


figure(4)
hist(Dist,50);%mettre le facteur de calibration en µm
```

```
close all
clear all

cd '/Users/sultandemirdis/Desktop/datas DECOS/0.49/IM39/700NM'
lambda1=0.7*10^-6; %en µm
lim=4*lambda1;

M=load('39F.txt'); %matrice en µm ordonnée sur la 2eme colonne
E=[];
Dist=[];
Force=[];

figure(1)
plot(M(:,1),M(:,2),'.');

for i=1:size(M,1)
    Xc=M(i,1);
   Yc=M(i,2);


J1=find(M(:,2)<Yc+lim);
J2=find(M(:,2)>Yc-lim);
J=[J2(1):J1(end)];

Mo=[M(J,1),M(J,2)];

[Mor1,H]=sort(Mo(:,1));

Mor=[Mor1,Mo(H,2)];


I1=find(Mor(:,1)<Xc+lim);
I2=find(Mor(:,1)>Xc-lim);
I=[I2(1):I1(end)];

M1=[Mor(I,1),Mor(I,2)];

% hold on
% plot(M1(:,1),M1(:,2),'.r');


D=[];

for k=1:size(M1,1)

    d=sqrt((Xc-M1(k,1))^2+(Yc-M1(k,2))^2);% en µm

    D=[D,d];

end
x=find(Dist>0);
Dist=Dist(x);
Dist=[Dist,D];



y=find(D>0);
D=D(y);

phi=2.067*10.^-15;
mu=4*pi*1^-7;
lambda=0.7*10^-6;
eint=phi^2/(2*pi*mu*lambda^2)*besselk(0,D./lambda1);
b=besselk(0,D./lambda1);
```

```
Fx=[];
Fy=[];

for k=1:size(M1,1)
Fix=(7.43*10^-7)*(1./D).*besselk(1,D/lambda)*(M1(k,1)-Xc);
Fiy=(7.43*10^-7)*(1./D).*besselk(1,D/lambda)*(M1(k,2)-Yc);
Fx=[Fx,Fix];
Fy=[Fy,Fiy];

end

F1x=sum(Fx);
F1y=sum(Fy);
F1=sqrt((F1x)^2+(F1y)^2);

Force=[Force,F1];
%save(['Force.txt'],'Force','-ascii','-double', '-tabs')



%figure(2)
%hold on
%plot(D,b,'.');
%hold off

Eint=sum(eint);
E=[E,Eint];
end



%Nor = E-min(E); %normalize E entre 0 et 1
%Enorm = Nor./max(Nor);

%Mf=[M,E'];
%save(['XYEint.txt'],'Mf','-ascii','-double', '-tabs')
E0=6.67*10.^-13
figure(3)
colormap(jet(100));
scatter(M(:,1),M(:,2),30,E/E0,'filled')
colorbar

Mf=[M,Force'];
save(['XYForce.txt'],'Mf','-ascii','-double', '-tabs')

figure(5)
colormap(jet(100));
scatter(M(:,1),M(:,2),30,Force,'filled')
colorbar
figure(6)
hist(Force,70)
```

. APPENDIX A

Appendix B

B.1 Heat Transfer

In the following I discuss possible energy transfer contributions that one should take into account during the design process of a cryostat.

B.1.1 Thermal conduction in a solid body

Heat transfer by conduction inside a solid is described by Fourier's law [87]. This equation expresses the transmitted power via thermal conduction between two different points which are at different temperatures. The one-dimensional form for the thermal current $\dot{Q}$ is given by

$$\dot{Q} = -k_t A \frac{dT}{dx}, \tag{1}$$

where k_t is the thermal conductivity of the material.

To simplify the study on heat transfer via conduction, we can assume a static model system in one dimension; Eq. (1) can then be written as

$$\dot{Q} \frac{dx}{A(x)} = -k_t dT \tag{2}$$

In the stationary regime the heat transfer is constant. Then Eq. (2) can be integrated. The integration limits x_h, and x_c correspond respectively to the position on the hot surface with temperature T_h, and to the position on the cold surface with temperature T_c.

$$\dot{Q} \int_{x_h}^{x_c} \left(\frac{dx}{A} \right) = - \int_{T_h}^{T_c} k_t \, dT = + \int_{T_c}^{T_h} k_t \, dT \tag{3}$$

Therefore,

$$Q = \frac{\int_{T_c}^{T_h} k_t \, dT}{\int_{x_c}^{x_h} \left(\frac{dx}{A}\right)} \tag{4}$$

where $\int_{x_c}^{x_h} \left(\frac{dx}{A}\right)$ is a geometrical factor that determines the heat transfer through a material under the effect of a temperature gradient. For a bar with a length l and a cross-sectional area A, Eq. (4) becomes

$$\dot{Q_{con}} = \frac{A}{l} \int_{T_c}^{T_h} k_t \, dT. \tag{5}$$

B.1.2 Thermal conduction in a gas

Thermal conduction in a gas is ensured by two well-defined regimes separated by a transition zone.The characteristic parameter separating this two regimes is the mean free path of the molecules L_p. Assuming that d is the distance between two walls held at temperatures T_1 and T_2 we will have :

classical conduction if $L_p \ll$ d
molecular conduction if $L_p \gg$ d
a transition zone for $L_p \simeq$ d.

In the classical conduction regime L_p is independent of the pressure and the heat exchange is satisfied by the collisions of molecules. For molecular conduction at very low pressures where the mean free path is now much larger than the distance d $L_p \gg$ d the heat transfer is essentially satisfied by the collisions of the molecules with the walls. In this latter case the thermal exchanges are proportional to the quantity of gas, and therefore to the pressure between the two walls. This thermal transfer mode is the most relevant case at low pressures. The mean free path of the molecules is given by [201]

$$L_p = 8.6 \times 10^3 \frac{\eta}{p} \sqrt{\frac{T}{M}}. \tag{6}$$

Here L_p[cm] is the mean free path, η[P] is the viscosity in (P=poise= 1g.cm^{-1} s^{-1}) at temperature T, P[μHg] is the pressure ,T[K] is the temperature and M is the molecular mass in unit of g.mole^{-1}. The conduction in a gas between two spherical or cylindrical surfaces at different temperatures is given by the formula of Knudsen [242], and Kennard [67] as

$$\dot{Q}_{gas\,cond} = k a_0 P A_i \Delta T, \tag{7}$$

where k is a constant (k=1.2 for air), P[Pa] is the pressure between two surfaces, A_i[cm^2] is the surface area ΔT[K] is the temperature difference and a_0 is a non dimensional constant related to the surface conditions; it has a value of 1 for classical geometries.

B.1.3 Contribution from convection

The contribution from convection to heat flow comes from the heat transfer incurred by the displacement of a fluid from a hot surface to a cold surface. There are two types of convections. One is forced convection, when the fluid is pumped, and the second one is natural convection which occurs when there is movement of the fluid due to a difference in density . In both cases, contribution to heat flow is given by

$$\dot{Q_{conv}} = h_c A(T_s - T_f) \tag{8}$$

here h_c is the transfer coefficient, T_s is the temperature at the surface and T_f is the temperature of the fluid. However, we are working in our case with a system which is under vacuum, i.e., the density of gas molecules is very low. Therefore, we will neglect the contribution from convection.

B.1.4 Contribution from radiation

The predominant contribution to heat transfer inside a cryostat is the contribution from thermal radiation. It is necessary to understand how this contribution acts. By definition, a thermal radiator is a black body. A black body is an idealizes physical body that absorbs all incident electromagnetic radiation, regardless of frequency or angle of incidence. In thermal equilibrium, it is an ideal emitter: it emits as much or more energy at every frequency than any other body at the same temperature. It is also a diffuse emitter: the energy is radiated isotropically, independent of direction. Wien's displacement law states that there is an inverse relationship between the wavelength λ_{max} at the peak of the emission of a black body and its temperature. Planck's law describes the energy distribution W(λ) radiated as a function of temperature T of the black body. From Planck' law this energy has a maximum value W_{max} at λ_{max}. Wien's law describes the relation between λ_{max} and the temperature T; it is given by

$$\lambda_{max} = \frac{hc}{4.965kT} = \frac{2.898 \times 10^{-3}}{T}, \tag{9}$$

where h is Planck's constant, k is Boltzmann's constant and c is the velocity of light.Thus we can define Wien's constant

$$\lambda_{max} T = 2897.8\mu \ m.K \tag{10}$$

In addition, one can also obtain the Stefan-Boltzman law: the total energy radiated per unit surface area of a black body per unit time for all wavelength by integrating Planck's equations

$$q = \sigma T^4; \tag{11}$$

here σ=5.669 $\times$ 10^{-8} W/m^2.K^4 is the Stefan-Boltzman constant. Real materials emit energy at some fraction of q, called the emissivity the radiation. By definition, a black body in thermal equilibrium has an emissivity of ϵ=1. A source with lower emissivity independent of frequency often is referred to as a gray body. apart from the emissivity there are characteristic properties of the gray body such as the absorption, the reflectivity and the transmittivity. The emissivity is the ratio between the energy emitted by a surface at a given temperature T, and the emitted energy at the same temperature by a black body. The reflectivity is the ratio between reflected energy from the surface and the incident energy. The transmittivity is the ratio of energy transmitted through the material and the incident energy. In general these properties depend on the wavelength, but here we only focus on the emissivity of our materials. We shall see that the power transmitted by radiation is directly proportional to the emissivity of the surface. When two gray bodies exchange radiative energy, a part of the emitted energy is not intercepted by the surface. The radiation configuration factor F_{i-j} describes the influence of radiation when two surfaces have a radiative exchange. This factor is defined as the ratio of the energy coming from surface 1, and the energy intercepted by surface 2. If the energy emitted by surface 1 is totally absorbed by surface 2, one will have F_{1-2}. Stefan-Boltzman's equation has to be modified in order to take this factor and the emissivity of the surfaces into account,

$$Q_R = EF_{1-2}\sigma A_{cold}(T_{hot}^4 - T_{cold}^4). \tag{12}$$

From this expression we can see that the contribution from thermal radiation is proportional to $\sim T^4$ and to the area of the cold surface A_{cold}, in order to reduce this contribution we installed some thermal screens between radiation emitter and receptor surfaces in our design.

B.1.5 Multi layer insulation of the cryostat

We have seen previously the thermal benefit of the installation of a screen inside the cryostat to reduce thermal radiation. If we consider n interposed screens the transmitted power by radiation will be divided by n+1. This is why it is recommended to use multi layer insulation, very thin sheets of Al or aluminized mylar separated by veils of fiber glass or nylon.

Figure 1 Multi layer insulation of the outer gold shielded copper screen with Al sheets

The thin sheets of mylar are contacted to the nylon veils only by some points . The thickness of the mylar sheets is of the order of 10 μm; they are covered by 0.02 μm of evaporated Al. One should take into account that even the slightest area not covered will react like a gray body and will cancel the positive effect of the superinsulation (see Figure 1) .

B.2 Description of the cryostat

Figure 2 shows a schematic view of our home designed cryostat housing the pulsed tube cryocooler. For the experiment presented here we used a commercial two stage pulsed tube SRP-052A series from SHI (Sumimoto Heavy Industries) Cryogenics group. This pulsed tube has a cooling capacity of 20W in the first col stage at 45K and 0.5W at the second cold stage at 4.2K. Figure 2 shows the outer stainless steel screen, as well as the two copper thermal screens which are gilded to avoid thermal radiation inside the cryostat. The red arrows indicate the thermal contribution from radiation and thermal conduction through

solid components, the amount of which needs to be known to compile the total contributed power, which influences the different cold stages.

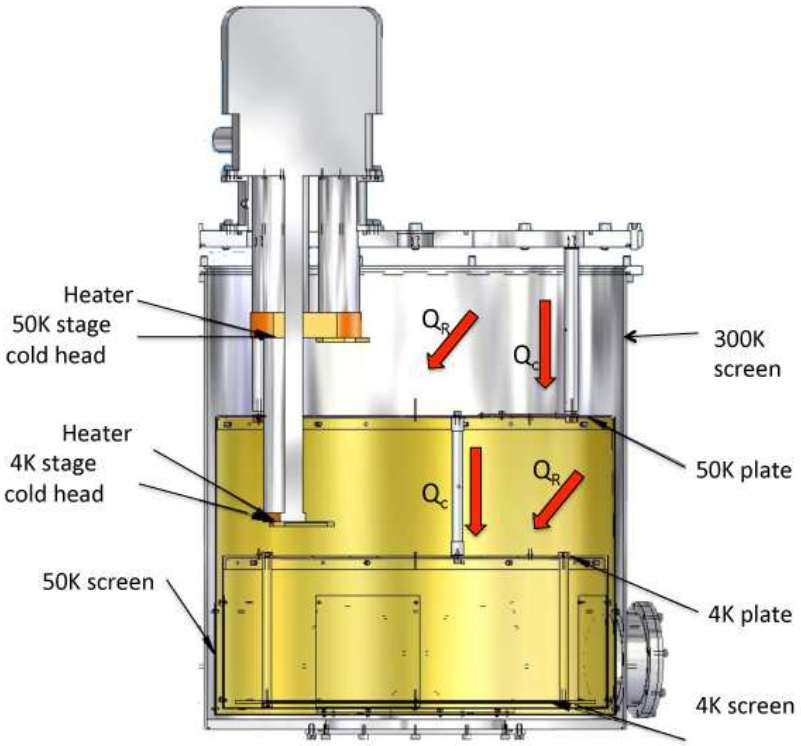

Figure 2 Schematic cross sectional view of the cryostat, red arrows indicate the heat flows by radiation Q_R from the screens and by conduction Q_C through different solid components

B.2.1 Power contribution from conduction through solids

The heat flow by thermal conduction through different components connected between the 300 K and the 50 K and 50 K and 4 K stages is calculated for the dimensioning of the cryostat. First one has to take into account the power contribution between 300K and the first cold stage at 50 K. The solid components involved are the three bars connected between the 300 K and 50 K stages (see fig. 3). These are made of stainless steel with a length l=18.2 cm and diameters ϕ_{in}=1.3cm, ϕ_{out}=1.5cm. Using eq. 5 we find a contribution of Q_{con}=2.121 W. The same procedure is used for the three fiber glass bars connecting the 50K and 4K stages. For three bars (see fig. 3) of length l=14.95cm and diameters ϕ_{in}=1cm, ϕ_{out}=1.2cm one obtains a power contribution of Q_{con}=5.86 mW.

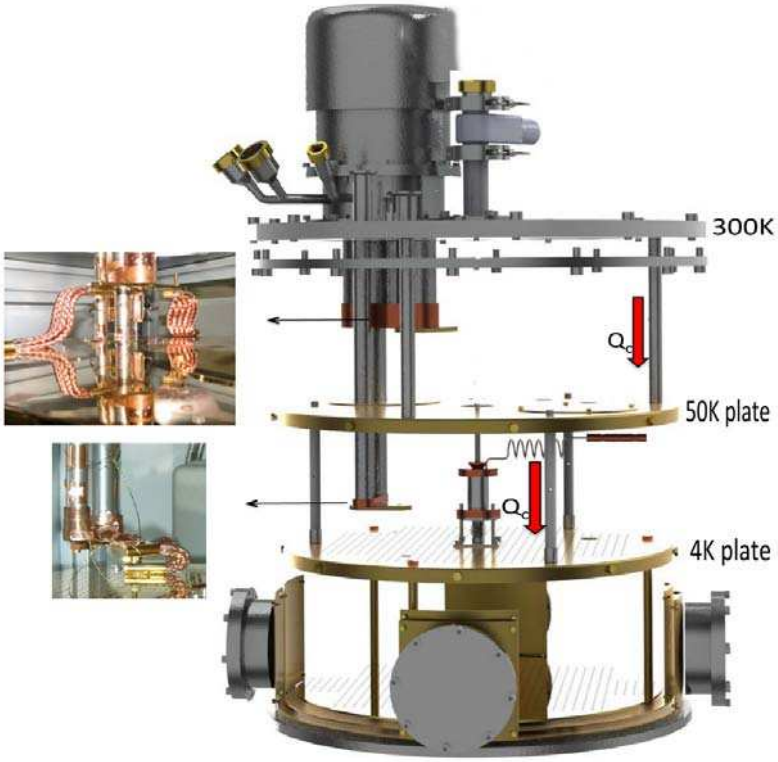

Figure 3 A rendered view from the drawings of the cryostat; red arrows indicate the heat flow by radiation from the screens. Photographs show the copper braids mounted between the two cold stage of the pulse tube, and the 50 K, and 4 K plates of the cryostat.

B.2.2 Power contribution from radiation

As we discuss in section B.1.4 the power transmitted by thermal radiation depends directly on the emissivity, which is defined as the ability of the involved surface to emit energy by radiation . We will consider the emissivity of different surfaces which act as gray bodies inside the cryostat. Lets consider the power transmitted from the outer stainless steel screen at 300 K with a diameter ϕ=0.464 m and an length l= 0.48 m and the inner copper screen at 50 K with diameter ϕ=0.444 m and length l= 0.32 m. We have extracted the emissivity between cylindrical surfaces from the following formula

$$E = \frac{\varepsilon_1 \varepsilon_2}{\varepsilon_2 + \frac{S_1}{S_2}(1-\varepsilon_2)\varepsilon_1}, \tag{13}$$

where ε_1=0.025 and ε_2=0.15 are respective emissivities of the cylindrical walls, and S_{cold} and S_{hot} are the respective areas of the surfaces.

. APPENDIX B

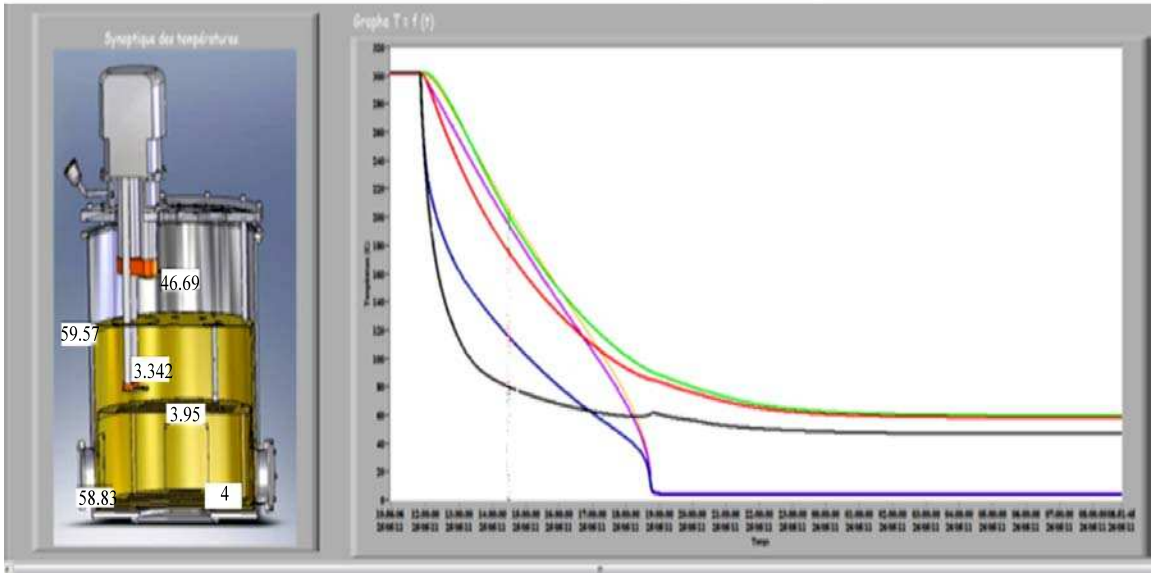

Figure 4 A screen shot of the labview program which shows the evolution of the temperatures of different cold stages inside the cryostat

Using eq. 12 one obtain Q_R=7.832 W for the transmitted power between the 300 K and 50 K screens. The same procedure for the transmitted power via radiation between the 50 K and 4 K screens yields a power o $\dot{Q}_R$=13.88 mW ($\varepsilon_1 = \varepsilon_2$=0.025 and). Figure 4 shows a screen shot of the Labview interface where we can follow the evolution of the temperature measured with diodes placed at different stages of the cryostat. The lowest temperature reached at the second cold stage after a cooling process which takes ∼10 hours is ∼ 4 K. This value of the stable temperature at the second cold stage is a consequence of the balance (compensation) between the power provided by the pulsed tube to the system, and the different power contributions by conduction through components or by thermal radiation.

Power test on the pulsed tube were performed to determine how much power the pulsed tube needs to provide for the system to be stabilized at 4 K. In figure 5 shows the constructor as well as the experimental power curves belong the pulsed tube used in our cryostat. We see from the experimental curve that the pulse tube provides 500 mW to stabilize the second cold stage temperature at 4 K. We will use this value in the following sections for our calculations.

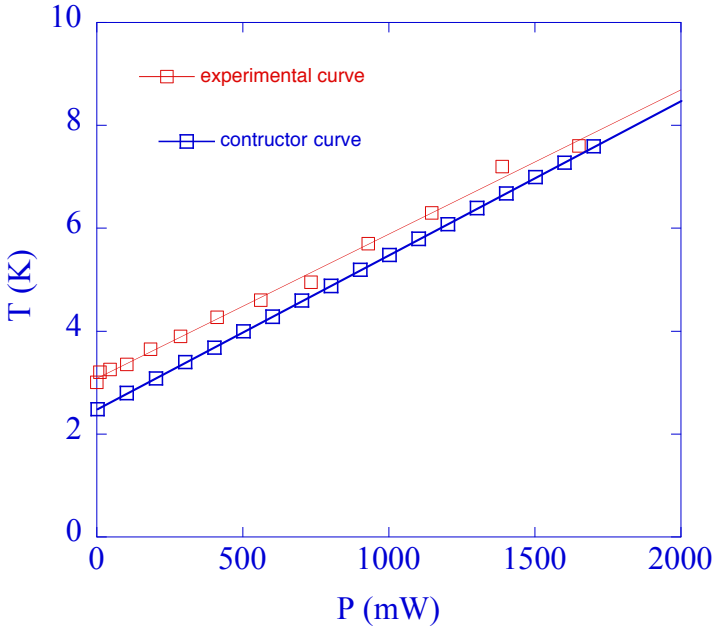

Figure 5 Power curves belong to the pulse-tube mounted on the cryostat

B.3 Dimensioning of the gas switch

The gas switch is most particular part of our cryostat, since this part will allows the sample to be cooled through the insertion on the top surface of the inner Cu tube in which the sample holder will be inserted . The thermal contact between the two conical surfaces will ensure the thermal flow between the top of the switch and the sample holder (see Figure 6). In this figure one can see a cross sectional cut of the gas switch presenting the inner homocentric tubes, and the charcoal pump mounted on it, in the right-hand panel a view of the sample holder .

The He gas switch is mounted on top of a support (see Figure 8.5) screwed to the Nb resonant cavity through the the 4K plate. Thus the warm sample is separated from the superconducting Nb (T_c =9K) cavity which can therefore be stabilized at low temperature. This is very important for surface resistance measurements.The bottom part of the switch is also stabilized at 4 K using three copper braids connected to the 4 K plate (see Figure 8.5). If we perform a simple calculation for the heat conduction through the three copper braids which contain 3900 wires with radius 0.07 mm and which are connected between

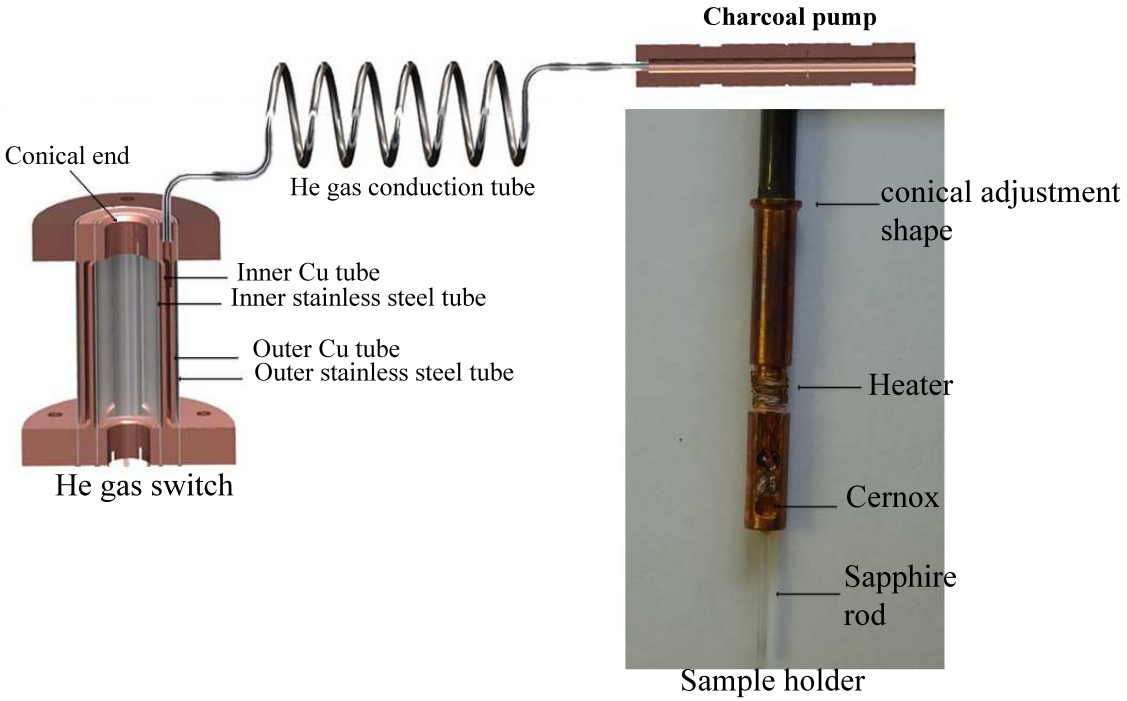

Figure 6 A cross sectional rendered view from the drawings of the gas switch, and a photograph of the sample holder with the sapphire rod.

the cold plate held at T_1=4K and the bottom of the switch at temperature T_2. One can obtain from $Q_{con}=\frac{A}{l}\int_{T_1}^{T_2} k_t\, dT$ that T_2=4.2K (see Figure 8 for the integral value table).The temperature on the top of the gas switch determines that of the sample , which is in thermal contact with it. To estimate the temperature that can be obtained on the top of the switch , let us consider the different power contributions from radiation, conduction, or from the heater. For the first, consider the total radiation received by the 4K plate (with a radius of 426 mm), and which is housed under the same conditions as the switch. From the equation of heat transfer by thermal radiation, $Q_R=EF_{1-2}\sigma\ A_{cold}(T_2^4 - T_1^4)$ one obtains Q_R=500mW for the 4K plate. If we consider that this value is directly proportional to the surface area, and that other parameters are the same, one can assume that the top of the switch which has a radius of 44 mm will receive a thermal radiation of $Q_R \approx 50$ mW is ten times smaller than that of the 4 K plate (see Figure 9 for the emissivity value table).

The charcoal pump, connected to the switch with a stainless steel tube contains small grains of activated charcoal that have the property of absorbing He gas at low temperatures

and desorbing it when it is heated above 20 K. In our conception, we need to use both properties of the activated charcoal, therefore we thermalize the pump on the 4 K plate by connecting it with copper wires, and we install an heater on it for the desorption of He gas above 20K. For two copper wires of diameter 1mm the thermal flow by conduction will be Q_{con}=5mW . This value tells us the amount of power that we should apply with the heater of the pump to proceed to the desorption of the He gas. The latter gives us the power contribution from conduction to the switch; thus we have the total power contribution $Q_{tot}= Q_{IR^2}+ Q_{Rad} +Q_{wires} \approx 60$mW, here we neglect the conduction through the different wires (for the heater on the pump and/or the temperature probes) which are thermalized along the 4K plate.

To know the temperature that can be reached on the sample holder we have to consider the conduction inside a gas in switch on mode. The total power received by the switch will then flow through the He gas between the concentric tubes. We need first to known in which conduction regime we are when we consider the conduction by the a gas: this can be the laminar or the molecular regime (see section B.1.2). Proceeding to the calculations for both cases we shall try to deduce in which we can expect to reach low temperature on top of the switch (in switch on mode: desorption of the He gas). One can obtain for the transition pressure of He P=1×10^{-4} mbar from Equation (6) [201]. Lets consider the conduction in the gas for the first case where the internal pressure is P$\ll$P$_a$ and $l_p \gg$d (here d=1×10^{-3}m is the distance between two walls inside the switch), this is the molecular conduction regime .

From Equation 7), and taking $P = 1\times 10^{-3}$ bar and A=2054.5×10^{-6}m^2 as the average value of the opposed surface areas the result is ΔT=10^6 K which is irrealistic for our case. Therefore we must be in the laminar conduction regime , and the pressure that we should apply inside the switch has to be comparable to the atmospheric pressure. In this regime the mean free path is smaller that the inter-wall distance L$_p\ll$d, and the conduction by the gas is independent of the pressure. One can obtain the temperature on top of the switch if we consider the equation Q_{con}=k$_t$ $A\,\frac{\Delta T}{d}$, here T$_1$=4.2K, the inter-wall distance d=1×10^{-3}m, and A is the average of the opposed surface areas. From this calculation one obtains T$_2\approx$5K on the switch top (in switch on mode) due to the conduction in the He gas. This result is in agreement with the experiment as can be seen on the screen shot of the Labview program front panel that we use for reading the temperatures of diodes see Figure 7. Therefore it is possible to obtain a relatively low temperature at the end of the copper sample holder (sapphire rod) on which we place the sample during the measurement. If one consider the thermal flow through the copper holder with the sapphire end from Eq. 5, $Q_{con} = \frac{A}{l}\int_{T_2}^{T_3} k_t\, dT$ we obtain T$_3\approx$6K which is also in agreement

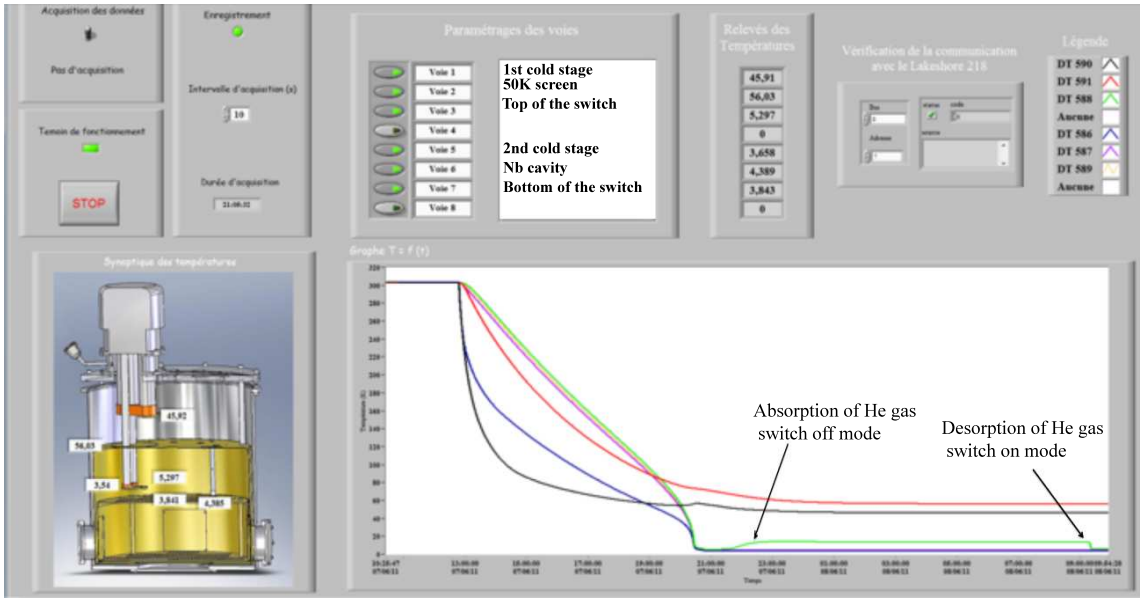

Figure 7 Screen shot of the Labview interface for the Lakeshore 218 temperature monitor that we use to read the temperature values indicated from different diodes installed inside the cyostat

with the experimental result .

Integral value table for the thermal conductivity

$$\int_{T_1}^{T_2} K_{(T)} dT \qquad (T_1 = 4\ °K)$$

T. (°K)	Watts /cm							Milliwatts /cm			T. (°K)
	Monel (recuit)	Monel (écroui)	Inconel (recuit)	Inconel (écroui)	Cu OFHC	Brass	Z,CN 18.10	Ver-re	Te-flon	Ny-lon	
6	0,0235	0,0123	0,0133	0,00712	6,1	0,053	0,0063	2,11	1,13	0,321	6
8	0,0605	0,0329	0,0348	0,0185	14,5	0,129	0,0159	4,43	2,62	0,807	8
10	0,112	0,0629	0,0653	0,0345	25,2	0,229	0,0293	6,81	4,4	1,48	10
15	0,315	0,181	0,182	0,0975	61,4	0,594	0,0816	13,1	9,85	4,10	15
20	0,618	0,364	0,356	0,195	110	1,12	0,163	20,0	16,4	8,23	20
25	1,01	0,614	0,592	0,325	168	1,81	0,277	27,9	23,9	13,9	25
30	1,48	0,929	0,882	0,488	228	2,65	0,424	36,8	32,2	20,8	30
35	2,01	1,30	1,22	0,685	285	3,63	0,607	47,1	41,3	29,0	35
40	2,58	1,73	1,60	0,918	338	4,76	0,824	58,6	50,8	38,5	40
50	3,85	2,73	2,47	1,48	426	7,36	1,35	84,6	71,6	60,4	50
60	5,23	3,88	3,45	2,15	496	10,4	1,98	115	93,6	85,9	60
70	6,69	5,13	4,52	2,94	554	13,9	2,70	151	116	113	70
76	7,61	5,92	5,19	3,47	586	16,2	3,17	175	130	131	76
80	8,24	6,47	5,66	3,84	606	17,7	3,49	194	139	142	80
90	9,86	7,91	6,85	4,84	654	22,0	4,36	240	163	173	90
100	11,5	9,40	8,06	5,93	700	26,5	5,28	292	187	204	100
120	15,0	12,6	10,6	8,33	788	36,5	7,26	408	237	269	120
140	18,7	15,9	13,1	11,0	874	47,8	9,39	542	287	336	140
160	22,5	19,5	15,7	13,8	956	60,3	11,7	694	338	405	160
180	26,4	23,2	18,3	16,8	1040	73,8	14,1	858	390	475	180
200	30,5	27,1	21,0	19,9	1120	88,3	16,6	1 030	442	545	200
250	41,2	37,3	28,0	28,1	1320	128	23,4	1 500	572	720	250
300	52,5	48,0	35,4	36,9	1520	172	30,6	1 990	702	895	300

Figure 8 Integral table of the thermal conductivity between 4K-300K for different materials.

. APPENDIX B

	Specular Reflection	Diffuse Reflection
Parallel Slabs . .	$\frac{e_1 e_2}{e_2+(1-e_2)e_1}$	$\frac{e_1 e_2}{e_2+(1-e_2)e_1}$
Coaxial cylinders $L \gg R$	$\frac{e_1 e_2}{e_2+(1-e_2)e_1}$	$\frac{e_1 e_2}{e_2+\frac{A_1}{A_2}(1-e_2)e_1}$
Concentric Spheres .	$\frac{e_1 e_2}{e_2+(1-e_2)e_1}$	$\frac{e_1 e_2}{e_2+\frac{A_1}{A_2}(1-e_2)e_1}$

Figure 9 Emissivity E of different geometries as a function of emissive power of surfaces A_1 and A_2 at temperatures T_1 and T_2.

Materials	Surface temperature (K)		
	300	78	4.2
Aluminium recuit électropoli	0,03	0,018	0,011
Aluminium commercial.	0,08	0,03	
Aluminium sur mylar (2 côtés)		0,04	
Cuivre (poli mécaniquement)	0,013	0,069	0,008
Cuivre (commercial poli électro)	0,030	0,019	0,015
Argent	0,020	0,008	
Laiton 65/35 poli	0,060	0,029	0,018
Laiton 65/35 oxydé	0,60	0,029	
Acier inox 302	0,08	0,048	
Acier inox 304	0,15	0,061	
Étain (25 μ).	0,05	0,013	0,012
Monel	0,17	0,11	
Or (37 μ sur verre ou plexi)	0,02	0,01	
Or (12 μ sur verre ou plexi)		0,016	
Or (0,25 μ sur verre ou plexi)		0,063	
Acier inox doré 12 μ		0,025	
Acier inox doré 2,5 μ		0,027	
Gilded Copper 12μ	0,04	0,025	

Figure 10 emissive power e for different materials.

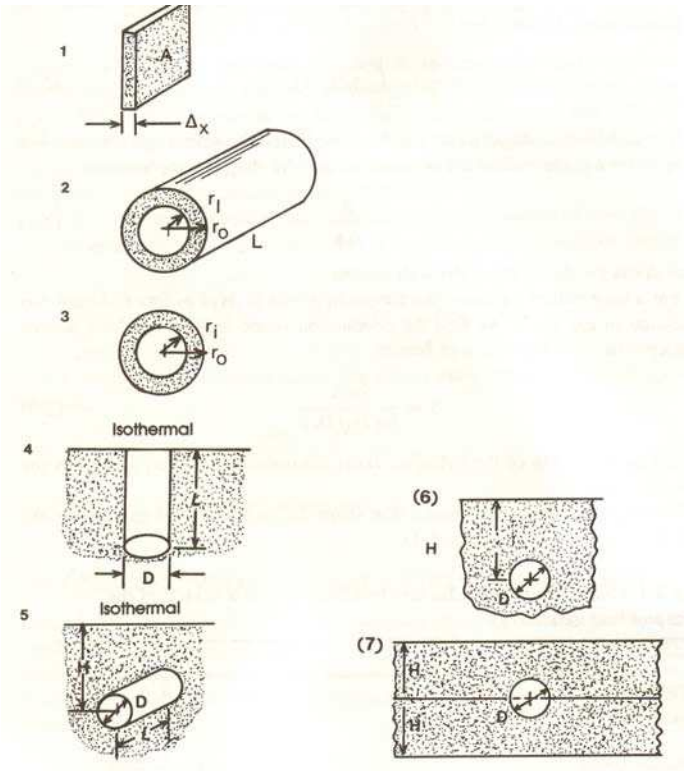

Figure 11 Sketch of possible geometries.

Geometry	Shape factor
[1] Plane wall or slab	$S = A/\Delta x$
[2] Hollow cylinder	$S = \dfrac{2\pi L}{\ln(D_0/D_1)}$
[3] Hollow sphere	$S = \dfrac{2\pi D_0 D_i}{D_0 - D_i}$
[4] Isothermal cylinder placed vertically in a semi-infinite medium	$S = \dfrac{2\pi L}{\ln(4L/D)}$
[5] Isothermal cylinder buried in a semi-infinite medium	$S = \dfrac{2\pi L}{\cosh^{-1}(2H/D)}$
[6] Isothermal sphere buried in a semi-infinite medium	$S = \dfrac{8\pi D}{1 - (D/4H)}$
[7] Cylinder centered in a large plate	$S = \dfrac{2\pi L}{\ln(4H/D)}$

Figure 12 Conduction shape factors for the geometries describe in Figure 11 .

. APPENDIX B

		He	H_2	Ne	N_2	O_2	Ar	CH_4
MASSE MOLECULAIRE	(g)	4,003	2,016	20,18	28,02	32,00	39,94	16,04
TEMPERATURE D'EBULLITION à P atmospherique = $1,013.10^5$ Pa	(K)	4,2	20,4	27,1	77,3	90,2	87,3	111,7
POINT TRIPLE — TEMPERATURE	(K)	néant	13,95	24,5	63,14	54,40	84,0	89,0
POINT TRIPLE — PRESSION	(mm Hg)		54	324	96	1,15	516	75
POINT TRIPLE — PRESSION	(10^2 Pa)		72	424	125	1,5	670	98
POINT CRITIQUE — TEMPERATURE	(K)	5,2	33,2	44,4	126,1	154,4	150,8	191,0
POINT CRITIQUE — PRESSION	(10^5 Pa)	2,23	12,8	26,6	33,1	49,5	47,7	45,2
VOLUME DE GAZ PROVENANT DE 1 l. DE LIQUIDE à T d'ébullition	(l)	7,2	46	121	178	260	240	213
VOLUME DE GAZ PROVENANT DE 1 l. DE LIQUIDE à T et P normale	(l)	700	790	1340	646	798	784	595
CHALEUR LATENTE à la température d'ébullition sous P. norm	($kJ.kg^{-1}$)	21	452	89,6	199	213	157	577
CHALEUR SENSIBLE entre T éb. et 300 K	($kJ.kg^{-1}$)	1550	3474	280	247	193	112	385
RAPPORT chaleur sensible / chaleur latente		74	7,70	3,13	1,24	0,90	0,71	0,67
TAUX D'EVAPORATION *	($Wh.l^{-1}$)	0,7	9	29	45	68	63	60
CONDUCTIVITE THERMIQUE DU GAZ à T éb. + ε	($mW K^{-1} m^{-1}$)	10	15	—	9,4	7	—	—
CONDUCTIVITE THERMIQUE DU GAZ à 300 K	($mW K^{-1} m^{-1}$)	145	181	—	26	2,7	—	—
MASSE VOLUMIQUE DU LIQUIDE BOUILLANT à P normale	($kg m^{-3}$)	125	71	1210	810	1140	1400	425
MASSE VOLUMIQUE DE LA VAPEUR SATURANTE à P normale	($kg m^{-3}$)	17	1,5	9,5	4,5	4,4	5,8	1,7
MASSE VOLUMIQUE DU GAZ à P et T normales	($kg m^{-3}$)	0,18	0,09	0,90	1,25	1,40	1,80	0,70
VISCOSITE DU LIQUIDE	(μPa s)	3,6	13,0	125	160	190	260	120
VISCOSITE DU GAZ à T ébul.	(μPa s)	1,0	1,0	4,5	5,0	7,0	—	4,4
VISCOSITE DU GAZ à T amb.	(μPa s)	20	9	30	17	20	22	11
CONSTANTE DIELECT. DU LIQUIDE		1,049	1,23	1,19	1,43	1,48	1,52	1,67

Figure 13 Cryogenic datas for different gas .

Bibliography

[1] A. A. Golubov and I. I. Mazin. *Phys. Rev. B*, **55**:15146–15152, (1997). 46

[2] A. A. Kordyuk, V.B. Zabolotnyy, D.V. Evtushinsky, T.K. Kim, I.V. Morozov, M.L. Kulic, R. Follath, G. Behr, B. Buchner, and S.V. Borisenko. *Phys. Rev. B*, **83**:134513, (2011). 45

[3] A. Abrikosov. *Rev. Mod. Phys.*, **76**:975, (2004). 17, 89

[4] A. B. Pippard. *Proc. R. Soc. London, Ser. A*, **216**:547, (1953). 10

[5] A. Carrington. *SCEF - 2012 Les Houches*. xxi, 165

[6] A. D. Christianson, M. D. Lumsden, S. E. Nagler, G. J. MacDougall, M. A. McGuire, A. S. Sefat, R. Jin, B. C. Sales, and D. Mandrus. *Phys. Rev. Lett.*, **103**:087002, (2009). 38, 53

[7] A. Glatz and A.E. Koshelev. *Phys. Rev. B*, **82**:012507, (2010). 56, 163, 164

[8] A. Gurevich and E.H. Brandt. *Phys. Rev. Lett.*, **73**:178–181, (1994). 26

[9] A. I. Larkin and Y. N. Ovchinnikov. *Sup. Sci. and Tech.*, **34**:409, (1979).

[10] A. Kawabata, S. C. Lee, T. Moyoshi, Y. Kobayashi, and M. Sato. *Journal of the Physical Society of Japan*, **77**:103704, (2008). 45, 163

[11] A. Olariu, F. Rullier Albenque, D. Colson, and A. Forget. *Phys. Rev. B*, **83**:054518, (2011). xiv, 59

[12] A. Soibel, E. Zeldov, M. Rappaport, Y. Myasoedov, T. Tamegai, S. Ooi, M. Konczykowski, and V. B. Geshkenbein. *Nature*, **406**(6793):282–287, (2000). 115

[13] A. Sudbø and E.H. Brandt. *Phys. Rev. Lett.*, **66**:1781–1784, (1991). 100

[14] A. V. CHUBUKOV, D. V. EFREMOV, AND I. EREMIN. *Phys. Rev. B*, **78**:134512, (2008). 44, 46

[15] A. YAMAMOTO, J. JAROSZYNSKI, C. TARANTINI, L. BALICAS, J. JIANG, A. GUREVICH, D.C. LARBALESTIER, R.J. JIN, A.S. SEFAT, M.A. MCGUIRE, B.C. SALES, D. K. CHRISTEN, AND D. MANDRUS. *Phys. Rev. Lett.*, **66**:062511, (2009). 60, 108

[16] A.I. SCHAWLOW. *Phys. Rev.*, **101**:573–579, (1956). 84

[17] A.S. SEFAT, R. JIN, M.A. MCGUIRE, B.C. SALES, D.J. SINGH, AND D. MANDRUS. *Phys. Rev. Lett.*, **101**:117004, (2008). 35, 163

[18] B. KALISKY, J.R. KIRTLEY, J. G. ANALYTIS, J.-H. CHU, I.R. FISHER, AND K.A. MOLER. *Phys. Rev. B*, **83**(6):064511, (2011). 61, 90, 91, 96, 107, 111, 112

[19] B. MANSART, E. PAPALAZAROU, M. FUGLSANG JENSEN, V. BROUET, L. PETACCIA, L. DE' MEDICI, G. SANGIOVANNI, F. RULLIER ALBENQUE, A. FORGET, D. COLSON, AND M. MARSI. *Phys. Rev. B*, **85**:144508, (2012). 52

[20] B. SHEN, B. ZENG, G. F. CHEN, J. B. HE, D. M. WANG, H. YANG, AND H. H. WEN. *EPL*, **96**:37010, (2011). 38

[21] B. SHEN, P. CHENG, Z. WANG, L. FANG, C. REN, L. SHAN, AND H.-H. WEN. *Phys. Rev. B*, **81**:014503, (2010). 61, 80

[22] L. YANG M. XU C. HE C. FEI Z. JIA-FENG O. HONG-WEI W. JIA X. BIN-PING W. TAO W. GANG A. MASASHI S. KENYA H. NAMATAME M. TANIGUCHI X. H. CHEN D. L. FENG B. ZHOU, Y. ZHANG. *Phys. Rev. B*, **81**:155124, (2010). 39

[23] B.M. BALASHOVA AND YU. V. SHARVIN. *Sov. Phys. Jetp*, **31**:40, (1956). 84

[24] B.S. CHANDRASEKHAR AND D. EINZEL. *Annalen der Physik*, **505**:535– 546, (1993). 47, 147

[25] C. BERNHARD, A. J. DREW, L. SCHULZ, V. K. MALIK, M. RASSLE, C.H. NIEDERMAYER, T.H. WOLF, G. D. VARMA, G. MU, H.-H. WEN, H. LIU, AND G.WUAND X. H. CHEN. *New Journal of Physics*, **11**:055050, (2009). 38

[26] C. C. TSUEI, J. R. KIRTLEY, C. C. CHI, L.-S. YU JAHNES, A. GUPTA, T. SHAW, J. Z. SUN, AND M. B. KETCHEN. *Phys. Rev. Lett.*, **73**:593–596, (1994). 44

[27] C.-H. LEE, A. IYO, H. EISAKI, HIJIRI KITO, M. T. FERNANDEZ DIAZ, T. ITO, K. KUNIHIRO, H. MATSUHATA, M. BRADEN, AND K. YAMADA. *Journal of the Physical Society of Japan*, **77**(8):083704, (2008). xiii, 38, 42, 45, 163

[28] C. J. VAN DER BEEK AND P.H. KES. *Phys. Rev. B*, **43**:13032–13041, (1991). 164

[29] C. J. VAN DER BEEK, S. DEMIRDIŞ, D. COLSON, F. RULLIER ALBENQUE, T. SHIBAUCHI, Y. MATSUDA, S. KASAHARA, P. GIERLOWSKI, AND M. KONCZYKOWSKI. *ArXiv:1209.3586*, (2012). 58, 60

[30] C. KITTEL. *Rev. Mod. Phys.*, **21**(541), (1949). 83, 85

[31] C. KUBERT AND P.J. HIRSCHFELD. *Solid State Comm.*, **105**:459 – 463, (1998). 49

[32] C. LIU, T. KONDO, A.D. PALCZEWSKI, G.D. SAMOLYUK, Y. LEE, M.E. TILLMAN, N. NI, E.D. MUN, R. GORDON, A.F. SANTANDER SYRO, S.L. BUD'KO, J.L. MCCHESNEY, A.V. FEDOROV E. ROTENBERG, T. VALLA, O. COPIE, M.A. TANATAR, C. MARTIN, B.N. HARMON, P.C. CANFIELD, R. PROZOROV, J. SCHMALIAN, AND A. KAMINSKI. *Physica C*, **469**:491– 497, (2009). 39

[33] C. MARTIN, M. E. TILLMAN, H. KIM, M.A. TANATAR, S.K. KIM, A. KREYSSIG, R.T. GORDON, M.D. VANNETTE, S. NANDI, V.G. KOGAN, S.L. BUD'KO, P.C. CANFIELD, A.I. GOLDMAN, AND R. PROZOROV. *Phys. Rev. Lett.*, **102**:247002, (2009). 47

[34] C. MARTIN, R.T. GORDON, M.A. TANATAR, H. KIM, N. NI, S.L. BUD'KO, P.C. CANFIELD, H. LUO, H.H. WEN, Z. WANG, A.B. VORONTSOV, V.G. KOGAN, AND R. PROZOROV. *Phys. Rev. B*, **80**:020501, (2009). xiv, 47, 48, 184, 188

[35] C. P. BEAN AND J.D. LIVINGSTON. *Phys. Rev. Lett.*, **12**:14–16, (1964). 119

[36] C. POOLE. *Electron Spin Resonance*. Interscience Publishers, (1967). 160

[37] C. TARANTINI, M. PUTTI, A. GUREVICH, Y. SHEN, R. K. SINGH, J. M. ROWELL, N. NEWMAN, D. C. LARBALESTIER, P. CHENG, Y. JIA, AND H.-H. WEN. *Phys. Rev. Lett.*, **104**:087002, (2010). 45, 57, 165, 185

[38] C. W. HICKS, T. M. LIPPMAN, M.E. HUBER, J. G. ANALYTIS, J.-H. CHU, A.S. ERICKSON, J.R. FISHER, AND K. A. MOLER. *Phys. Rev. Lett.*, **103**:127003, (2009). xiv, 47, 48

[39] C.J. GORTER AND H.B.G. CASIMIR. *Physica*, **1**:305–320, (1934). 9

[40] C.J. OLSON, C. REICHHARDT, AND F. NORI. *Phys. Rev. Lett.*, **80**:2197–2200, (1998). 135

[41] C.J. VAN DER BEEK, G. RIZZA, M. KONCZYKOWSKI ZND P. FERTEY, I. MONNET, T. KLEIN, R. OKAZAKI, M. ISHIKADO, H. KITO, A. IYO, H. EISAKI, S. SHAMOTO, M.E. TILLMAN, S.L. BUD'KO, P.C. CANFIELD, T. SHIBAUCHI, AND Y. MATSUDA. *Phys. Rev. B*, **81**:174517, (2010). 28, 38, 58, 59, 60, 89, 92, 107, 108, 111, 115, 123, 124, 174

[42] C.J. VAN DER BEEK, G.J. NIEUWENHUYS, P.H. KES, H.G. SCHNACK, AND R. GRIESSEN. 26

[43] C.J. VAN DER BEEK, M. KONCZYKOWSKI, A. ABAL'OSHEV, I. ABAL'OSHEVA, P. GIERLOWSKI, S. J. LEWANDOWSKI, M.V. INDENBOM, AND S. BARBANERA. *Phys. Rev. B*, **66**:024523, (2002). 32, 107, 108, 124, 127, 137

[44] C.J. VAN DER BEEK, M. KONCZYKOWSKI, S. KASAHARA, T. TERASHIMA, R. OKAZAKI, T. SHIBAUCHI, AND Y. MATSUDA. *Phys. Rev. Lett.*, **105**:267002, (2010). 1, 58, 59, 60, 111, 112, 174

[45] C.J. VAN DER BEEK, S. DEMIRDIŞ, M. KONCZYKOWSKI, Y. FASANO, N.R. CEJAS BOLECEK, H. PASTORIZA, D. COLSON, AND F. RULLIER ALBENQUE. *Physica B*, **407**:1746 – 1749, (2012). 58, 60

[46] C.J. VAN DER BEEK, S. DEMIRDIŞ, Y. FASANO, N.R. CEJAS BOLECEK, H. PASTORIZA, D. COLSON, AND F. RULLIER ALBENQUE. *Physica B*, **407**:1746 – 1749, (2012). 111, 115, 174, 190

[47] C.P. BEAN. *Phys. Rev. Lett.*, **8**:250–253, (1962). 94, 115

[48] C.W. CHU, F. CHEN, M. GOOCH, A.M. GULOY, B. LORENZ, B. LV, K. SASMAL, Z.J. TANG, J.H. TAPP, AND Y.Y. XUE. *Physica C*, **469**:326 – 331, (2009). 35

[49] D. DAGHERO, M. TORTELLO, R. S. GONNELLI, V. A. STEPANOV, AND N. D. ZHIGADLOAND J. KARPINSKI. *Phys. Rev. B*, **80**:060502, (2009). 55

[50] D. J. SINGH AND M.-H. DU. *Phys. Rev. Lett.*, **100**:237003, (2008). xiii, 40, 41

[51] D. PARKER, O.V. DOLGOV, M.M. KORSHUNOV, A.A. GOLUBOV, AND I.I. MAZIN. *Phys. Rev. B*, **78**:134524, (2008). 163

[52] D. S. FISHER, M.P.A. FISHER, AND D. A. HUSE. *Phys. Rev. B*, **43**:130–159, 1991. 27

[53] D. S. INOSOV, A. LEINEWEBER, X. YANG, J. T. PARK, N. B. CHRISTENSEN, R. DINNEBIER, G. L. SUN, C.H. NIEDERMAYER, D. HAUG, P. W. STEPHENS, J. STAHN, O. KHVOSTIKOVA, C. T. LIN, O. K. ERSEN, B. KEIMER, AND V. HINKOV. *Phys. Rev. B*, **79**:224503, (2009). 53

[54] D. S. INOSOV, J. T. PARK, P. BOURGES, D. L. SUN, Y. SIDIS, A. SCHNEIDEWIND, V. HRADIL, D. HAUG, C. T. LIN, B. KEIMER, AND V. HINKOV. *Nature*, **6**:178, (2010). 53

[55] D.C. MATTIS AND J. BARDEEN. *Phys. Rev.*, **111**:412–417, (1958). 148

[56] D.J. BISHOP, P.L. GAMMEL, D.A. HUSE, AND C. A. MURRAY. *Science*, **255**:165–172, (1992). 84

[57] D.J. CRAIK AND P.M. GRIFFITHS. *British Journal of Applied Physics*, **9**:279, (1958). 83

[58] D.K. PRATT, W. TIAN, A. KREYSSIG, J.L. ZARESTKY, S. NANDI, N. NI, S.L. BUD'KO, P.C. CANFIELD, A.I. GOLDMAN, AND R.J. MCQUEENEY. *Phys. Rev. Lett.*, **103**, (2009). 38

[59] D.S. INOSOV, T. SHAPOVAL, V. NEU, U. WOLFF, J.S. WHITE, S. HAINDL, J.T. PARK, D.L. SUN, C.T. LIN, E.M. FORGAN, M.S. VIAZOVSKA, J.H. KIM, M. LAVER, K. NENKOV, O. KHVOSTIKOVA, S. KÜHNEMANN, AND V. HINKOV. *Phys. Rev. B*, **81**:014513, (2010). 53, 61, 90, 96, 109, 111, 112

[60] D.V. EFREMOV, M.M. KORSHUNOV, O.V. DOLGOV, A.A. GOLUBOV, AND P.J. HIRSCHFELD. *Phys. Rev. B*, **84**:180512, (2011). 46, 56, 165

[61] E. D. ISAACS, P. ZSCHACK, C. L. BROHOLM, C. BURNS, G. AEPPLI, A. P. RAMIREZ, T. T. M. PALSTRA, R. W. ERWIN, N. STUCHELI, AND E. BUCHER. *Phys. Rev. Lett.*, **75**:1178–1181, (1995).

[62] E. H. BRANDT. *Phys. Rev. B*, **54**:4246–4264, (1996). xv, 74, 75, 115, 173

[63] E. H. BRANDT. *Phys. Rev. B*, **58**:6506–6522, (1998). 92, 94

[64] E. H. BRANDT. *Phys. Rev. B*, **60**:11939–11942, (1999). 119

[65] E. ZELDOV, A. I. LARKIN, V.B. GESHKENBEIN, M. KONCZYKOWSKI, D. MAJER, B. KHAYKOVICH, V. M. VINOKUR, AND H. SHTRIKMAN. *Phys. Rev. Lett.*, **73**:1428–1431, (1994). 23

[66] E. ZELDOV, J.R. CLEM, M. MCELFRESH, AND M. DARWIN. *Phys. Rev. B*, **49**:9802–9822, (1994). 23, 94, 115

[67] E.H. KENNARD. *Kinetic Theory of Gases With Introduction to Statistical Mechanics*. Mcgraw-Hill, New York, pp 70, (1938). 198

[68] E.V. THUNEBERG, J. KURKIJÄRVI, AND D. RAINER. *Phys. Rev. Lett.*, **48**:1853–1856, (1982). 28, 58, 174

[69] E.V. THUNEBERG, J. KURKIJARVI, AND D. RAINER. *Phys. Rev. B*, **29**:3913–3923, (1984). 58, 174

[70] F. BITTER. *Phys. Rev.*, **38**:1903, (1931). 83

[71] F. GROSS, B.S. CHANDRASEKHAR, D. EINZEL, K. ANDRES, P.J. HIRSCHFELD, H.R. OTT, J. BEUERS, Z. FISK, AND J.L. SMITH. *Zeitschrift fur Physik B*, **64**:175–188, (1986). 47

[72] F. HARDY, P. BURGER, T. WOLF, R. A. FISHER, P. SCHWEISS, P. ADELMANN, R. HEID, R. FROMKNECHT, R. EDER, D. ERNST, H. V. LONHNEYSEN, AND C. MEINGAST. *EPL*, **91**:47008, (2010). 51

[73] F. LONDON AND H. LONDON. *Proc. Roy. Soc.*, **A149**, (1935). 7, 8, 139

[74] F. MA, W. JI, Z.-Y. LU J. HU, AND T. XIANG. *Phys. Rev. Lett.*, **102**:177003, (2009). 41

[75] F. MASSEE, Y. HUANG, R. HUISMAN, S. DE JONG, J.B. GOEDKOOP, AND M.S. GOLDEN. *Phys. Rev. B*, **79**:220517, (2009). 2, 55, 91, 109

[76] F. PARDO, F. DE LA CRUZ, P.L. GAMMEL, E. BUCHER, C. OGELSBY, AND D.J. BISHOP. *Phys. Rev. Lett.*, **79**:1369–1372, (1997). 99, 104

[77] F. RULLIER ALBENQUE, D. COLSON, A. FORGET, AND H. ALLOUL. *Phys. Rev. Lett.*, **103**:057001, (2009). xiv, 59, 81, 175

[78] F. RULLIER ALBENQUE, H. ALLOUL, AND R. TOURBOT. *Phys. Rev. Lett.*, **91**:047001, (2003). 166

[79] F. RULLIER ALBENQUE, P. A. VIEILLEFOND, H. ALLOUL, A. W. TYLER, P. LEJAY, AND J. F. MARUCCO. *EPL*, **50**:81, (2000). 166

[80] F. WANG, H. ZHAI, AND D.-H. LEE. *Phys. Rev. B*, **81**:184512, (2010). 56

[81] F.C. HSU, J.Y. LUO, K.W. YEH, T.K. CHEN, T.W. HUANG, P.M. WU, Y.C. LEE, Y.L. HUANG, Y.Y. CHU, AND D.C. YAN. *PNAS*, **105**:14162, (2008). 34

[82] G. BLATTER, M.V. FEIGEL'MAN V.B. GESHKENBEIN, A.I. LARKIN, AND V.M. VINOKUR. *Rev. Mod. Phys.*, **66**:1125–1388, (1994). 29, 30, 80

[83] G. E. BLONDER AND M. TINKHAM. *Phys. Rev. B*, **27**:112–118, (1983). 54

[84] G. E. VOLOVIK. *JETP Lett.*, **58**, (1993). 49

[85] G. FOURNET. *Phys. Lett.*, **17**(210), (1965). 85

[86] G. MU, B. ZENG, P. CHENG, Z. WANG, L. FANG, B. SHEN, L. SHAN, C. REN, AND H.-H. WEN. *Chin. Phys. Lett.*, **27**:037402, (2010).

[87] G.K. WHITE AND P.J. MEESON. *Experimental Techniques in Low-Temperature Physics*. Oxford Science Publications, first edition edition, (2002). 197

[88] H. DING, P. RICHARD, K. NAKAYAMA, K. SUGAWARA, T. ARAKANE, Y. SEKIBA, A. TAKAYAMA, S. SOUMA, T. SATO, T. TAKAHASHI, Z. WANG, X. DAI, Z. FANG, G.F. CHEN, J.L. LUO, AND N.L. WANG. *EPL*, **83**:47001, (2008). 39, 51, 163

[89] H. FUKAZAWA, T. YAMAZAKI, K. KONDO, Y. KOHORI, N. TAKESHITA, P. M. SHIRAGE, K. KIHOU, K. MIYAZAWA, H. KITO, H. EISAKI, AND A. IYO. *Journal of the Physical Society of Japan*, **78**:033704, (2009). 37, 53

[90] H. KAWANO FURUKAWA, C.J. BOWELL, J.S. WHITE, R.W. HESLOP, A.S. CAMERON, E.M. FORGAN, K. KIHOU, C.H. LEE, A. IYO, H. EISAKI, T. SAITO, H. FUKAZAWA, Y. KOHORI, R. CUBITT, C.D. DEWHURST, J.L. GAVILANO, AND M. ZOLLIKER. *Phys. Rev. B*, **84**:024507, (2011). 61, 111, 112

[91] H. KIM, M. A. TANATAR, Y.J. SONG, Y. S. KWON, AND R. PROZOROV. *Phys. Rev. B*, **83**:100502, (2011). 48

[92] H. KONTANI AND S. ONARI. *Phys. Rev. Lett.*, **104**:157001, (2010). 44

[93] H. KONTANI AND S. ONARI. *Phys. Rev. Lett.*, **104**:157001, (2010). 45

[94] H. KONTANI AND S. ONARI. *Phys. Rev. Lett.*, **104**:157001, (2010). 56

[95] H. LUETKENS, K. HASSELBACH, M. KRAKEN, F. J. LITTERST, T. DELLMANN, R. KLINGELER, C. HESS, R. KHASANOV, A. AMATO, C. BAINES, M. KOSMALA, M. BRADEN O. J. SCHUMANN, J. HAMANN BORRERO, N. LEPS, A. KONDRAT,

J. WERNER G. BEHR, AND B BUCHNER. *Nature Material*, **4**:1476, (2009). xiii, 35

[96] H. OGINO, Y. MATSUMURA, Y. KATSURA, K. USHIYAMA, S. HORII, K. KISHIO, AND J. SHIMOYAMA. *Sup. Sci. and Tech.*, **22**:075008, (2009). xiii, 33

[97] H. SHISHIDO, A.F. BANGURA, I. COLDEA, S. TONEGAWA, K. HASHIMOTO, S. KASAHARA, P.M.C. ROURKE, H. IKEDA, T. TERASHIMA, R. SETTAI, Y. OONUKI, D. VIGNOLLES, C. PROUST, B. VIGNOLLE, A. MCCOLLAM, Y. MATSUDA, T. SHIBAUCHI, AND A. CARRINGTON. *Phys. Rev. Lett.*, **104**:057008, (2010). 34, 37, 58, 134, 190

[98] H. TRÄUBLE AND U. ESSMANN. *Phys. Stat. Sol. B*, **18**:813–828, (1966). 84

[99] H. TRÄUBLE AND U. ESSMANN. *J. Appl. Phys.*, **39**:4052, (1968). 84

[100] H. VICHERY, F. RULLIER ALBENQUE, H. PASCARD, M. KONCZYKOWSKI, R. KORMAN, D. FAVROT, AND G. COLLIN. *Physica C*, **159**. 166

[101] H. WADATI, I. ELFIMOV, AND G.A. SAWATZKY. *Phys. Rev. Lett.*, **105**:157004, (2010). 163

[102] H. YANG, B. SHEN, Z. WANG, L. SHAN, C. REN, AND H.-H. WEN. *Phys. Rev. B*, **85**:014524, (2012). 61, 111, 112, 128

[103] H. YANG, H. LUO, Z. WANG, AND H.-H. WEN. *Appl. Phys. Lett.*, **93**:142506, (2008). 58

[104] H.G. SCHNACK, R. GRIESSEN, J.G. LENSINK, C.J. VAN DER BEEK, AND P.H. KES. 26

[105] H.K. ONNES. *Leiden Comm.*, **120 B**, (1911). 5

[106] HTTP://WWW.LSI.POLYTECHNIQUE.FR/ACCUEIL/EQUIPEMENTS/ACCELERATEUR SIRIUS/. 171, 190

[107] I.I. MAZIN. *Nature*, **464**(7286):183–186, (2010). 163

[108] I.I. MAZIN. *Physics*, **4**:26, (2011). xiv, 44

[109] I.I. MAZIN, D.J. SINGH, M.D. JOHANNES, AND M. H. DU. *Phys. Rev. Lett.*, **101**:057003, (2008). 42, 44, 46

[110] I.V. GRIGORIEVA. *Sup. Sci. and Tech.*, **7**:161, (1994). 84

[111] J. BARDEEN, L.N. COOPER, AND J.R. SCHRIEFFER. *Phys. Rev.*, **108**:1175, (1957). 10, 145

[112] J. BARDEEN AND M. J. STEPHEN. *Phys. Rev.*, **140**:(a1197–a1207), (1965). 20

[113] J. D. JACKSON. *Classical Electrodynamics*, **2**. John Wiley Sons, Inc., (1962). 157

[114] J. DONG, H. J. ZHANG, G. XU, Z. LI, G. LI, W. Z. HU, D. WU, G. F. CHEN, X. DAI, J. L. LUO, Z. FANG, AND N. L. WANG. *Eu. Phys. Lett.*, **83**:27006, (2008).

[115] J. E. SONIER, M. F. HUNDLEY, J. D. THOMPSON, AND J. W. BRILL. *Phys. Rev. Lett.*, **82**:4914–4917, (1999). 49, 163

[116] J. G. DAUNT AND K. MENDELSSOHN. *Proc. Roy. Soc.*, **A185**:235, (1946). 6, 12

[117] J. GILCHRIST AND M. KONCZYKOWSKI. *Physica C*, **212**:43 – 60, (1993). 63, 78

[118] J. GUO, S. JIN, G. WANG, S. WANG, K. ZHU, T. ZHOU, M. HE, AND X. CHEN. *Phys. Rev. B*, **82**:180520, (2010). 45

[119] J. HALBRITTER. *Z. Physik*, **266**:209–217, (1974). xx, 145, 147, 148

[120] J. HANISCH, L. KAZUMASA, S. HAINDL, F. KURTH, F. KAUFFMANN, M. KIDSZUN, T. THERSLEFF, J. FREUDENBERGER, L. SCHULTZ, AND B. HOLZAPFEL. *IEEE Trans. Appl. Supercond.*, **21**, (2011). 100

[121] J. KNOLLE, I. EREMIN, A. AKBARI, AND R. MOESSNER. *Phys. Rev. Lett.*, **104**:257001, (2010). 56

[122] J. LARMOR. *Aether and Matter*. Cambridge University Press, (1900). 67

[123] J. LI, Y. GUO, S. ZHANG, S. YU, Y. TSUJIMOTO, H. KONTANI, K. YAMAURA, AND E. TAKAYAMA MUROMACHI. *Phys. Rev. B*, **84**:020513, (2011). 165

[124] J. LI, Y.F. GUO, S.B. ZHANG, J. YUAN, Y. TSUJIMOTO, X. WANG, C.I. SATHISH, Y. SUN, S. YU, W. YI, K. YAMAURA, E. TAKAYAMA MUROMACHIU, Y. SHIRAKO, M. AKAOGI, AND H. KONTANI. *Arxiv:1206.0811*, (2012). 165

[125] J.-PH. REID, M.A. TANATAR, A. JUNEAU FECTEAU, R.T. GORDON, S.R. DE COTRET, N. DOIRON LEYRAUD, T. SAITO, H. FUKAZAWA, Y. KOHORI, K. KIHOU, C.H. LEE, A. IYO, H. EISAKI, R. PROZOROV, AND L. TAILLEFER. *Phys. Rev. Lett.*, **109**:087001, (2012). 56

[126] J.-PH. REID, M.A. TANATAR, X.G. LUO, H. SHAKERIPOUR, N. DOIRON LEYRAUD, N. NI, S.L. BUD'KO P.C. CANFIELD, R. PROZOROV, AND L. TAILLEFER. *Phys. Rev. B*, **82**:064501, (2010). 50, 51, 56, 184, 188

[127] J. Q. YAN, S. KREYSSIG, N. NI, S. L. BUD'KO, A. KRACHER, R. J. MCQUEENEY, R. W. MCCALLUM, T. A. LOGRASSO, A. I. GOLDMAN, AND P.C. CANFIELD. *Phys. Rev. B*, **78**:024516, (2008). 58

[128] J. ŠIMŠOVÁ, R. GEMPERLE, AND J.C. LODDER. *Journal of Magnetism*, **95**:85–94, (1991). 83

[129] K. A. MOLER, D. J. BAAR J. S. URBACH, R. LIANG, W. N. HARDY, AND A. KAPITULNIK. *Phys. Rev. Lett.*, **73**:2744–2747, (1994). 49

[130] K. GOFRYK, A.B. VORONTSOV, I. VEKHTER, A.S. SEFAT, T. IMAI, E.D. BAUER, J.D. THOMPSON, AND F. RONNING. *Phys. Rev. B*, **83**:064513, (2011). 49

[131] K. GOTO AND T. SAKURAI. *Appl. Phys. Lett.*, **30**(7):355–356, (1977). 83

[132] K. HASHIMOTO, K. CHO, T. SHIBAUCHI, S. KASAHARA, Y. MIZUKAMI, R. KATSUMATA, Y. TSURUHARA, T. TERASHIMA, H. IKEDA, M.A. TANATAR, H. KITANO, N. SALOVICH, R.W. GIANNETTA, P. WALMSLEY, A. CARRINGTON R. PROZOROV, AND Y. MATSUDA. *Science*, **336**:1554–1557, (2012). xiv, 48, 56, 127, 134, 163

[133] K. HASHIMOTO, M. YAMASHITA, S. KASAHARA, Y. SENSHU, N. NAKATA, S. TONEGAWA, K. IKADA, A. SERAFIN, A. CARRINGTON, T. TERASHIMA, H. IKEDA, T. SHIBAUCHI, AND Y. MATSUDA. *Phys. Rev. B*, **81**:220501, (2010). 51

[134] K. HASHIMOTO, T. SHIBAUCHI, S. KASAHARA, K. IKADA, S. TONEGAWA, T. KATO, R. OKAZAKI, C.J. VAN DER BEEK, M. KONCZYKOWSKI, H. TAKEYA, K. HIRATA, T. TERASHIMA, AND Y. MATSUDA. *Phys. Rev. Lett.*, **102**:207001, (2009). 47

[135] K. HASHIMOTO, T. SHIBAUCHI, T. KATO, K. IKADA, R. OKAZAKI, H. SHISHIDO, M. ISHIKADO, H. KITO, A. IYO, H. EISAKI, S. SHAMOTO, AND Y. MATSUDA. *Phys. Rev. Lett.*, **102**:017002, (2009). xiv, xx, 46, 47, 48, 56, 60, 124, 130, 135, 163, 176

[136] K. ISHIDA, Y. NAKAI, AND H. HOSONO. *journal of the physical society of japan*, **78**:062001, (2009). xiii, 33, 34

[137] K. KANEKO, A. HOSER, N. CAROCA CANALES, A. JESCHE, C. KRELLNER, O. STOCKERT, AND C. GEIBEL. *Phys. Rev. B*, **78**:212502, (2008). 40

[138] K. KUROKI, H. USUI, S. ONARI, R. ARITA, AND H. AOKI. *Phys. Rev. B*, **79**:224511, (2009). xxi, 40, 43, 163, 164

[139] K. KUROKI, S. ONARI, R. ARITA, H. USUI, Y. TANAKA, H. KONTANI, AND H. AOKI. *Phys. Rev. Lett.*, **101**:087004, (2008). 40, 43

[140] K. KUROKI, S. ONARI, R. ARITA, H. USUI, Y. TANAKA, H. KONTANI, AND H. AOKI. *New Journal of Physics*, **11**(2):025017, (2009). 40, 43

[141] K. SASMAL, L.V. BING, B. LORENZ, A. M. GULOY, F. CHEN, Y.-Y. XUE, AND C.-W. CHU. *Phys. Rev. Lett.*, **101**:107007, (2008). 40

[142] K. TERASHIMA, Y. SEKIBA, J.H. BOWEN, K. NAKAYAMA, T. KAWAHARA, T. SATO, P. RICHARD, Y.-M. XU, L.J. LI, G.H. CAO, Z.-A. XU, H. DING, AND T. TAKAHASHI. *PNAS*. 163

[143] K. W. YEH, T.W. HUANG, Y.L. HUANG, T.K. CHEN, F.C. HSU, P.M. WU, Y. C. LEE, Y.Y. CHU, C.L. CHEN, J.Y. LUO, D.C. YAN, AND M.K. WU. *Europhysics Letters*, **84**:37002, (2008). 34

[144] KAWANO-FURUKAWA *et.al.* *ICSM 2012 Abstract Book*, page 641, (2012). 61, 111, 112, 134

[145] L. A. DOROSINSKII, M.V. INDENBOM, V.I. NIKITENKO, Y.A. OSSIP'YAN, A.A. POLYANSKII, AND V.K. VLASKO VLASOV. *Physica C*, **203**:342. 115

[146] L. FANG, Y. JIA, J.A. SCHLUETER, A. KAYANI, Z.L. XIAO, H. CLAUS, U. WELP, A.E. KOSHELEV, G.W. CRABTREE, AND W.-K. KWOK. *Phys. Rev. B*, **84**:140504, (2011). 61, 113, 126, 137

[147] L. J. LI, Y. K. LUO, Q. B. WANG, H. CHEN, Z. REN, Q. TAO, Y. K. LI, X. LIN, M. HE, Z. W. ZHU, G. H. CAO, AND Z. A. XU. *New Journal of Physics*, **11**:025008, (2009). 35, 57, 163, 184

[148] L. LUAN, O.M. AUSLAENDER, T.M. LIPPMAN, C.W. HICKS, B. KALISKY, J. CHU, J. G. ANALYTIS I.R. FISHER, J.R. KIRTLEY, AND K. A. MOLER. *Phys. Rev. B*, **81**:100501, (2010). xiv, 47, 48, 61, 90, 96, 100, 104, 111, 112

[149] L. YA. VINNIKOV, J. KARPINSKI, S.M. KAZAKOV, J. JUN, J. ANDEREGG, S.L. BUD'KO, AND P.C. CANFIELD. *Phys. Rev. B*, **67**:092512, (2003). 84

[150] L. ZHANG AND D. J. SINGH. *Phys. Rev. B*, **79**:174530, (2009). xiii, 40, 41, 55

[151] L.P. GORKOV AND A. ABRIKOSOV. *Zh. Eksp. Teor. Fiz*, **39**:1781, (1960). 45

[152] L.Y. VINNIKOV, T.M. ARTEMOV, I.S. VESHCHUNOV, N.D. ZHIGADLO, J. KARPINSKI, P. POPOVICH, D.L. SUND, C.T. LIND, AND A.V. BORIS. *JETP Lett.*, **90**:299, (2009). 61, 90, 96, 111, 112

[153] M. A. TANATAR, J.-PH. REID, H. SHAKERIPOUR, X.G. LUO, N. DOIRON LEYRAUD, N. NI, S.L. BUD'KO, P.C. CANFIELD, R. PROZOROV, AND L. TAILLEFER. *Phys. Rev. Lett.*, **104**:067002, (2010). xiv, 51, 163

[154] M. D. JOHANNES AND I. I. MAZIN. *Phys. Rev. B*, **79**:220510, (2009). 41

[155] M. FUGLSANG JENSEN, V. BROUET, E. PAPALAZAROU, A. NICOLAOU, A. TALEB IBRAHIMI, P. LE FEVRE, F. BERTRAN, AND D. COLSON A. FORGET. *Phys. Rev. B*, **84**:014509, (2011). 39

[156] M. KONCZYKOWSKI, C.J. VAN DER BEEK, M.A. TANATAR, H. LUO, Z. WANG, B. SHEN, H.-H. WEN, AND R. PROZOROV. *Phys. Rev. B*, **86**:024515, (2012). xix, 124, 125, 173, 174, 180

[157] M. KONCZYKOWSKI, C.J. VAN DER BEEK, M.A. TANATAR, V. MOSSER, Y.J. SONG, Y.S. KWON, AND R. PROZOROV. *Phys. Rev. B*, **84**:180514, (2011). xix, 115, 121, 123, 173, 174

[158] M. KONCZYKOWSKI, S. DEMIRDIŞ, C.J. VAN DER BEEK, R. PROZOROV, M.A. TANATAR, P.C. CANFIELD, S. KASAHARA, T. SHIBAUCHI, AND Y. MATSUDA. *Bulletin of the American Physical Society*, (56), (2011). 58, 174

[159] M. KONCZYKOWSKI, V. M. VINOKUR, F. RULLIER ALBENQUE, Y. YESHURUN, AND F. HOLTZBERG. *Phys. Rev. B*, **47**:5531–5534, 1993. 26

[160] M. R. TRUNIN. *Journal of Superconductivity*, **11**:381–408, (1998). xxi, 159, 160

[161] M. ROTTER, C. HIEKE, AND D. JOHRENDT. *Phys. Rev. B*, **82**:014513, (2010). 37, 134, 163

[162] M. ROTTER, M. PANGERL, M. TEGEL, AND D. JOHRENDT. *Angewand Te Chemie International Edition*, **47**:7949–7952, (2008). 35, 163

[163] M. ROTTER, M. TEGEL, AND D. JOHRENDT. *Phys. Rev. Lett.*, **101**:107006, (2008).

[164] M. TINKHAM. *Introduction to Supeconductivity*. Dover Publications, inc, second edition edition, (2004). xxi, 12, 84, 146, 148

[165] M. TORTELLO, D. DAGHERO, G. A. UMMARINO, V. A. STEPANOV, J. JIANG, J. D. WEISS, E. E. HELLSTROM, AND R. S. GONNELLI. *Phys. Rev. Lett.*, **105**:237002, (2010). 55

[166] M. V. FEIGEL'MAN, V. B. GESHKENBEIN, A. I. LARKIN, AND V. M. VINOKUR. *Phys. Rev. Lett.*, **63**:2303–2306, (1989). 26, 29

[167] M. YAMASHITA, Y. SENSHU, T. SHIBAUCHI, S. KASAHARA, K. HASHIMOTO, D. WATANABE, H. IKEDA, T. TERASHIMA, I. VEKHTER, A.B. VORONTSOV, AND Y. MATSUDA. *Phys. Rev. B*, **84**:060507, (2011). 44, 52, 112

[168] M. YI, D. H. LU, J. G. ANALYTIS, J.-H. CHU, S.-K. MO, R.-H. HE, M. HASHIMOTO, R. G. MOORE, I.I. MAZIN, D. J. SINGH, Z. HUSSAIN, I. R. FISHER, AND Z.-X. SHEN. *Phys. Rev. B*, **80**:174510, (2009). 39

[169] FOURNET G. FRANZINETTI M. MILLERON, P.F. *J. Low Temp. Phys.*, **4**(545), (1971). 85

[170] M.P. MALEY, J.O. WILLIS, H. LESSURE, AND M.E. MCHENRY. *Phys. Rev. B*, **42**:2639–2642, (1990). 124

[171] M.R. ESKILDSEN, L. YA. VINNIKOV, I.S. VESHCHUNOV, T.M. ARTEMOVA, T.D. BLASIUS, J.M. DENSMORE, C.D. DEWHURST, N. NI, A. KREYSSIG, S.L. BUD'KO, P.C. CANFIELD, AND A.I. GOLDMAN. *Physica C*, **469**:529, (2009). 61, 90, 96, 109, 111, 112

[172] M.R. ESKILDSEN, L. YA. VINNIKOV, T.D. BLASIUS, I.S. VESHCHUNOV, T.M. ARTEMOVA, J.M. DENSMORE, C.D. DEWHURST, N. NI, A. KREYSSIG, S. L. BUD'KO, P.C. CANFIELD, AND A. I. GOLDMAN. *Phys. Rev. B*, **79**:100501, (2009). 61, 111, 112

[173] M.ROTTER, M. TEGEL, I. SCHELLENBERG, F. M. SCHAPPACHER, R. POTTGEN, J. DEISENHOFER, A. GUNTHER, F. SCHRETTLE, A. LOIDL, AND D. JOHRENDT. *New Journal of Physics*, **11**:025014, (2009). 37

[174] M.V. MARCHEVSKY. PhD thesis, Leiden University, (1997). 89

[175] P. CHENG, B. SHEN, J. HU, AND H.-H. WEN. *Phys. Rev. B*, **81**:174529, (2010). 165

[176] P. H. KES, J. AARTS, J. VAN DEN BERG, C. J. VAN DER BEEK, AND J. A. MYDOSH. *Sup. Sci. and Tech.*, **1**:242, (1989). 27

[177] P. J. HIRSCHFELD, M. M. KORSHUNOV, AND I. I. MAZIN. *Reports on Progress in Physics*, **74**:124508, (2011). xiv, 44, 45, 46, 56

[178] P. KIM, Z. YAO, C.A. BOLLE, AND C.M. LIEBER. *Z. Phys.*, **11**:609, (1910). 90

[179] P. KIM, Z. YAO, C.A. BOLLE, AND C.M. LIEBER. *Phys. Rev. B*, **60**:12589–12592, (1999). 26, 90

[180] P. MOREL AND P. W. ERSON. *Phys. Rev.*, **125**:1263–1271, (1962). 6

[181] P. SAMUELY, Z. PRIBULOVA, P. SZABO, G. PRISTAS, S.L. BUD'KO, AND P.C. CANFIELD. *Physica C*, **469**:507 – 511, (2009). 55

[182] P. SPATHIS, S. COLSON, F. YANG, C.J. VAN DER BEEK, P. GIERLOWSKI, T. SHIBAUCHI, Y. MATSUDA, M. GAIFULLIN, M. LI, AND P.H. KES. *Phys. Rev. B*, **77**:104503, (2008). 166

[183] P. SZABO, Z. PRIBULOVA, G. PRISTAS, S.L. BUD'KO, P.C. CANFIELD, AND P. SAMUELY. *Phys. Rev. B*, **79**:012503, (2009). 55

[184] P. W. ERSON. *Phys. Rev. Lett.*, **9**:309, (1962). 6

[185] Q. HUANG, Q. QIU, W. BAO, M.A. GREEN, J. W. LYNN, Y. C. GASPAROVIC, T. WU, G. WU, AND X. H. CHEN. *Phys. Rev. Lett.*, **101**:257003, (2008). 40

[186] R. A. WALDRON. *Theory of Guided Electromagnetic Waves.* London: van Nostr, Reinhold., (1970). 156

[187] R. E. GLOVER AND M. TINKHAM. *Phys. Rev.*, **104**:844, (1956). 7, 12

[188] R. GRIESSEN. *Physica C*, **172**:441 – 449, (1991). 27

[189] R. HARRINGTON. *Time-Harmonic Electromagnetic Fields.* Mc Graw Hill Newyork, (1961).

[190] R. JIN, M. H. PAN, X. B. HE, G. LI, D. LI, R.-W. PENG, J. R. THOMPSON, B. C. SALES, A. S. SEFAT, M. A. MCGUIRE, D. M. RUS, J. F. WENDELKEN, V. KEPPENS, AND E. W. PLUMMER. *Sup. Sci. and Tech.*, **23**:054005, (2010). 55

[191] R. KLINGELER, N. LEPS, I. HELLMANN, A. POPA, U. STOCKERT, C. HESS, V. KATAEV, H.J. GRAFE, F. HAMMERATH, G. LANG, S. WURMEHL, G. BEHR, L. HARNAGEA, S. SINGH, AND B. BUCHNER. *Phys. Rev. B*, **81**:024506, (2010). 40

[192] R. M. FERNANDES AND J. SCHMALIAN. *Phys. Rev. B*, **82**:014521, (2010). 39

[193] R. OSBORN, S. ROSENKRANZ, E.A. GOREMYCHKIN, AND A.D. CHRISTIANSON. *Physica C*, **469**:498, (2009). 54

[194] R. PROZOROV, M.A. TANATAR, B. SHEN, P. CHENG, H.-H. WEN, S.L. BUD'KO, AND P.C. CANFIELD. *Phys. Rev. B*, **82**:180513, (2010). 128

[195] R. PROZOROV, M.A. TANATAR, N. NI, A. KREYSSIG, S. NANDI, S.L. BUD'KO, A.I. GOLDMAN, AND P.C. CANFIELD. *Phys. Rev. B*, **80**:174517, (2009). 95

[196] R. PROZOROV, M.A. TANATAR, R.T. GORDON, C. MARTIN, H. KIM, V.G. KOGAN, N. NI, M.E. TILLMAN, S.L. BUD'KO, AND P.C. CANFIELD. *Physica C*, **469**:582–589, (2009). 47, 60, 80, 89, 100, 126

[197] R. PROZOROV, N. NI, M. A. TANATAR, V.G. KOGAN, R.T. GORDON, C. MARTIN, E.C. BLOMBERG, P. PROMMAPAN, J.Q. YAN, S.L. BUD'KO, AND P.C. CANFIELD. *Phys. Rev. B*, **78**:224506, (2008). 60, 95

[198] R. PROZOROV AND V. G. KOGAN. *Reports on Progress in Physics*, **74**:124505, (2011). 56, 57, 164

[199] R. S. GONNELLI, D. DAGHERO, M. TORTELLO, G. A. UMMARINO, V. A. STEPANOV, J. S. KIM, AND R. K. KREMER. *Phys. Rev. B*, **79**:184526, (2009). 55

[200] R.I. HUTCHINSON, P.A. LAVIN, AND J.R. MOON. *Journal of Scientific Instruments*, **42**, (1965). 83, 84

[201] R.R. CONTE. *Eléments de Cryogénie*. Masson et Cie, (1970). 198, 207

[202] R.T. GORDON, C. MARTIN, H. KIM, N. NI, M.A. TANATAR, J. SCHMALIAN, I.I. MAZIN, S.L. BUD'KO, P.C. CANFIELD, AND R. PROZOROV. *Phys. Rev. B*, **79**:100506, (2009). 56, 57

[203] R.T. GORDON, H. KIM, M.A. TANATAR, R. PROZOROV, AND V.G. KOGAN. *Phys. Rev. B*, **81**:180501, (2010). 56, 57

[204] R.T. GORDON, N. NI, C C. MARTIN, M.A. TANATAR, M.D. VANNETTE, H. KIM, G.D. SAMOLYUK, J. SCHMALIAN, S. NANDI, A. KREYSSIG A.I. GOLDMAN, J.Q. YAN, S.L. BUD'KO, P.C. CANFIELD, AND R. PROZOROV. *Phys. Rev. Lett.*, **102**:127004, (2009). 47, 56, 57

[205] S. DEMIRDIŞ, C. J. VAN DER BEEK, Y. FASANO, H. PASTORIZA, M. KONCZYKOWSKI, S. KASAHARA, T. SHIBAUCHI, AND Y. MATSUDA. *(Preprint)*, (2012). 60, 174

[206] S. DEMIRDIŞ, C. J. VAN DER BEEK, Y. FASANO, N. R. CEJAS BOLECEK, H. PASTORIZA, D. COLSON, AND F. RULLIER ALBENQUE. *Phys. Rev. B*, **84**:094517, (2011). xxiii, 59, 60, 111, 112, 126, 127, 128, 130, 132, 170, 190

[207] S. JIANG, H. XING, G. XUAN, C. WANG, Z. REN, C. FENG, J. DAI, Z.A. XU, AND G. CAO. *Journal of Physics: Condensed Matter*, **21**:382203, (2009). 35, 163, 182

[208] S. K. KIM, M. E. TILLMAN, H. KIM, A KRACHER, S. L. BUD'KO, R. PROZOROV, AND P. C. CANFIELD. *Sup. Sci. and Tech.*, **23**:054008, (2010). 49

[209] S. KASAHARA, T. SHIBAUCHI, K. HASHIMOTO, K. IKADA, S. TONEGAWA, R. OKAZAKI, H. SHISHIDO, H. IKEDA, H. TAKEYA, K. HIRATA, T. TERASHIMA, AND Y. MATSUDA. *Phys. Rev. B*, **81**:184519, (2010). 81, 112, 115, 127

[210] S. LI, C. DE LA CRUZ, Q. HUANG, Y. CHEN, J.W. LYNN, J. HU, Y.-L. HUANG, F.-C. HSU, K.-W. YEH, M.-K. WU, AND P. DAI. *Phys. Rev. B*, **79**:054503, (2009). 41

[211] S. ONARI AND H. KONTANI. *Phys. Rev. Lett.*, **103**:177001, (2009). 45, 56, 163, 164

[212] S. ONARI AND H. KONTANI. *Phys. Rev. B*, **84**:144518, (2011). 54

[213] S. ONARI AND M. SATO H. KONTANI. *Phys. Rev. B*, **81**:060504, (2010). 54

[214] S. SHARMA, A. BHARATHI, R. SHARAT, V. RAGHAVENDRA, S. PAULRAJ, A.T. SATYA, V.S. SASTRY, A. GUPTA, AND C. S. SUNDAR. *Phys. Rev. B*, **81**:174512, (2010). 35, 163

[215] S. YUKO AND K. HIROSHI. *Journal of The Physical Society of Japan*, **77**:113710, (2008). 163

[216] S.L. BUD'KO, N. NI, AND P.C. CANFIELD. *Phys. Rev. B*, **79**:220516, (2009). xiv, 49, 50

[217] T. GIAMARCHI AND P. LE DOUSSAL. *Phys. Rev. B*, **55**:6577–6583, (1997). 90

[218] T. HANAGURI, S. NIITAKA, K. KUROKI, AND H. TAKAGI. *Science*, **328**:474–476, (2010). 56

[219] T. IYE, Y. NAKAI, S. KITAGAWA, K. ISHIDA, S. KASAHARA, T. SHIBAUCHI, Y. MATSUDA, AND T. TERASHIMA. *journal of the physical society of japan*, **81**:033701, (2012). 112

[220] T. KONDO, R. M. FERNANDES, R. KHASANOV, C. LIU, A. D. PALCZEWSKI, N. NI, M. SHI, A. BOSTWICK, E. ROTENBERG, J. SCHMALIANAND S. L. BUD'KO, P. C. CANFIELD, AND A. KAMINSKI. *Phys. Rev. B*, **81**:060507, (2010). 39, 52

[221] T. PARK AND M. B. SALAMON. *Mod. Phys. Lett. B*, **18**:1205–1223, (2004). 49

[222] T. QIAN, X.-P. WANG, W.-C. JIN, P. ZHANG, P. RICHARD, G. XU, X. DAI, Z. FANG, J.-G. GUO, X.-L. CHEN, AND H. DING. *Phys. Rev. Lett.*, **106**:187001, (2011). 163

[223] T. TAMEGAI, T. TAEN, Y. TSUCHIYA, Y. NAKAJIMA, S. OKAYASU, AND M. SASASE. *Journal of Superconductivity And Novel Magnetism*, **23**:605–608, (2010). 80

[224] T. Y. CHEN, Z. TESANOVIC, R. H. LIU, X. H. CHEN, AND C. L. CHIEN. *Nature*, **453**:0028–0836, (2008). 55

[225] T. YILDIRIM. *Phys. Rev. Lett.*, **101**:057010, (2008). 41

[226] T.M. CHUANG, M. P. ALLAN, J. LEE, Y. XIE, N. NI, S. L. BUD'KO, G. S. BOEBINGER, P. C. CANFIELD, AND J. C. DAVIS. **327**:181–184, (2010). 56

[227] V. B. GESHKENBEIN AND A. I. LARKIN. *Zh. Eksp. Teor. Fiz.*, **95**:1108–1112, (1989). 27

[228] V. BARZYKIN AND L. GOR'KOV. *JETP Lett.*, **88**:131–135, (2008). 44

[229] V. BROUET, F. RULLIER ALBENQUE, M. MARSI, B. MANSART, M. AICHHORN, S. BIERMANN, J. FAURE, L. PERFETTI, A. TALEB IBRAHIMI, P. LE FEVRE, F. BERTRAN, A. FORGET, AND D. COLSON. *Phys. Rev. Lett.*, **105**:087001, (2010). 39

[230] V. BROUET, M. FUGLSANG JENSEN, P. H. LIN, A. TALEB IBRAHIMI, P. LE FEVRE, F. BERTRAN, C. H. LIN, W. KU, A. FORGET, AND D. COLSON. *Phys. Rev. B*, **86**:075123, (2012). 39

[231] V. BROUET, M. MARSI, B. MANSART, A. NICOLAOU, A. TALEB IBRAHIMI, P. LE FEVRE, F. BERTRAN, F. RULLIER ALBENQUE, A. FORGET, AND D. COLSON. *Phys. Rev. B*, **80**:165, (2009). 52

[232] V. L. GINZBURG AND AU L. D. L. *Zh. Eksperim. I. Teor. Fiz.*, **20**:1064, (1950). 14, 15

[233] V. M. VINOKUR, M. V. FEIGEL'MAN, AND V.B. GESHKENBEIN. *Phys. Rev. Lett.*, **67**:915–918, 1991. 27

[234] V. MISHRA, G. BOYD, S. GRASER, T. MAIER, P.J. HIRSCHFELD, AND D.J. SCALAPINO. *Phys. Rev. B*, **79**:094512, (2009). 165

[235] V.B. GESHKENBEIN, M.V. FEIGEL'MAN, AND V.M. VINOKUR. *Physica C*, **185-189, Part 4**:2511 – 2512, (1991). 124

[236] V.G. KOGAN. *Phys. Rev. B*, **80**:214532, (2009). 47, 56, 57, 164

[237] V.L. GINZBURG. *Il Nuovo Cimento*, **2**:1234, (1955). 14, 15

[238] W. BAO, Q-.Z. HUANG, G.-F. CHEN, M. A. GREEN, D.-M. WANG, J.-B. HE, AND Y.-M. QIU. *Chinese Phys. Lett.*, **28**:086104, (2011). 45, 55

[239] W. C. ELMORE. *Physical Review*, **54**:1092–1095, (1938). 83

[240] W. EIDELLOTH AND R.L. SANDSTROM. *Appl. Phys. Lett.* 116

[241] W. H. HARTWIG AND C. PASSOW. *Appl. Sup.*, **11**:541, (1975). 157

[242] W. KNUDSEN. *Annalen der Physik*, **6**:6577–6583, (1930). 198

[243] W. L. MCMILLAN. *Phys. Rev.*, **167**:331–344, (1968). 6

[244] W. MALAEB, T. YOSHIDA, A. FUJIMORI, M. KUBOTA, K. ONO, K. KIHOU, P. M. SHIRAGE, HIJIRI KITO, A. IYO, H. EISAKI, Y. NAKAJIMA, T. TAMEGAI, AND R. ARITA. *Journal of the Physical Society of Japan*, **78**:123706, (2009). 39

[245] W. MEISSNER AND R. OCHSENFELD. *Natur Wissen Schaffen*, **787**, (1933). 5

[246] W. S. CORAK, B. B. GOODMAN, C. B. SATTERTHWAITE, AND A. WEXLER. *Phys. Rev.*, **96**:1442–1444, (1954). 7

[247] W. S. CORAK, B. B. GOODMAN, C. B. SATTERTHWAITE, AND A. WEXLER. *Phys. Rev.*, **102**:656, (1956). 7

[248] W.H. KLEINER, L.M. ROTH, AND S.H. AUTLER. *Phys. Rev. A*, **133**:1226, (1964). 17

[249] W.N. HARDY, D.A. BONN, D.C. MORGAN, R. LIANG, AND K. ZHANG. *Phys. Rev. Lett.*, **70**:3999–4002, (1993). 156

[250] W.N. HARDY, S. KAMAL, AND D.A. BONN. *The Gap Symmetry , Fluctuations in High-T_c Superconductors.* J. Bok, G. Deutscher, D. Pavuna, S. A. Wolf, Plenum Press, (1998). 156

[251] X. G. LUO, M. A. TANATAR, J.-PH. REID, H. SHAKERIPOUR, N. DOIRON LEYRAUD, N. NI, S. L. BUD'KO, P. C. CANFIELD, H. LUO, Z. WANG, H.-H. WEN, R. PROZOROV, AND L. TAILLEFER. *Phys. Rev. B*, **80**:140503, (2009). 51

[252] X.-L. WANG, S.R. GHORBANI, S.-I. LEE, S.X. DOU, C.T. LIN, T.H. JOHANSEN, K.-H. MÜLLER, Z.X. CHENG, G. PELECKIS, M. SHABAZI, A.J. QVILLER, V.V. YURCHENKO, G.L. SUN, AND D. L. SUN. *Phys. Rev. B*, **82**:024525, (2010). 58

[253] X. LIN, C. SHEN, C. LV, J. MIAO, H. TAN, G. CAO, AND Z.-A. XU. *Journal of Physics: Condensed Matter*, **23**:464203, (2011). 57

[254] X. LU, W. K. PARK, H. Q. YUAN, G. F. CHEN, G. L. LUO, N. L. WANG, A. S. SEFAT, M. A. MCGUIRE, R. JIN, B. C. SALES, AND J. GILLETT S. E. SEBASTIAN L. H. GREENE D. M., RUS. *Sup. Sci. and Tech.*, **23**:054009, (2010). 38

[255] X. LU, W. K. PARK, H. Q. YUAN, G. F. CHEN, G. L. LUO, N. L. WANG, A. S. SEFAT, M. A. MCGUIRE, R. JIN, B. C. SALES, AND S. E. SEBASTIAN L. H. GREENE D. M. RUS, J. GILLETT. *Sup. Sci. and Tech.*, **23**:054009, (2010). 55

[256] X.C. WANG, Q.Q. LIU, Y.X. LV, W.B. GAO, L.X. YANG, R.C. YU, F.Y. LI, AND C.Q. JIN. *Solid State Comm.*, **148**:538 – 540, (2008). 35

[257] Y. ABULAFIA, A. SHAULOV, Y. WOLFUS, R. PROZOROV, I. BURLACHKOV, Y. YESHURUN, D. MAJER, E. ZELDOV, AND V. M. VINOKUR. *Phys. Rev. Lett.*, **75**:2404–2407, (1995). xix, 124, 125

[258] Y. BANG. *Sup. Sci. and Tech.*, **25**:084002, (2012). 112

[259] Y. BANG, H.-Y. CHOI, AND H. WON. *Phys. Rev. B*, **79**:054529, (2009). 46

[260] Y. FASANO. PhD thesis, Instituto Balseiro, CNEA Bariloche, Argentina, (2003).

[261] Y. FASANO, I. MAGGIO APRILE, N.D. ZHIGADLO, S. KATRYCH, J. KARPINSKI, AND Ø. FISCHER. *Phys. Rev. Lett.*, **105**:167005, (2010). 91

[262] Y. FASANO, M. DE SETA, M. MENGHINI, H. PASTORIZA, AND F. DE LA CRUZ. *PNAS*, **102**:3898–3902, (2005). 101

[263] Y. FASANO AND M. MENGHINI. *Sup. Sci. and Tech.*, **21**:023001, (2008). 84, 92, 95

[264] Y. KAMIHARA, H. HIRAMATSU, M. HIRANO, R. KAWAMURA, H. YANAGI, T. KAMIYA, AND H. HOSONO. *J. Am. Chem. Soc.*, **128**:10012–10013, (2006). 33

[265] Y. KAMIHARA, T. WATANABE, M. HIRANO, AND H. HOSONO. *JACS*, **130**:3296–3297, (2008). 33, 34

[266] Y. LAPLACE, J. BOBROFF, F. RULLIER ALBENQUE, D. COLSON, AND A. FORGET. *Phys. Rev. B*, **80**:140501, (2009). 38

[267] Y. MIZUGUCHI, F. TOMIOKA QND S. TSUDA, T. YAMAGUCHI, AND Y. TAKANO. *Appl. Phys. Lett.*, **94**:012503, (2009). 34

[268] Y. NAGAI AND K. KUROKI. *Phys. Rev. B*, **83**:220516, (2011). 54

[269] Y. NAKAI, T. IYE, S. KITAGAWA, K. ISHIDA, S. KASAHARA, T. SHIBAUCHI, Y. MATSUDA, AND T. TERASHIMA. *Phys. Rev. B*, **81**:020503, (2010). 44, 53

[270] Y. NAKAI, T. IYE, S. KITAGAWA, K. ISHIDA, S. KASAHARA, T. SHIBAUCHI, Y. MATSUDA, AND T. TERASHIMA. *Phys. Rev. B*, **81**:020503, (2010). 53

[271] Y. NAKAJIMA, T. TAEN, Y. TSUCHIYA, T. TAMEGAI, H. KITAMURA, AND T. MURAKAMI. *Phys. Rev. B*, **82**:220504, (2010). 45, 57, 165, 166

[272] Y. QIU, W. BAO, Q. HUANG, T. YILDIRIM, J.M. SIMMONS, M.A. GREEN, J.W. LYNN, Y.C. GASPAROVIC, J. LI, T. WU, G. WU, AND X.H. CHEN. *Phys. Rev. Lett.*, **101**:257002, (2008). 38, 53

[273] Y. SU, P. LINK, A. SCHNEIDEWIND, T. WOLF, P. ADELMANN, Y. XIAO, M. MEVEN, R. MITTAL, M. ROTTER, D. JOHRENDT, T. BRUECKEL, AND M. LOEWENHAUPT. *Phys. Rev. B*, **79**:064504, (2009). 40

[274] Y. WANG, A. KREISEL, P.J. HIRSCHFELD, AND V. MISHRA. *arXiv:1210.7474v1*, (2012). 188

[275] Y. WANG, B. REVAZ, R. ERBAND, AND A. JUNOD. *Phys. Rev. B*, **63**:094508, (2001). 49

[276] Y. YIN, M. ZECH, T. L. WILLIAMS, X. F. WANG, G. WU, X. H. CHEN, AND J. E. HOFFMAN. *Phys. Rev. Lett.*, **102**:097002, (2009). 89, 91

[277] Y. YIN, M. ZECH, T.L. WILLIAMS, AND J.E. HOFFMAN. *Physica C*, **469**:535–544, 2009. xiv, 2, 58, 90, 91, 109

[278] YA. G. PONOMAREV, S. A. KUZMICHEV, M. G. MIKHEEV, M. V. SUDAKOVA, S. N. TCHESNOKOV, O. S. VOLKOVA, A. N. VASILIEV, T. HANKE, C. HESS, G. BEHR, R. KLINGELER, AND B. BUCHNER. *Phys. Rev. B*, **79**:224517, (2009). 41

[279] Y.N. OVCHINNIKOV AND B.I. IVLEV. *Phys. Rev. B*, **43**:8024–8029, (1991). 30